

Engineering Journal

Fourth Quarter 2022 | Volume 59, No. 4



Smarter.
Stronger.
Steel.

- 239 A Critical Evaluation of Moment Gradient (C_b) Factor Calculation Procedures for Singly Symmetric I-Section Members
Ryan Slein, Woo Yong Jeong, and Donald W. White
- 275 A Novel Performance-Based Evaluation Method of Built-Up Wide-Flange Steel Columns Subjected to Close-Range Detonations
Yongwook Kim, Salvatore Florio, and Qian Wang
- 313 Reliability of HSS Cross Connections in Branch Axial Compression
Dillon F. Rudman, Quanhan Xi, Jeffrey A. Packer, and Kyle Tousignant
- Steel Structures Research Update
- 337 Future Hot-Rolled Asymmetric Steel I-Beams
Judy Liu

Engineering Journal

American Institute of Steel Construction

Dedicated to the development and improvement of steel construction, through the interchange of ideas, experiences, and data.

Editorial Staff

Editor	Margaret A. Matthew, PE
Managing Editor	Keith A. Grubb, SE, PE
Research Editor	Judy Liu, PhD
Production Editor	Kristin Hall

Officers

Chair
Stephen H. Knitter

Vice Chair
Hugh J. McCaffrey

Secretary/Legal Counsel
Edward Seglias

President
Charles J. Carter, SE, PE, PhD

Senior Vice Presidents
Scott L. Melnick
Mark W. Trimble, PE

Vice Presidents
Todd Alwood
Carly Hurd, CAE
Lawrence F. Kruth, PE
Christopher H. Raebel, SE, PE, PhD
Michael Mospan
Brian Raff

The articles contained herein are not intended to represent official attitudes, recommendations or policies of the Institute. The Institute is not responsible for any statements made or opinions expressed by contributors to this Journal.

The opinions of the authors herein do not represent an official position of the Institute, and in every case the officially adopted publications of the Institute will control and supersede any suggestions or modifications contained in any articles herein.

The information presented herein is based on recognized engineering principles and is for general information only. While it is believed to be accurate, this information should not be applied to any specific application without competent professional examination and verification by a licensed professional engineer. Anyone making use of this information assumes all liability arising from such use.

Manuscripts are welcomed, but publication cannot be guaranteed. All manuscripts should be submitted in duplicate. Authors do not receive a remuneration. Guidelines for authors are printed on the inside back cover.

Engineering Journal (ISSN 0013-8029) is published quarterly. Subscriptions: Members: one subscription, \$40 per year, included in dues; Additional Member Subscriptions: \$40 per year. Non-Members U.S.: \$160 per year. Foreign (Canada and Mexico): Members \$80 per year. Non-Members \$160 per year. Published by the American Institute of Steel Construction at 130 E Randolph Street, Suite 2000, Chicago, IL 60601.

Copyright 2022 by the American Institute of Steel Construction. All rights reserved. No part of this publication may be reproduced without written permission. The AISC logo is a registered trademark of AISC.

Subscriptions: subscriptions@aisc.org
312.670.2400

Archives: Search at aisc.org/ej.
Article downloads are free for current members and are available for a nominal fee for non-members.

A Critical Evaluation of Moment Gradient (C_b) Factor Calculation Procedures for Singly Symmetric I-Section Members

Ryan Slein, Woo Yong Jeong, and Donald W. White

ABSTRACT

This paper explores the manual calculation of the elastic lateral-torsional buckling resistance of prismatic singly symmetric I-section members having a variation in the bending moment between the brace points. The paper shows that the quarter-point moment gradient factor, C_b , equation in the AISC *Specification* (2016), as modified by its Commentary, is inaccurate for reverse-curvature bending of singly symmetric I-section members. The modified equation cannot accurately represent the behavior for reverse-curvature bending of singly symmetric members in general because it is blind to the sign of the bending moment. That is, it does not recognize the influence of different patterns of compression and tension in the different size flanges. Furthermore, the AISC *Specification* Commentary (ASC) calculation exhibits substantial discontinuities in its C_b values as a function of the loading considered. This is due to the application of a modifier, termed R_m , creating a step-function behavior that gives substantially conservative results in certain situations and substantially unconservative results in other cases.

In addition, the paper explains that the C_b equations in the current AASHTO *Specifications* (2020) provide some accounting for the different patterns of compression in the separate flanges for cases involving moment reversal. However, these equations are based only on the moments at the ends and at the middle of the unbraced length. Hence, they are limited in their ability to capture the influence of nonlinear variations in moment along the unbraced length. Furthermore, the AASHTO procedure uses $C_b = 1.0$ when the moment within the unbraced length is larger than the maximum brace point moment, causing compression in the flange under consideration (in single- or reverse-curvature bending). This practice can result in substantial conservatism. AASHTO recommends other methods such as the ASC approach in these cases. Lastly, the AASHTO C_b values can exhibit substantial discontinuities as a function of the loading considered. This is due to changes in the governing flange in the AASHTO procedure. This attribute also produces substantially conservative results in certain cases.

To rectify the limitations of the ASC and AASHTO methods, the paper recommends a modified form of an alternative quarter-point C_b equation proposed by Wong and Driver (2010). For singly symmetric cases involving moment reversal, the terms in the quarter-point equation are replaced by the ratio of the moments to the corresponding elastic buckling moment based on $C_b = 1$, considering which flange is in compression at each of the locations where the moments are sampled. The studies show that the Wong and Driver equation, with this modification, provides substantially improved accuracy compared to the existing AASHTO and ASC equations for reverse-curvature bending with slightly less calculation effort. In addition, the paper demonstrates the accuracy of the direct application of the Wong and Driver equation for single-curvature bending cases.

Keywords: lateral-torsional buckling, moment gradient, singly symmetric I-section members.

INTRODUCTION

Singly symmetric welded I-section members are widely employed for optimized member designs due to their structural efficiency. In the AISC *Specification for Structural Steel Buildings* (2016) and the AASHTO *LRFD Bridge Design Specifications* (2020), the lateral-torsional buckling

(LTB) resistance of unbraced lengths subjected to moment gradient is determined by multiplying the LTB resistance for uniform bending by the moment gradient factor C_b . The resistance is capped by the “plateau strength” of the member in flexure (equal to the plastic moment, M_p , for compact web I-section members, and equal to the yield moment of the compression flange multiplied by the bending strength reduction factor, $R_{pg}M_{yc}$, for slender-web members).

To determine the LTB resistance accurately under moment gradient loading, it is important to calculate an accurate C_b . The C_b factor is influenced generally by:

1. The shape of the moment diagram between the braced points.
2. The extent of the monosymmetry of the cross section.
3. The length-to-depth ratio and cross-section dimensions,

Ryan Slein, Research Affiliate, Georgia Institute of Technology, Atlanta, Ga.
Email: ryan.slein@gatech.edu; ryan.slein@dot.gov

Woo Yong Jeong, Senior Software Lead, HEXAGON (GT STRUDL), Email:
wooyong.jeong@hexagon.com

Donald W. White, Professor, Georgia Institute of Technology, Atlanta, Ga.
Email: don.white@ce.gatech.edu (corresponding)

Paper No. 2018-05R2

ISSN 0013-8029

ENGINEERING JOURNAL / FOURTH QUARTER / 2022 / 239

which influence the relative contribution of the St. Venant and warping torsional stiffnesses to the LTB resistance.

4. The elevation of the applied load relative to the mid-height of the web.
5. The degree of lateral, rotational, and warping restraint at the ends of the unbraced lengths (including continuity with and buckling interaction with adjacent unbraced segments).

Steel design specifications typically simplify their calculation procedures by considering only item 1 or items 1 and 2 in the calculation of C_b and by considering items 2 and 3 in the base calculation of the elastic LTB resistance. For slender-web members, AISC (2016) and AASHTO (2020) set the St. Venant torsion constant, J , to zero to account for the influence of web distortion. Transverse load-height effects typically are neglected. Helwig et al. (1997) provide a thorough discussion of when this simplification is and is not appropriate. In addition, warping and minor-axis rotations are assumed unrestrained at the ends of member unbraced lengths, and the influence of continuity with adjacent unbraced lengths (typically referred to as interaction buckling) is neglected. For this reason, this paper evaluates manual C_b calculations that consider only the influence of item 1 for single-curvature bending, and include both items 1 and 2 for reverse-curvature bending. Comparisons are made to benchmark elastic LTB numerical solutions that account for items 1, 2, and 3. These benchmark solutions are conducted with any transverse loads applied at the mid-height of the web. Helwig et al. show that this position, rather than the shear center, is the proper transverse load location for the development of base C_b equations that neglect load height. Helwig et al. find, for single-curvature bending cases, that the degree of monosymmetry does not affect the C_b values and also that the base C_b values derived for doubly symmetric members work well when the load position is defined at the web mid-height rather than the shear center. Downward transverse loads applied at a location above the web mid-height cause destabilizing effects, and downward transverse loads applied at a location below the web mid-height cause stabilizing effects. Helwig et al. recommend a simple adjustment to the base C_b equations that gives a coarse approximation of load height effects, and they discuss in detail when these effects need or do not need to be included in design calculations.

Studies of the moment gradient factor, C_b , often have emphasized cases where the entire span is unbraced and subjected to applied transverse loads and the end moments are based on ideally pinned or fixed boundary conditions. While it is important to predict the LTB resistance in these cases, there is at least some bracing within the span in many situations. The moment diagrams within the individual unbraced lengths tend to be close to linear when only

a few intermediate braces are provided. Furthermore, the moment diagrams for vertical members such as columns commonly are close to being linear. In addition, fixed end conditions are rare in practice, typically occurring only due to symmetry of the loading and the geometry. In this study, a broad range of loadings are considered, producing both linear and near-linear moment diagrams as well as a range of end moments relative to the moments from transverse loading. The loading cases studied encompass and expand upon the loadings considered in the prior studies by Helwig et al. (1997) and Wong and Driver (2010).

While the AASHTO (2020) C_b equations apply to both doubly and singly symmetric I-section members, the AISC *Specification* (2016) provides only one equation for C_b and references its Commentary for the handling of single symmetry. This paper shows that the current AASHTO and AISC *Specification* Commentary (ASC) predictions of the LTB resistance for singly symmetric I-section members subjected to moment reversal are often poor. To address this problem, the paper investigates and demonstrates a modification of the Wong and Driver (2010) C_b equation that results in a significant improvement in the accuracy of the LTB assessment for a complete range of doubly and singly symmetric member design situations while maintaining simplicity of the calculations. In addition to addressing the challenges for reverse-curvature bending, the paper demonstrates the accuracy of the direct application of this equation for single-curvature bending cases. These gains are achieved with effectively no change in the overall calculation effort relative to the current methods.

BACKGROUND

Calculations of C_b for singly symmetric I-section members typically involve modifications or extensions of C_b equations developed for doubly symmetric members. Therefore, it is essential to understand several particulars of C_b estimates for doubly symmetric members when considering predictions involving single symmetry. Wong and Driver (2010) evaluated a broad range of approaches recommended in the literature for the calculation of C_b for doubly symmetric I-section members. They proposed a new quarter-point C_b formula that maintains simplicity of the design calculations and provides measurable improvements in overall accuracy relative to other methods in the literature, including the AISC (2016) and AASHTO (2020) C_b equations. Figure 1 compares the result from the Wong and Driver C_b equation to the corresponding AISC and AASHTO equations for the basic case of linear moment diagrams. The AASHTO equation, discussed subsequently, uses a maximum cap of 2.3 and was originally developed as a lower-bound fit to solutions from Salvadori (1956) for linear moment diagram cases. However, other references [e.g., Ziemian (2010)] have

employed a larger cap of 2.5 or 2.56 with this equation. The AASHTO equation with a cap of 2.5 is shown to provide an appropriate lower bound of benchmark C_b values for a comprehensive range of cases in Slein et al. (2021) and is thus employed in Figure 1. Wong and Driver (2010) also suggest a maximum cap of 2.5 on their equation, although they state that their equation produces good results without this limit. Slein et al. confirm this is the case. For linear moment diagrams, the Wong and Driver equation gives a maximum value of 2.41.

Figure 2 plots the ratio of the Wong and Driver equation and AISC *Specification* Equation F1-1 to the AASHTO equation for linear moment diagram cases. This paper demonstrates that the AASHTO equation with a maximum limit of 2.5 provides the most accurate (largest) lower bound of the equations considered for these types of moment diagrams. The Wong and Driver quarter-point equation provides a reasonable conservative estimate for this case. One can observe that the AISC equation, which is also a quarter-point formula, gives results as much as 5.0% conservative

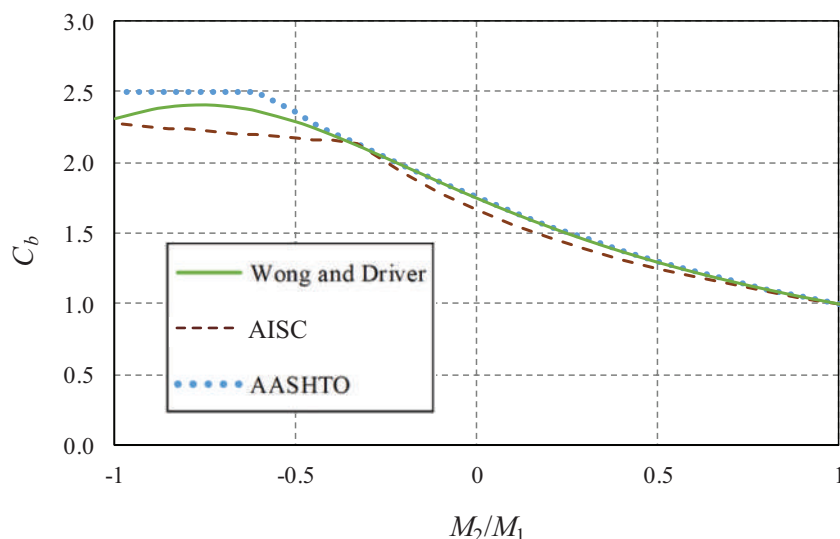


Fig. 1. Comparison of Wong and Driver, AISC, and AASHTO C_b values versus the ratio of the smaller to larger end moments, M_1/M_2 , for linear moment diagram cases.

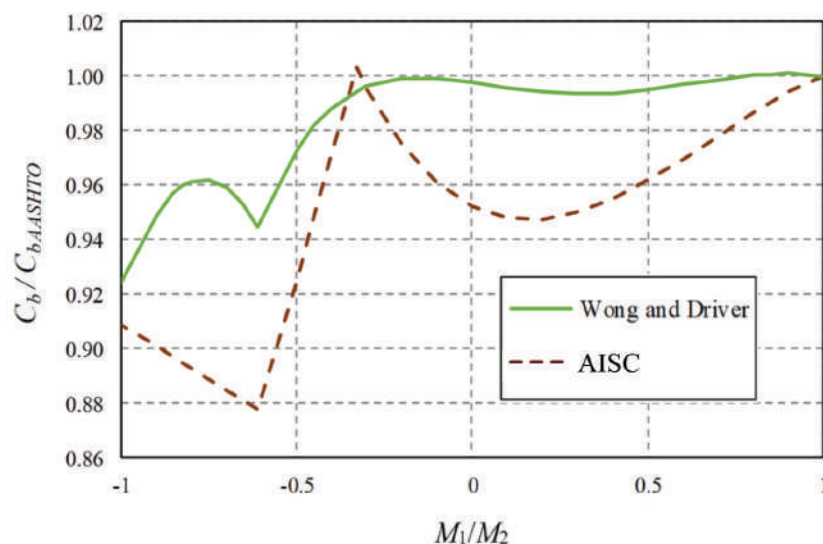


Fig. 2. Ratio of C_b values from Wong and Driver and AISC to the AASHTO lower-bound C_b estimate versus the ratio of the smaller-to-larger end moments, M_1/M_2 , for linear moment diagram cases.

even for single-curvature bending (corresponding to a positive ratio of the smaller-to-larger end moments, M_1/M_2). For reverse-curvature bending cases, the AISC estimate can be as much as 12% conservative relative to the AASHTO lower-bound estimate.

Furthermore, Wong and Driver show that the AISC equation overestimates the C_b values from refined benchmark solutions for unbraced lengths containing a concentrated transverse load at the mid-length combined with restraining end moments as shown in Figure 3 when $0.6 < \beta < 1.1$, where β is the ratio of the actual end moments to the end moments for a fixed-end beam. They find that the largest unconservative error occurs for the case with $\beta = 1.0$. For this case with $\beta = 1.0$, the quarter-point Equation F1-1 in the AISC Specification gives $C_b = 1.92$, whereas benchmark solutions in this research range from 1.69 to 1.72, depending on the relative contributions from St. Venant and warping torsion. The proposed Wong and Driver formula gives $C_b = 1.41$, whereas the AASHTO procedure conservatively gives $C_b = 1.0$ for this problem.

While these improvements are relatively minor, they are measurable, and they provide specific reference points indicating that the Wong and Driver equation may also serve as a more appropriate base than the AISC Specification Equation F1-1 for the estimation of moment gradient effects in the context of singly symmetric I-section members.

The following subsections summarize the particulars of the AISC Specification Commentary (ASC), AASHTO, recommended, and benchmark calculations of C_b considered in this paper for singly symmetric I-section members. Appendix B provides a specific design example illustrating the relative efficiency of the ASC, AASHTO, and recommended calculations.

AISC Specification Commentary (ASC) Procedure

The AISC Specification Commentary (ASC) procedure uses the equation:

$$C_b = \left(\frac{12.5M_{max}}{2.5M_{max} + 3M_A + 4M_B + 3M_C} \right) R_m \leq 3.0 \quad \text{(AISC Spec. Comm. Eq. C-F1-3)}$$

where

M_A, M_B, M_C = absolute value of the moments at the quarter, middle, and three-quarter point locations, respectively, of the unbraced length, kip-in. (N-mm)

M_{max} = absolute value of maximum moment within the unbraced length, L_b , kip-in. (N-mm)

$R_M = 1.0$ (1a)

for doubly symmetric members and for singly symmetric members subjected to single-curvature bending, and

$$= 0.5 + 2 \left(\frac{I_{y,opp}}{I_y} \right)^2 \quad \text{(1b)}$$

for singly symmetric members subjected to reverse-curvature bending, in which

I_y = weak-axis moment of inertia of the entire section, in.⁴ (mm⁴)

$I_{y,opp}$ = moment of inertia of the flange on the opposite side of the web mid-height from the direction of the transverse loading, in.⁴ (mm⁴)

Equation 1b is the same as Equation C-F1-4 in the ASC but with $I_{y,Top}$ labeled as $I_{y,opp}$. As stated in the ASC, Equation C-F1-4 was developed by focusing on gravity loading on horizontal beams. The ASC indicates that for general cases, such as columns subjected to transverse loads, the “top” flange is defined as the flange on the opposite side of the web mid-height from the direction of the transverse loading. The notation $I_{y,opp}$ is employed in this study to avoid any confusion regarding the reference to the “top” and “bottom” flanges.

In the ASC procedure, when the unbraced length is subjected to reverse-curvature bending, C_b is first calculated from the ASC Equation C-F1-3 and Equation 1b. It is then applied to the separate elastic LTB resistances under uniform bending, M_{cr1} , corresponding to flexural compression in each of the flanges to estimate the maximum moment, causing flexural compression in the given flange, at incipient elastic LTB. The corresponding elastic buckling load ratio may be written as:

$$\gamma_{eLTB} = \min \left(\frac{C_b M_{cr1,top}}{M_{max,top}}, \frac{C_b M_{cr1,bot}}{M_{max,bot}} \right) \quad \text{(2)}$$

where the subscripts *top* and *bot* designate the “top” and “bottom” flanges of the section, as defined in the preceding text. It should be observed that Equation 2 is based on equating $\gamma_{eLTB} M_{max,top}$ to $C_b M_{cr1,top}$ for the top flange and

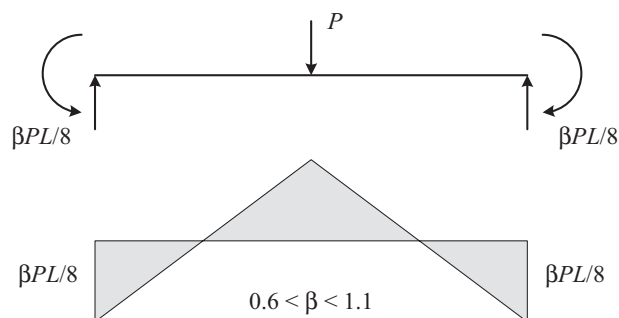


Fig. 3. Cases from Wong and Driver where the AISC C_b equation overpredicts benchmark solutions.

$\gamma_{LTB} M_{max.bot}$ to $C_b M_{cr1.bot}$ for the bottom flange. For single-curvature bending, only the direction of bending causing compression in the single compression flange is considered.

In the ASC procedure, the C_b value calculated from ASC Equation C-F1-3 applies in all cases when evaluating the elastic LTB resistance corresponding to flexural compression in the “critical flange,” which is defined as the flange having the largest M_{max}/M_{cr1} in Equation 2.

It can be observed that ASC Equation C-F1-3 is blind to the sign of the bending moment. The values input to ASC Equation C-F1-3 are all absolute values of the moments at the corresponding locations. In addition, the R_m factor does not include any consideration of the sign or the shape of the moment diagram along the unbraced length. As such, the ASC C_b calculation does not account for different patterns of compression and tension in the different size flanges for a general case involving moment reversal. The single ASC C_b value is applied to the two distinct member LTB resistances for uniform positive and negative bending, $M_{cr1.top}$ and $M_{cr1.bot}$. However, the C_b modifier being applied to these resistances does not account for where and to what extent the different flanges are being placed in flexural compression. As a result, the final solution for the LTB resistance has limited accounting for these effects.

Equation 1b for the R_m factor was derived considering only moment diagrams for fixed-fixed and propped cantilever members that have no lateral bracing throughout their entire span. Helwig et al. (1997) state that ASC Equation C-F1-3 is quite conservative for cases with linear moment diagrams in reverse-curvature bending and smaller values of $I_{y,opp}/I_y$. They refer to Kitipornchai et al. (1986) for more accurate C_b estimates in these situations. For linear moment diagrams, the AASHTO procedure gives accurate to moderately conservative calculations relative to the more complex equations presented by Kitipornchai et al. It is submitted that accurate solutions for near linear moment diagram cases are important to the design efficiency in many situations. This is because, when a member has at least some lateral bracing within its span, the shape of the moment diagram becomes relatively close to linear within each unbraced length. Furthermore, the moment diagrams for column members are typically close to being linear.

AASHTO Procedure

The AASHTO procedure is presented in terms of elastic flange stresses in Article 6.10.8, and in terms of moments in Article A6.3.3. For noncomposite prismatic I-section members, the stresses in a given flange are simply the moments divided by the elastic section modulus to the flange; therefore, the same result is obtained whether the demands are written as flange stresses or as moments. As such, for the

purposes of this paper, the AASHTO procedure is expressed entirely in terms of member moments:

For unbraced lengths where $M_{mid}/M_2 \geq 1.0$, or when $M_2 = 0$,

$$C_b = 1.0 \quad (3)$$

Otherwise,

$$C_b = 1.75 - 1.05 \frac{M_1}{M_2} + 0.3 \left(\frac{M_1}{M_2} \right)^2 \leq 2.5 \quad (4)$$

where

M_{mid} = the moment at the middle of the unbraced length taken as positive when it causes compression and negative when it causes tension in the flange being considered, kip-in. (N-mm)

M_0 = the actual moment at the brace point opposite to the one corresponding to M_2 , taken as positive when it causes compression and negative when it causes tension in the flange under consideration, kip-in. (N-mm)

M_1 = the equivalent moment at the brace point opposite to the one corresponding to M_2 , calculated as the intercept of the most critical assumed linear moment variation passing through M_2 and either M_{mid} or M_0 , whichever produces the smaller value of C_b , kip-in. (N-mm); M_1 is calculated as follows:

- When the variation in the moment along the entire unbraced length is concave in shape corresponding to the flange in compression (i.e., the stress in the flange under consideration is a smaller compressive value or a larger tensile value at the mid-length, compared to a value obtained as the average of the end moments),

$$M_1 = M_0 \quad (5)$$

- Otherwise, the moment diagram is defined as convex in shape, and

$$M_1 = 2M_{mid} - M_2 \geq M_0 \quad (6)$$

M_2 = the largest moment at either end of the unbraced length causing compression in the flange under consideration, taken as a positive value kip-in. (N-mm), except as noted in the following text; if the moment is zero or causes tension in the flange under consideration at both ends of the unbraced length, M_2 is taken as zero

The AASHTO method amounts to fitting a line from the maximum end moment through the mid-point of the moment diagram if the moment diagram is convex, and to fitting a line through both end points of the diagram if the diagram is concave. The actual maximum limit of 2.3 in AASHTO (2020) is increased to 2.5 in Equation 4 as discussed in the Background section of this paper.

For reverse-curvature bending cases, the AASHTO procedure applies Equations 3 through 6 separately to calculate a different C_b for each flange. Nonlinear moment diagrams are always concave on one flange and convex on the other in these cases. The corresponding elastic buckling load ratio is:

$$\gamma_{eLTB} = \min\left(\frac{C_{b,top}M_{cr1,top}}{M_{max,top}}, \frac{C_{b,bot}M_{cr1,bot}}{M_{max,bot}}\right) \quad (7)$$

For single-curvature bending, only the direction of bending causing compression in the single compression flange is considered.

If Equations 5 and 6 are substituted into Equation 4, the resulting calculation can be written more directly as:

$$C_b = 1.75 - 1.05\frac{M_0}{M_2} + 0.3\left(\frac{M_0}{M_2}\right)^2 \leq 2.5 \quad (8)$$

for a concave moment diagram, and

$$C_b = 3.10 - 3.30\frac{M_{mid}}{M_2} + 1.2\left(\frac{M_{mid}}{M_2}\right)^2 \leq 2.5 \quad (9)$$

for a convex moment diagram.

For reverse-curvature bending, the C_b value for the flange that governs the calculation of γ_{eLTB} in Equation 7 is considered as the “governing” C_b .

Clearly, the AASHTO procedure has a major limitation in that, when the maximum moment causing compression in the flange under consideration occurs within the unbraced length instead of at one of the ends, it simply uses $C_b = 1$. The AASHTO Commentary suggests that other methods such as the ASC procedure should be considered for the calculation of C_b in these cases.

One advantage of the AASHTO procedure is that it only requires the end moments and the moment at the middle of the unbraced length for its calculations; therefore, it may be considered as being simpler to apply. The end moments typically are readily available from a structural analysis. The quarter-point formulas require the moments at the quarter- and mid-points as well as the maximum moment within the unbraced length, requiring some additional work. However, the subsequent strength design checks also require the calculation of the maximum positive and negative moments within the unbraced length in any case; therefore, it can be argued that the quarter-point formulas are not significantly more difficult to apply.

Recommended Procedure

For singly symmetric cases, the recommended moment gradient factor calculation directly applies the quarter-point formula developed by Wong and Driver:

$$C_b = \frac{4M_{max}}{\sqrt{M_{max}^2 + 4M_A^2 + 7M_B^2 + 4M_C^2}} \quad (\text{AISC Spec. Comm. Eq. C-F1-2b})$$

However, for singly symmetric sections subjected to reverse-curvature bending, the Wong and Driver equation is modified to the following form:

$$C_b = \frac{4\left(\frac{M}{M_{cr1}}\right)_{max}}{\sqrt{\left(\frac{M}{M_{cr1}}\right)_{max}^2 + 4\left(\frac{M}{M_{cr1}}\right)_A^2 + 7\left(\frac{M}{M_{cr1}}\right)_B^2 + 4\left(\frac{M}{M_{cr1}}\right)_C^2}} \quad (10)$$

where

M_{cr1} = base elastic critical moment corresponding to the cross section at the location under consideration (i.e., location A, B, C, or the location of the maximum M/M_{cr1}), based on uniform bending causing moment producing compression in the flange subjected to compression at this location, kip-in. (N-mm)

In the recommended procedure, the elastic buckling load ratio is estimated simply as:

$$\gamma_{eLTB} = \frac{C_b}{\left(\frac{M}{M_{cr1}}\right)_{max}} \quad (11)$$

where C_b is calculated from ASC Equation C-F1-2b for single-curvature bending and from Equation 10 for reverse-curvature bending. It should be observed that Equation 11 is derived by equating $\gamma_{eLTB}M$ to C_bM_{cr1} at the location where M/M_{cr1} is maximum. For single-curvature bending, only the direction of bending causing compression in the single compression flange is considered. For reverse-curvature bending, $(M/M_{cr1})_{max}$ is taken as the largest value of $M/M_{cr1,top}$ from all the cross sections where the top flange is in compression, and $M/M_{cr1,bot}$ from all the cross sections where the bottom flange is in compression, inclusive. This is equivalent to the use of the ASC-based Equation 2, but with a more accurate C_b .

For reverse-curvature bending cases, Equation 10 incorporates essential information about the shape of the moment diagram and the demands versus a corresponding base capacity in uniform bending at the different sampling points throughout the unbraced length. The simplicity of the C_b calculation is improved relative to the current methods, because $M_{cr1,top}$ and $M_{cr1,bot}$ need to be calculated in all the procedures, and the calculations of R_m in the ASC procedure and multiple C_b values in the AASHTO procedure are avoided.

A major advantage of the recommended method is that it provides comparable or greater accuracy in capturing the results from benchmark C_b calculations in all cases, compared to the ASC and AASHTO approaches, while maintaining essentially the same degree of simplicity as these procedures. The recommended method solves the problem of sharp discontinuities in the ASC and AASHTO C_b estimates, where the ASC solution gives either significantly conservative or unconservative results, and where the AASHTO solution gives significantly conservative results. These attributes are investigated in detail in the following sections of the paper.

Calculation of Benchmark C_b Values

The most rigorous method of determining the elastic LTB resistance is via an elastic buckling analysis based on the same thin-walled open-section (TWOS) beam theory that the AISC *Specification* flexural resistance equations are based upon. This research employs a general-purpose TWOS frame finite element developed by Jeong (2014) to generate a large dataset of converged benchmark solutions. The torsionally and flexurally simply supported unbraced lengths considered in this study are analyzed using 32 elements, although eight elements within the unbraced length are sufficient to obtain converged results within 1% of the analytical solution in all cases. The reader is referred to Jeong (2014) and White et al. (2021) for various validation studies demonstrating the efficacy of this finite element.

The first step of the computational solution is to determine the first (lowest) eigenvalue from an elastic linear buckling analysis conducted for a given finite element model of a selected physical beam. This eigenvalue is precisely the benchmark γ_{eLTB} . Given this eigenvalue, the moment gradient factor for the top flange, when the top flange is subjected to flexural compression, is:

$$C_{b,top} = \frac{\gamma_{eLTB} M_{max,top}}{M_{cr1,top}} \quad (12)$$

and the moment gradient factor for the bottom flange, when the bottom flange is subjected to flexural compression, is:

$$C_{b,bot} = \frac{\gamma_{eLTB} M_{max,bot}}{M_{cr1,bot}} \quad (13)$$

The governing C_b is the one corresponding to the critical flange, which is defined as the flange that has the largest M_{max}/M_{cr1} . This converged numerically generated value of C_b may be taken as the “exact” moment gradient factor corresponding to flexural compression in the critical flange.

PARAMETRIC STUDY DESIGN— LOADING CASES

As noted in the Introduction and Background, design expressions for C_b should be accurate for near-linear moment diagrams as well as for highly nonlinear moment diagram cases. This objective is addressed in this study by:

1. Directly evaluating the performance of the different methods for a complete range of linear moment diagram cases.
2. Varying the “nonlinearity” of the moment diagrams as a direct function of the ratio of the moments due to the transverse loads to the maximum end moments on the unbraced lengths.

Figure 4 shows the parametric variations selected for linear moment diagram cases in this study. In these cases, the “right-hand” end of the unbraced length is subjected to the moment M_R and the “left-hand” end is subjected to the moment $M_L = \alpha M_R$. The reader should note that “left-” and “right-hand” end are actually immaterial in these studies, because if the reader walks around to the opposite side of the member being considered and views the member from there, the “left” end becomes the “right” and vice versa. These moments are equilibrated by the shear forces applied at the ends of the unbraced length, and it is assumed that any other loadings within the unbraced length are negligible. For doubly symmetric members, one need only consider values of α between -1.0 and 1.0 , as considered previously in Figures 1 and 2. However, for singly symmetric members, it is important to consider reverse-curvature bending cases in which the inflection point is located at various locations throughout the unbraced length; furthermore, both sections with a larger as well as a smaller “top” flange should be addressed. The variation in the relative flange sizes is captured in this study by the monosymmetry parameter:

$$\rho = \frac{I_{y,top}}{I_y} \cong \frac{1}{1 + \frac{I_{y,bot}}{I_{y,top}}} \quad (14)$$

where

I_y = weak-axis moment of inertia of the entire cross section, in.⁴ (mm⁴)

$I_{y,bot}$ = moment of inertia of the bottom flange about an axis in the plane of the web, in.⁴ (mm⁴)

$I_{y,top}$ = moment of inertia of the top flange about an axis in the plane of the web, in.⁴ (mm⁴)

The maximum and minimum limits on ρ of 0.9 and 0.1 employed in this work are the same as in the AISC *Specification* Equation F13-2. Values of $\rho = 0.1, 0.3, 0.5, 0.7,$ and 0.9 are considered.

Regarding practical cases involving “nonlinear” moment diagrams, two types of transverse loading are considered within the unbraced lengths in this research:

1. A concentrated load, P , applied at the web mid-height and middle of the unbraced length.
2. A uniformly distributed load, w , applied throughout the unbraced length.

These loadings encompass all of the loading cases considered by Helwig et al. (1997) as well as the majority of the loading cases studied by Wong and Driver. However, in this research, loadings that involve a small deviation from the basic linear moment diagrams are emphasized in addition to loadings that are more akin to transversely loaded members that do not have any bracing within their entire span. This is accomplished by varying two parameters,

$$\alpha = \frac{M_L}{M_R} \quad (15)$$

and

$$\zeta = \frac{M_{ss}}{M_R} \quad (16)$$

where M_{ss} is the maximum “simply supported” moment associated with a given transverse loading, located at the middle of the unbraced length. For the first transverse loading case,

$$M_{ss} = \frac{PL_b}{4} \quad (17)$$

and for the second loading case,

$$M_{ss} = \frac{wL_b^2}{8} \quad (18)$$

The following values of α and ζ are considered for the nonlinear moment diagram cases:

- α values of + 1.0, + 0.5, 0, -0.5, and -1.0.
- ζ values ranging from -2.0 to + 2.0 for each of these α values, with $\Delta\zeta$ taken as 0.1.

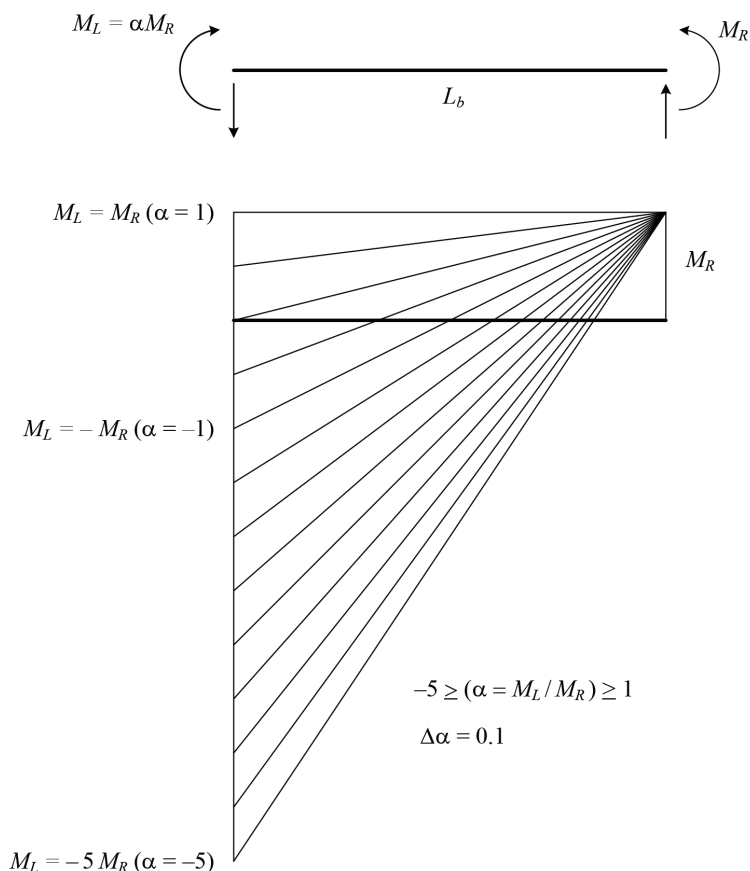


Fig. 4. Linear moment diagrams considered in this study.

These combinations of α and ξ produce the moment diagrams illustrated in Figure 5. The “base” linear moment diagrams corresponding to $\xi = 0$ are indicated by the dashed lines in each of the plots, and the moment diagrams corresponding to nonzero transverse loads for $\xi = 2.0, 1.0, -1.0,$ and $-2.0,$ applied in addition to the end moments, are indicated by the solid lines.

Simply supported unbraced lengths with zero end moments are not considered in this study. The specified loadings produce a range of cases combined with applied end moments that are considered sufficient to validate the application of the C_b design expressions, which were developed originally for doubly symmetric I-section unbraced lengths, to singly symmetric I-section members subjected to single-curvature bending. Given the validations shown here, the specific single-curvature bending cases investigated in Helwig et al. (1997) and the wider range of single-curvature bending cases investigated by Wong and Driver are considered as further validation of use of the C_b design expressions for doubly and singly symmetric members subjected to single-curvature bending. The current study focuses on cases where there is always a nonzero moment of some sign at one or both ends of the unbraced length.

In addition to simply supported unbraced lengths, Helwig et al. (1997) considered fixed-fixed and propped cantilever beams with uniformly distributed transverse load as well as a single concentrated transverse load at their mid-span. These loading cases correspond to the following specific (α, ξ) combinations:

- For the transverse concentrated load cases, $(\alpha, \xi) = (1.0, -2.0)$ for the fixed-fixed beams and $(0.0, -1.33)$ for the propped cantilever beams.
- For the uniformly distributed transverse load cases, $(\alpha, \xi) = (1.0, -1.5)$ for the fixed-fixed beams and $(0.0, -1.0)$ for the propped cantilever beams.

Wong and Driver considered a wider range of loadings, but only for doubly symmetric beams, and with an emphasis on (1) beams with no bracing within their entire span and (2) loadings in which the end moments are small compared to the simply supported moments. In addition to their cases that fit within the range of the loadings studied in this work, they studied:

- Simply supported beams with a concentrated transverse load applied at a variable location between the beam end and the mid-span (referred to as their loading type 6).
- Simply supported beams with two concentrated transverse loads applied at a variable equal distance from the end supports (referred to as their loading type 7).
- Concentrated transverse loads applied at the third points of the unbraced length, combined with equal

and opposite variable end moments (referred to as their loading type 11).

- Concentrated transverse loads applied at the third points of the unbraced length, combined with zero moment at one end and a variable applied moment at the opposite end of the unbraced length (referred to as their loading type 12).

The authors submit that the two transverse loading cases combined with the α and ξ values considered in this study, plus the additional cases from Wong and Driver, gives a comprehensive assessment of the behavior of the different C_b design expressions for all types of loadings on both doubly and singly symmetric I-section members. The loadings considered in the current study produce practical moment diagrams for cases where there are one or more braced points within the span as well as for cases in which there is no bracing within the entire span.

Wong and Driver also considered several loading cases in which concentrated moments are applied to the member within the unbraced length. They demonstrated that none of the available C_b equations are sufficient to evaluate the LTB resistance for beams subjected to these types of loadings. These types of loadings are considered as appropriate candidates for the direct application of computational tools such as SABRE2 (White et al., 2021).

As noted previously, Helwig et al. (1997) showed that the web mid-height, rather than the shear center, is the proper transverse load position for development of base C_b equations that neglect load height. For instance, members with a very large “top” flange have a shear center close to the top flange. There is a definite destabilizing effect of downward transverse loads applied “high” on the cross section—say, at this shear center location—and a stabilizing effect of downward transverse loads applied “low” in the cross section (but relative to the web mid-height, not relative to the shear center). Helwig et al. found that if the load position is defined at the web mid-height rather than the shear center, the degree of monosymmetry does not affect the C_b values. In addition, they found that the base C_b values derived for doubly symmetric members work well for single-curvature bending cases. Furthermore, it can be stated that:

- For cases where significant end moments are applied to the unbraced length, particularly when these moments cause single-curvature bending, the influence of the height of the applied loads within the unbraced length tends to be relatively small. Simply stated, this is because the portion of the moment coming from the transverse loading is small in these cases.
- In addition, regarding load-height effects, it should be understood that in many situations involving transverse loads, the application of the load itself involves “tipping

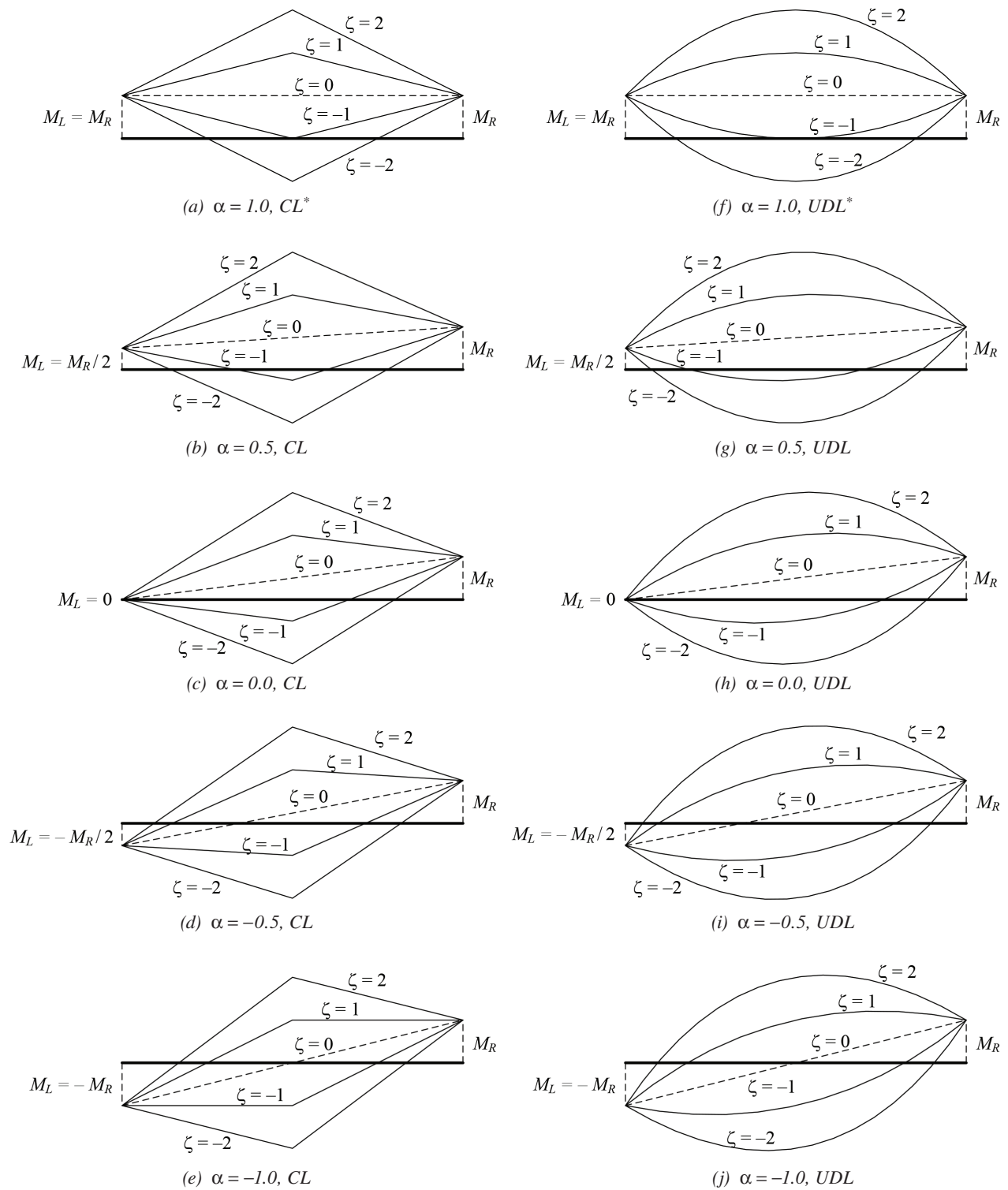


Fig. 5. Nonlinear moment diagrams considered in this study (CL = concentrated load; UDL = uniformly distributed load).

restraint” from the loading mechanism (e.g., from decking), which tends to nullify the influence of any load height. Helwig et al. provide a thorough discussion of this behavioral attribute.

All of the solutions generated in this research are based on loads applied at the web mid-height.

PARAMETRIC STUDY—MEMBER GEOMETRIES

The I-section geometries for the current study are generated from the base doubly symmetric cross section shown in Figure 6. This cross section is similar to the base doubly symmetric girder cross section employed by Helwig et al. (1997). The web of the base cross section considered in this research is 60 in. \times 0.5 in., which qualifies as a noncompact web but has a slenderness close to the AISC *Specification* noncompact web limit of $5.7\sqrt{E/F_y} = 137$ for $F_y = 50$ ksi. The section employed by Helwig et al. had h_o (the distance between the flange centroids) = 60 in. and a web thickness of $t_w = 0.736$ in., which satisfies the AISC *Specification* compact-web requirements for the base cross section. The flanges of the base cross section considered in this research are 18 in. \times 1.5 in., which satisfy the compact flange requirements. The flanges considered by Helwig et al. were 12 in. \times 1 in. The larger base 18 in. \times 1.5 in. flanges employed in this study allow for the variation in the ρ factor (Equation 14), by reducing the flange widths, without producing excessively narrow flanges relative to the section depth.

As stated at the beginning of the discussion of the loading cases for the parametric study, ρ factors of 0.1, 0.3, 0.5 (the base doubly symmetric I-section), 0.7, and 0.9 are considered in this work. In this study, the flange widths

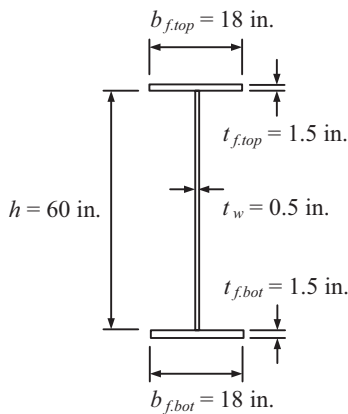


Fig. 6. Base doubly symmetric I-section employed in the current studies.

are reduced without changing the flange thickness to produce the targeted singly symmetric I-sections. For $\rho = 0.1$ and 0.3, the top flange width is reduced to $b_{f,top} = 8.65$ and 13.57 in., respectively. Similarly, for $\rho = 0.7$ and 0.9, the bottom flange width is reduced to $b_{f,bot} = 13.57$ and 8.65 in., respectively. The overall maximum web depth to flange width, h/b_f is therefore $60/8.65 = 6.94$ in this study, which is allowed by the AISC *Specification* (with a reduced girder tension field action web shear resistance), and is only slightly larger than the largest h/b_f allowed by AASHTO for bridge girders. Helwig et al. appear to reduce the flange widths and thicknesses proportionally to vary ρ in their research. This requires a minimum flange width of 6.94 in. for their girders, giving a maximum h/b_f of 8.53.

In addition to the effect of the monosymmetry factor, the LTB resistance of both doubly and singly symmetric I-section members is influenced significantly by the nondimensional factor

$$W = \frac{\pi}{L_b} \sqrt{\frac{EC_w}{GJ}} \quad (19)$$

where C_w and J are the warping and St. Venant torsion constants of the cross section, respectively. The factor W is a measure of the contribution of the warping rigidity relative to the St. Venant torsional rigidity to the elastic LTB resistance.

The elastic LTB moment of a singly symmetric I-section beam may be expressed analytically as:

$$M_{cr} = C_b \frac{\pi^2 EI_y}{L_b^2} \left[\frac{\beta_x}{2} + \sqrt{\left(\frac{\beta_x}{2}\right)^2 + \frac{C_w}{I_y} \left(1 + \frac{1}{W^2}\right)} \right] \quad (20)$$

where the coefficient of monosymmetry, β_x , may be approximated by the equation

$$\beta_x = 0.9h_o\rho_f \left(\frac{I_{yc}}{I_{yt}} - 1 \right) \quad (21)$$

(Ziemian, 2010). An exact expression for β_x consistent with the thin-walled open-section FEA model employed in this research is presented by Ziemian. Equation 20 for M_{cr} is employed with the exact calculation of β_x in the evaluation of all the C_b estimates considered in this paper.

In the previous equations, h_o is the distance between flange centroids, ρ_f is defined as:

$$\rho_f = \frac{1}{1 + \frac{I_{yc}}{I_{yt}}} \quad (22)$$

and I_{yc} and I_{yt} are the moments of inertia of the compression and tension flanges, respectively, about an axis in the plane of the web. In addition, the warping constant may be written as:

Table 1. Range of W Values Considered in the Current Parametric Study

L_b/h_o	J (in. ⁴)	W ($\rho = 0.1$ & 0.9)	W ($\rho = 0.3$ & 0.7)	W ($\rho = 0.5$)
10	0.0	∞	∞	∞
5	> 0	1.57	2.50	3.03
10	> 0	0.786	1.25	1.51
20	> 0	0.393	0.626	0.758
30	> 0	0.262	0.417	0.504

$$C_w = h_o^2 I_{yc} \rho_f \quad (23)$$

Therefore, the different terms in Equation 20 may be approximated as follows:

$$\beta_x = 0.9 h_o \frac{\frac{I_{yc}}{I_{yt}} - 1}{\frac{I_{yc}}{I_{yt}} + 1} \quad (24)$$

$$\begin{aligned} W &= \frac{\pi}{L_b} \sqrt{\frac{EC_w}{GJ}} \quad (25) \\ &= \frac{\pi}{(L_b/h_o)} \sqrt{\frac{EI_{yc} \rho_f}{GJ}} \\ &= \frac{\pi}{(L_b/h_o)} \sqrt{\frac{E}{G} \frac{1}{J} \frac{I_{yc} I_{yt}}{I_{yc} + I_{yt}}} \end{aligned}$$

and

$$\frac{C_w}{I_y} = \frac{h_o^2 I_{yc}}{I_{yt}} \frac{1}{I_{yc} + I_{yt}} = \frac{h_o^2 I_{yc} I_{yt}}{(I_{yc} + I_{yt})^2} = \frac{h_o^2}{\left(\frac{I_{yc}}{I_{yt}} + 1\right) \left(\frac{I_{yt}}{I_{yc}} + 1\right)} \quad (26)$$

Considering these equations, it can be observed that for a given singly symmetric cross section, there is one J value, one C_w value, one C_w/I_y value, and one W value irrespective of which flange is in compression. That is, the selected singly symmetric cross sections with $\rho = 0.1$ and 0.9 have the same J , C_w , C_w/I_y , and W values. Also, the singly symmetric cross sections with $\rho = 0.3$ and 0.7 have the same J , C_w , C_w/I_y , and W values, but these are different from the values for $\rho = 0.1$ and 0.9 . The coefficient of monosymmetry, β_x , is influenced by which flange is in flexural compression. Furthermore, it can be observed in general that the nondimensional parameters I_{yc}/I_{yt} and W have a substantial influence on the elastic LTB resistance. By inference, it can be expected that these parameters may also have an impact on the moment gradient factor, C_b .

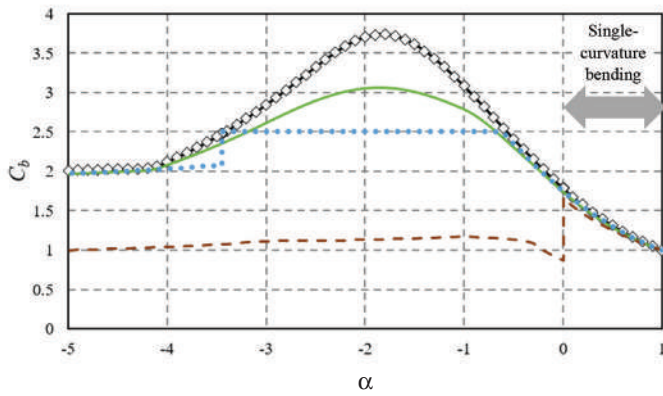
Considering the behavior associated with Equations 20 through 26, one can conclude that W needs to be varied over a comprehensive range, in addition to the variation of ρ , to fully evaluate the ability of design expressions to capture benchmark C_b values obtained from converged numerical solutions. In the current study, this is achieved by varying L_b/h_o as well as by varying the St. Venant torsion constant J via the selected cross-section dimensional variations.

The values of L_b/h_o considered in this research are 5, 10, 20, and 30. Further, one additional suite of parametric study beams is considered with $L_b/h_o = 10$ and with J taken equal to zero. For $J = 0$, the thin-walled open-section beam theory solution for the compression flange stress at elastic LTB is essentially independent of L_b/h_o . The assumption of $J = 0$, which is applied in the AISC and AASTHO *Specifications* when the web classifies as slender, effectively gives $W = \infty$, while $L_b/h_o = 30$ with a finite J (calculated from AASHTO Equation A6.3.3-9 in this work) gives representative practical minimum values for W . The W values considered in the current study, as a function of L_b/h_o and finite or zero J , are summarized in Table 1.

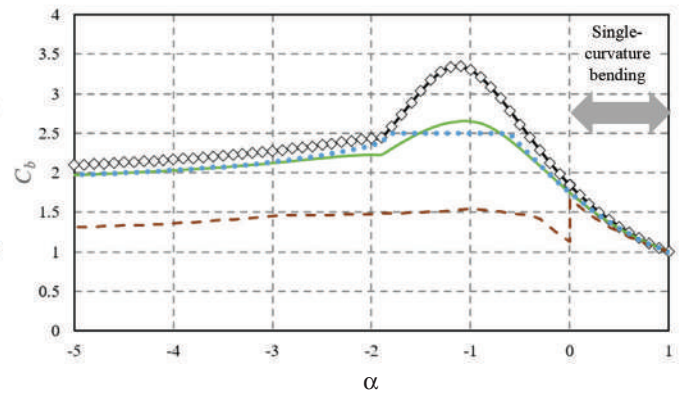
RESULTS

Figures 7 through 12 present sample results from this study as plots of the benchmark and estimated C_b values versus the independent variables ρ , α , and ξ , all for members with $L_b/h_o = 10$. The unbraced length to depth ratio $L_b/h_o = 10$ is selected for the plots in these figures because this is a representative intermediate value of L_b/h_o .

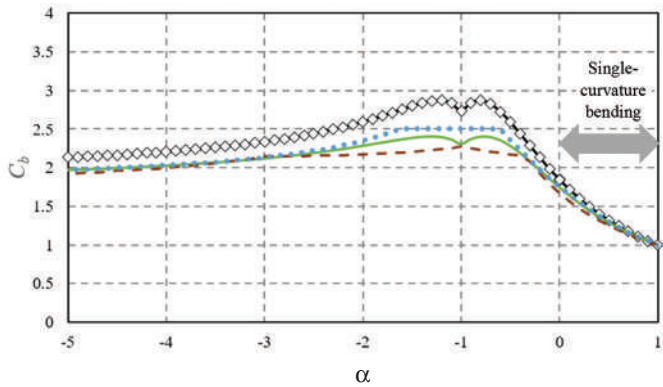
Figure 7 summarizes the results for the linear moment cases ($\xi = 0$). This is followed by Figures 8 through 12, which summarize the results for nonlinear moment cases with a uniformly distributed transverse load. Slein et al. (2021) show plots that parallel Figures 8 through 12 for nonlinear moment cases involving members subjected to a transverse concentrated load at the middle of the unbraced length. Each of the figures are arranged into five plots to convey the physical behavior, and the predictions of this behavior by the C_b design expressions, for different ρ , α , and ξ values.



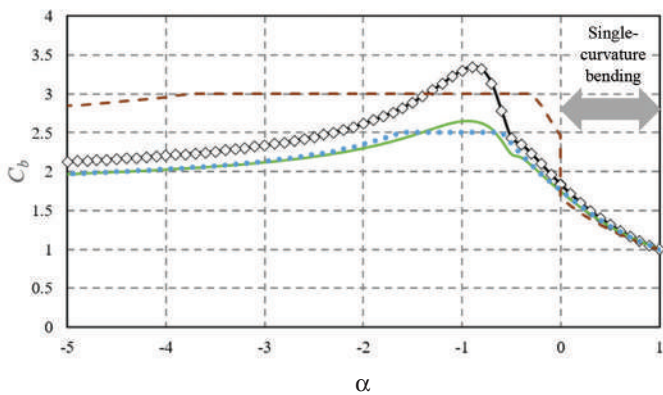
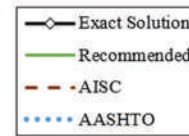
(a) $\rho = 0.1$



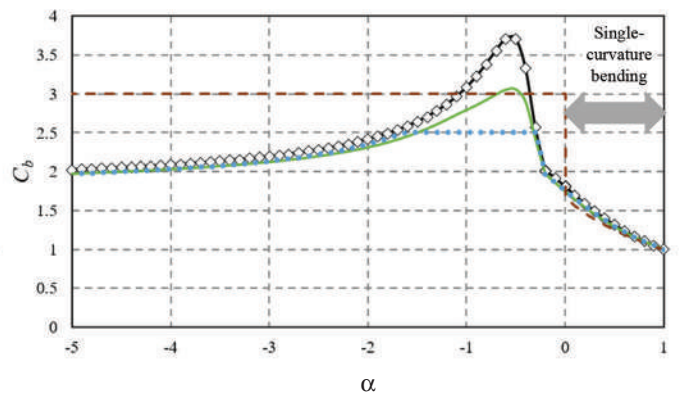
(b) $\rho = 0.3$



(c) $\rho = 0.5$

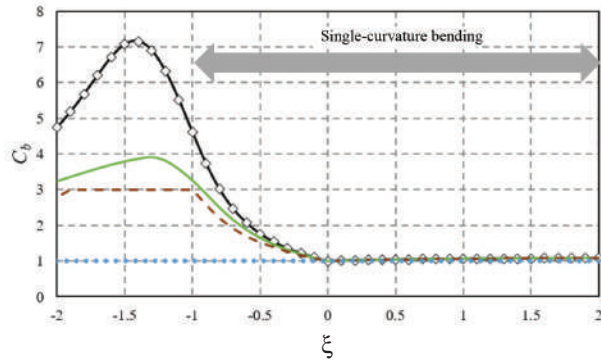


(d) $\rho = 0.7$

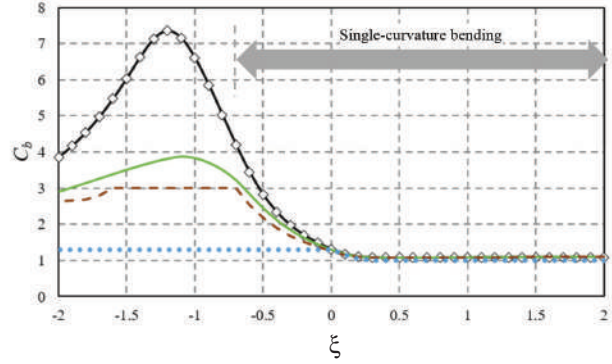


(e) $\rho = 0.9$

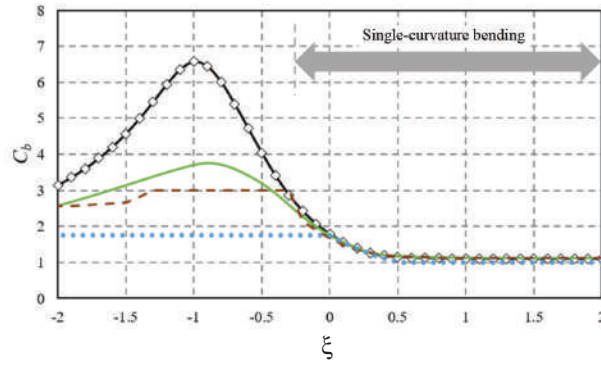
Fig. 7. Governing C_b values for linear moment cases ($\zeta = 0.0$), $L_b/h_o = 10$.



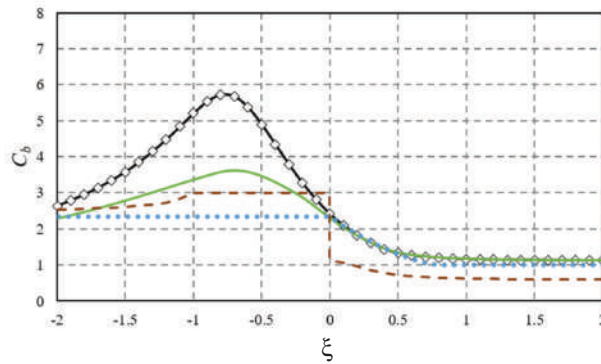
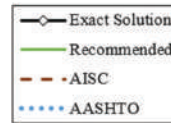
(a) $\rho = 0.1, \alpha = 1.0$



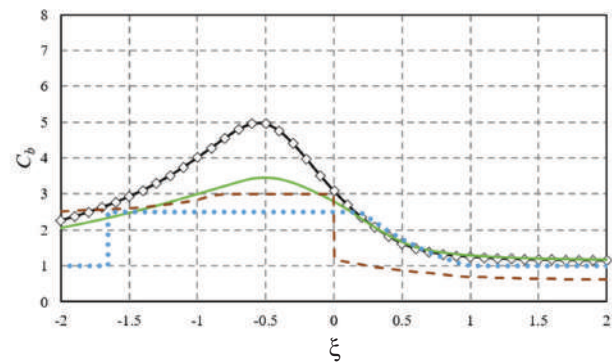
(b) $\rho = 0.1, \alpha = 0.5$



(c) $\rho = 0.1, \alpha = 0.0$

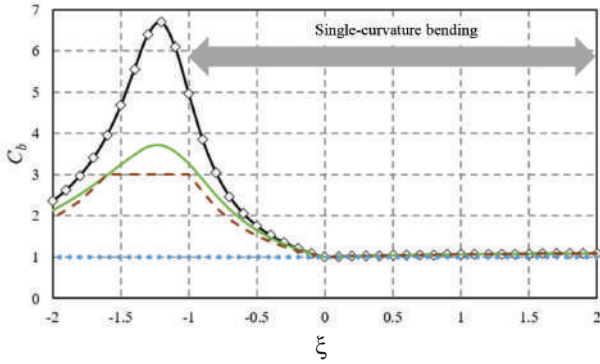


(d) $\rho = 0.1, \alpha = -0.5$

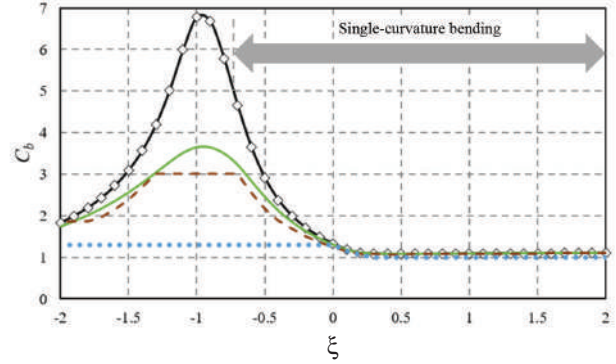


(e) $\rho = 0.1, \alpha = -1.0$

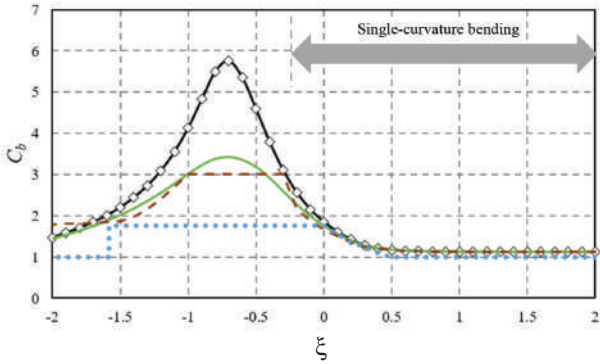
Fig. 8. Governing C_b values for members with $\rho = 0.1$ and $L_b/h_0 = 10$, subjected to a uniformly distributed transverse load: $\alpha = 1.0, 0.5, 0.0, -0.5, \text{ and } -1.0$; ξ ranging from -2.0 to 2.0 .



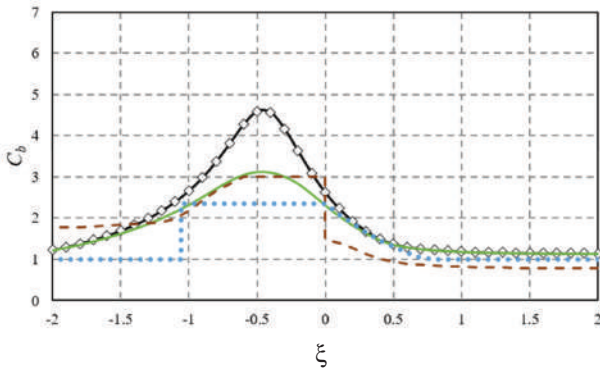
(a) $\rho = 0.3, \alpha = 1.0$



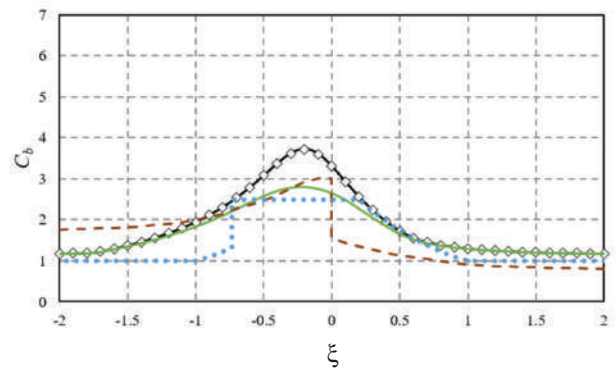
(b) $\rho = 0.3, \alpha = 0.5$



(c) $\rho = 0.3, \alpha = 0.0$

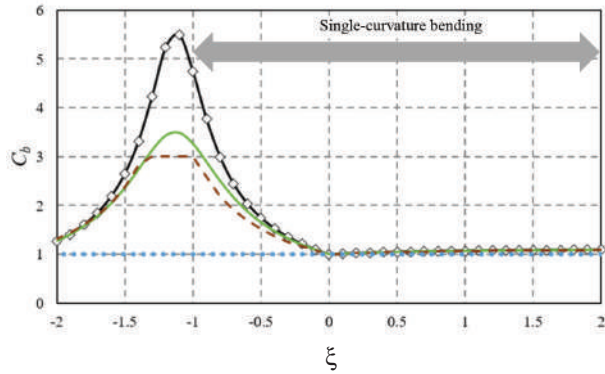


(d) $\rho = 0.3, \alpha = -0.5$

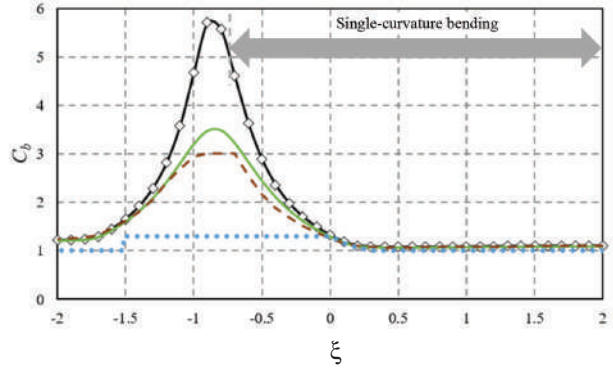


(e) $\rho = 0.3, \alpha = -1.0$

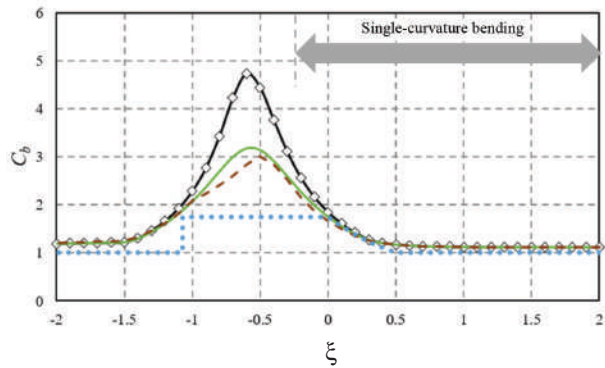
Fig. 9. Governing C_b values for members with $\rho = 0.3$ and $L_b/h_o = 10$, subjected to a uniformly distributed transverse load: $\alpha = 1.0, 0.5, 0.0, -0.5$, and -1.0 ; ξ ranging from -2.0 to 2.0 .



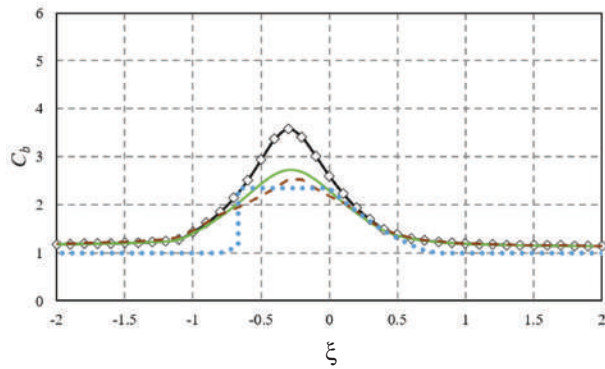
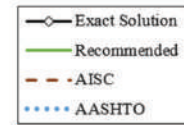
(a) $\rho = 0.5, \alpha = 1.0$



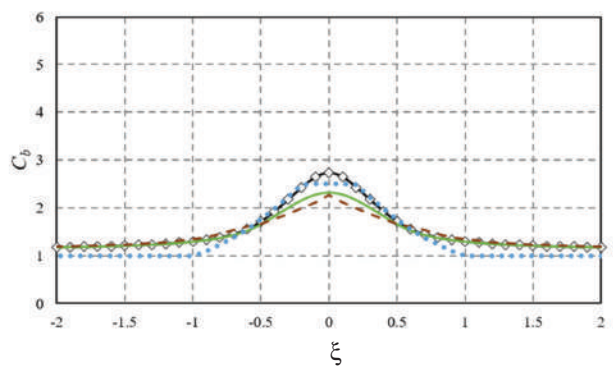
(b) $\rho = 0.5, \alpha = 0.5$



(c) $\rho = 0.5, \alpha = -0.0$



(d) $\rho = 0.5, \alpha = -0.5$



(e) $\rho = 0.5, \alpha = -1.0$

Fig. 10. Governing C_b values for members with $\rho = 0.5$ and $L_b/h_o = 10$, subjected to a uniformly distributed transverse load: $\alpha = 1.0, 0.5, 0.0, -0.5$, and -1.0 ; ξ ranging from -2.0 to 2.0 .

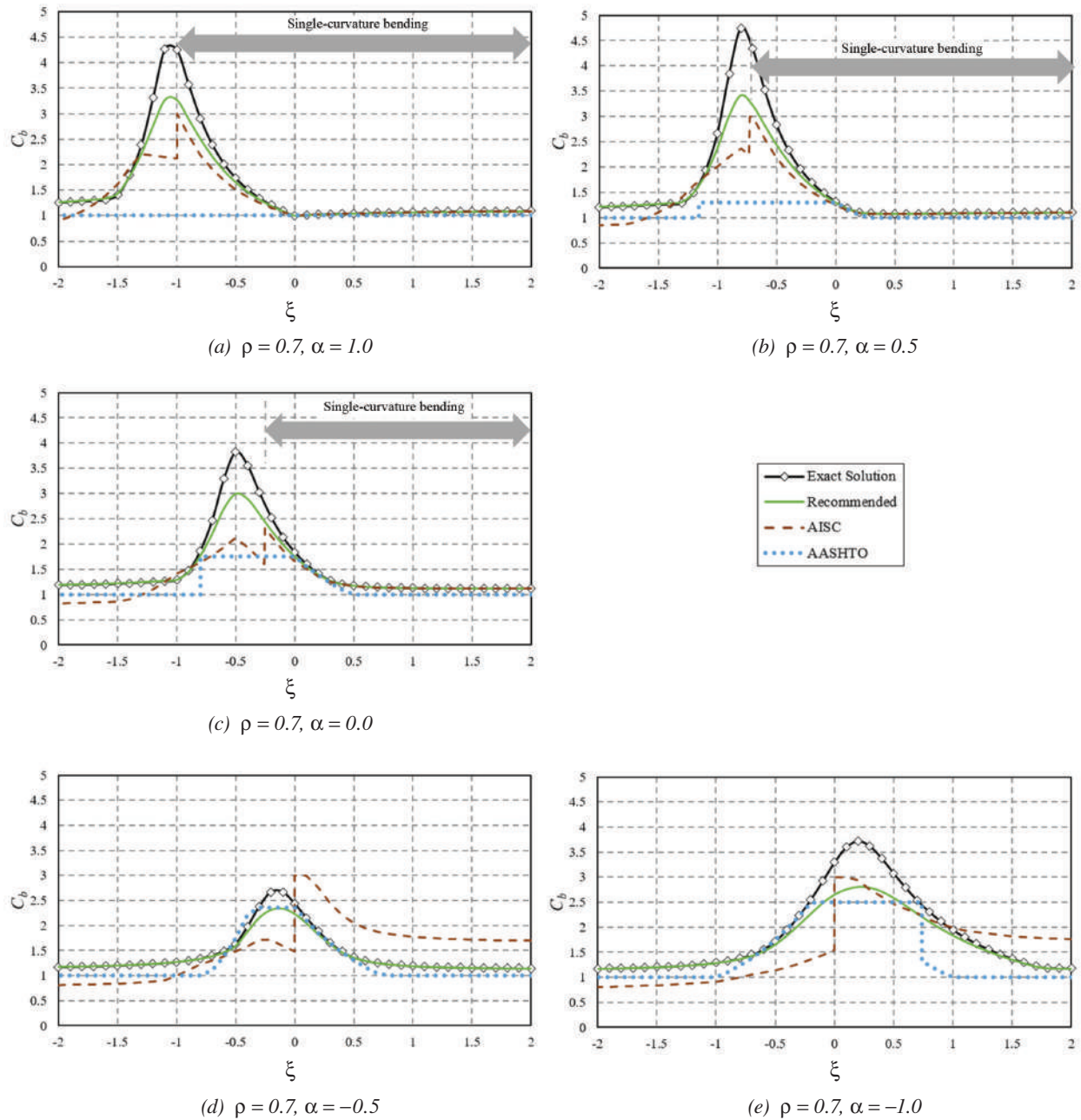


Fig. 11. Governing C_b values for members with $\rho = 0.7$ and $L_b/h_0 = 10$, subjected to a uniformly distributed transverse load: $\alpha = 1.0, 0.5, 0.0, -0.5$, and -1.0 ; ξ ranging from -2.0 to 2.0 .

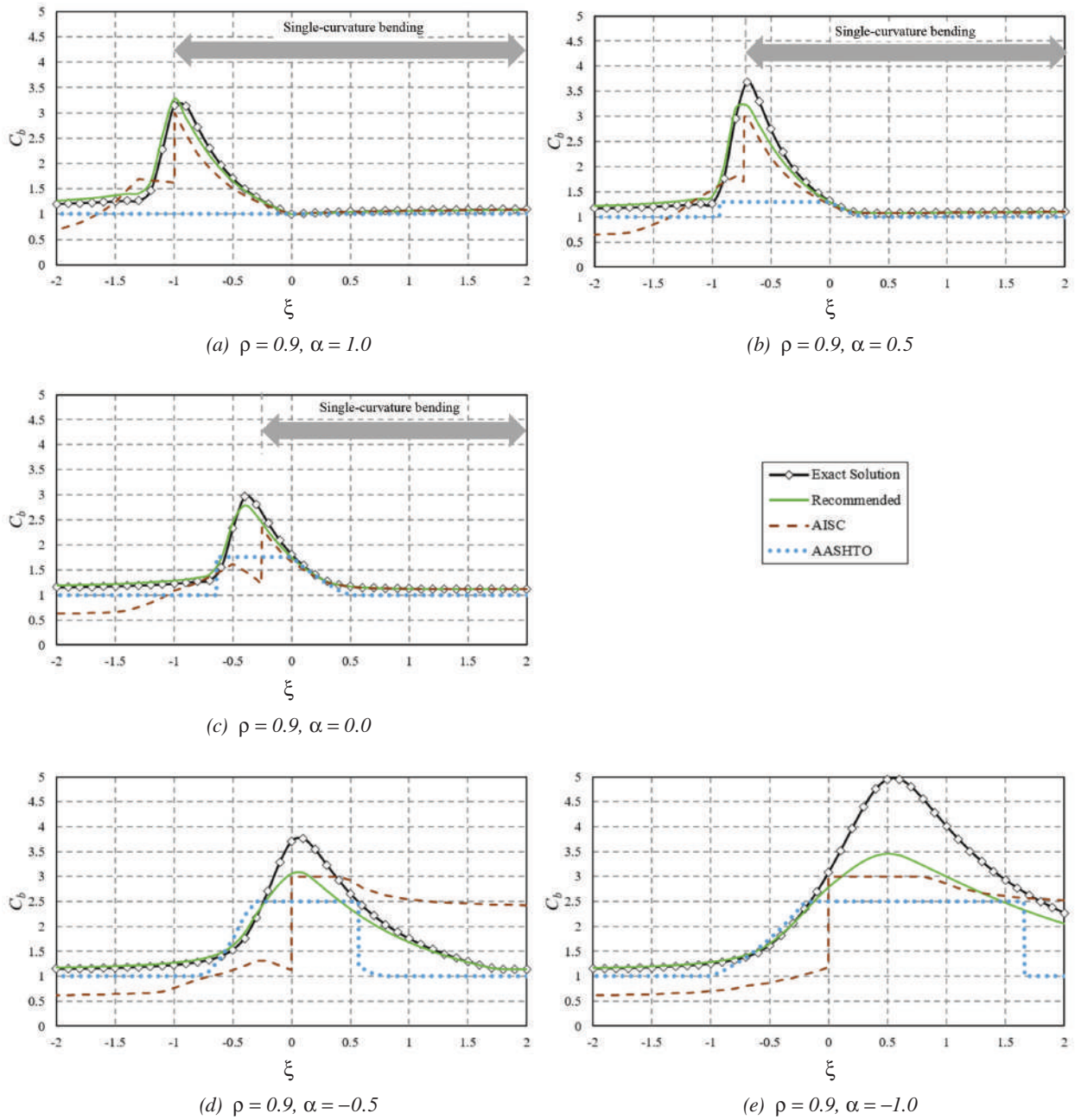


Fig. 12. Governing C_b values for members with $\rho = 0.9$ and $L_b/h_o = 10$, subjected to a uniformly distributed transverse load: $\alpha = 1.0, 0.5, 0.0, -0.5$, and -1.0 ; ξ ranging from -2.0 to 2.0 .

Value	Recommended	ASC	AASHTO	Recommended (ASC)
Max	1.70	5.16	2.33	1.84
Mean	1.10	1.38	1.12	1.13
Min	0.920	0.608	0.892	0.930
COV	0.104	0.569	0.180	0.112

Value	Recommended	ASC	AASHTO	Recommended (ASC)
Max	3.26	5.13	12.43	3.01
Mean	1.11	1.24	1.55	1.11
Min	0.769	0.454	0.722	0.666
COV	0.191	0.344	0.577	0.204

In Figure 7, each of the five plots corresponds to a different ρ value, $\rho = 0.1, 0.3, 0.5, 0.7,$ and 0.9 . Values of ρ less than 0.5 correspond to a smaller “top” flange, values of ρ greater than 0.5 correspond to a larger “top” flange, and $\rho = 0.5$ corresponds to doubly symmetric cross sections. The horizontal axis in each of these plots corresponds to the variation in α from -5.0 to 1.0 as illustrated in Figure 4. Values of α ranging from 0.0 to 1.0 correspond to single-curvature bending. This attribute is highlighted by the annotation in the upper-right corner of the plots.

Each of Figures 8 through 12 corresponds to a specific ρ value (i.e., $\rho = 0.1, 0.3, 0.5, 0.7,$ or 0.9). The five plots in each of these figures correspond to different end moment ratios (α) (i.e., $\alpha = 1.0, 0.5, 0.0, -0.5,$ and -1.0). The ratio of the simple-span moment to the maximum end moment, ξ , is varied from -2.0 to 2.0 on the horizontal axis of these plots. The moment diagrams produced by these ranges of α and ξ are illustrated in Figure 5.

For the members subjected to uniformly distributed transverse load (Figures 8 through 12), the following cases correspond to single-curvature bending:

- For $\alpha = 1.0, \xi \geq -1.0$
- For $\alpha = 0.5, \xi \geq -0.729$
- For $\alpha = 0.0, \xi \geq -0.25$

These cases are highlighted by the annotation in the upper-right corner of the plots, where applicable. All of the other α and ξ values correspond to reverse-curvature bending. All the cases in Figures 8 to 12 parts (d) and (e), corresponding to $\alpha = -0.5$ and -1.0 , involve reverse-curvature bending.

Figures 13 and 14 show arrays of boxplots for the ratio of the benchmark C_b values from the converged FEA

solutions, labeled as $C_{b \text{ exact}}$, to the C_b obtained from the design expressions (i.e., $C_{b \text{ exact}}/C_b$) for all of the cross sections and W values considered in this study. Emphasis is given to having an unbiased, evenly distributed sampling throughout the design space of which Figures 7 through 12 are a subset. The main box of the boxplots conveys the 25th percentile, median, and 75th percentile values for $C_{b \text{ exact}}/C_b$, and the upper and lower whiskers convey the maximum and minimum $C_{b \text{ exact}}/C_b$ in each of the data sets. As discussed in the previous section, W is varied in this work by considering L_b/h_o values of $5, 10, 20,$ and 30 , and by analyzing members with $L_b/h_o = 10$ taking $J = 0$. Figure 13 corresponds to the linear moment cases ($\xi = 0.0$), while Figure 14 corresponds to all the nonlinear moment cases, both concentrated transverse load at the middle of the unbraced length and uniformly distributed transverse load throughout the unbraced length.

The plots in Figures 13 and 14 are arranged in five columns corresponding to $\rho = 0.1, 0.3, 0.5, 0.7,$ and 0.9 , and the rows correspond to L_b/h_o ranging from the maximum of 30 at the bottom of the array down to $L_b/h_o = 5$ in the next to top row of the array. As discussed previously, $L_b/h_o = 30$ gives the smallest values of W (Equation 25) for the selected member cross sections, and $L_b/h_o = 5$ gives the largest finite values of W . The range of W values corresponding to each row of the plot arrays is summarized on the right-hand side of the figure. The specific W values for the different cases also are summarized in Table 1. The top row of the array of plots in Figures 13 and 14 corresponds to the idealized case in which the St. Venant torsion constant, J , is taken equal to zero. This gives an effective W value of infinity.

Tables 2 and 3 summarize the statistics for $C_{b \text{ exact}}/C_b$ corresponding to all of the data from the box plot arrays of

Figures 13 and 14. The dispersion in the ASC and AASHTO data is substantial. The ASC $C_{b\ exact}/C_b$ data is essentially tri-modal. That is, the $C_{b\ exact}/C_b$ values coalesce largely into three groups: results for $R_m > 1.0$, results for $R_m < 1.0$, and results for $R_m = 1.0$. Furthermore, the $C_{b\ exact}/C_b$ AASHTO data is essentially bimodal, coalescing largely into two groups: results where $C_{b\ AASHTO}$ is simply taken equal to 1.0 and results where $C_{b\ AASHTO}$ is greater than 1.0. From an overall perspective, the recommended method clearly outperforms both of the current methods. However, even for the recommended method, there are some cases where the converged numerical benchmark $C_{b\ exact}$ values are over-predicted. These are discussed further in the following sections. First, it is important to explain the overall behavior of each of the expressions for C_b .

One additional column is added to Tables 2 and 3 to address the question of how the quarter-point equation given by the AISC *Specification* Equation F1-1 performs if applied in the same way that the Wong and Driver formula, ASC Equation C-F1-2b, is adapted in Equation 10. This column is labeled “Recommended (ASC).” One can observe that the Wong and Driver equation offers some minor improvement in the overall statistics relative to the AISC *Specification* Equation F1-1.

Behavior of the ASC C_b Equations

The ASC design expressions (ASC Equation C-F1-3 and Equation 1) exhibit the following behavior with variations

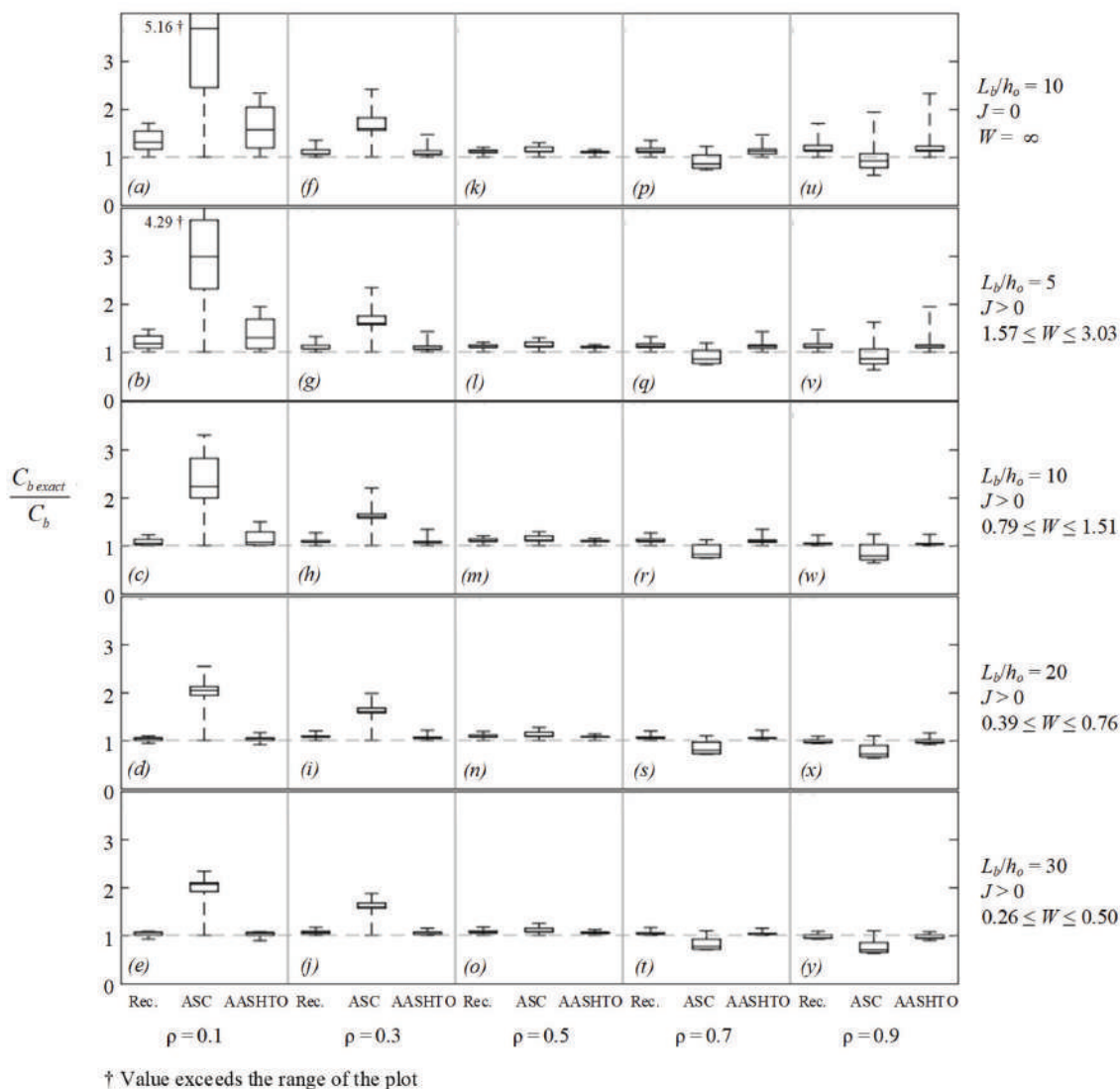


Fig. 13. Boxplots of $C_{b\ exact}/C_b$ for linear moment cases.

in the independent variable ρ for the members considered in this study:

- For all single-curvature bending cases, $R_m = 1.0$ from Equation 1a.
- For the reverse-curvature bending cases with $\rho = 0.1$, $I_{y.top} = 0.1 I_y$:
 - When $\xi > 0.0$, the transverse loading is “downward”; therefore, $I_{y.opp} = I_{y.top} = 0.1 I_y$ and $R_m = 0.520$ from Equation 1b.

- When $\xi < 0.0$, the transverse loading is “upward”; therefore, $I_{y.opp} = I_{y.bot} = 0.9 I_y$ and $R_m = 2.118$ from Equation 1b.
- For the reverse-curvature bending cases with $\rho = 0.3$, $I_{y.top} = 0.3 I_y$:
 - When $\xi > 0.0$, the transverse loading is “downward”; therefore, $I_{y.opp} = I_{y.top} = 0.3 I_y$ and $R_m = 0.680$ from Equation 1b.
 - When $\xi < 0.0$, the transverse loading is “upward”; therefore, $I_{y.opp} = I_{y.bot} = 0.7 I_y$ and $R_m = 1.479$ from Equation 1b.

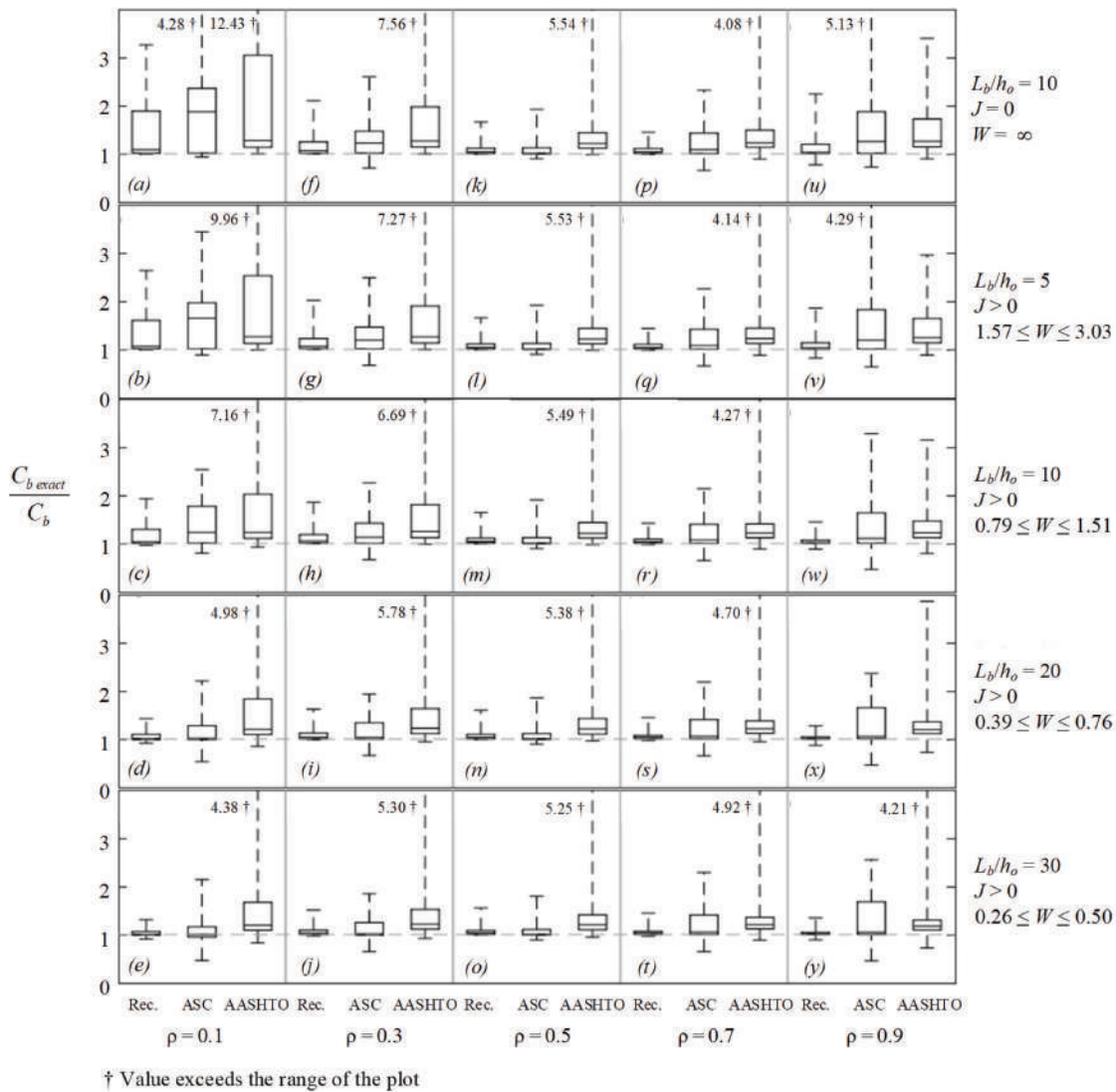


Fig. 14. Boxplots of $C_{b\text{ exact}}/C_b$ for nonlinear moment cases—concentrated transverse load at the middle of the unbraced length and uniformly distributed transverse load.

$\rho = I_{y,top}/I_y$	ξ	$I_{y,opp}/I_y$	R_m
0.1	≥ 0.0	0.1	0.520
0.1	< 0.0	0.9	2.118
0.3	≥ 0.0	0.3	0.680
0.3	< 0.0	0.7	1.479
0.5	All values	0.5	1.000
0.7	≥ 0.0	0.7	1.479
0.7	< 0.0	0.3	0.680
0.9	≥ 0.0	0.9	2.118
0.9	< 0.0	0.1	0.520

- For the reverse-curvature bending cases with $\rho = 0.7$, $I_{y,top} = 0.7I_y$:
 - When $\xi > 0.0$, the transverse loading is “downward”; therefore, $I_{y,opp} = I_{y,top} = 0.7I_y$ and $R_m = 1.479$ from Equation 1b.
 - When $\xi < 0.0$, the transverse loading is “upward”; therefore, $I_{y,opp} = I_{y,bot} = 0.3I_y$ and $R_m = 0.680$ from Equation 1b.
- For the reverse-curvature bending cases with $\rho = 0.9$, $I_{y,top} = 0.9I_y$:
 - When $\xi > 0.0$, the transverse loading is “downward”; therefore, $I_{y,opp} = I_{y,top} = 0.9I_y$ and $R_m = 2.118$ from Equation 1b.
 - When $\xi < 0.0$, the transverse loading is “upward”; therefore, $I_{y,opp} = I_{y,top} = 0.1I_y$ and $R_m = 0.520$ from Equation 1b.

In the limit $\xi = 0.0$, there is no transverse load, and therefore, one can infer that there is no gravity load direction and that R_m should be taken equal to 1.0. However, it is common that the self-weight moments in horizontal members may be small compared to the moments from the applied loads. In these cases, there is indeed a gravity load direction, but the moment diagrams are linear for all practical purposes. The results plotted in Figure 7 are based on this situation. The gravity direction is taken as downward, and the “top” flange is taken as the “opposite” flange in this case.

The variations of R_m with ρ and ξ are summarized in Table 4. These results are important toward understanding the various discontinuities in the ASC C_b curves shown in Figures 7 through 12.

Generally, discontinuities in the ASC C_b values can occur where:

1. The moment diagram changes from single-curvature to reverse-curvature bending. The values of α and ξ

corresponding to this occurrence are highlighted, and the horizontal position on the plots where this occurs are clearly marked in Figures 8 through 12. The following are examples of these situations:

- Considering Figure 7(a), where $\xi = 0$ but it is assumed that there is a small downward transverse load on the members, the unbraced length goes into reverse-curvature bending when $\alpha = M_L/M_R$ becomes negative. As such, R_m changes from 1.0 for positive α to 0.520 for negative α . This causes an abrupt downward shift of the ASC C_b curve for negative α .
- A similar discontinuity occurs in Figure 7(d), where R_m changes from 1.0 for positive α to 1.479 for negative α , causing an abrupt upward shift in the ASC C_b curve for negative α .
- Considering Figure 11(a), R_m changes from 1.0 for $\xi \geq -1.0$ to 0.680 for $\xi < -1.0$, causing an abrupt downward shift in the ASC C_b values for $\xi < -1.0$.

A number of other similar discontinuities appear throughout Figures 8 through 12.

2. The unbraced length is subjected to reverse-curvature bending, due to the values of the end moments (i.e., $\alpha = 0.5$ or -1.0), and the direction of the transverse loading changes from positive ξ (downward), to negative ξ (upward). The following are examples of these situations:

- Considering Figure 8(d), R_m changes from 0.520 for $\xi > 0.0$ to 2.118 for $\xi < 0.0$. The magnitude of the shift in the ASC C_b curve in this case is limited by the cap of 3.0 in the ASC Equation CF1-3.
- Considering Figure 11(d), R_m changes from 1.479 for $\xi > 0.0$ to 0.680 for $\xi < 0.0$. The ASC C_b curve shifts in the opposite direction with increasing ξ in this case because the top flange is larger than the bottom flange, rather than smaller, while the variation in the

loading direction from downward to upward is the same. Again, the magnitude of the shift in the ASC C_b curve is limited by the maximum cap of 3.0 in the ASC Equation C-F1-3.

Again, a number of other similar discontinuities appear throughout Figures 8 to 12.

Slein et al. (2021) also discuss the attributes of the calculations producing discrete changes in the slope of the ASC and other C_b curves in Figures 7-12, plotted versus $\alpha = M_L/M_R$.

Clearly the discontinuities in the ASC C_b values as a function of α and ξ are nonphysical. For ρ values significantly different than 0.5, these discontinuities can introduce both substantial conservatism and unconservatism into the ASC LTB predictions. The largest conservatism in the ASC calculations tends to occur for cases where there is only a minor amount of reverse-curvature bending causing compression on the smaller flange. However, the R_m calculation (Equations 1) gives a substantial indiscriminant reduction in the C_b value without considering the actual pattern of tension and compression within the smaller flange. The largest unconservatism in the ASC calculations tends to occur for cases where there is only a minor amount of reverse-curvature bending causing compression on the larger flange. However, the R_m calculation (Equations 1) gives a substantial indiscriminant increase in the C_b value without considering the actual pattern of tension and compression within the larger flange. Nevertheless, one can observe that the discontinuities in the ASC C_b values do follow the trends in the benchmark C_b exact curves to some extent for cases subjected to significant transverse loads and significant simply supported moments, M_{ss} (Equations 17 and 18). This is evidenced by the larger ASC C_b predictions, due to larger R_m for negative ξ values, in Figures 8 and 9, and the smaller ASC C_b predictions, due to smaller R_m for negative ξ values, in Figures 11 and 12.

It should be noted that as a check of the benchmark thin-walled open-section beam theory solutions from SABRE2 (White et al., 2021) employed in this paper, as well as to check the intended application of the ASC C_b expressions, the authors analyzed all the cases corresponding to loadings applied at the web mid-height from Helwig et al. (1997). A close match was obtained with the original solutions by Helwig et al. The difference in the accuracy of the results for the broader studies conducted in this work versus the original studies by Helwig et al. appears to be due to the fact that only simply supported, fixed-fixed and propped cantilever beams were considered in the development of the ASC R_m factor by Helwig et al. As stated previously, the solutions in this paper focus on loadings involving a more general variation of the end moments. The reader is referred

to Wong and Driver (2010) for additional solutions involving simply supported beams.

For the concentrated transverse load cases, shown in Slein et al. (2021), the fixed-fixed and propped cantilever end conditions correspond to $\xi = -2$ and -1.33 for $\alpha = -1.0$ and 0.0 , respectively. For the uniformly distributed load cases shown in Figures 8 through 12, the fixed-fixed and propped cantilever end conditions correspond to $\xi = -1.5$ and -1.0 in plots (a) and (c), respectively. One can observe that the predictions by the ASC equations are relatively accurate for these specific load cases.

Behavior of the AASHTO C_b Equations

Different values are calculated for $C_{b,top}$ and $C_{b,bot}$ in the AASHTO procedure (see Equation 7). This practice is aimed at accounting for the different patterns of compression and tension in the separate flanges for cases involving moment reversal. However, due to the different $C_{b,top}$ and $C_{b,bot}$ values calculated using this approach, this method produces a discontinuity in the governing C_b value when there is a change in the flange governing the calculation of γ_{eLTB} . This behavior does not occur with the other methods evaluated in this study. For the other methods (i.e., the ASC method, the recommended method, and the benchmark calculations from elastic linear buckling analysis), the C_b curves are continuous at any α or ξ values where there is a change in the governing flange.

This behavior of the AASHTO equations appears at $\alpha = -3.45$ in Figure 7(a), at $\xi = -0.74$ in Figure 9(e), at $\xi = -0.66$ in Figure 10(d), and at $\xi = +0.74$ in Figure 11(e).

The AASHTO procedure also gives a sharp discontinuity in its C_b value at any ξ where the maximum moment within the unbraced length becomes larger than the maximum end moment of the same sign. At these values of ξ , the AASHTO method switches from a calculation of $C_b > 1$ based on Equation 9 to the simplistic estimate of $C_b = 1$. This occurs at $\xi = -1.66$ in Figure 8(e), at $\xi = -1.58$ in Figure 9(c), at $\xi = -1.06$ in Figure 9(d), at $\xi = -1.52$ in Figure 10(b), at $\xi = -1.07$ in Figure 10(c), at $\xi = -1.16$ in Figure 11(b), and at $\xi = -0.80$ in Figure 11(c).

These discontinuities occur across a broad range of ρ , α , and ξ values, and it can be observed that, generally, they are appropriate and a part of the ability of the AASHTO method to account for the different patterns of compression and tension in the separate flanges in unbraced lengths subjected to reverse-curvature bending. That is, the AASHTO C_b curves tend to follow the trends in the increasing or decreasing values of the benchmark solutions. However, the physical behavior captured by the benchmark solutions does not involve any discontinuities in the C_b values. As such, any solution having sharp discontinuities will exhibit inaccuracies at these locations. In the case of the AASHTO

method, these inaccuracies are always conservative for the plots shown in this work. Nevertheless, the simplistic AASHTO solution of taking $C_b = 1.0$ when the maximum moment within the unbraced length is larger than the maximum end moment of the same sign is a critical flaw that is acknowledged in the AASHTO Commentary. This flaw makes the AASHTO method overly conservative for spans that have a limited number of intermediate brace points. These situations may exist in short-span bridges and in longer-span bridges during construction.

Behavior of the Recommended C_b Calculations

Considering Figures 7 through 12, one can observe that the recommended C_b calculation procedure does not exhibit any discontinuities in its value as a function of ρ , α , or ξ . The recommended C_b predictions generally follow the trends in the benchmark solutions quite well. The result from the recommended C_b calculations tends to be conservative in the vicinity of the largest benchmark and estimated C_b values. This is an attribute of the calibration of the ASC Equation C-F1-2b by Wong and Driver. As presented in detail in the subsequent discussions, members with large contributions from St. Venant torsion relative to the warping torsion tend to have smaller C_b values. These cases are encountered at larger L_b/h_o for a given member cross section and for heavy column type members, which generally have large St. Venant torsional rigidity, GJ , compared to their warping rigidity, EC_w . In essence, these are cases with the smallest W values (see Equation 25). Since the design expressions only account for variations in the moment along the unbraced length, and do not account for this significant attribute of the elastic LTB behavior, they need to be calibrated to give accurate results for practical situations having the smallest W .

At the opposite extreme, singly symmetric members with (1) the St. Venant torsion constant idealized as zero (such that there is no assistance from St. Venant torsion in resisting elastic LTB), (2) $\rho = 0.1$ (i.e., a small “top” flange), and (3) a moment diagram producing compression within the larger flange within the span but where the smaller flange loaded in maximum compression at one or both braced points governs [corresponding to the moment diagrams for $\xi = -1.5$ in Figure 5(f), or for $\xi = -1.2$ in Figure 5(g)], the C_b values are a whopping 12.43 and 12.83, respectively! For these cases, the recommended calculations give $C_b = 3.94$ and 3.95, respectively. The latter of these cases corresponds to the largest C_b values of 3.26 for the recommended calculations shown in Figure 14(a) and listed in Table 3. The ASC equations take on their maximum value of 3.0 for this case, resulting in C_b values of 12.83/3.0 = 4.28, whereas the AASHTO procedure gives only $C_b = 1.3$ for this case, resulting in C_b values of 12.83/1.3 = 9.87 (the first of these cases gives the largest conservatism of the AASHTO

calculations of C_b values of 12.43/1.0 = 12.43).

Therefore, the recommended procedure tends to be conservative at large C_b values for members with unbraced lengths having large values of W . Nevertheless, an estimated C_b of 3.95 will often place the LTB resistance, M_n , at the “plateau” strength. Hence there is limited need for more liberal estimates of these very large C_b values. The reader can observe from Figure 8 that for the singly symmetric cross sections targeted in this study, $L_b/h_o = 10$, and with similar moment diagrams compared to those just discussed, the largest benchmark C_b values are between 5.0 and 7.3, and these trends are captured conservatively by the recommended C_b calculations.

There is a specific unusual case for $J = 0$ ($W = \infty$) and $\rho = 0.9$ where there is an extreme sensitivity in the calculation of the governing elastic LTB resistance and the recommended equations exhibit a minimum C_b values of 0.769 [see Figure 14(u) and Table 3]. This case is discussed in detail in the following section.

Consideration of Cases with the Smallest C_b for the Different C_b Design Expressions

By far, the most important attribute of all structural design procedures is that they do not result in situations in which structural capacities are significantly overestimated. Therefore, it is most important that the subject design calculations be scrutinized for any situations where C_b values are significantly less than 1.0.

Figure 15(a) provides a plot from the complete set of studies conducted in this research that exhibits the smallest values of C_b specifically for linear moment diagrams for all the considered design estimates. Figures 15(b) through 15(d) show the specific worst-case loadings, their moment diagrams, other pertinent parameters, and the corresponding C_b design estimates. For these cases, $L_b/h_o = 30$ and $\rho = 0.9$, resulting in the minimum values for W (see Table 1). A small downward distributed load, corresponding to $\xi = 0.01$, is considered. This makes the moment diagrams slightly nonlinear. In the cases labeled in Figure 15(a), the ASC procedure significantly overestimates the benchmark solution by applying $R_m = 2.118$ for $\alpha < 0$. This gives a predicted ASC C_b equal to the ASC maximum limit of 3.0. The specific cases labeled in Figure 15(a) are as follows:

- The smallest C_b values occur for negative α values close to zero (i.e., where there is only a minor amount of reverse-curvature bending causing compression in the larger top flange). This is labeled as Case 1 in Figure 15(a). The specific parameters and C_b values for this case are shown in Figure 15(b).
- C_b values also become quite small at larger negative α values, leading to C_b values of 0.624 at $\alpha = -5$. This is labeled as Case 2 in Figure 15(a) and the specific

parameters and C_b values are summarized for this case in Figure 15(c).

- The recommended and the AASHTO C_b calculations both follow the benchmark $C_{b \text{ exact}}$ trends in Figure 15(a). However, they both tend to slightly overshoot the $C_{b \text{ exact}}$ values for cases with $\alpha < -1.0$. The smallest $C_{b \text{ exact}}/C_{b \text{ AASHTO}}$ of 0.892 occurs at $\alpha = -1.7$, where $C_{b \text{ AASHTO}}$ starts to reduce below its maximum limit of 2.5. This is labeled as Case 3 in Figure 15(a), and the specific parameters and C_b values are summarized for this case in Figure 15(d). It should be noted that lowering the cap on $C_{b \text{ AASHTO}}$ from 2.5 to 2.3 would only shift the point at which $C_{b \text{ AASHTO}}$ starts to reduce below the maximum limit to $\alpha = -2.2$ in Figure 15(a), and would result in an improvement in the smallest $C_{b \text{ exact}}/C_{b \text{ AASHTO}}$ to only 0.914.
- The recommended method has the smallest unconservative error of all the considered design procedures in Figure 15(a), correctly following the trends in the benchmark $C_{b \text{ exact}}$ curve but giving a smallest $C_{b \text{ exact}}/C_{b \text{ Rec}}$ of 0.920 at $\alpha = -1.5$. This specific case is not illustrated in Figure 15, but it is very similar to the case in Figure 15(d). This amount of unconservatism for the most extreme case of large ρ and small W values is considered acceptable.

Figure 15 can be compared to Figure 7(e) to gain a perspective of the influence of the extreme value of $L_b/h_o = 30$ compared to the intermediate value of $L_b/h_o = 10$ for this problem. One can observe that in Figure 7(e), the recommended C_b calculation is always slightly conservative compared to the benchmark $C_{b \text{ exact}}$ values.

Figure 16 provides a plot from the complete set of studies conducted in this research and documented in Slein et al. (2021). This figure shows Case 4, a concentrated transverse load case exhibiting the smallest values of $C_{b \text{ exact}}/C_b$ from the ASC calculations for the nonlinear moment diagrams considered. The specific parameters and C_b values for Case 4 are detailed in Figure 16(b). In Figure 16, again $L_b/h_o = 30$ and $\rho = 0.9$, resulting in the minimum values for W . The following observations can be gleaned from this figure:

- The ASC method properly scales down its C_b values by $R_m = 0.520$ for negative ξ values. This results in substantial conservatism between $\xi = 0.0$ and -0.5 and produces C_b values less than 1.0 for $\xi < -0.7$.
- However, for $\xi > 0$, the ASC method improperly scales up its C_b values by $R_m = 2.118$, with a maximum cap on its C_b of 3.0. This results in the minimum $C_{b \text{ exact}}/C_{b \text{ ASC}}$ of 0.454 at $\xi = 0.7$, which is labeled as Case 4. This case is particularly worrisome since $C_{b \text{ exact}}$ is only 1.22, while $C_{b \text{ ASC}}$ is 2.67.

- It can be observed that the recommended and the AASHTO C_b calculations both provide a reasonably accurate estimate of the benchmark $C_{b \text{ exact}}$ values throughout the range $-2.0 \leq \xi \leq 2.0$ for this problem, with the recommended procedure giving a highly accurate prediction of the shape of and the values from the $C_{b \text{ exact}}$ curve.

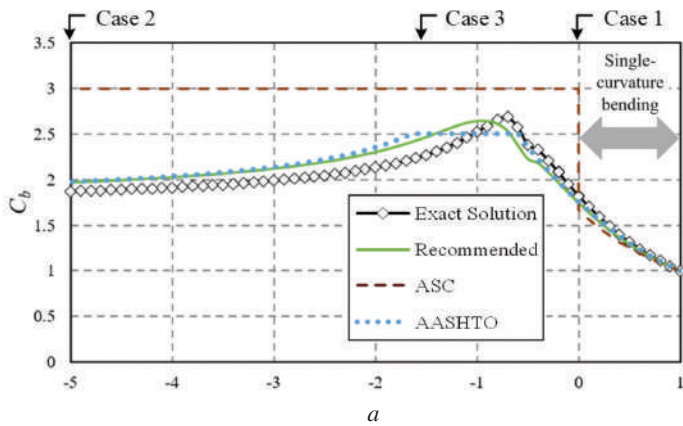
Figure 16(a) may be compared to the corresponding predictions for $L_b/h_o = 10$ [see Slein et al. (2021)] to gain a perspective of the influence of $L_b/h_o = 30$ compared to more intermediate length-to-depth ratios for this problem. For $L_b/h_o = 10$, the recommended C_b calculation is accurate to slightly conservative compared to the benchmark $C_{b \text{ exact}}$ values for all of the studied ξ values.

Figure 17 shows another example from the studies conducted in this research that exhibits small values of $C_{b \text{ exact}}/C_b$ from the ASC procedure for nonlinear moment diagrams. This plot corresponds to $L_b/h_o = 30$, $\rho = 0.3$, and $\alpha = -1.0$. Considering Figure 17(a), the ASC procedure appropriately scales down its C_b value by $R_m = 0.680$ for $\xi > 0$, although this leads to significantly conservative estimates for small ξ values. However, its use of $R_m = 1.479$ for negative ξ results in a low $C_{b \text{ exact}}/C_{b \text{ ASC}}$ of 0.650 at $\xi = -1.4$. This specific loading and geometry is labeled as Case 5 and is detailed in Figure 17(b). Again, the fact that $C_{b \text{ exact}}$ is only 1.27 but $C_{b \text{ ASC}}$ is significantly larger at 1.95 is troubling. It should be noted that this problem is equivalent to $L_b/h_o = 30$, $\rho = 0.7$, equal but opposite end moments corresponding to $\alpha = -1.0$, and a downward load corresponding to $\xi = +1.4$.

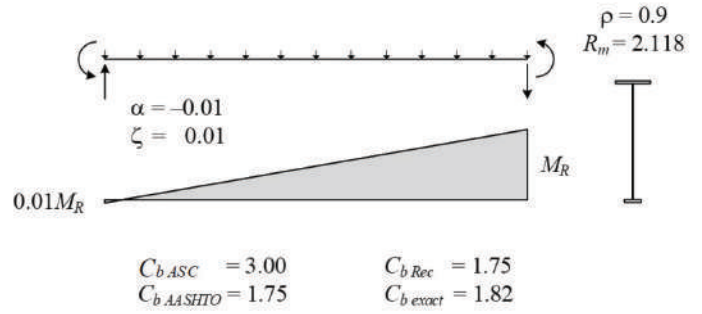
Figure 17(a) may be compared to the corresponding predictions for $L_b/h_o = 10$ [see Slein et al. (2021)] to gain a perspective of the influence of the extreme $L_b/h_o = 30$ compared to more intermediate length-to-depth ratios for this problem. Again, for $L_b/h_o = 10$, the recommended C_b calculation is accurate to slightly conservative compared to the benchmark $C_{b \text{ exact}}$ values for all of the studied ξ values. The $C_{b \text{ exact}}$ for $L_b/h_o = 10$ increases significantly for increasing ξ values starting from the local minimum $C_{b \text{ exact}}$ at $\xi = -2.0$.

Figure 18 highlights another case (Case 6) similar to that of Case 5 in Figure 17, but where the $C_{b \text{ exact}}/C_{b \text{ ASC}}$ is particularly small at $\xi = -2.0$. This is due to a smaller ρ of 0.1 in this problem. The $C_{b \text{ ASC}}$ for Case 6 is 2.79, whereas $C_{b \text{ exact}}$ is only 1.30. In addition, one can observe that the AASHTO predictions are quite conservative for $\xi < -0.7$ in Figure 18(a). Furthermore, the recommended calculations range from highly accurate, to slightly conservative, to slightly overestimating the benchmark solutions in this plot.

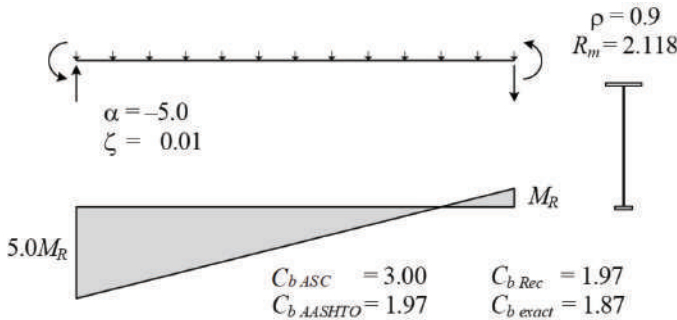
Figure 18 can be compared to the corresponding predictions for $L_b/h_o = 10$ [see Slein et al. (2021)] to gain a perspective of the influence of the extreme $L_b/h_o = 30$ compared to intermediate length-to-depth values for this problem. For



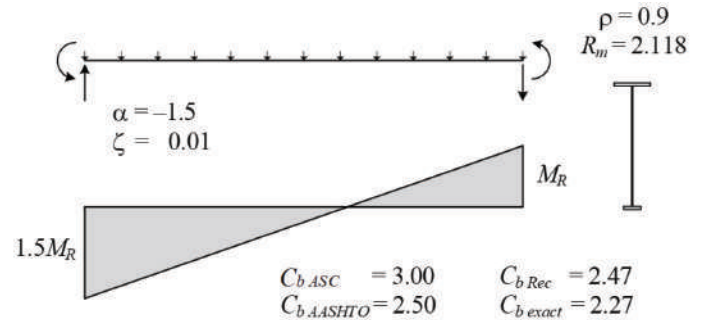
(a) C_b versus α



(b) Case 1 parameters and C_b values

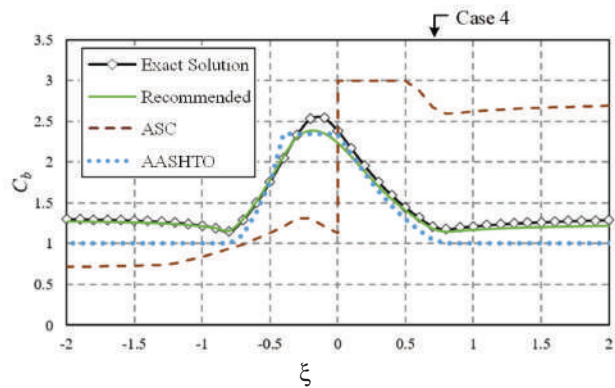


(c) Case 2 parameters and C_b values

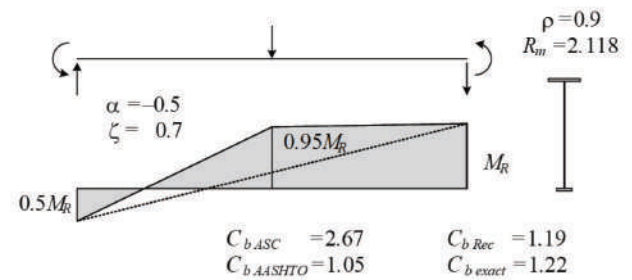


(d) Case 3 parameters and C_b values

Fig. 15. Cases exhibiting smallest $C_{b\text{ exact}}/C_b$ for the ASC, AASHTO, and recommended procedures for linear moment: $L_b/h_o = 30$, $\rho = 0.9$ ($C_{b\text{ exact}}/C_{b\text{ ASC}} = 0.608$ at $\alpha = 0$, $C_{b\text{ exact}}/C_{b\text{ AASHTO}} = 0.892$ at $\alpha = -1.7$, $C_{b\text{ exact}}/C_{b\text{ Rec}} = 0.920$ at $\alpha = -1.5$).

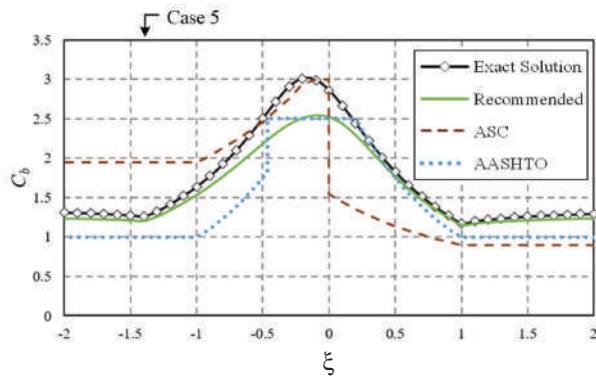


(a) C_b versus ξ

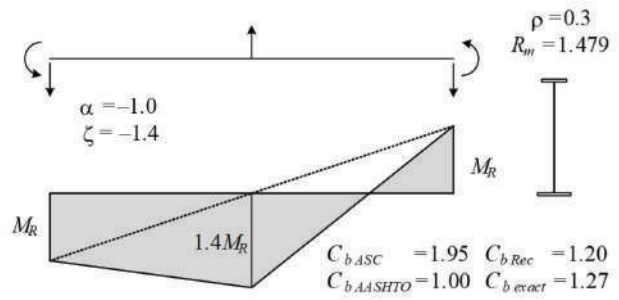


(b) Case 4 parameters and C_b values

Fig. 16. Worst-case $C_{b\text{ exact}}/C_b$ for ASC procedure, nonlinear moment—Case 4: concentrated transverse load, $L_b/h_o = 30$, $\rho = 0.9$, $a = -0.5$ ($C_{b\text{ exact}}/C_{b\text{ ASC}} = 0.454$ at $\xi = 0.7$).

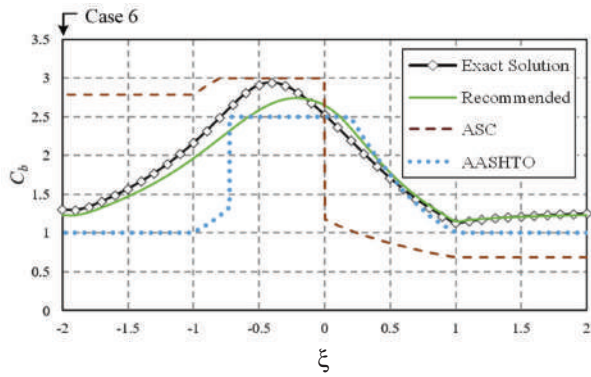


(a) C_b versus ξ

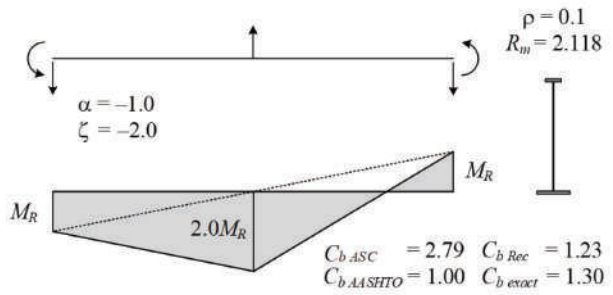


(b) Case 5 parameters and C_b values

Fig. 17. Illustration of small $C_{b,exact}/C_b$ for ASC procedure, nonlinear moment—Case 5: concentrated transverse load, $L_b/h_0 = 30$, $\rho = 0.3$, $\alpha = -1.0$ ($C_{b,exact}/C_{b,ASC} = 0.650$ at $\xi = -1.4$).

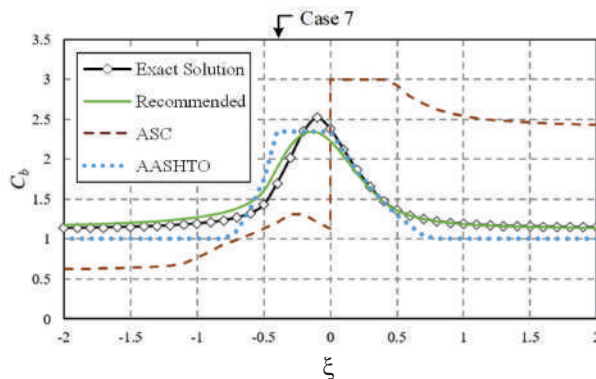


(a) C_b versus ξ

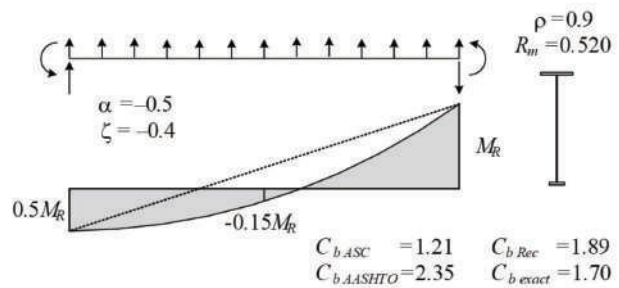


(b) Case 6 parameters and C_b values

Fig. 18. Example small $C_{b,exact}/C_b$ for ASC procedure, nonlinear moment—Case 6: concentrated transverse load, $L_b/h_0 = 30$, $\rho = 0.1$, $\alpha = -1.0$ ($C_{b,exact}/C_{b,ASC} = 0.466$ at $\xi = -2.0$).



(a) C_b versus ξ



(b) Case 7 parameters and C_b values

Fig. 19. Worst-case $C_{b,exact}/C_b$ for AASHTO procedure, nonlinear moment—Case 7: $L_b/h_0 = 30$, $\rho = 0.9$, $\alpha = -0.5$, distributed transverse load ($C_{b,exact}/C_{b,AASHTO} = 0.722$ at $\xi = -0.4$).

$L_b/h_o = 10$, the recommended method gives accurate to conservative predictions for all the cases.

Figure 19 highlights Case 7, which has the smallest values of $C_{b \text{ exact}}/C_b$ from the AASHTO procedure for the nonlinear moment diagrams considered. Figure 19(a) corresponds to $L_b/h_o = 30$, $\rho = 0.9$, $\alpha = -0.5$, and uniformly distributed transverse load. The AASHTO calculations provide a reasonable capture of the benchmark solutions in Figure 19(a). However, at the Case 7 value of $\xi = -0.4$, where $C_{b \text{ AASHTO}}$ starts to reduce below the value of 2.35, due to a change in location of the moment causing the maximum compression on the smaller bottom flange from the left-hand end to the interior of the span, $C_{b \text{ exact}}/C_{b \text{ AASHTO}} = 0.722$. Changing the maximum cap on the AASHTO results to $C_b = 2.3$ does little to change this overestimation of the benchmark solution.

It should be noted that Case 7 is equivalent to $L_b/h_o = 30$, $\rho = 0.1$, $\alpha = -2.0$, and a downward load corresponding to $\xi = +0.8$. In fact, for any of the cases presented in Figures 7 through 21, an equivalent case is produced by:

- Negating the moment diagram.
- Setting ρ to $(1 - \rho)$.
- Setting ξ to $-\xi/\alpha$.
- Setting α to $1/\alpha$.

The parameters $\rho = 0.1$, $\alpha = -2.0$, and $\xi = +0.8$ are representative of a potential unbraced length adjacent to an interior support in a continuous-span girder with a smaller top flange, large negative moment at the interior support on the left-hand end, downward distributed load, and a smaller positive moment equal to one-half of the maximum negative end moment at the right-hand end of the unbraced length. Appendix B illustrates calculations for a similar bridge girder having $L_b/h_o = 15$, $\rho = 0.229$, $\alpha = -2.0$, and $\xi = +0.5$.

Figure 19 can be compared to Figure 12(d) to gain a perspective of the influence of the extreme $L_b/h_o = 30$ compared to the more intermediate value of $L_b/h_o = 10$ for this problem. One can observe that in Figure 12(d), the maximum over-estimation of the benchmark solution by the AASHTO result (at $\xi = -0.3$) is slightly smaller than in Case 7.

Figure 20 highlights Case 8, which exhibits the smallest values of $C_{b \text{ exact}}/C_b$ from the recommended method for the nonlinear moment diagrams considered. This figure corresponds to a very different set of loadings and geometry compared to those discussed in the preceding text. Figure 20 corresponds to $L_b/h_o = 10$, but with J taken equal to zero, which makes the benchmark solution essentially independent of L_b/h_o . In Case 8, where $\alpha = 0.0$ (zero moment at the left-hand end), the unbraced length is subjected to a concentrated transverse load at its mid-length such that, given $\xi = -0.5$, the entire left half of the unbraced length is subjected to zero moment while the right half is subjected to a linearly varying moment from zero at the mid-span to a maximum value at the right-hand support. For this case, the unbraced length is in single-curvature bending with the flexural compression occurring in the larger top flange. As such, $C_{b \text{ Rec}}$ is relatively large at 2.83. The ASC calculations give a $C_{b \text{ ASC}}$ of 3.0. However, for decreasing ξ values infinitesimally smaller than -0.5 , the unbraced length is subjected to reverse-curvature bending with larger and larger compression in the member's small bottom flange on its left half. This results in a dramatic reduction in the C_b values for decreasing ξ slightly less than -0.5 . Both the recommended and ASC C_b methods capture this substantial sensitivity in the LTB resistance.

In the benchmark solution for this problem, the elastic LTB resistance starts to reduce significantly with decreasing ξ values for $\xi < -0.4$. It appears that the behavior is such that the tension added to the small bottom flange at $\xi = -0.4$ helps stiffen that flange against lateral displacement,

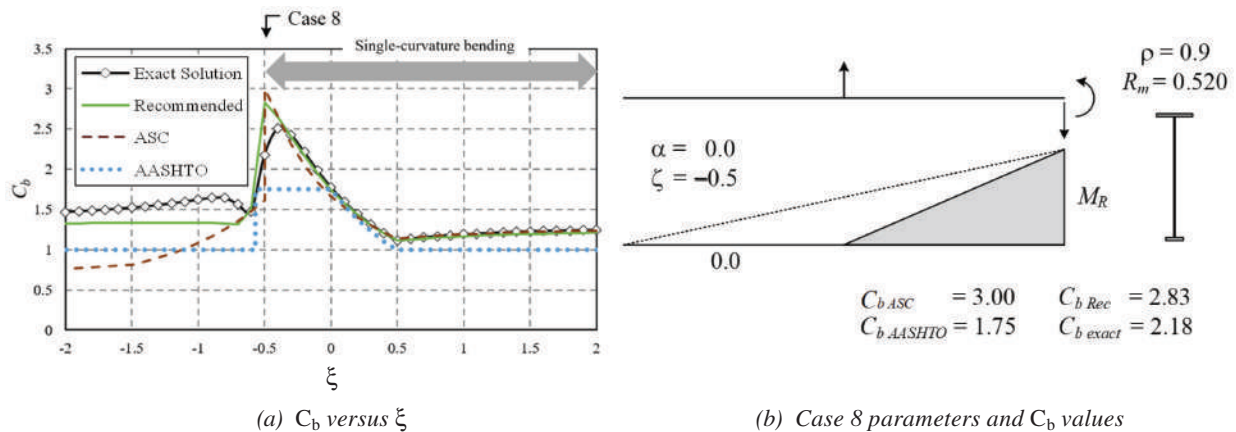


Fig. 20. Worst-case $C_{b \text{ exact}}/C_b$ for recommended procedure, nonlinear moment—Case 8: $L_b/h_o = 10$, $J = 0$, $\rho = 0.9$, $\alpha = 0.0$, concentrated transverse load at the middle of the unbraced length ($C_{b \text{ exact}}/C_{b \text{ Rec}} = 0.769$ at $\xi = -0.5$).

resulting in a larger LTB resistance, although the larger top flange is seeing larger flexural compression for this case. The buckling mode for $\xi = -0.5$ shows substantially larger lateral movement of the bottom flange within the left-half of the beam compared to the result for $\xi = -0.4$ (see Figure 21).

The sensitivity at $\xi = -0.5$ for this problem results in a $C_{b\ exact}/C_{b\ Rec} = 0.769$. It should be noted that $C_{b\ exact}/C_{b\ ASC} = 0.725$ at this value of ξ .

Figure 20(a) may be compared to the corresponding concentrated transverse load plot with J included [see Slein et al. (2021)] to gain a perspective of the influence the extreme assumption of $J = 0$. With J included, the recommended procedure gives a reasonably accurate characterization of $C_{b\ exact}$ for the entire range of the ξ values. The idealized elastic LTB solution assuming $J = 0$ is a common one employed in the ASC and AASHTO *Specifications* for slender-web members. This idealization is employed to provide some accounting for the potential reductions in the LTB resistance of these types of members due to web distortion. However, there is always some influence from St. Venant torsion, which tends to make the elastic LTB predictions assuming $J = 0$ slightly conservative. As can be seen from the minimum whisker for the recommended

method in Figures 14(u) and 14(v), the consideration of a relatively large but finite W value measurably reduces the unconservative errors shown in Figure 20. The minimum $C_{b\ exact}/C_{b\ Rec}$ in Figure 14(v) is 0.836. In addition, for $L_b/h_o = 5$, the LTB resistance will tend to be in the inelastic buckling range, which tends to further reduce the effect of potential overestimation of the benchmark elastic LTB resistance for the locally sensitive Case 8 in Figure 20.

Consideration of C_b Design Estimates for Long Heavy Column Members

The authors submit that the targeted doubly symmetric girder cross sections based on Figure 6, and the singly symmetric girder cross sections obtained after reducing the flange widths from the base values specified in this figure, combined with a maximum $L_b/h_o = 30$, provide reasonable minimum W values (see Table 1) representative of practical steel beam and girder designs. However, for heavy column sections, smaller W values are possible. Based on the synthesis in Figures 13 and 14, it is clear that the smallest benchmark $C_{b\ exact}$ values are obtained in cases where W is the smallest. As such, Slein et al. (2021) show additional studies investigating the behavior for W14x873 members with $L_b/d = 30$ as a representative extreme case of a long

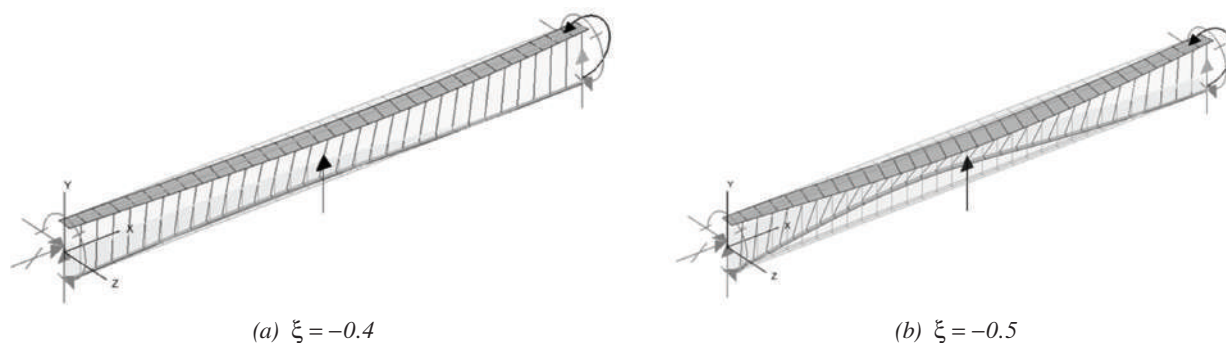


Fig. 21. Buckling mode shapes for $L_b/h_o = 10$, $J = 0$, $\rho = 0.9$, $\alpha = 0.0$, concentrated transverse load, with $\xi = -0.5$ versus $\xi = -0.4$; applied loads are indicated by black arrows, reactions are indicated by grey arrows.

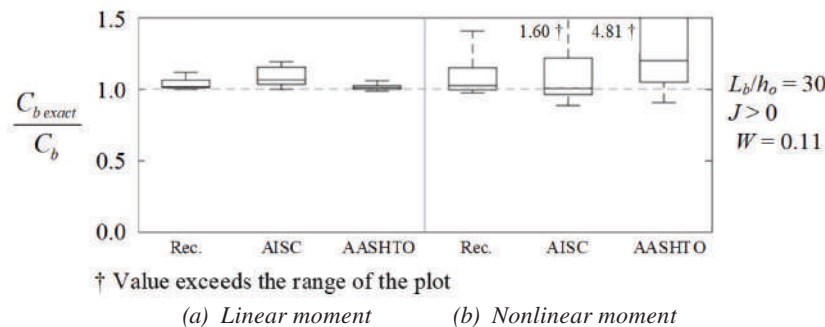


Fig. 22. Boxplots of $C_{b\ exact}/C_b$ considering W14x873 members.

heavy column to investigate the behavior of the C_b design estimates for this practical extreme.

Figure 22 shows boxplots for linear and nonlinear moment studies of the W14×873 members. For the linear moment studies, the AASHTO procedure clearly gives the best accuracy, while the recommended method provides a mean $C_{b \text{ exact}}/C_{b \text{ Rec}}$ of 1.03 and a COV of 0.034. The AISC *Specification* Equation F1-1 calculation is, on average, 9% conservative and has the largest COV of 0.055. The recommended method provides the best accuracy for the nonlinear moment cases, giving a mean $C_{b \text{ exact}}/C_{b \text{ Rec}}$ of only 1.05 and a COV of 0.084. The AISC *Specification* Equation F1-1 has a similar mean of 1.06 in these cases but a higher COV of 0.125. However, the recommended calculation never gives a $C_{b \text{ exact}}/C_{b \text{ Rec}}$ less than 0.972, whereas $C_{b \text{ exact}}/C_{b \text{ AISC}}$ is as small as 0.884.

SUMMARY AND CONCLUSIONS

This paper has presented a comprehensive evaluation of the results from the moment gradient factor (C_b) equations in the AISC (2016) *Specification* Commentary (ASC) and the AASHTO (2020) *Specifications* for prismatic singly symmetric I-section members. The investigation reveals that the ASC procedure produces both grossly conservative as well as significantly unconservative results in numerous practical situations. The causes of this behavior lie in the fact that the ASC quarter-point C_b equation is blind to the sign of the bending moment. The ASC calculation does not recognize the influence of different patterns of compression and tension in the different size flanges of a singly symmetric I-section member subjected to moment reversal. Furthermore, the ASC calculation exhibits substantial discontinuities in its C_b values as a function of the loading considered. This is due to its R_m factor. In recent developments, Reichenbach et al. (2020) recommend additional conditions on the application of R_m in the ASC C_b equation for members under reverse-curvature bending. These recommendations are considered in Appendix A. This modified ASC procedure gives improved results for a limited subset of specific cases but continues to show significant errors in general.

The C_b equations in the AASHTO *Specifications* provide some accounting for the different patterns of compression and tension in the separate flanges of singly symmetric I-section members subjected to moment reversal. However, these equations are based only on the moments at the ends and at the middle of the unbraced length. Hence, they are limited in their ability to capture the influence of nonlinear variations in moment along the unbraced length. In addition, the AASHTO procedure uses $C_b = 1.0$ in situations where the corresponding moment within the unbraced length is larger than the maximum brace point moment, causing compression in the flange under consideration. Furthermore, the AASHTO calculation can give significant

discontinuities in the calculated C_b as a function of the loading considered. This is due to changes in the governing flange in its procedure and can produce substantially conservative results in certain cases.

To rectify the limitations of the current ASC and AASHTO methods, a modified form of an alternative quarter-point C_b equation proposed by Wong and Driver (2010) is recommended. For cases involving moment reversal within the unbraced length of singly symmetric members, the moment terms in the Wong and Driver equation are replaced by the ratio of the moments to the corresponding elastic buckling moment based on $C_b = 1$ (i.e., M/M_{cr1}), considering the flange that is in compression at each of the locations where the moments are sampled. The studies show that the Wong and Driver equation, with this modification, provides substantially improved accuracy compared to the current AASHTO and ASC methods. With respect to the current ASC equations:

- For singly symmetric members where the moment diagrams are close to linear, the recommended approach gives C_b values that are, on average, 25% larger than the ASC Equation CF1-3, and with a tighter COV on $C_{b \text{ exact}}/C_b$ (0.104 vs. 0.569).
- For singly symmetric members with nonlinear moment diagrams, due to transverse loading with the unbraced length, the recommended approach gives C_b values that are on average 12% larger than the ASC Equation C-F1-3, again with a tighter COV on $C_{b \text{ exact}}/C_b$ (0.191 vs. 0.344).
- Unconservative $C_{b \text{ exact}}/C_b$ values, illustrated by a specific example to be as small as 0.466, corresponding to $C_{b \text{ exact}} = 1.30$ while $C_{b \text{ ASC}} = 2.79$, are avoided.

In addition, substantial conservatism of the AASHTO provisions, particularly for single-curvature cases where $C_{b \text{ AASHTO}}$ is taken equal to 1.0 when $C_{b \text{ exact}}$ is significantly larger than 1.0, is eliminated.

These improvements are achieved with a small reduction in the overall calculation effort relative to the current methods since the calculations of R_m in the ASC procedure and multiple C_b values in the AASHTO procedure are avoided. This aspect of the recommended method is highlighted by a practical design example in Appendix B.

In addition, the present studies show that the recommended equations do not require any cap on the maximum value of C_b obtained from the application of the actual and modified Wong and Driver quarter-point equations. As illustrated in the Background section of this paper and demonstrated further by Slein et al. (2021), the recommended equations show moderate improvements relative to the current AISC and AASHTO equations in benchmark solutions for doubly symmetric I-sections. Therefore, the Wong and Driver quarter-point equation, with the recommended modification to address singly symmetric I-section members

subjected to reverse-curvature bending, can be recommended as a simple single approach that can be applied to all routine situations involving moment gradient loading on I-section member unbraced lengths.

Lastly, the studies presented in the paper indirectly and independently confirm the findings from Helwig et al. (1997) that the web mid-height serves as the appropriate reference position on the cross-section profile from which load-height effects should be calculated, where appropriate. In all the studies conducted in this research, the transverse loads are applied at the web mid-height. The authors observed that this load position through the depth of the cross section clearly results in the best correlation between benchmark solutions and the predictions from the C_b equations targeted at singly symmetric I-section members. Furthermore, the studies in this paper provide independent confirmation of the benchmark results collected by Wong and Driver for specific doubly symmetric member cases.

As noted in the Introduction to the paper, the consideration of load-height effects, where appropriate, is an advanced topic that is commonly not addressed directly within design specifications. Readers are referred to Helwig et al. for detailed consideration of load-height effects. The practical C_b equation modifications recommended by Helwig et al. are considered applicable with the recommended base C_b equations presented in this paper. In addition, as discussed in the Introduction to the paper, the degree of lateral, rotational, and warping restraint provided at the ends of unbraced lengths, including continuity with and buckling interaction with adjacent unbraced segments, is not considered in the evaluation of the C_b procedures in this paper. Software such as SABRE2 (White et al., 2021), which has been employed to generate the benchmark solutions presented in this paper, provides one advanced option that allows these attributes to be readily addressed. Other general loading and boundary condition effects such as discussed by Wong and Driver (e.g., members with concentrated applied moments within their lengths), unbraced cantilevers with fixed supports or with flexible back-spans, etc., where manual estimates can become more challenging, can be readily addressed by modern computational methods such those as provided in SABRE2.

APPENDIX A

Recent Improvements to the ASC Method in the Literature

Reichenbach et al. (2020) recently recommended additional conditional requirements for the application of R_m in the ASC C_b equation for members under reverse-curvature bending. Reichenbach et al. specify in their Equation 10

that R_m should be taken equal to 1.0 for cases in which both $-0.5 < M_{small}/M_{large} < 0$ and $x_{inf} \leq 0.375L_b$, where M_{small} and M_{large} are the smaller and larger end moments on the unbraced length, and x_{inf} is the distance between the inflection point and the braced end corresponding to M_{small} .

Therefore, in the modified approach recommended by these authors,

$$R_m = 1.0 \quad (\text{A-1a})$$

for (1) doubly symmetric members; (2) singly symmetric members subjected to single-curvature bending; and (3) singly symmetric members subjected to reverse-curvature bending when both the ratio of the end moments is between 0 and -0.5 , exclusive, and the inflection point is located within $0.375L_b$ of the braced end with the smallest end moment in magnitude, inclusive. Otherwise,

$$R_m = 0.5 + 2 \left(\frac{I_{y,opp}}{I_y} \right)^2 \quad (\text{A-1b})$$

The ratio of M_{small}/M_{large} is directly related to the term α . The limit $-0.5 < M_{small}/M_{large} < 0$ corresponds to $-0.5 < \alpha < 0$ and $\alpha < -2.0$. In the parametric study cases presented in the current paper, α ranges between -1.0 and 1.0 for nonlinear moment diagrams and between -5.0 and 1.0 for linear moment diagram cases. For the linear moment diagram cases (e.g., see Figure 7), the results are plotted at a small increment in α such that the plots are effectively continuous; however, the nonlinear moment diagram cases are evaluated at $\alpha = -1.0, -0.5, 0.0, 0.5,$ and 1.0 . As such, when the modifications to R_m recommended by Reichenbach et al. are applied to the studies in this paper, there is no change in the results for the nonlinear moment diagram cases. Furthermore, for the linear moment diagram cases, the $0.375L_b$ limit on the inflection point location corresponds to $M_{small}/M_{large} = -0.6$, so the condition on the inflection point is always satisfied. Therefore, in effect, only the limits on α apply.

To evaluate the performance of the modified procedure recommended by Reichenbach et al. (2020) in the limit of linear moment diagrams, Figure A-1 is considered. This figure is an adaptation of Figure 15 in which the AASHTO results are replaced by the results from the modified ASC method recommended by Reichenbach et al. (2020), labeled as ASC*. Figure A-1 shows improvements by neglecting R_m when $-0.5 < \alpha < 0$ and $\alpha < -2.0$; however, for $-2.0 \leq \alpha \leq 0.5$, the ASC* procedure uses the same R_m as the ASC method, resulting in $C_{b\text{ exact}}/C_{b\text{ ASC}^*}$ as small as 0.710, or a 40.8% overestimation. Furthermore, it is important to note that there are two discrete shifts in $C_{b\text{ ASC}^*}$ instead of the one discrete shift in $C_{b\text{ ASC}}$ in Figure 15(a).

In Figure A-1(a), the behavior of R_m as a function of α in the ASC* method is as follows:

- For $\alpha \geq 0$, $R_m = 1.0$ due to single-curvature bending.
- For $-0.5 < \alpha < 0$, $R_m = 1.0$ since $-0.5 < M_{small}/M_{large} < 0$. The particulars for $\alpha = -0.49$, labeled as Case 11, are shown in Figure A-1(d).
- For $-1.0 \leq \alpha \leq -0.5$, $R_m = 2.118$ since $M_{small}/M_{large} \leq -0.5$. The particulars for $\alpha = -0.51$, labeled as Case 10, are shown in Figure A-1(c).
- For $-2.0 < \alpha \leq -1.0$, $R_m = 2.118$ since M_{small}/M_{large} is less than -0.5 (note that left end moment now has the larger magnitude). The particulars for $\alpha = -1.99$, labeled as Case 9, are shown in Figure A-1(b).
- For $\alpha < -2.0$, $R_m = 1.0$ since $-0.5 < M_{small}/M_{large} < 0$.

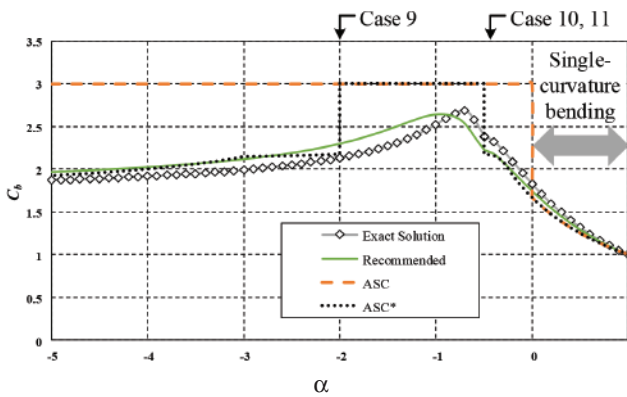
These cases demonstrate that the recommendations by Reichenbach et al. (2020) do improve the results within a portion of the design space; however, the results are still highly inaccurate elsewhere.

Figure A-2 is an adaptation of Figure 16, where again the results for the AASHTO methodology are replaced with the results based on the ASC* method recommended by Reichenbach et al. (2020). Figure A-2(a) shows that the

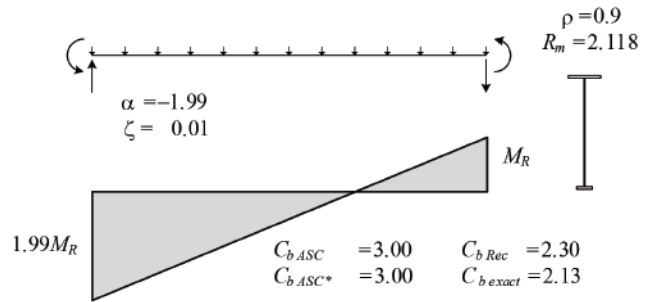
updated ASC methodology fixes the unconservative error illustrated in Figure 16(a). However, it does not fix the conservative error. In the plot in Figure A-2(a), R_m is included once the inflection point moves within $0.375L_b$ from the location of M_{small} . This occurs at $\xi \leq -0.050$. This inclusion of R_m results in $C_{b\ exact}/C_{b\ ASC^*}$ values as large as 2.11. Figure A-2(b) shows the particulars for Case 12, exhibiting the largest error.

Figure A-3(a) has the same loadings as Figure A-2(a), but ρ is changed from 0.9 to 0.1. In Figure A-3(a), the updated methodology fixes the conservative errors, but it does not fix the unconservative errors. Figure A-3(b) shows the worst case, Case 13, where $C_{b\ exact}/C_{b\ ASC^*} = 0.497$, with the ASC* procedure overpredicting by more than a factor of 2.0.

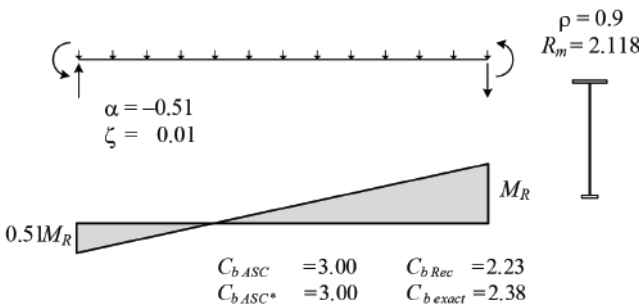
Based on the results illustrated in Figures A-1, A-2, and A-3, it is apparent that further adjustments would be needed to the ASC* procedure to limit the large conservative and unconservative errors still exhibited. The recommended adaptation of the Wong and Driver procedure presented in the current paper avoids the complexities of the various conditional tests associated with the ASC* method while maintaining simplicity of the calculations and giving an accurate estimate of the benchmark C_b .



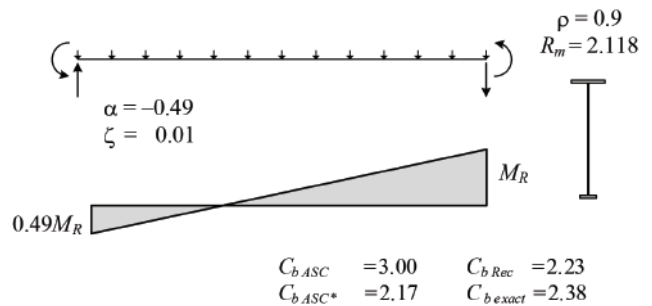
(a) C_b versus α



(b) Case 9 parameters and C_b values

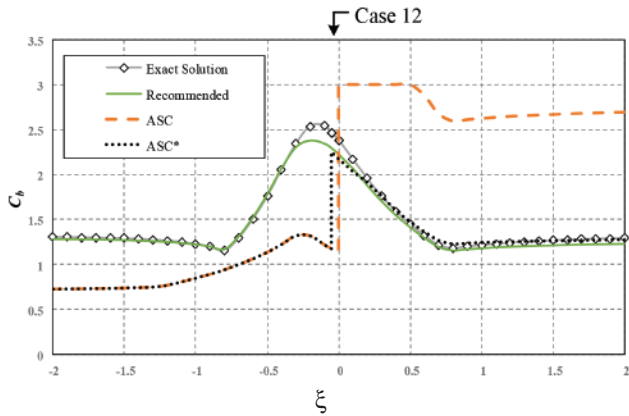


(c) Case 10 parameters and C_b values

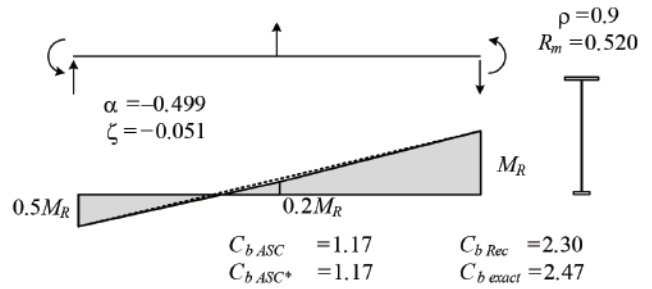


(d) Case 11 parameters and C_b values

Fig. A-1. Cases exhibiting smallest $C_{b\ exact}/C_b$ for the ASC, ASC* (Reichenbach et al., 2020) and recommended procedures for linear moment: $L_b/h_0 = 30$, $\rho = 0.9$ ($C_{b\ exact}/C_{b\ ASC} = 0.608$ at $\alpha = 0$, $C_{b\ exact}/C_{b\ ASC^*} = 0.710$ at $\alpha = -1.99$, $C_{b\ exact}/C_{b\ Rec} = 0.920$ at $\alpha = -1.5$).

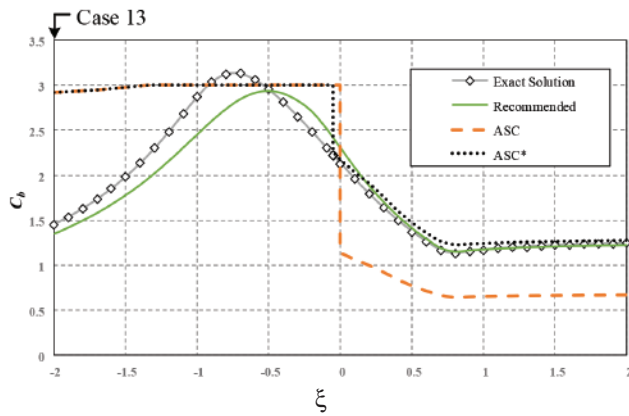


(a) C_b versus ξ

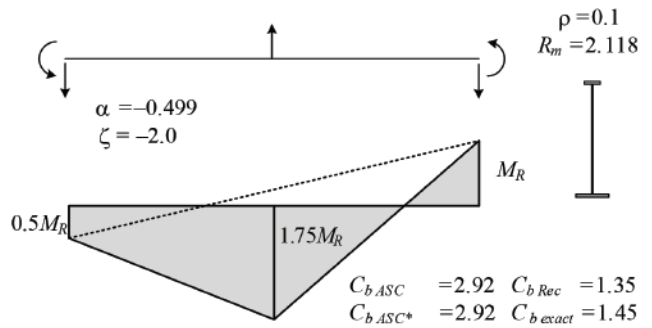


(b) Case 12 parameters and C_b values

Fig. A-2. Partially improved performance of $C_{b\text{ exact}}/C_b$ for the modified ASC procedure recommended by Reichenbach et al. (2020), nonlinear moment—Case 12: concentrated transverse load, $L_b/h_o = 30$, $\rho = 0.9$, $\alpha = -0.499$ ($C_{b\text{ exact}}/C_{b\text{ ASC}^*} = 2.11$ at $\xi = -0.051$).



(a) C_b versus ξ



(b) Case 13 parameters and C_b values

Fig. A-3. Worst-case $C_{b\text{ exact}}/C_b$ for the modified ASC procedure recommended by Reichenbach et al. (2020), nonlinear moment—Case 13: concentrated transverse load, $L_b/h_o = 30$, $\rho = 0.1$, $\alpha = -0.499$ ($C_{b\text{ exact}}/C_{b\text{ ASC}^*} = 0.497$ at $\xi = -2.0$).

APPENDIX B

Reverse-Curvature Bending Design Example

The following example design calculations consider a two-span continuous bridge girder with equal span lengths. The focus of the calculations is on determining the distributed load the girder can safely support during construction, considering the LTB limit state. It is assumed that the girder is braced at the abutments, at the pier section, and at each mid-span location. It is assumed that form supports distribute a portion of the load to the bottom flange; therefore, mid-height loading is assumed as in the example presented by Helwig et al. (1987).

The girder cross section is the same as the cross section considered in example design calculations by Helwig et al. (1987), except all the dimensions are scaled by a factor of 1.5. This gives a 12 in. \times 1.5 in. top flange, an 18 in. \times 1.5 in. bottom flange, and a 60 in. \times 0.75 in. web. The span length of the girder is taken as 150 ft, giving an unbraced length of $L_b = 75$ ft.

Load and resistance factors are not included in the calculations.

This problem has some similarity to the Case 7 example shown in Figure 19, except the monosymmetry is not as severe in this problem ($\rho = 0.229$) and the length-to-depth ratio of the unbraced length is smaller ($L_b/h_o = 15$). Figure B-1 shows the moment diagram for the right-hand span, with the pier section located on the left-hand end of the span. The unbraced length under consideration is the one subjected to reverse-curvature bending adjacent to the pier. The maximum negative and positive moments as well as the quarter-point moments are labeled in the figure. The moment diagram in the subject unbraced length corresponds to $\alpha = -2.0$ and $\xi = +0.5$.

The following calculations are the same for the three methods being evaluated:

$$r_{t.top} = \frac{b_{f.top}}{\sqrt{12 \left(1 + \frac{1}{3} \frac{D_{c.top} t_w}{b_{f.top} t_{f.top}} \right)}} = 2.87$$

$$r_{t.bot} = \frac{b_{f.bot}}{\sqrt{12 \left(1 + \frac{1}{3} \frac{D_{c.bot} t_w}{b_{f.bot} t_{f.top}} \right)}} = 4.65$$

$$M_{cr1.top} = \frac{\pi^2 E S_{xc.top}}{\left(\frac{L_b}{r_{t.top}} \right)^2} \sqrt{1 + 0.078 \frac{J}{S_{xc.top} h_o} \left(\frac{L_b}{r_{t.top}} \right)^2} = 788 \text{ kip-ft}$$

$$M_{cr1.bot} = \frac{\pi^2 E S_{xc.bot}}{\left(\frac{L_b}{r_{t.bot}} \right)^2} \sqrt{1 + 0.078 \frac{J}{S_{xc.bot} h_o} \left(\frac{L_b}{r_{t.bot}} \right)^2} = 1,740 \text{ kip-ft}$$

The calculations for the three primary methods evaluated in the paper are presented in the following subsections and are compared to a converged numerical benchmark solution of the distributed load the girder can safely support during construction of $\gamma_{e.exact}(1 \text{ kip/ft}) = 1.38 \text{ kip/ft}$ from SABRE2 (White et al., 2021).

ASC and ASC* Procedures

For the ASC* procedure, the updated exclusion criteria for the calculation of R_m ,

$$M_{small}/M_{large} < -0.5 \quad x_{inf} \leq 0.375 L_b \text{ from } M_{small}$$

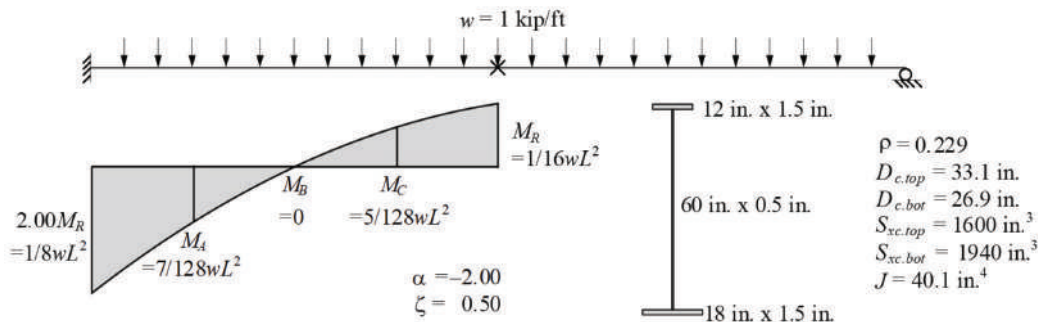


Fig. B-1. Moment diagram and cross-section properties for an example bridge girder during construction having $L_b/h_o = 15$, $\rho = 0.229$, $\alpha = -2.0$, and $\xi = +0.5$.

are violated for this example. Therefore, R_m is calculated using Equation 1b and the ASC* method gives the same result as the ASC method:

$$R_m = 0.5 + 2 \left(\frac{I_{y.top}}{I_y} \right)^2 = 0.604$$

$$C_b = \frac{12.5M_{max}}{2.5M_{max} + 3M_A + 4M_B + 3M_C} R_m = 1.59 \leq 3.0$$

Using Equation 2, considering the largest moment and the base elastic buckling capacities associated with each flange, the elastic buckling load ratio is calculated as

$$\gamma_{eLTB} = \min \left(\frac{C_b M_{cr1.top}}{M_{max.top}}, \frac{C_b M_{cr1.bot}}{M_{max.bot}} \right) = 0.890$$

$$w_{cr} = \gamma_{eLTB} (1 \text{ kip/ft}) = 0.890 \text{ kip/ft}$$

The resulting distributed load the girder can safely support during construction through the ASC and ASC* procedure is highly conservative, at 64% of the benchmark solution. Note that if R_m were taken equal to 1.0, the resulting distributed load the girder can safely support is estimated as 1.47 kip/ft, or approximately 6.5% larger than the benchmark solution.

AASHTO Procedure

For reverse-curvature bending cases, the AASHTO procedure requires assessment of the concavity or convexity the moment diagram with respect to each flange. Using Equations 8 and 9, the moment gradient factors for each flange are calculated as

$$C_{b.bot} = \min \left[1.75 - 1.05 \frac{M_0}{M_2} + 0.3 \left(\frac{M_0}{M_2} \right)^2, 2.5 \right] = 2.35$$

$$C_{b.top} = \min \left[3.10 - 3.30 \frac{M_{mid}}{M_2} + 1.2 \left(\frac{M_{mid}}{M_2} \right)^2, 2.5 \right] = 2.5$$

Using Equation 7, considering the respective moment gradient factor, largest moment, and elastic buckling capacity in each flange, the elastic buckling load ratio is calculated as

$$\gamma_{e.AASHTO} = \min \left(\frac{C_{b.top} M_{cr1.top}}{M_{max.top}}, \frac{C_{b.bot} M_{cr1.bot}}{M_{max.bot}} \right) = 1.40$$

$$w_{cr} = \gamma_{eLTB} (1 \text{ kip/ft}) = 1.40 \text{ kip/ft}$$

The resulting distributed load the girder can safely support through the AASHTO procedure is slightly unconservative, 1.4% larger than the benchmark solution.

Recommended Procedure

The recommended procedure considers the ratios of the moment demands to the critical elastic moment of the flange in compression, either $M_{cr1.top}$ or $M_{cr1.bot}$, along the length of the member.

$$C_b = \frac{4 \left(\frac{M}{M_{cr1}} \right)_{max}}{\sqrt{\left(\frac{M}{M_{cr1}} \right)_{max}^2 + 4 \left(\frac{M}{M_{cr1}} \right)_A^2 + 7 \left(\frac{M}{M_{cr1}} \right)_B^2 + 4 \left(\frac{M}{M_{cr1}} \right)_C^2}} = 2.24$$

Using Equation 11, the elastic buckling load ratio is calculated as

$$\gamma_{e.Recommended} = \frac{C_b}{\left(\frac{M}{M_{cr1}} \right)_{max}} = 1.26$$

$$w_{cr} = \gamma_{eLTB} (1 \text{ kip/ft}) = 1.26 \text{ kip/ft}$$

The resulting distributed load the girder can safely support through the recommended procedure is slightly conservative, at approximately 91% of the benchmark solution.

REFERENCES

- AASHTO (2020), *AASHTO LRFD Bridge Design Specifications*, 9th Ed., American Association of State and Highway Transportation Officials, Washington, D.C.
- AISC (2016), *Specification for Structural Steel Buildings and Commentary*, ANSI/AISC 360-16, American Institute of Steel Construction, Chicago, Ill.
- Helwig, T.A., Frank, K.H., and Yura, J.A. (1997), "Lateral-Torsional Buckling of Singly-Symmetric I-Beams," *Journal of Structural Engineering*, ASCE, Vol. 123, No. 9, pp. 1,172–1,179.
- Jeong, W.Y. (2014), "Structural Analysis and Optimized Design of General Nonprismatic I-Section Members," Doctoral Dissertation, Georgia Institute of Technology, Atlanta, Ga.
- Kitipornchai, S., Wang, C.M., and Trahair, N.S. (1986), "Buckling Properties of Monosymmetric I-Beams under Moment Gradient," *Journal of Structural Engineering*, ASCE, Vol. 112, No. 4, pp. 781–799.
- Reichenbach, R.C., Liu, Y., Helwig, T.A., and Engelhardt, M.D. (2020), "Lateral-Torsional Buckling of Singly-Symmetric I-Girders with Stepped Flanges," *Journal of Structural Engineering*, ASCE, doi:10.1061/(ASCE)ST.1943-541X.0002780.

Salvadori, M.G. (1956), "Lateral Buckling of I-Beams," *ASCE Transactions*, American Society of Civil Engineers, Vol. 120, pp. 1,165–1,177.

Slein, R., Jeong, W.Y., and White, D.W. (2021), "A Critical Evaluation of Moment Gradient (C_b) Factor Calculation Procedures for Singly Symmetric I-Section Members," Structural Engineering, Mechanics and Materials Report No. 5, School of Civil and Environmental Engineering, Georgia Institute of Technology, Atlanta, Ga.

White, D.W., Slein, R., Toğay, O., and Jeong, W.Y. (2021), "SABRE 2," white.ce.gatech.edu/sabre (August 31, 2021).

Wong, E. and Driver, R. (2010), "Critical Evaluation of Equivalent Moment Factor Procedures for Laterally Unsupported Beams," *Engineering Journal*, AISC, Vol. 47, No. 1, pp. 1–20, and Closure, Vol. 47, No. 4, pp. 281–283.

Ziemian, R. (2010), *Guide to Stability Design Criteria for Metal Structures*, 6th Ed., Wiley, N.Y.

A Novel Performance-Based Evaluation Method of Built-Up Wide-Flange Steel Columns Subjected to Close-Range Detonations

Yongwook Kim, Salvatore Florio, and Qian Wang

ABSTRACT

Transportation facilities are crucial civil engineering structures, which are vulnerable to increasing risks of potential explosive loadings. The structural members of older facilities were typically made of steel and built up from angles and plates joined together with rivets, rather than directly rolled in steel mills. Most existing blast mitigation design approaches were made for military or petrochemical facilities in rural areas with significant stand-off distances. However, transportation facilities, which are located in congested major cities, with structural members exposed to pedestrians and passengers, are subject to the risks of potential close-range or near-contact detonations. Recently, new approaches were developed to address the potential progressive collapse of high-rise buildings in urban environment, but the approaches do not address the localized deformations or failures on column flange or web elements that are common in close-range or near-contact detonations. For this reason, the existing approaches are not appropriate to the blast mitigation design of the urban transportation structures. Instead, a high-fidelity, nonlinear, explicit finite element analysis is suggested. Typical practicing structural engineers do not have opportunities for education or training for such analysis due to technical challenges, cost, and time constraints. The main goal of the present research is to provide practical guides of the nonlinear, explicit finite element analyses for close-in or near-contact detonation problems that can be followed by practicing structural engineers and to provide simple design charts that can be used as a preliminary tool without performing the analyses. To accomplish the goal, more than 200 parametric study models were built for nonlinear, explicit finite element analysis of built-up steel columns subjected to close-in detonations. Characteristics of the steel materials for the built-up columns were investigated and incorporated in the numerical models. The models were determined so that they can cover practical ranges of columns, stand-off distances, and charge weights. The analysis results were presented on contour graphs using novel performance-based damage criteria. The graphs and design methodology presented in this study can be used as an efficient and practical tool to quickly assess blast resistance of built-up steel columns in transportation structures.

KEYWORDS: steel column, close-in detonation, near-contact detonation, blast, performance-based, built-up, transportation, security.

INTRODUCTION

Transportation passengers, vehicles, structures, and facilities have been targeted by terrorists for the past century, and more frequent occurrences have been observed in recent years (e.g., Jenkins, 1997; Jenkins and Gersten, 2001). Public- and private-sector buildings were frequent targets of blast attacks as well (Marchand and Alfawakhiri, 2004). Many transportation structures, such as bridges, bus terminals, rail stations, or rail tunnels, have been designed and built in such a way that their essential structural skeletons are exposed to the general public without

any architectural coverings. Due to the congested nature of a typical urban environment, where major transportation facilities are located, it is difficult, or even impossible to maintain significant stand-off distances around each structural member or component elements to protect structural members (Williamson and Winget, 2005; FEMA, 2007). Thus, urban transportation structures are prone to potential blast attacks in close proximity. Close-range blast loads, frequently referred to as near-contact charges, even with a small charge weight, could result in a column failure. The failure of either a single column or a group of columns could lead to a progressive collapse of a structure and devastating consequences, including significant casualties as well as economic, functional, and social losses (NYPD, 2009).

For the design of structures to resist blast loadings, there are several approaches available in public resources (e.g., ASCE, 2010; DOD, 2014; U.S. Army, 1986; Gilsanz et al., 2013). However, none of the approaches are applicable to structures subjected to close-in (or near-contact) detonations because these approaches were developed mainly for structures with greater stand-off distances, such as rural military or petrochemical facilities. There are some blast-resistant design approaches developed for bridges (e.g., Davis et al.,

Yongwook Kim, Ph.D., P.E., Assistant Professor, Manhattan College, Riverdale, N.Y. Email: yongwook.kim@manhattan.edu (corresponding)

Salvatore Florio, Graduate Student, Manhattan College, Riverdale, N.Y. Email: sflorio01@manhattan.edu

Qian Wang, Ph.D., P.E., Associate Professor, Manhattan College, Riverdale, N.Y. Email: qian.wang@manhattan.edu

Paper No. 2019-13R2

ISSN 0013-8029

ENGINEERING JOURNAL / FOURTH QUARTER / 2022 / 275

2017; Winget et al., 2005; Baylot et al., 2003); however, application of these approaches to transportation facilities or urban building structures is limited or not appropriate.

For structures subjected to far-field detonations, the blast pressure, which is initially a spherical shape, becomes almost uniform when it reaches the surface of a target structure. The entire length of a structural member is engaged to resist the blast pressure, and subject to bending failures, after forming plastic hinges. However, for structures subjected to close-in detonations, the loading is intensely amplified within a small area and damages a target structural member severely and locally; its amplitude then decays much more quickly. The resulting damages are mostly localized deformations to the members, such as bulging, puncturing (breaching), or severing, which are not typical modes of failure observed in civil engineering structures. The local deformations cause weakening of the member due to a change of stress flow path, substantial section property loss, or component instability. When the local damage is excessive to a column member, the column may eventually collapse under the presence of gravity loads. The column collapse involves mostly vertical downward crushing, but no significant lateral deformations. Publicly available experimental evidences of the failure modes of steel members subjected to close-in detonations are found in limited literature (e.g., Krishnappa et al., 2014; Remennikov and Uy, 2014; Mazurkiewicz et al., 2015).

For long-span suspension bridges, steel cellular towers were often used as the major gravity load supporting structures. The steel towers are potentially subjected to close-in detonations due to close proximity to a roadway. The main type of blast load is generated from a large-truck Vehicle-Borne Improvised Explosive Device (VBIED) potentially detonated a few feet away from the tower's surface. For the steel towers, blast mitigation design approaches were developed and provided in the *Bridge Security Design Manual* by Davis et al. (2017).

For transportation facilities, such as rail and subway tunnels and stations, steel columns are often used as the major gravity load carrying structures. The steel columns are potentially subjected to close-in detonations due to close exposure to passenger traffic. Man-Portable Improvised Explosive Devices (MPIEDs) are more common in transportation facilities because vehicular accessibility to underground tunnels and stations is limited (NYPD, 2009). In order to be carried by hand, historically the charge weights attempted for transportation facilities and buildings have been relatively lighter than for other targets (Jenkins, 1997; NYPD, 2009). However, light charge weights can be lethal when detonated in close proximity or near-contact, as quoted from FEMA (2007):

...protection of primary vertical load-carrying members by designing architectural or structural features

that can keep an explosive even a few feet away can make a big difference. For portable devices, a few inches or a couple of feet may be critical...

Both steel towers of a suspension bridge and steel columns in a transportation facility are critical load-carrying members potentially subjected to close-in detonations, although the order of magnitudes in charge weights, stand-off distances, and overall dimensions are significantly different between them. However, the behavior of steel columns subjected to close-in detonations can be significantly different from the bridge towers due to geometric differences. For example, a typical wide-flange steel column has the three-sided flow boundary formed by the web and the two flanges where blast pressure can be amplified, while a typical bridge tower has a flat surface on all sides. No published blast evaluation or mitigation design approaches are available for steel columns subjected to close-in (or near-contact) detonations.

Recently, blast analysis and design approaches were developed for high-rise buildings in urban settings to account for progressive collapse, such as Sideri et al. (2017). In the literature, the approach focused on far-field detonations, which were generated from a large vehicle, or VBIED, located on a nearby street. The approach assumed a uniform blast pressure applied to each of the lower-level column members, which were modeled with stick models or beam elements. Some of the columns subjected to the uniform pressure experienced a bending failure, engaging the entire member length. The gravity loads applied to the failed columns were redistributed to adjacent columns, which in turn caused failures of more columns. The approach is not directly applicable to the transportation facility columns in this study because (1) the localized deformations or failure modes that are dominant in near-contact detonations, such as bulging, puncturing (breaching) or severing, cannot be addressed in the stick models or beam elements used in the literature, and (2) the nature of loading from the far-field detonations used in the literature is substantially different from the close-range or near-contact detonations that are prevalent in the present study.

The analysis of steel columns subjected to close-field detonations is a complex problem, where published experimental data are extremely limited for a few selected members (e.g., Krishnappa et al., 2014; Remennikov and Uy, 2014; Mazurkiewicz et al., 2015). Thus, typically high fidelity explicit nonlinear finite element analyses (FEAs) are required for evaluation or mitigation design of structures subjected to close-in detonations, as suggested by literature (e.g., ASCE, 2011; Krauthammer, 2008; Davis et al., 2017). The members are generally modeled with shell or plate models to account for the geometric features of component elements, such as flanges and web. Although there are a few published studies for close-in detonations using numerical

simulations (e.g., Krishnappa et al., 2014; Remennikov and Uy, 2014; Mazurkiewicz et al., 2015; Ngo et al., 2015; Shin et al., 2014), they did not cover a wide range of shapes or suggest any practical evaluation or mitigation means or methods for general structural engineers to use. Also, their focus was placed mainly on a few standard hot-rolled steel shapes and not built-up shapes, which are more common in historic transportation facilities. In addition, most structural engineers do not have direct access to high-fidelity, explicit, nonlinear FEA due to technical difficulties, the time-consuming nature of analyses, and budgetary concerns. These challenges, along with other reasons, have discouraged state or local agencies, which have jurisdiction over transportation facilities, from performing urgent and necessary security hardening projects. In addition, concerns about quality controls have been raised in the engineering community due to a lack of guidance, standards, specifications, or codes for close-in (or near-contact) detonations.

The present study focuses on built-up, wide-flange-shaped steel columns, subjected to extremely close-in detonations with relatively smaller charge weights. The objective of this study is to (1) perform a series of comprehensive numerical studies and present the resulting patterns on charts, (2) present the details of a numerical method that can be followed by general structural engineers, and (3) suggest practical design approaches based on the charts that can be used without the numerical tool.

The numerical studies use complex high-fidelity, explicit, nonlinear FEA method, while the suggested design approaches use simple design charts that are suitable for use in the preliminary blast-resistant design and/or for cost estimate purposes of existing built-up transportation structural members. To accomplish this, performance-based damage criteria are suggested, which are then used to develop a series of design curves and graphs in this study. The conditions and limitations required to use the design curves and graphs are specified for preliminary designs. With the developed graphs, structural engineers can determine whether or not each structural member under consideration is subject to failure for a set of given design parameters, including a column size, charge weight, and stand-off distance. For the situation where a column is subject to failure, practical blast mitigation design strategies are also suggested.

PARAMETERS AFFECTING BLAST RESISTANT STRENGTH

Standard wide-flange steel shapes (W-shapes) in AISC *Steel Construction Manuals* (AISC, 1927, 1934, 1946, 1963, 2017) have been traditionally popular structural members for buildings and transportation facilities. A typical W-shape is composed of two parallel, flat-flange elements

and one perpendicular web element, connecting the flanges to form a capital letter I or H shape.

The most controlling factors that affect the resistance of a steel column subjected to close-in blast loads are a stand-off distance, a charge weight, and a column size. Traditionally, the stand-off distance has been defined as the distance from the surface of a structure to the explosive center. However, in this study, the stand-off distance (SOD) is defined as the clear distance between the structure and the explosive, or the distance from the center of a column to the nearest face of the explosive. This is because the web element is most affected in W-shape columns, and the distance is significantly affected by the explosive dimensions. A comparison of the traditional and clear stand-off distances is shown in Figure 1.

In this study, six different SODs, of which the maximum is not more than a few column depths, were considered for each column. This is because, practically, an architect would not likely use more than a few column depths as a cladding radius to cover up each column for aesthetical, functional, or space-use reasons. The six SODs were used for all columns in the parametric study: 0.2X, 0.4X, 0.6X, 0.8X, 1.0X, and 1.2X. The X is a fixed and common number for all the columns, but for security reasons and concerns, the value X is unrevealed in this study. The architectural covering would be a light-gage metal cladding, sheetrock, gypsum board, plywood, or other material, which do not have enough stiffness to significantly reduce the effects of blast loads considered in this study so as not to damage the column as fragments. Instead, it would function as fire-proofing or simply an aesthetical cover. For the purpose of this study, it was assumed that the covering radius simply provides a clear SOD, as seen in Figure 1. It is known that the smaller the SOD, the more the damage to a column.

In this study, the charge weight (CW) is defined as the TNT charge weight. Due to limitations in vehicular accessibility to underground transportation facilities, such as rail or subway stations and tunnels, this study focused on typical CWs of the MPIED, which are light enough to be carried by pedestrians in bags without relying on other means of transportation. For each of the columns investigated, five different CWs were used in the parametric study: 0.12Y, 0.23Y, 0.44Y, 0.86Y, and 1.32Y. The Y is also a fixed and common number for all the columns, but for security reasons and concerns, the value Y is undisclosed in this study. The CWs are within comparable ranges to the physical weight of a 1 ft column length. It is known that the larger the CW, the more the damage to a column.

In addition, the position of the explosive is assumed to face the web directly (0° case in Figure 1). This is because the detonation pressure from the position is trapped most in the area surrounded by the three flat components of

the column (two flanges and web). The reflective pressure within the region escalates to a much larger magnitude, which damages the column most significantly. The damages from the position could often lead to puncturing a hole on the web, which can be fatal to the column. Similar observations and discussions are also found in literature (e.g., Mazurkiewicz et al., 2015; Krishnappa et al., 2014). Other positions, such as an angle to face flanges directly (90° case in Figure 1) and a skew angle (45° case in Figure 1), are not considered in this study because the detonation pressures from these positions tend to wash out around the column surface, resulting in much less amplitudes and damages than the 0° case. The same analysis approaches can be taken as the 0° case in this study, for the analysis of the 90° or 45° cases.

Presently each standard W-shape is hot-rolled from a steel mill as a single member. In the early 1900s, however, built-up shapes were prevalent in steel construction when major transportation facilities were built in the United States, such as commuter rail and subway stations. The built-up shapes resemble the standard wide-flange shapes, but they were composed of four L-shaped angles, one web plate, and, in some cases, two cover plates, joined together with rivets. This study focused on the built-up wide-flange shapes, of which geometries are equivalent to standard W14 series wide-flange steel members listed in the AISC *Steel Construction Manual* (AISC, 2017). These shapes and series are very common as steel columns in buildings and transportation facilities. Out of all 38 W14 standard steel

members listed in the 15th edition AISC *Steel Construction Manual*, six different uniformly dispersed shapes were chosen for the study to cover a wide but practical size range of built-up columns, as summarized in Table 1. The size designations in parentheses in Table 1 represent sizes in the SI unit system per AISC (2017).

The maximum size of the built-up shapes used for the present study was limited to the built-up shape equivalent to standard W14x426 because it is not common to observe built-up shapes with cover plates thicker than 3 in. (76 mm). For equivalent cross-sectional properties of a built-up shape, the thickness and width of the cover plates were closely matched with the flange thickness and width of the equivalent standard W-shape; the thickness and width of the web plate were closely matched with the web thickness and depth of the same equivalent standard W-shape. Two sample pairs of standard and equivalent built-up shapes are graphically exemplified in Table 1.

For the four larger shapes in Table 1, angles are not considered in the section property calculations because the angles are used as connection elements to hold the cover and web plates together. For the two lighter shapes, however, the thickness and width of the angles' horizontal legs are closely matched with the flange thickness and width of each equivalent W-shape because there are no separate cover plates for these shapes. For each column shape, six different SODs and five different CWs were applied, resulting in a total of 30 different models per column. Altogether, 180 blast analysis models were built to cover the six

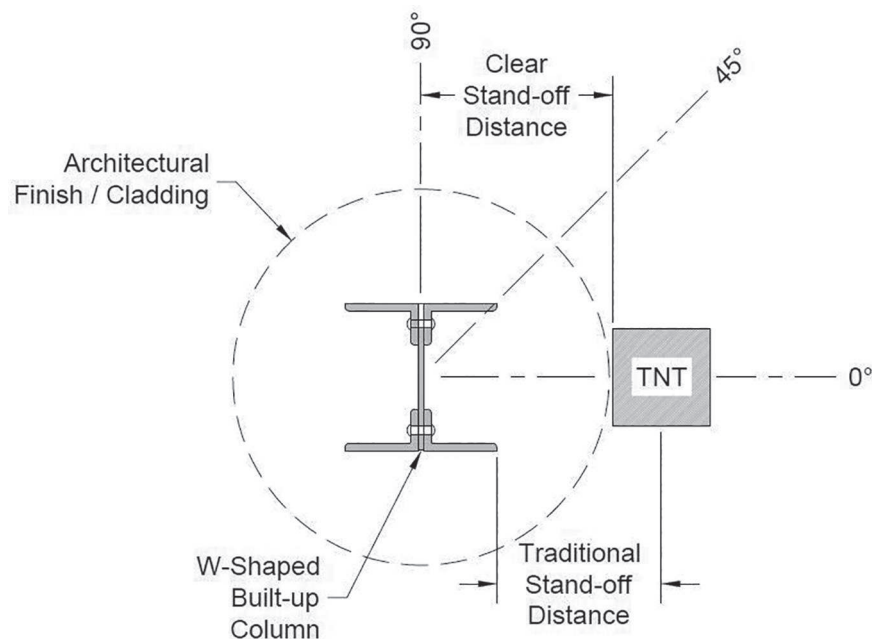
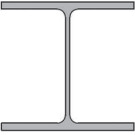
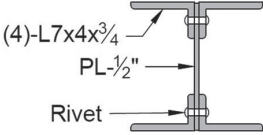

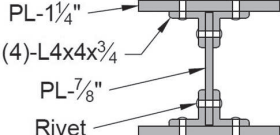


Fig. 1. Definitions of clear and traditional stand-off distances.

Table 1. Dimensions of Built-Up Shapes Used for Parametric Study

Equivalent AISC Standard Shapes	Components of Built-Up Shapes		
	(4) Angles	Web Plate	(2) Cover Plates
W14x43 (W360x64)	L3½x3½x½ (L89x89x12.7)	PL½x13 (PL7.94x330)	—
W14x99 (W360x147)	L7x4x¾ (L178x102x19.1)	PL½x14 (PL12.7x356)	—
W14x176 (W360x262)	L4x4x¾ (L102x102x19.1)	PL⅞x12½ (PL22.2x318)	PL¼x15⅝ (PL31.8x397)
W14x257 (W360x382)	L4x4x¾ (L102x102x19.1)	PL1⅙x12½ (PL28.6x318)	PL1⅞x16 (PL47.6x406)
W14x342 (W360x509)	L4x4x¾ (L102x102x19.1)	PL1½x12½ (PL38.1x318)	PL2½x16⅝ (PL63.5x416)
W14x426 (W360x634)	L4x4x¾ (L102x102x19.1)	PL1⅞x12½ (PL47.6x318)	PL3x16⅝ (PL76.2x422)
 Standard W14x99	 Built-Up Shape Equiv. to W14x99	 Standard W14x176	 Built-Up Shape Equiv. to W14x176

different columns with the variations of CW and SOD. For the first 180 models, column service loads were not considered. However, the column service loads were accounted for later in additional 180 models.

NUMERICAL MODELS FOR CLOSE-IN DETONATIONS

For high-fidelity analyses of close-in detonations, the Ansys/Autodyn program (Ansys, 2015) was used. A thorough, but practical investigation was made for historic steel materials to be used in the analyses. Each steel member was modeled for explicit nonlinear FEA, while detonation was simulated through computational fluid dynamics analyses. Both the solid and fluid analyses were fully coupled so that the blast pressure could be exerted onto the column model (Century Dynamics, 2005).

Steel Material for Built-Up Transportation Facility Columns

It is a daunting task to cover the wide variety of steel materials used for the currently active transportation infrastructures in the United States because they have been built over the past few centuries. However, most transportation facilities, such as commuter rails and subways, were built within the last 100 years. Thus, the focus has been made

on the 20th century, in which the historical changes of the mechanical properties of the steel materials were investigated in building construction.

Based on the various editions of the AISC *Steel Construction Manuals* (AISC, 1927, 1934, 1946, 1963, 2017), other AISC documents (AISC, 1953; Brockenbrough and Schuster, 2018), and American Manufacturer (1900), historic changes of structural steel are summarized in Table 2.

In the first third of the 20th century, a majority of structural steel shapes in buildings were manufactured per ASTM A9 (1936). During the second third of the century, the minimum yield stress slightly increased, along with the frequent changes to the ASTM standards. In the last third of the century, ASTM A36 (2014) steel became the popular material specification for steel shapes and plates. The AISC *Steel Construction Manuals* (AISC, 1927, 1934, 1946, 1963, 2017) have evolved accordingly, reflecting the changes of preferred steel materials, since 1927. Throughout the century, the minimum tensile strength has not been changed significantly, nor the minimum percent elongation.

When the stress-strain diagram for the ASTM A9 steel (Camp and Francis, 1920) is compared to the recent ASTM A36 steel (Salmon et al., 2008), it is apparent that the overall stress-strain relationships of the two steel materials are similar, as shown in Figure 2.

Comparing the stress-strain curves and the mechanical properties of the preferred structural steel materials in

From	To	Source/Grade	F_y Minimum Yield Stress	F_u Minimum Tensile Strength	Minimum Percent of Elongation
1901	1931	ASTM A9, medium steel, structural steel	30 ksi	55 ksi	
1927		AISC (1927) 1st Ed., structural steel	30 ksi ¹	55 ksi	22
1932	1961	ASTM A7, A9, A140, structural steel	33 ksi	60 ksi	
1936	1962	AISC (1934) 2nd Ed.– AISC (1946) 5th Ed.	33 ksi	60 ksi	22
1962	Present	ASTM A36, AISC (1963) 6th Ed.– AISC (2017) 15th Ed. ²	36 ksi	58 ksi	20

¹.The value listed accounts for the larger of 30 ksi and $F_u/2$.
².Other higher strength steels are available but are not compared in this table.

Table 2, and without substantial experimental data available for built-up transportation structural members, it would be practically reasonable to assume that the behavior of structural steel materials in historic transportation facilities are similar to ASTM A36. This assumption is consistent with the material selection for blast analyses of over 50-year-old steel bridge towers in the *Bridge Security Design Manual* (Davis et al., 2017). The ASTM A36 steel was used throughout the analyses in the present study.

Material Models

In accordance with UFC 3-340 (DOD, 2014), static yield stress from typical tensile coupon tests may be increased using two factors to compute dynamic yield stress for structural steel subject to blast loading. The first factor is the average strength increase factor to use the average yield stress in blast resistant design, as opposed to the minimum yield stress used in conventional structural steel design. The factor is a constant value of 1.1 for steel with a minimum

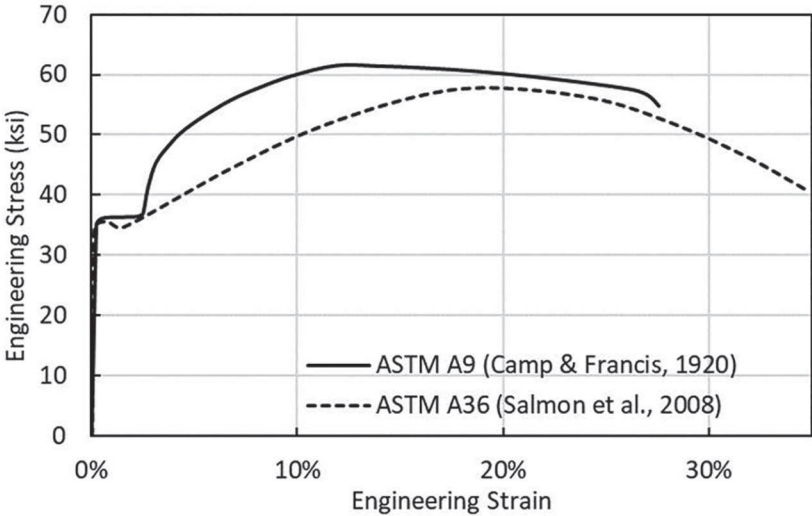


Fig. 2. Uniaxial tensile stress-strain relationships between ASTM A9 and A36 steel.

yield stress of 50 ksi or less. The average strength increase factor is not readily available for historic structures. However, the use of this factor in the nonlinear explicit FEA in this study does not affect the numerical simulations significantly because a failure in the near-contact detonations occurs well beyond the initiation of yielding but close to the ultimate stress. The second factor is the dynamic increase factor, which changes per the strain rate (strain per unit time) of a structure. As each and every part of a steel member has a different strain rate at different times throughout a blast analysis, it is unrealistic or inappropriate to use a single factor for the entire steel member during a complete cycle of a blast analysis.

A more realistic and accurate dynamic increase factor is recognized in nonlinear explicit FEA through appropriate material models. Johnson and Cook (1983, 1985) suggested a stress-strain constitutive model based on three material characteristics: strain hardening, strain-rate effects, and temperature change. Each expression within a pair of parentheses of Equation 1 represents one of the three characteristics, respectively.

$$\sigma = (A + B\epsilon^n)(1 + C \ln \dot{\epsilon}^*)(1 - T^{*m}) \quad (1)$$

where

- A = yield stress, ksi (MPa)
- B = hardening constant, ksi (MPa)
- C = strain rate constant
- T^* = homologous temperature
- m = thermal softening exponent
- n = hardening exponent
- ϵ = true plastic strain
- $\dot{\epsilon}^*$ = strain rate/reference strain rate
- σ = true stress, ksi (MPa)

Johnson and Cook (1983, 1985) listed the five parameters (A , B , n , C , m) of Equation 1 from experiments for various materials but did not include the ASTM A36 (2014) steel. For the blast analysis of steel columns in transportation facilities, the strain-hardening constants (A , B , n) were determined in this study by curve-fitting of the strain-hardening expression, separated from Equation 1, to the experimental data for ASTM A36 steel by Salmon et al. (2008):

$$\sigma = (A + B\epsilon^n) \quad (2)$$

For the curve-fitting, the following steps were taken, based on the published mechanical properties of ASTM A36 steel, summarized in Table 2. First, the minimum yield stress was increased by 10% to account for the average strength increase factor, while the minimum tensile (ultimate) stress, F_u , remained unchanged. Second, intermediate data points were selected from the experimental stress-strain curve, which were increased linearly between

the yield and ultimate stresses. The minimum percentage elongation was assumed to be the strain value corresponding to the ultimate stress, or the ultimate strain, ϵ_u . Third, the engineering stress-strain curve data were converted to the true stress and the true strain so that they could be consistent with the Johnson-Cook material model. The conversions for the stress and strain are expressed in Equations 3 and 4, respectively, based on the typical strength of material theory (Ugural and Fenster, 1994).

$$\sigma = \sigma_o(1 + \epsilon_o) \quad (3)$$

$$\epsilon = \ln(1 + \epsilon_o) \quad (4)$$

where

- ϵ = true strain
- ϵ_o = engineering strain
- σ = true stress, ksi (MPa)
- σ_o = engineering stress, ksi (MPa)

Fourth, for a trial value of the hardening exponent, n , the hardening constant, B , was computed using Equation 2, at the known boundary values of the ultimate strain, ϵ_u , and ultimate stress, F_u . This process was repeated for eight different trial values of hardening exponent, n , and curve-fitted to the ASTM A36 experimental data in Figure 3.

As seen in Figure 3, the best curve fitting of the ASTM A36 steel was obtained when the hardening exponent, n , was 0.75. The other two parameters in Equation 1 for strain rate, C , and temperature changes, m , were obtained from Schwer (2007) for ASTM A36 steel. The five parameters for ASTM A36 steel are summarized in Table 3.

In use of Ansys/Autodyn, the air was defined by the equation of state for the ideal gas with properties published by Rogers and Mayhew (1995). For the generation of blast pressure, TNT was modeled with the JWL (Jones, Wilkins, Lee) equation of state, which was originally developed by Lee et al. (1973) to appropriately fit various explosive materials in pressure-volume-energy behavior, based on a three-term equation (Century Dynamics, 2005).

Model Geometry and Boundary Conditions

Two separate meshes were generated in the numerical simulation model. For air and TNT, multi-material Eulerian meshes were created for computational fluid dynamics analysis, while for the steel column, Lagrangian meshes were created for nonlinear explicit FEA. Figure 4(a) shows only the outlines of the two meshes, where detailed mesh grids were turned off for visual clarity. As the steel column is loaded by blast pressure, the Lagrangian mesh grids deform. On the other hand, the Eulerian mesh grids stay the same, when the air and TNT materials flow between the meshes. The two meshes are solved independently via corresponding solvers and fully coupled for interaction.

Table 3. Five Constants of Johnson-Cook Material Model Estimated for ASTM A36 Steel					
Constants	A	B	n	C	m
ASTM A36	39.7 ksi (273 MPa)	108 ksi (744 MPa)	0.75	0.017	0.917

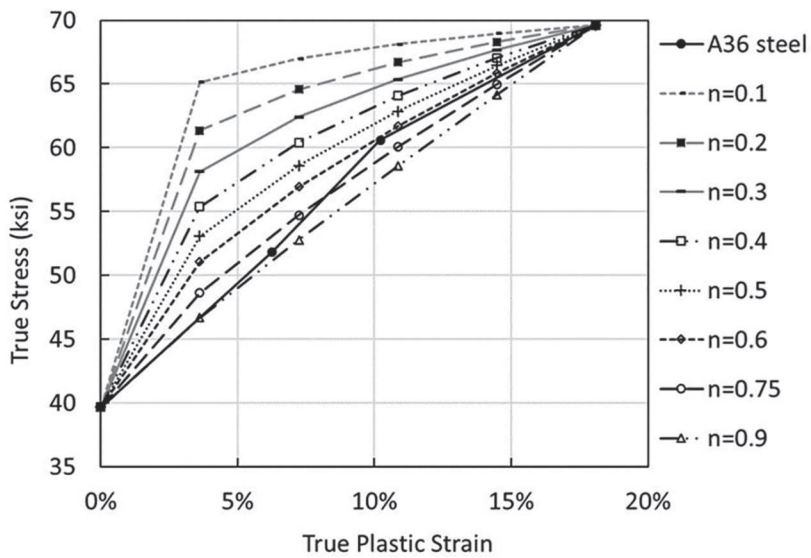


Fig. 3. Curve-fitting of ASTM A36 steel (Salmon et. al., 2008) with various trial-and-error hardening exponents, n , of the Johnson-Cook material model.

During the coupling, the air and TNT meshes apply detonation pressure to the column meshes, while the column meshes block the flows of the air and TNT meshes and deform in accordance with the detonation pressure time history (Century Dynamics, 2005). The overall dimensions of the Eulerian meshes are shown in Figure 4(a). The Eulerian meshes in Figure 4(a) are composed of uniform repeated box-shaped elements, of which individual size is (0.98 in.) (1.97 in.)(0.98 in.) or (25 mm)(50 mm)(25 mm) in (x)(y)(z) directions. This results in 320,000 Eulerian elements.

The overall vertical dimension, 8.20 ft (2500 mm), of the Eulerian mesh domain in Figure 4(a) was determined per an approximate rail station platform ceiling height. However, there would be nearly no limitations in the transverse directions because typical rail station spaces are wide open. To minimize computational efforts, the transverse dimensions were limited to 6.56 ft (2000 mm) in each direction. Instead, a flow-out boundary condition was applied at the four sides of the domain so that the blast pressure could flow away at the side boundaries to simulate the wide-open space without increasing the number of elements. At the head and base of the Eulerian domain, a bounce-back condition was applied to simulate the blast pressure to be physically reflected at the floor and ceiling of a station space.

The overall Eulerian domain dimensions and boundary conditions are summarized in Figure 4(a).

The overall length of the column is 8.86 ft (2700 mm), which extends out by 3.94 in. (100 mm) above and below the Eulerian meshes. The extensions simulate the column embedded in concrete floor slab above and below the air space. Lagrangian meshes are composed of uniform rectangular-shaped shell elements. Overall discretizations of the shell elements for each steel column resulted in eight elements across the flange width, eight or ten elements across the web width, and 27 elements along the column length. Details of the discretizations of the shell models are summarized in Table 4.

Figure 4(b) shows a snapshot of the mesh discretization with boundary conditions. The three-dimensional pin boundary conditions at the two consecutive rows of the column bottom nodes function as a fixed boundary condition. The fixed boundary condition represents a welded steel base plate rigidly anchored and embedded in a thick layer of concrete. On the other hand, a roller boundary condition was applied at the top of the steel column to represent a column lateral support at each floor beam intersection.

As the centerlines along the mid-thicknesses of the plates and angles are taken to model a steel built-up column for

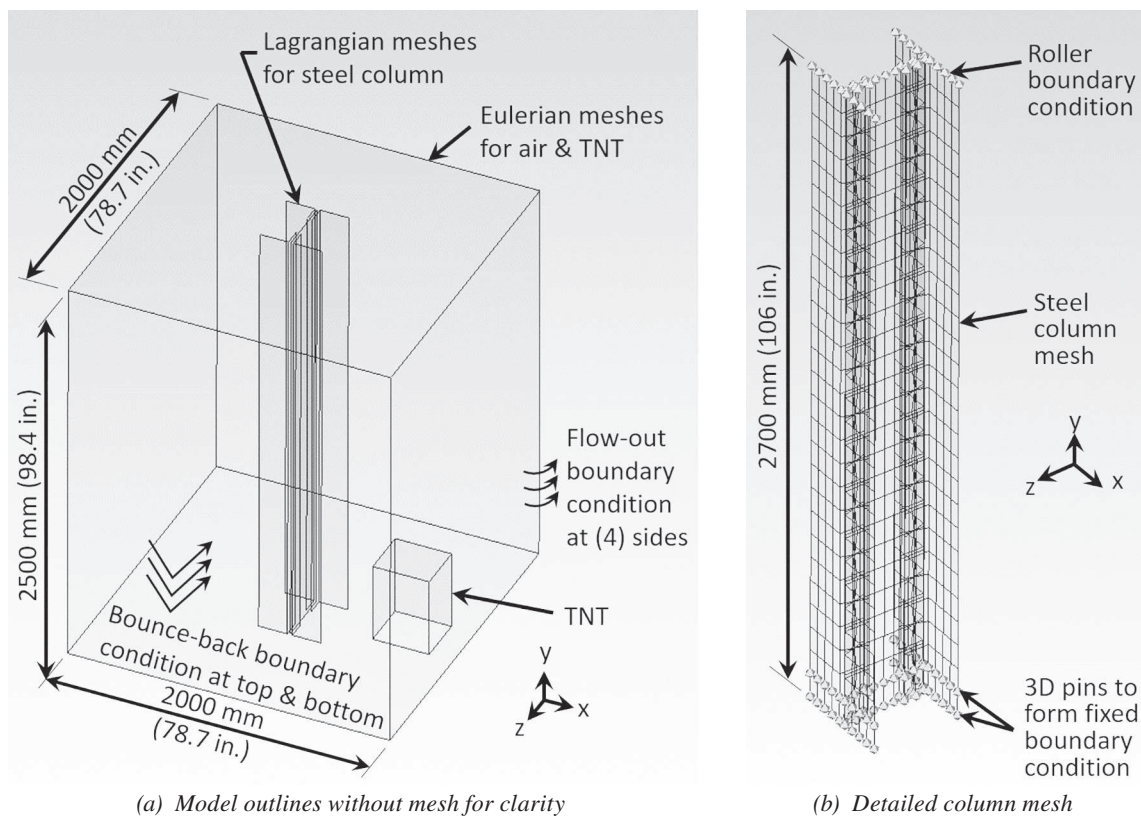


Fig. 4. The standard numerical simulation model for a built-up column equivalent to W14x99 with boundary conditions.

Equivalent AISC Standard Shape	Component Elements in Shape	Cross-Sectional Dimension		Number of FEA Elements	FEA Element Size (average)	
		in.	mm		in.	mm
W14×43 (W360×64)	Angle leg in flange	3.5	88.9	4	0.88	22
	Angle leg in web	3.5	88.9	2	1.75	44
	Cover plate	—	—	—	—	—
	Web plate	13.0	330.2	8	1.63	41
W14×99 (W360×147)	Angle in flange	7.0	177.8	4	1.75	44
	Angle in web	4.0	101.6	2	2.00	51
	Cover plate	—	—	—	—	—
	Web plate	14.0	355.6	8	1.75	44
W14×176 (W360×262)	Angle in flange	4.0	101.6	2	2.00	51
	Angle in web	4.0	101.6	2	2.00	51
	Cover plate	15.6	396.9	8	1.95	50
	Web plate	12.5	317.5	10	1.25	32
W14×257 (W360×382)	Angle in flange	4.0	101.6	2	2.00	51
	Angle in web	4.0	101.6	2	2.00	51
	Cover plate	16.0	406.4	8	2.00	51
	Web plate	12.5	317.5	8	1.56	40
W14×342 (W360×509)	Angle in flange	4.0	101.6	2	2.00	51
	Angle in web	4.0	101.6	2	2.00	51
	Cover plate	16.4	415.9	8	2.05	52
	Web plate	12.5	317.5	10	1.25	32
W14×426 (W360×634)	Angle in flange	4.0	101.6	2	2.00	51
	Angle in web	4.0	101.6	2	2.00	51
	Cover plate	16.6	422.3	8	2.08	53
	Web plate	12.5	317.5	10	1.25	32

FEA, there are small gaps between the shell elements due to the thicknesses of the plates and angles. To simplify the riveted connections, a nodal point at each riveted connection in the web plate is directly joined to the counterpart nodal point in the angle after moving the nodal point slightly to match coordinates. Similarly, each angle and each cover plate were joined at rivet locations. Rivet spacing is assumed to be 7.87 in. (200 mm) on-center in the column longitudinal direction. This numerical simplification of the riveted connections would be practically reasonable because the typical failure modes of the columns subjected to close-in detonations are localized breach, but not involving overall bending of the columns; see the Failure Modes of Steel Columns Subjected to Close-in Detonations and Sensitivity of Variables Considered in Modeling sections for further discussions about the failure modes. The *Bridge Security Design Manual* (Davis et al., 2017) also focused

on front panel failures rather than connection failures of the bridge towers subjected to close-in detonations for similar practical reasons.

The sizes of meshes were determined from a series of mesh sensitivity analyses. Figure 5 shows the three different meshes of the same column subjected to the same CW and SOD. The deformed shapes of the column models are presented on von Mises stress contour in the figure. Compared to the standard meshing in Figure 5(b), used throughout the present study, the mesh size of the model in Figure 5(a) is twice the standard size in the transverse direction. On the other hand, the mesh size of the model in Figure 5(c) is half the standard size in the longitudinal direction.

All three models resulted in a similar punctured hole on the web and similar flaring deformations on the flanges. Each hole was made when certain elements reach the failure and erosion criteria, as discussed in the Failure Criteria,

Erosion, and Failure Mechanism section. As analyses continue, some parts of the web were eroded, detached, flown away, or bent and rolled up around the hole, which were also observed in the experiments by Krishnappa et al. (2014), Remennikov and Uy (2014), and Mazurkiewicz et al. (2015). Due to the individual element size difference among the three models in Figure 5, the three holes have similar but slightly different sizes and perimeter deformations. This is one of the reasons the stress contours of the three meshes in Figure 5 are similar but do not match exactly. A similar

difference was also observed when time-history von Mises stress curves were plotted and compared in Figure 5(d) for the three models at the same gauge location. There are fluctuations or oscillations of the stress values over time due to the dynamic nature of the analysis (as further discussed in the Effects of Preloading section). The fluctuations result in numerous local maximums and minimums, which do not match among the three models. However, the overall trend is practically the same among the three models; each of the three models reached the highest maximum stress quickly

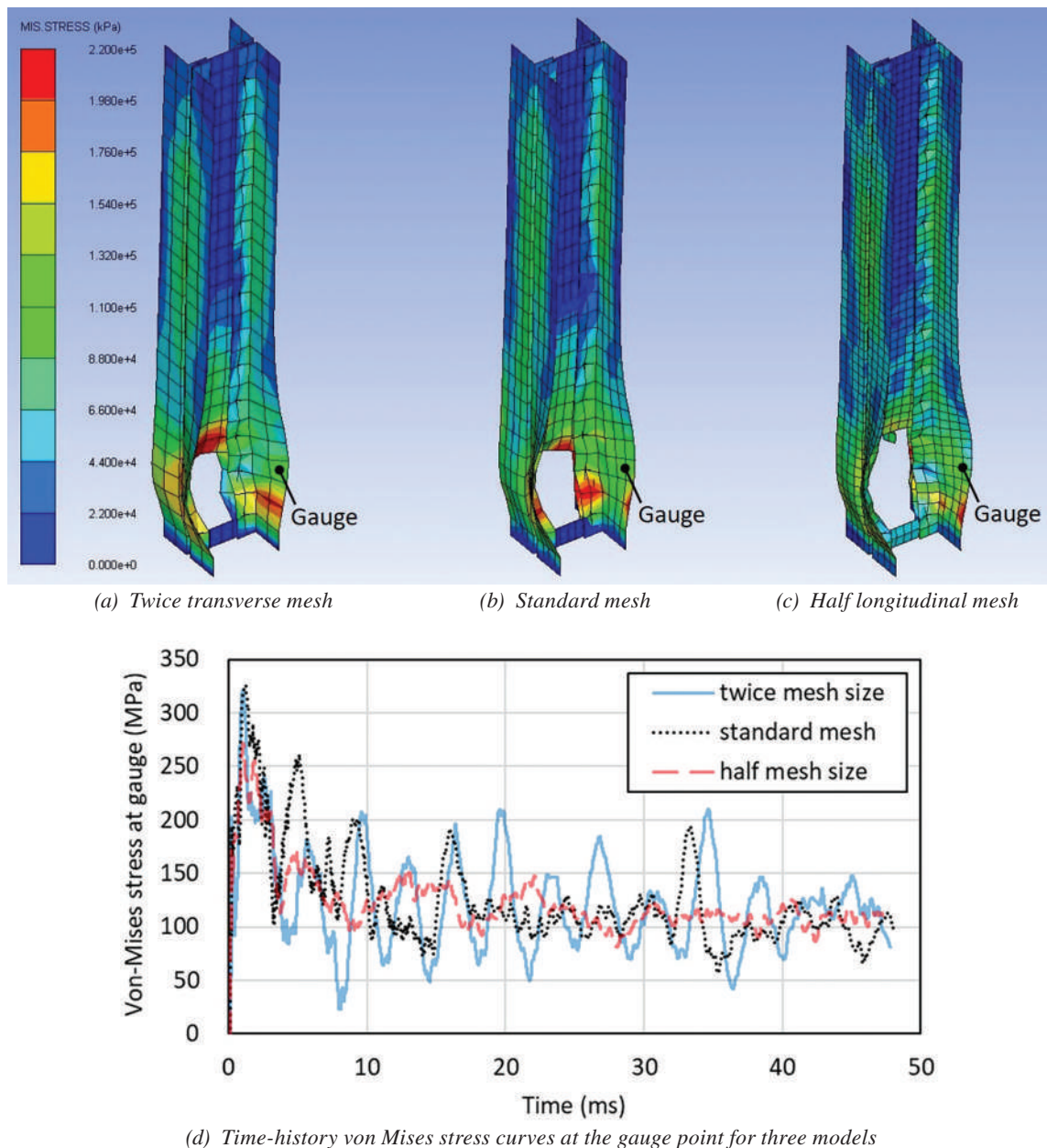


Fig. 5. Deformed shapes with von Mises stress contour of three models at 43 ms with various mesh sizes along with time history stress plot for mesh sensitivity study of column W14x99 subjected to CW = 0.12Y at SOD = 0.8X.

around 1 millisecond (ms), followed by an exponential decay and a convergence to a constant value.

Regardless, the analysis results of the three models reached the same critical conclusion: A hole was punctured on the web. A column subjected to this level of damage (or damage level 4) likely results in a column collapse under service loads, as further discussed in the Failure Modes of Steel Columns Subjected to Close-in Detonations, Performance-Based Damage Criteria and Application, and Effects of Preloading sections. For this reason, finer meshes may improve the similarity in stress contours or time history plots, but such an improvement does not seem practical or necessary for the purpose of the analysis to determine the column collapse. Through the mesh sensitivity study, it is concluded that the standard mesh in Figure 5(b) is practically accurate and reasonable for the purpose of this study.

Failure Modes of Steel Columns Subjected to Close-In Detonations

For built-up steel columns subjected to close-in detonations to face web directly (0° direction in Figure 1), the loading is highly concentrated on a small area with a greater magnitude, and its amplitude decays much more quickly like an impulse, within a few milliseconds. When the intense, but short duration, blast pressure is applied to a localized area of a column, none of the individual components of the column have enough stiffness to resist such an acute and high pressure, nor do they have time to engage the entire length to bend globally to the pressure. Instead, the structure experiences localized deformations or failures, such as bulging, puncturing, or even severing. Typical failure modes are exemplified in Figure 6, obtained from the numerical simulations in this study.

The failure modes are not typically observed in civil engineering structures, but they are similar to punching shear without significant bending. The bulging is mostly observed in web elements, as detonation pressure builds up within the confined space surrounded by the web and two flanges of a wide flange steel member. Flaring or spreading of flanges often appear together with the bulging of the web, as seen in Figure 6(a). When the bulging deformation on the web increases, and passes the tensile limit, the web begins to open up. The breach of the steel material may result in the puncturing of a large hole on the web, as shown in Figure 6(b). With this level of deformation, flange flaring or spreading becomes apparent.

The bulging, cracking, and puncturing of wide flange shape columns were observed through experiments (e.g., Krishnappa et al., 2014; Mazurkiewicz et al., 2015). When the column is subject to a larger CW, a smaller SOD, or both, the entire cross section could be completely severed, as seen in Figure 6(c). Severing was observed in experiments by Remennikov and Uy (2014) for a square hollow

section (SHS), which is equivalent to a square HSS shape, in addition to the other failure modes.

The three failure modes observed in Figure 6 are the three most representative failure modes or deformation patterns for steel columns subjected to close-in or near-contact detonations. When the puncturing deformation occurs, the stress flow through the web as a result of gravity loads is diverted to the flanges due to the lost section in the web. The stress on the flanges increase even more due to the eccentric moment caused by the flange deformations. The flange elements become more susceptible to plate buckling because the adjacent web element that works as the lateral support is removed. The column is about to collapse at this stage. Most of the time in this study, the overall column straightness was maintained without forming a kink, regardless of the weakening through the local deformations in Figures 6(a) or 6(b). The kink, however, may appear when the column has very weak flexural stiffness or when detonation occurs near the mid-height of a column, which are beyond the scope of this study.

Numerical simulations based on high-fidelity, explicit nonlinear FEA, similar to what is presented in this study, have also been presented by others (e.g., Krishnappa et al., 2014; Mazurkiewicz et al., 2015; Remennikov and Uy, 2014; Ngo et al., 2015), which were validated through comparison to experiments. Similarly, the validation of numerical simulations in the present study is demonstrated in the Validation of the Numerical Model section. Because available test data are extremely rare and limited, it is a common practice, instead, to perform explicit nonlinear FEA for close-field blast effects, as suggested by ASCE/SEI 59 (2011).

None of the existing blast evaluation or mitigation design approaches available in the current codes or specifications (e.g., ASCE, 2010; DOD, 2014; U.S. Army, 1986; Gilsanz et al., 2013) address the three deformation patterns of steel columns shown in Figure 6 because the approaches are based on far-field blast effects. The *Bridge Security Design Manual* (Davis et al., 2017) addresses similar close-in detonation failure modes, but the approach focuses on steel bridge towers composed of multiple cells with flat exterior surfaces subjected to a large-truck VBIED. The manual categorizes the deformation patterns of exterior steel plates as elastic, plastic, and catastrophic damage levels; plastic damage is similar to bulging; and catastrophic damage is similar to puncturing. However, the approach presented in the manual cannot be directly applied to wide-flange steel columns because the region surrounded by the two flanges and web of a typical wide-flange steel column can function as the three-sided flow boundary, resulting in the build-up of blast pressure.

None of the three failure modes or deformation patterns in Figure 6 can be addressed in the progressive collapse analysis using only stick models or beam elements, such as

Sideri et al (2017). The analysis approach in the literature cannot account for the escalated reflective pressure within the region surrounded by the flanges and web element, causing a potential catastrophic localized failure.

In current literature, there is no simplified evaluation approach for steel columns subjected to close-in or near-contact detonations. The present study intends to provide practical guidance of nonlinear explicit FEA and develop simple evaluation or design approaches based on charts or equations, accounting for the three close-in detonation failure modes.

Performance-Based Damage Criteria and Application

It is not straightforward to check the structural adequacy of a steel column subjected to close-in detonations, using conventional strength of material or steel design approaches, due to the extraordinary failure modes or dynamic behaviors, which are different from typical civil engineering structures. Instead, performance-based damage criteria are proposed in this study, so that practicing structural engineers can come up with a practical damage mitigation design. Based on a set of given conditions, such as a column size, an SOD, and a CW, a damage level for each numerical

parametric study model was evaluated. For the convenience of defining the significance of damages, six different damage levels were proposed as shown in Table 5.

A damage level was determined at the end of each analysis, in which a total accumulated time step was large enough not to result in any further significant deformations to the steel column. Each of the parametric study models was analyzed up to 2000 cycles, which is typically equivalent to 3 to 7 ms after detonation. The analysis for each parametric study model took approximately 1 to 2 hr to reach the 2000 cycles with a workstation computer with 2.4 GHz 8 core (16 threads) CPU and 32 GByte RAM.

If damage level is evaluated for the three failure modes in Figure 6, based on Table 5, bulging [Figure 6(a)] occurs at Levels 0 through 3, depending on the degree of deformation compared to member width. The puncturing shown in Figure 6(b) would be classified as Level 4 because only the column web is punctured; the flanges are still attached, but significantly deformed and flared. The severing shown in Figure 6(c) is Level 5 because the entire cross-section is vanished. As a minimum, practicing structural engineers must avoid Level 4 or 5 damages so that a column collapse, which can lead to a subsequent progressive collapse of a structure, can be prevented.

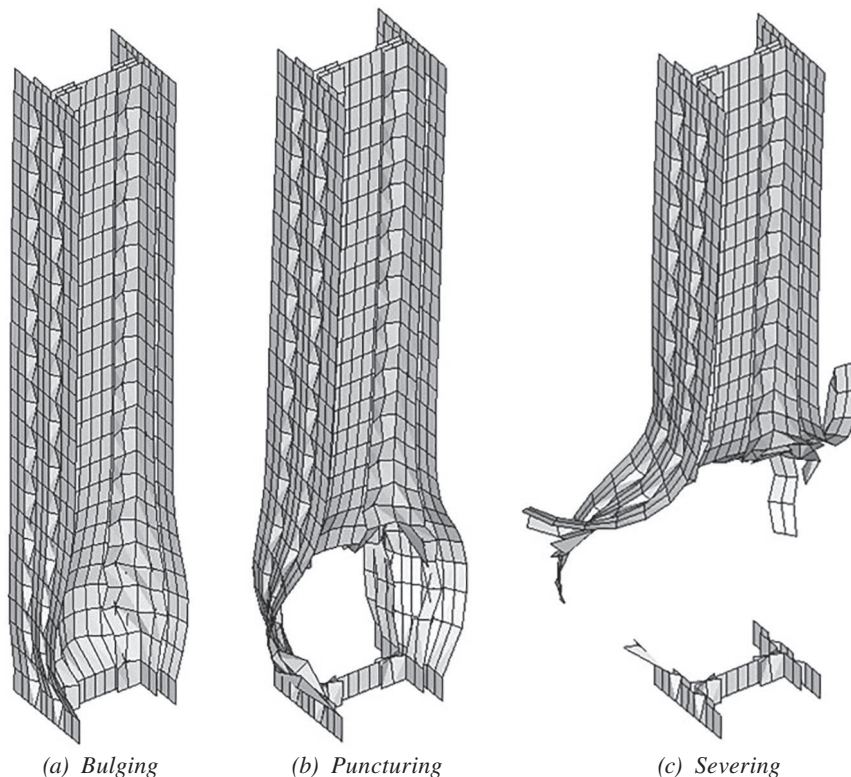


Fig. 6. Typical deformation patterns or failure modes in close-in detonations for built-up wide flange steel columns equivalent to W14x176.

Level	Damage Criteria	Failure Modes
5	The steel column flanges are significantly or completely severed, and the web is completely perforated. The cross-sectional area loss is approximately 50% or greater. This could result in immediate column failure even without the presence of service loads.	Severing, puncturing
4	The steel column web is perforated, and flanges are mostly attached but significantly deformed and flared. The cross-section area loss is less than 50%. This could result in column failure with the presence of service loads.	Puncturing
3	The steel column is not severed or perforated but is significantly deformed (greater than or equal to 10% of member width). Web is swollen and flanges are flared locally, adjacent to the detonation center. This may not result in immediate column failure but may require immediate evacuation of occupants and immediate repair or replacement of the column.	Bulging
2	The steel column is not severed or perforated but is somewhat deformed (greater than or equal to 4% of member width). The deformation patterns are similar to Level 3, but less intense. Partial repairs are still needed to the column.	Bulging
1	The steel column is not severed or perforated but is slightly deformed (greater than or equal to 2% of member width). The deformation patterns are similar to Level 2, but less intense. Partial repairs are still needed to the column.	Bulging
0	The steel column is not noticeably deformed (deformation less than 2% of member width). Column should be adequate, but still needs inspections.	Bulging

Sensitivity of Variables Considered in Modeling

To optimize the computational time and effort, the overall dimension of Eulerian mesh domain was limited to 6.56 ft (2000 mm) in each of the transverse directions with the flow-out boundary condition at the four sides, as shown in Figure 4(a). This model is called the standard mesh and is shown in Figure 7(b), resulting in 320,000 Eulerian elements. To investigate the effectiveness of the flow-out boundary condition, two additional models were created: one with doubled Eulerian domain dimensions in transverse directions, as shown in Figure 7(c), resulting in 1,280,000 Eulerian elements, and the other with half the standard z-dimension and three-quarter of the standard x-dimension, as shown in Figure 7(a), resulting in 120,000 Eulerian elements. In the new models, all other conditions remain unchanged, but the number of Eulerian elements was either increased or decreased with the dimensional changes. The computational time was also increased or decreased almost proportionally to the number of elements. As compared in Figures 7(a), 7(b), and 7(c), the deformed shape and the level of damage of the steel column stayed the same, regardless of the Eulerian mesh domain sizes.

The response of the steel column subjected to the close-in detonations was not sensitive to the size of the Eulerian mesh domain due to the flow-out boundary condition. Thus, it could be concluded that the flow-out boundary condition was effective for the purpose of this study.

The length of the standard column model is a constant

value of 8.86 ft (2700 mm), as shown in Figure 4(b). This was determined based on a probable platform ceiling height of typical rail stations. However, the ceiling height varies depending on different parts of a rail station, or different transportation facilities. To investigate whether or not column responses to close-in detonations are sensitive to the variation of the column length, two additional models were created: One model had one-half the length of the standard model, while the other model had twice the length of the standard model. As seen in Figure 8, the deformation pattern and the level of damage remained unchanged among the three models, regardless of the column length.

This is because the three typical failure modes of a built-up steel column subjected to close-in detonations as depicted in Figure 6 are localized deformations without engaging any significant bending deformations of the member. Most damages to the column occur within a relatively short time period (less than a few milliseconds) over a very small and localized area. With the presence of gravity loads, all three columns in Figure 8 will likely collapse due to local buckling of the flanges adjacent to the punctured hole at the bottom. The effects of the gravity loads and subsequent collapses are discussed extensively in the Effects of Preloading section. This is one of the major differences with the existing blast evaluation or mitigation design approaches available in the current codes or specifications (e.g., ASCE, 2010; DOD, 2014; U.S. Army, 1986; Gilsanz et al., 2013), in which far-field detonations are considered. In the far-field

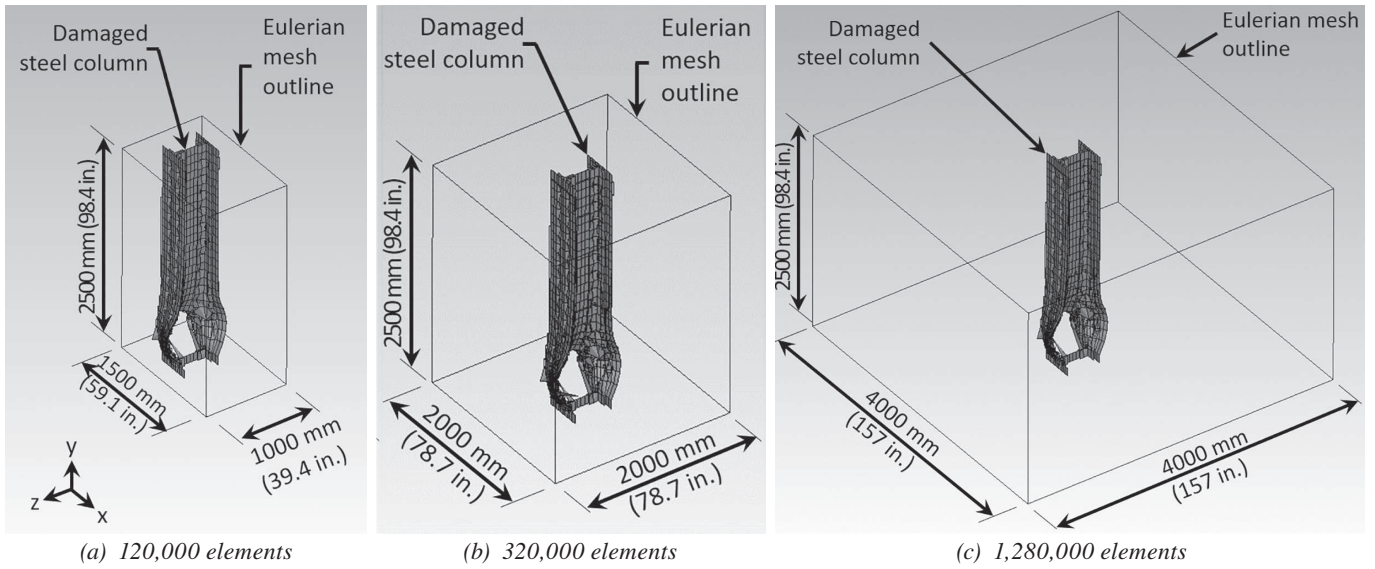


Fig. 7. Damage on built-up steel column equivalent to W14×176 in three models with various numbers of Eulerian elements when all other conditions are the same.

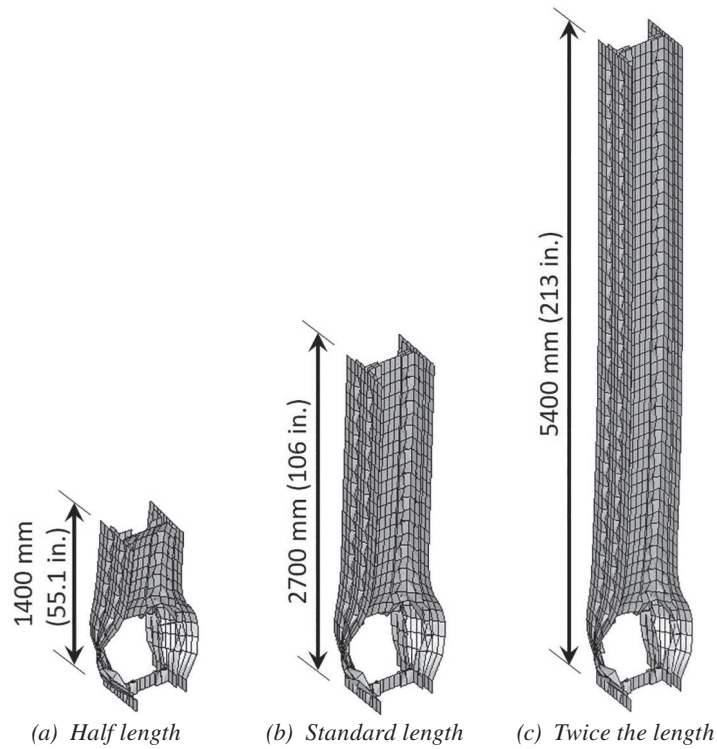


Fig. 8. Damage on built-up steel column equivalent to W14×176 in three models with various model lengths.

detonations, there is significant time and distance between a detonation center and a target structure for a column to form a plastic hinge and to engage the entire member length to resist the blast pressure. Thus, the column length is a critical variable for far-field detonations but not for close-in (or near-contact) detonations. Thus, the constant column length used for the numerical model is reasonable for the purpose of the present study.

Validation of the Numerical Model

For the validation of the numerical model developed in this study, comparison with physical tests would be useful. However, publicly available experimental data of steel columns subjected to close-in detonations are extremely rare. Even if experimental evidence is available, critical data, such as CWs and/or SODs, used for the experiments are frequently hidden from public release for security reasons. A well-documented paper with detailed critical experimental data was presented by Remennikov and Uy (2014), which is used for the validation purpose of the numerical model used

in this present work. The overall numerical model used to simulate the experiment is depicted in Figures 9(a) and 9(b).

The tested specimen to compare with the numerical model was Australian SHS 100×5 without concrete fill (specimen C3 in the paper), in which the overall cross-sectional dimension was 3.94 in. (100 mm) in each side, and thickness was 0.197 in. (5 mm). The TNT charge weight (CW) was 5.73 lb (2.6 kg-g) in cube shape, of which the bottom was placed 3.94 in. (100 mm) above the specimen (SOD) right at the span center. The overall length of the column was 6.56 ft (2000 mm), of which ends were considered as simply supported (one end is pin; the other end is roller). The steel column was placed horizontally to facilitate the experiment.

The steel column was made of Australian C350 steel, of which tensile coupon test results from the specimen were reported by Remennikov and Uy (2014). The stress-strain curve from the tensile test was used to curve-fit the strain-hardening constants (A , B , and n) for the Johnson and Cook material model, in the same approach as described in the Material Models section. The other two constants (C and n)

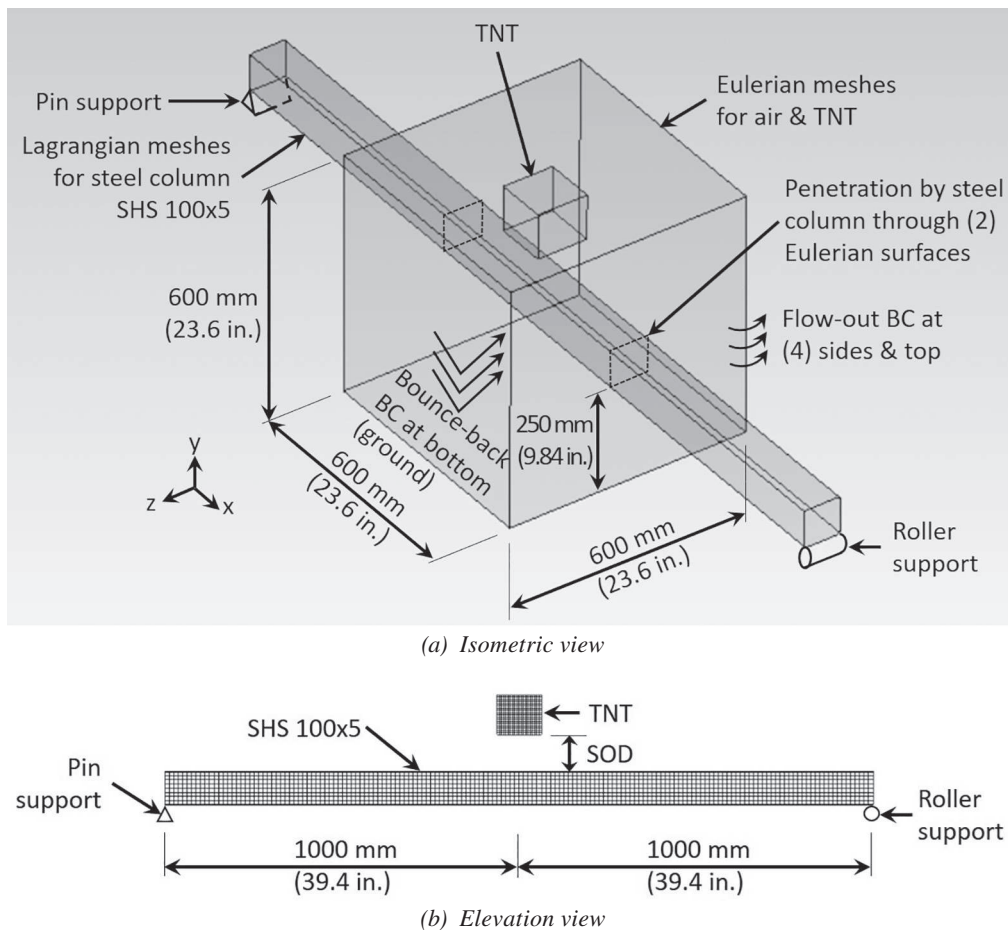


Fig. 9. Model geometry for numerical simulation in this study of specimen C3 in the experiment by Remennikov and Uy (2014).

Table 6. Five Constants of Johnson-Cook Material Model Estimated, Based on Stress-Strain Curve Obtained from Specimen (C350 Steel)					
Constants	A	B	n	C	m
C350	58.2 ksi (401 Mpa)	76.8 ksi (530 Mpa)	0.6	0.017	0.917

were assumed to be similar to ASTM A36 steel. The five constants for the tested specimen are summarized in Table 6.

Lagrangian shell elements were used to model the side-walls of the SHS steel column through the mid-thickness, discretized with 8 elements across each side wall and 160 elements in the longitudinal direction, which resulted in a total of 5120 elements for the steel column. The typical Lagrangian element size was 0.469 in. \times 0.492 in. (11.9 mm \times 12.5 mm). Eulerian meshes to model air and TNT were discretized with 96 elements in each of the three perpendicular directions of the Eulerian domain, resulting in a total of 884,736 elements. The typical Eulerian element size was 0.246 in. (6.25 mm) along each edge of the cube shape element.

The flow-out boundary condition (BC) was applied to the four sides and the top of the Eulerian domain to mimic the open-air space of the actual test, while the bounce-back BC was applied to the bottom to mimic the ground surface, as shown in Figure 9(a). Failure was defined with a plastic strain of 21% based on the stress-strain curve from the test, while the erosion strain was set to 100% to match the erosion strain in the parametric study model described in the Failure Criteria, Erosion, and Failure Mechanism section. All other input parameters and modeling considerations are consistent with what is provided in the previous sections for the parametric study model.

At an early stage of 0.3 ms or 1000 cycles, the top wall was already breached, followed by the bottom wall breach shortly after, as shown in Figures 10(a) and 10(b). The puncturing failure mode, similar to Figure 6(b), constitutes Level 4 damage, which would likely result in a column collapse. To compare the deformed shape of the picture from the experiment, the analysis was continued. Due to the lost portions at the center of the column, the column was weakened and began to bend and form a kink as a result of the remaining blast pressure. The analysis was discontinued when the kinked portion of the column touched the ground surface. The final deformed shape is shown in Figures 10(c) and 10(d).

The punctures on the top and bottom walls, along with the symmetrical flaring-out deformations with the ripples of the two side walls of the SHS cross-section, match closely to the experiment picture of specimen C3 shown in Figure 10(e) by Remennikov and Uy (2014). This validates

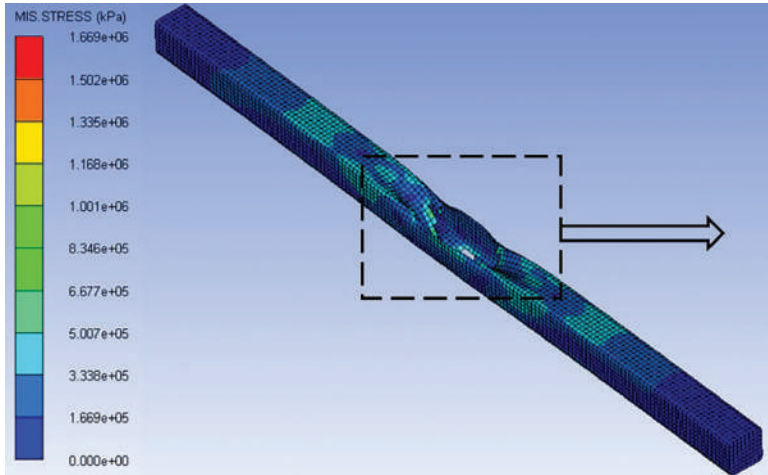
the numerical approach presented in this paper. The analysis took approximately 2.5 hr to reach the breaches of top and bottom walls at 0.3 ms or 1,000 cycles, but took 61 hr to reach the ground touch at 8.5 ms or 20000 cycles with a workstation computer with 2.4 GHz 8 core (16 threads) CPU and 32 GByte RAM.

Failure Criteria, Erosion, and Failure Mechanism

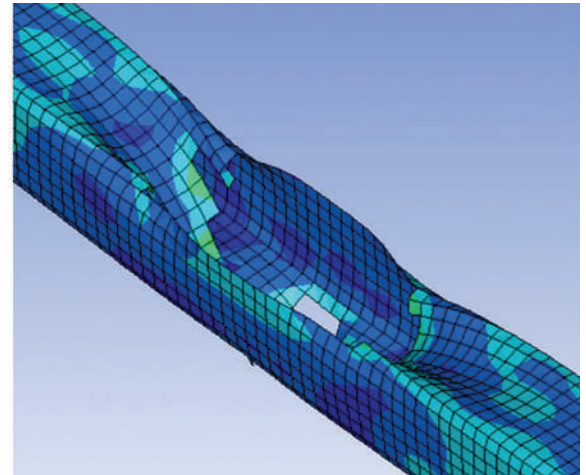
To define the failure of steel material during the explicit dynamics FEA, the plastic strain failure criteria available in Ansys/Autodyn was used. Under the failure criteria, once the effective plastic strain in an element reaches a specified value, instantaneous failure occurs, and the element stress is set to zero and remains zero in the subsequent calculations (Ansys, 2015). In this study, the effective plastic strain for failure was set to 25%, which is slightly higher than the minimum percent of elongation in Table 2, to account for the average value.

In Ansys/Autodyn (Ansys, 2015), there are three major material status flags for steel: elastic, plastic, and failure based on the current effective plastic strain value. These three flags are graphically shown in different colors on the column and exemplified at multiple time-steps in Figure 11(a) for a built-up column W14 \times 99 subjected to CW = 0.12Y at SOD = 0.6X. As analysis time increases, the area boundary flagged as either plastic or failure becomes larger. The punctured hole at 500 cycles and beyond is caused by erosion, which is discussed later. To facilitate the understanding of the failure mechanism, the element where Gauge 1 is attached in the figure is focused. The element was labeled as plastic in 300 cycles, which becomes failure in 400 cycles.

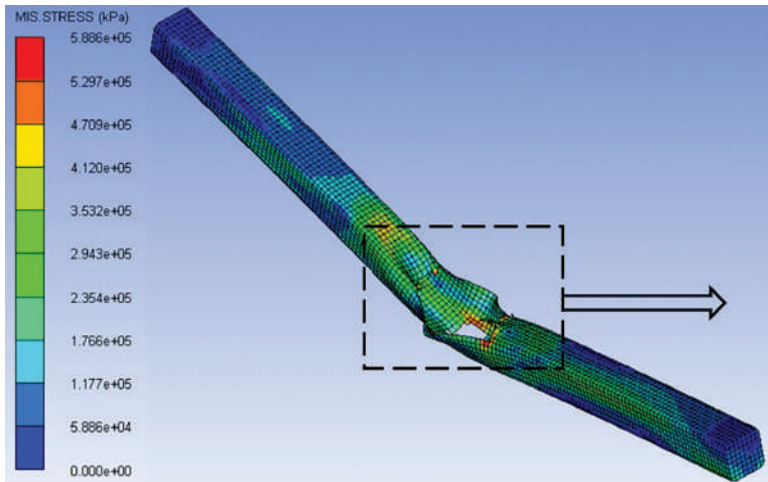
In Figure 11(b), von Mises stress plots on the column are also presented for the same time-steps as Figure 11(a). Shortly after the element with Gauge 1 partially reaches the maximum stress range (red in the stress scale) at 300 cycles, the element's effective plastic strain reaches the 25% failure limit, and the von Mises stress approaches zero at 400 cycles (blue range in the stress scale). Thus, the areas flagged as failure in Figure 11(a) closely match the areas with zero or the lowest stress scale range in Figure 11(b), which remains zero during the remaining analysis cycles. Thus, the comparison between the material status and von Mises stress plots demonstrates the failure mechanism.



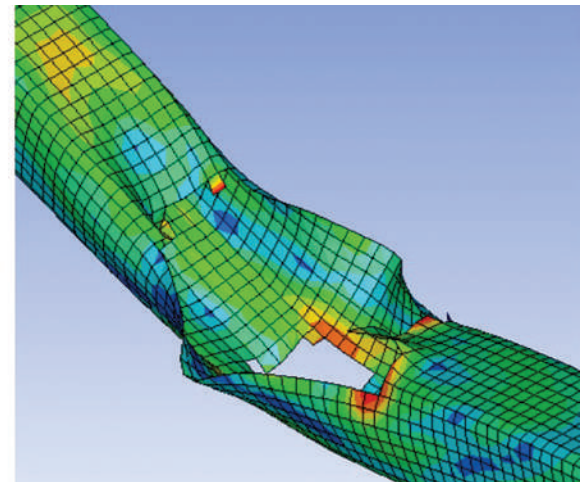
(a) Overall view of deformed shape at 0.3 ms



(b) Enlarged view at 0.3 ms



(c) Overall view of deformed shape at 8.5 ms

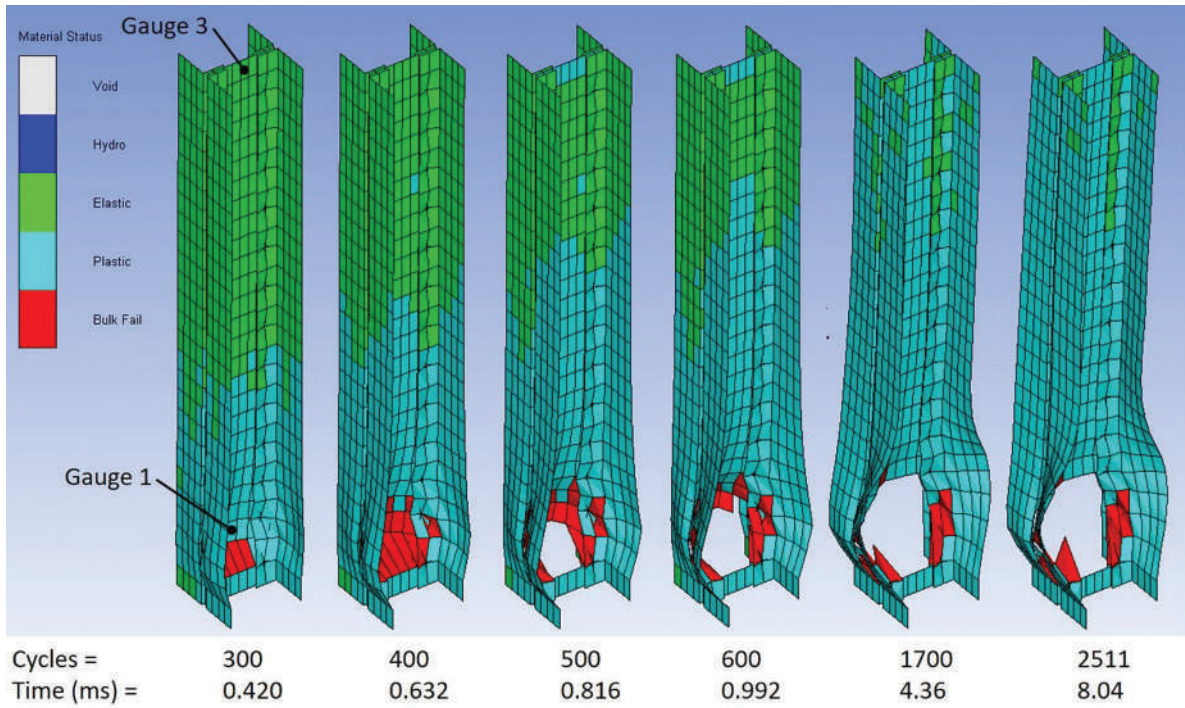


(d) Enlarged view at 8.5 ms

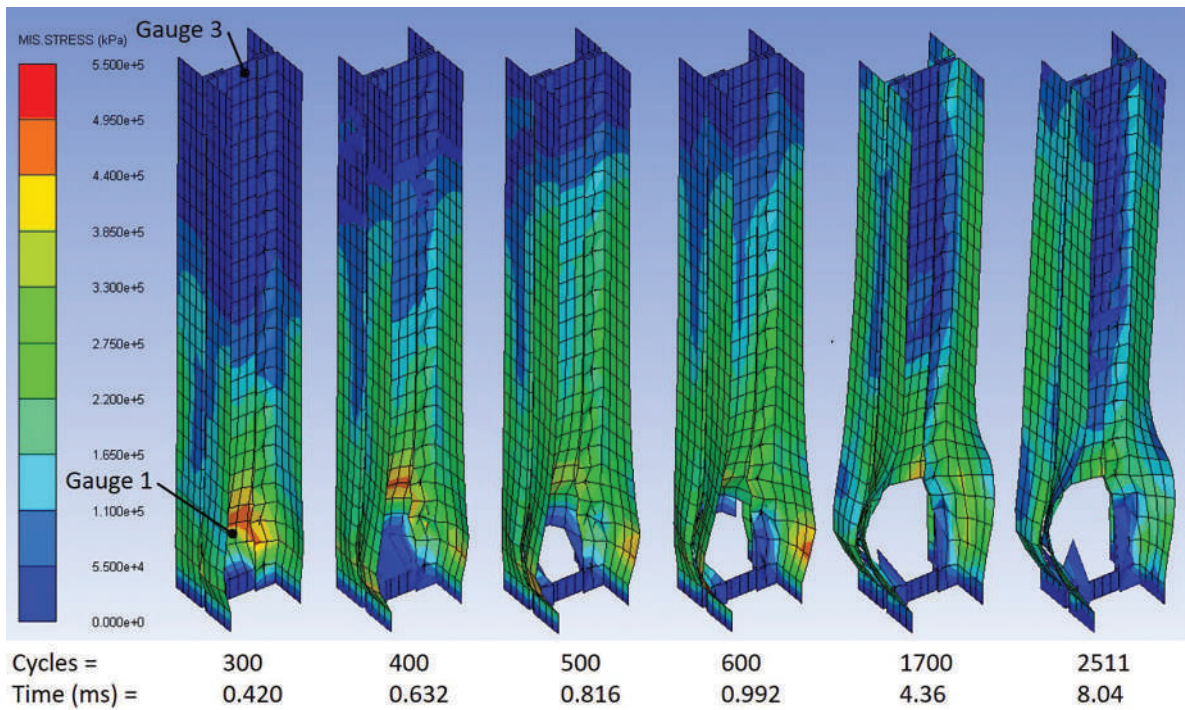


(e) Experimental photo by Remennikov and Uy (2014)

Fig. 10. Comparison of the numerical simulation in this study and the experiment photo by Remennikov and Uy (2014); reprinted from the Journal of Constructional Steel Research, Copyright 2014, with permission from Elsevier.



(a) Material status plots



(b) Von Mises stress plots

Fig. 11. Changes of deformed shape of built-up column W14×99 subjected to $CW = 0.12Y$ at $SOD = 0.6X$.

As the strain value becomes excessively high, any highly distorted elements can result in numerical errors, which can diverge the solution. In order to avoid such errors, when the effective strain of an element reaches a preset value, the element is automatically removed from the model during the remaining calculations. This mechanism is called erosion (Ansys, 2015). Although the original purpose of erosion is to avoid such numerical errors, the hole made from erosion also releases blast pressure. The hole and the pressure release would result in a more realistic physical representation of a column subject to close-in detonations, as evidenced in Figure 10. In this study, the erosion strain limit was conservatively set to 100% so that the steel column could take blast pressure slightly longer.

In Figure 11(a), at the bottom of the column, close to where TNT is detonated, more elements are flagged as failure at 400 cycles than 300 cycles with larger deformations. At 500 cycles, the boundary of the failed area increases, but the elements at the center of the failed area are removed, leaving a large hole. This is because the elements are further stretched, and the corresponding effective strain value meets or exceeds the erosion strain limit. The triggering values to cause plastic strain failure and erosion were determined as a result of a series of sensitivity studies.

At the bottom of the column, Gauge 1 was attached to the column, as shown in Figures 11(a) and 11(b), to monitor detailed analysis values. For the same column and CW, four models with different SODs, ranging from 0.6X through 1.2X, were monitored. For the four models, the time history curves of von Mises stress at Gauge 1 are plotted in Figure 12(a), which is enlarged for visual clarity in Figure 12(b). For models with SOD = 0.6X and 0.8X, shortly after each of the curves reached the maximum value, the stress suddenly dropped to zero and stayed at zero during the remaining analysis. This is because the effective plastic strain for the element with Gauge 1 reached the failure limit. The maximum von Mises stress values are also significantly larger than the ultimate stress of 480 MPa (69.6 ksi) in Figure 3. The failure of the element with Gauge 1 was followed by the erosion, as part of the punctured hole at the base of the column model in Figure 11. Thus, these two models resulted in Level 4 damages.

For the other two models with SOD = 1.0X and 1.2X, when each of the curves reached the maximum value, the stress did not drop to zero but continued to vary over time to imply that the element sustained the blast pressure. This is because the effective plastic strain for the Gauge 1 element did not reach the failure limit. The maximum von Mises stress was also smaller than the ultimate stress. Eventually, these two models did not cause any hole puncturing on the web, but resulted in Level 3 damages, as discussed in the Effects of Preloading section.

Effects of Preloading

Columns are typically subjected to axial compressive stresses, due to applied service loads such as dead and live loads, as defined in the building code of a jurisdiction. In this study, focus has been made on built-up steel columns subjected to close-in detonations without any service loads. However, it is likely that the axial compressive stress from the service loads would worsen the damages on the columns due to detonations, as is the case in a typical progressive collapse analysis, such as Sideri et al. (2017). In the literature, columns were preloaded with a service load of $1.2D + 0.5L$ (where D = dead load and L = live load) per DOD (2009), prior to the detonation pressure application. The service load was applied uniformly to floor slab, which was distributed to beams and girders, and subsequently to columns below. The columns were then subjected to detonation pressures for a few milliseconds, after which the columns were loaded further with additional vertical loads until failure.

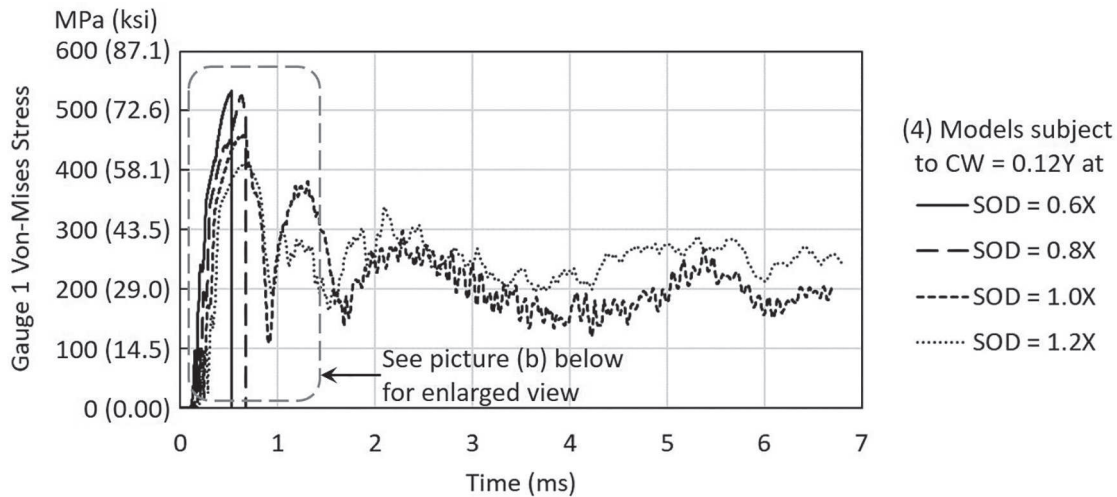
However, such a load combination cannot be applicable to the present study, where the analysis is focused on element-level local deformations of an individual column rather than the member-level deformations of the entire building frame in the literature. The analysis of an individual column is needed to model flanges and web components using shell elements to address the localized failure modes or deformation patterns exemplified in Figure 6, which cannot be addressed using the stick models or beam elements used in the literature. The modeling difference fundamentally stems from the different blast loading scenarios: a small MPIED with close-range or near-contact detonations in the present study versus a large VBIED with far-field detonations in the literature. The far-field detonations apply a uniformly distributed lateral load to the entire span of the affected columns, which causes a typical bending failure and simultaneously facilitates a flexural column buckling failure. On the other hand, the close-range or near-contact detonations apply highly concentrated pressures to a small region bound by flanges and web, in which the detonation pressure is escalated further to cause localized flange and web deformations and failures without causing significant member-level deformations or failures.

In order to investigate the effects of the service loads and potential subsequent damage changes, additional sets of models were created in the present study to apply the service loads as a preloading stage prior to the detonation stage. Due to the different modeling focus mentioned earlier between the literature and the present study, the preloading was assumed to be equal to 60% of the yield stress, $0.6F_y$, axially compressed all over the entire column, accounting for practical ranges of service loads in steel columns. In the progressive collapse analysis by Sideri et al. (2017), the preloading was applied via simple static

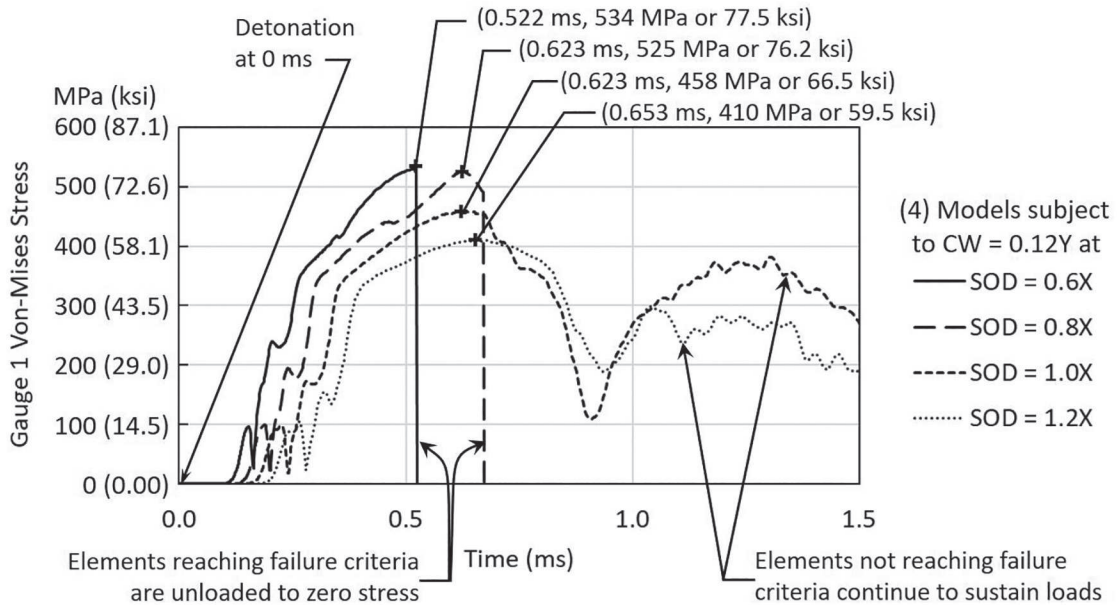
analysis, prior to the dynamic analysis for blast loading. However, it is not straightforward to apply static preloading to an explicit dynamics FEA using Ansys/Autodyn because a separate static analysis tool is not available within the program. Instead, the static stress state can be generated using the available explicit dynamics program. When the preloading is applied on top of a column to cause an axial uniform compression, as shown in Figure 13(a), the stress wave propagates over time and position toward the bottom of the column [Figure 13(b)]. The stress wave reflects at the bottom and then at the top of the column. The reflections

continue endlessly between the top and bottom of the column, while the desired constant static stress from the preloading is not attainable.

The stress change over time can also be monitored at a fixed position in a column. Gauge 1 was attached to the column model near the bottom, as shown in Figure 13(a), at the same location as Figure 11. When the time history curve of von Mises stress at Gauge 1 is plotted in Figure 14(a), the model labeled as “no damping” shows that the stress oscillates between approximately 30 MPa and 270 MPa (or 4.4 ksi and 39.2 ksi) with an average of 150 MPa (21.8 ksi).



(a) For the entire time range from 0 to 7 ms



(b) For the enlarged view from 0 to 1.5 ms

Fig. 12. Von Mises stress curves of built-up column W14x99 at Gauge 1 subject to CW = 0.12Y at various SOD without preloading.

The average stress is close to the applied preloading of $0.6F_y$ (149 MPa or 21.6 ksi).

In order to avoid the oscillation, but to imitate the practical constant static compressive stress in the explicit dynamics FEA, static damping was used. Static damping changes the dynamic analysis to a relaxation iteration converging to a state of stress equilibrium (Ansys, 2015). For an optimized convergence, the calculation for the static damping constant, R , recommended in Ansys is in accordance with Equation 5:

$$R = 2(\Delta t)/T \quad (5)$$

where

T = longest period of vibration, ms

Δt = time step, ms

Based on the typical period of vibration $T \approx 3.3$ ms [as observed in Figure 14(a)] and the typical time step, $\Delta t = 4.7 \times 10^{-4}$ ms (from analysis outputs), the static damping constant, R , becomes 2.8×10^{-4} , using Equation 5. A series of analyses were performed with various damping constants around the computed value. The most optimal damping constant is obtained when the model converges most quickly to

the constant stress equal to the applied preloading stress. The most optimal damping constant was found to be 2.6×10^{-4} , which is close to the computed value. For the model with the most optimal damping constant, the von Mises stress converged to a uniform compressive stress of $0.6F_y$ (149 MPa or 21.6 ksi) at around 4.7 ms or 10,000 cycles, as shown in Figure 14(a). The constant stress is uniformly distributed all over the column as shown in Figure 13(c), except for the base of the column, where the fixed boundary condition is located.

When the damping constant was too low (2.6×10^{-5}), the time history curve of von Mises stress oscillated too long to converge to the constant preloading, as shown in Figure 14(a). On the other hand, when the damping constant was too high (2.6×10^{-3}), the time-history stress curve did not oscillate, and it took even longer to converge to the constant preloading, as shown in the figure. Considering that additional blast analysis must follow each of the preloading analyses and there are numerous models to run, it is practically crucial to find the most optimal damping constant. When the CPU times are compared in Figure 14(b), it took 6 to 10 times longer time in the models with the too high or too low damping constants than the most optimal damping

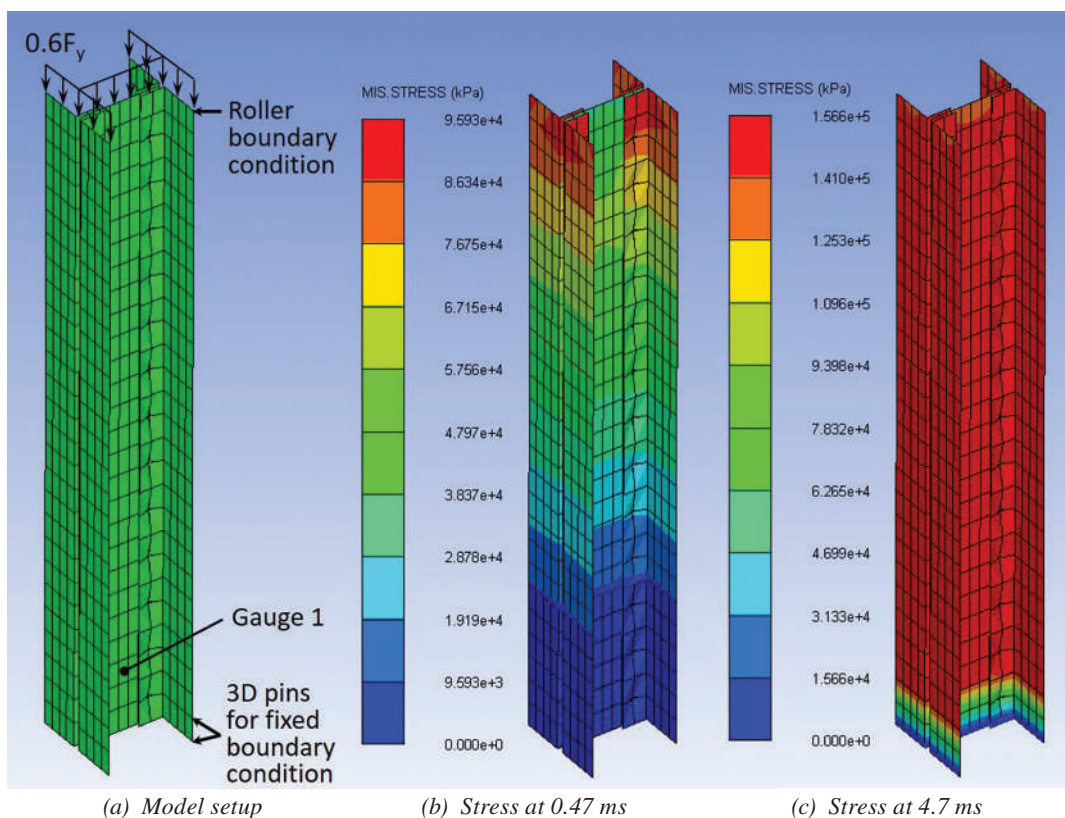


Fig. 13. Preloading stage for a built-up column W14x99 with a von Mises stress contour at an early cycle of preloading stage (1,000 cycles or 0.47 ms) vs. a final and converged cycle of preloading stage (10,000 cycles or 4.7 ms).

constant. Also, in order to shorten the overall analysis time, including both preloading and blast analysis stages, the model with 120,000 Eulerian elements was adopted, which reduced approximately additional 50% of the total analysis time, compared to the original model with 320,000 Eulerian elements, as shown in Figure 14(b). Comparison of various Eulerian models are shown in Figure 7.

After the preloading analysis was completed, the damping constant was removed or set to zero prior to detonation initiation for blast analysis. This is because the damping constant can attenuate damages to the column subject to blast pressure, which is not conservative or intended. As a summary, the following overall steps were taken:

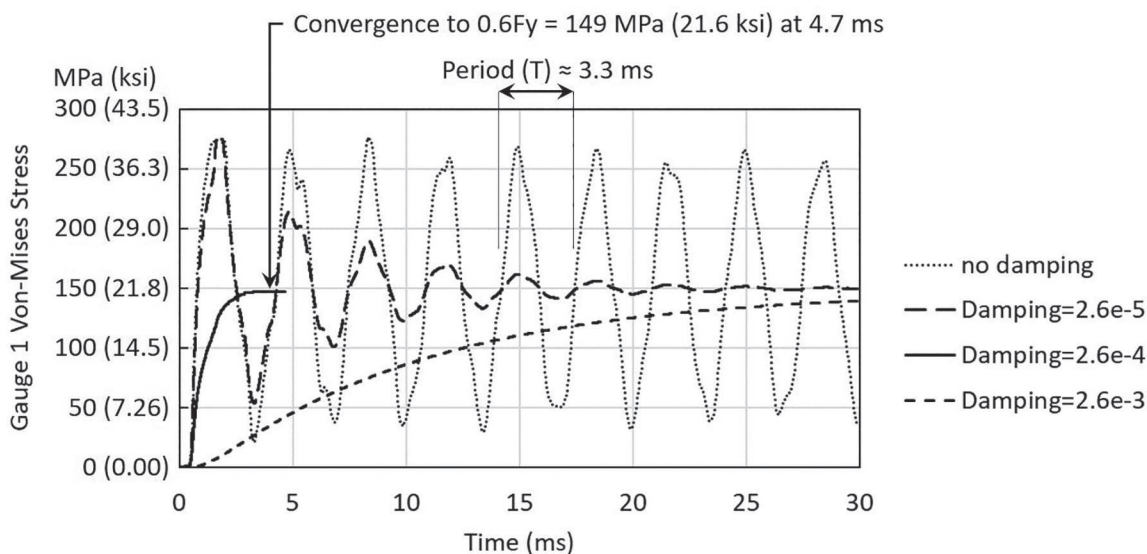
- Stage 1, axial preloading: To make the column subject to uniform compressive stress of service loads, use the most optimized damping constant from Equation 5 and trial analyses with various damping constants.
- Stage 2, preparation for blast analysis: Remove damping

constant (or set it to zero) and set the detonation initiation time right after the last time-step of Stage 1.

- Stage 3, blast analysis: Perform close-in detonation blast analysis on the column preloaded with the service loads.

These three stages are demonstrated in Figure 15 for the same four column models as Figure 12, except for the additional Stages 1 and 2. The time history curves of von Mises stress at Gauge 1 are plotted in Figure 15(a), which is enlarged for visual clarity in Figure 15(b).

For models with $SOD = 0.6X$ and $0.8X$, shortly after each of the curves reached the maximum value, the stress suddenly dropped to zero to constitute failure. These two models resulted in Level 4 damages. However, for the other two models with $SOD = 1.0X$ and $1.2X$, when each of the curves reached the maximum value, the stress did not drop to zero, but continued to vary over time to imply that the element sustained the blast pressure without failure. These two models resulted in Level 3 damages.



(a) Von Mises stress plots over time

Damping	Convergence to $0.6F_y$ at analysis		CPU time (hrs) when Eulerian elements =	
	cycle	time (ms)	120k	320k
2.6E-03	106619	50	13	-
2.6E-04	10000	4.7	1.2	2.3
2.6E-05	63886	30	7.4	18

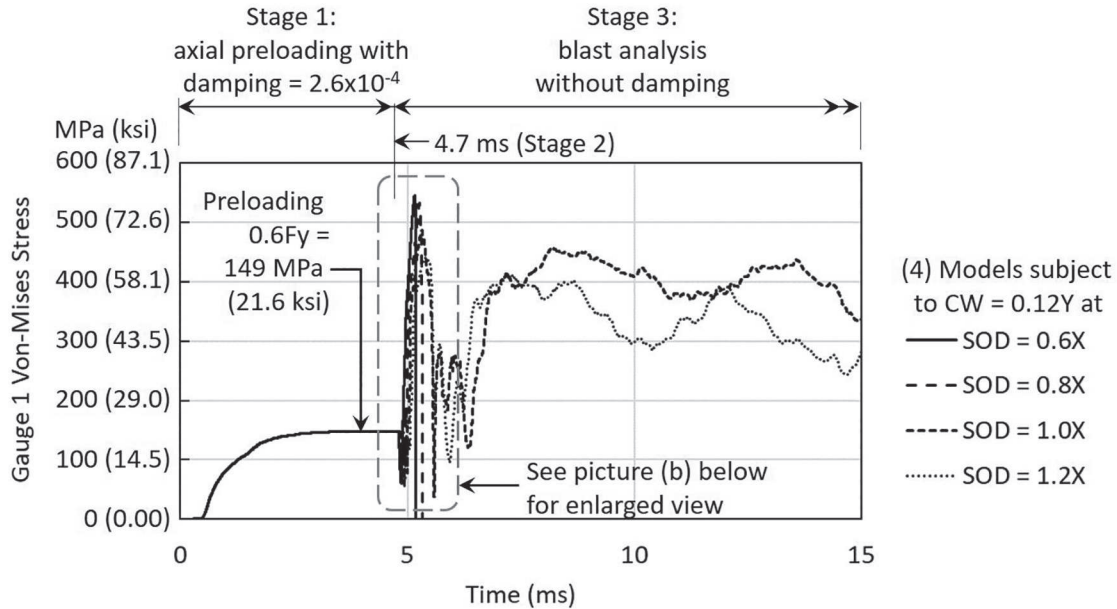
(b) Total computation times for convergence

Fig. 14. Comparison of analysis results at Gauge 1 of built-up column $W14 \times 99$ for various damping constants.

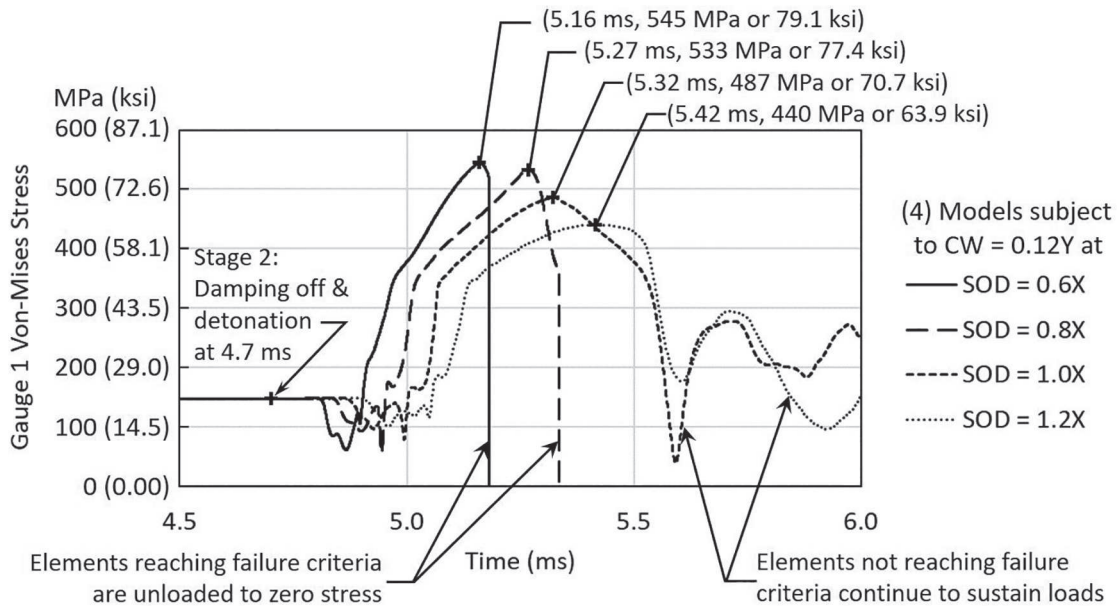
When these four column models accounting for the service loads in Figure 15 are compared to the previous models without considering the service loads in Figure 12, there is no change to the damage level in each model. Although there was a slight increase in the maximum stress value in each of the four models, the difference is much less than the preloading stress. For all four models, the increase of the

maximum stress in each model was less than 8%, and thus, there were no changes to the damage levels between the models with and without the preloading.

This shows that the preloading stress as a result of service loads are not directly additive to the stress due to blast pressure. A few reasons could be considered for this observation. First, the system of equations is highly nonlinear, and



(a) For the entire time range from 0 to 15 ms



(b) For the enlarged view from 4.5 to 6 ms

Fig. 15. Von Mises stress plots over time at Gauge 1 of built-up column W14x99 subject to $CW = 0.12Y$ at various SOD with preloading.

thus, the principle of superposition does not apply. Second, the constant in-plane stress from the preloading is in compression, while the prevailing in-plane stress from the detonation is in tension. For example, web bulging deformation demonstrated in Figure 6(a) would be similar to the behavior of a pressurized tank, where in-plane tensile stresses are dominant. For this reason, the relationship between the in-plane stresses from the preloading and the detonation would be somewhat subtractive rather than purely additive in nature. This is also observed in the time-history plots of von Mises stress in Figure 15(b). Right after Stage 2, when detonation pressure reached the steel column approximately in between 4.8 and 4.9 ms, the von Mises stress curves suddenly dropped significantly before they began to increase toward the maximum values. Thus, it was observed for the short term (until the maximum stress) that the effect of the service loads would be insignificant for steel columns subjected to close-in or near-contact detonations.

To investigate further the effects of the service loads for a long term beyond the maximum stress, various types of deformations were investigated as follows. Typical out-of-plane deformations from close-in detonations, such as bulging and flaring in Figure 6(a), result in significant eccentricities for the axial compressive stress from the undeformed centerlines of the flange and web elements. The axial compressive stress applied away from an element's undeformed centerline causes secondary moments and, in turn, additional flexural stresses on the flanges and the web. In addition, a punctured hole or partial severing reduces the cross section area of the column, with which the compressive stress of the remaining area would also increase.

In order to investigate whether or not the stress increase due to the out-of-plane deformations or the area reduction would cause column failure and subsequent collapse, the blast analysis stage was continued until no significant deformations were observed or until a column collapse was observed. For the first column model (SOD = 0.6X) with the preloading in Figure 15, the deformed shapes are demonstrated in Figure 16 at a number of time steps.

At 12,000 and 19,000 cycles in Figure 16, the deformed shapes of the model with the preloading are qualitatively similar to the counterpart 600 and 1700 cycles in Figure 11(b) without the preloading. Notice that the time to initiate the detonation or the preloading stage duration, 4.7 ms, was subtracted from the time steps of the model with the preloading so that only the time-steps after the detonation could be matched for the deformation comparisons. The deformed shapes of the model without the preloading remained nearly the same between 1700 and 2511 cycles [Figure 11(b)], while the deformed shapes of the model with the preloading were significantly different between

counterpart 19,000 and 27,000 cycles (Figure 16). Severe erosions were observed on the flanges at 27,000 cycles due to the addition of the preloading. Regardless of the changes observed at 27,000 cycles in Figure 16, the damages on the column are still considered as Level 4 damages in this study because the flange erosions occurred during the collapse of the column due to the preloading. Both the models with and without the preloading could be judged equally as Level 4 damages, based on the observation of the deformed shape changes over time and the damage level criteria given in Table 5.

To measure the collapse behavior quantitatively and facilitate the comparison between the models with and without the preloading, Gauge 3 was attached near the top of the column, as shown in Figure 16. When the vertical displacements at Gauge 3 are compared over time in Figure 17(a) for the model with SOD = 0.6X, the vertical displacement of the model without the preloading remained nearly the same with minor fluctuations between 4 and 10 ms. For the same time range, however, the vertical displacement of the model with the preloading kept increasing in the negative direction, which indicated falling. The column collapse is further evident in the deformed shape at 10 ms in Figure 17(a) for the model with the preloading.

For the second column model (SOD = 0.8X) in Figures 12 and 15, each of the models without and with the preloading resulted in a puncture hole on the web, but the model with the preloading resulted in a collapse as shown in Figure 17(b), similar to the first model. For the same reason discussed earlier, the damage level remained unchanged as Level 4. Therefore, for the first and second column models in Figure 15, the short-term behavior of the column subjected to close-in detonation remained the same, leaving a punctured hole on the web, with and without the preloading. However, the long-term behavior resulted in a collapse with the presence of the preloading. Both of the models resulted in Level 4 damages, regardless of the preloading, based on the damage level criteria in Table 5.

For the third and fourth models (SOD = 1.0X and 1.2X) in Figures 12 and 15, each of the models without and with the preloading converged to a constant vertical displacement, but the model with the preloading had slightly more deformations than the model without the preloading, as shown in Figures 17(c) and 17(d). In addition, each of the deformed shapes in the figures did not result in a punctured hole or a collapse.

Additionally, horizontal out-of-plane displacements were measured for the last two models (SOD = 1.0X and 1.2X) on the web at Gauge 2 and on the flange at Gauge 7, of which locations are shown in Figure 16. The time-history curves of the out-of-plane displacements for the two models are plotted in Figure 18. For both models without and

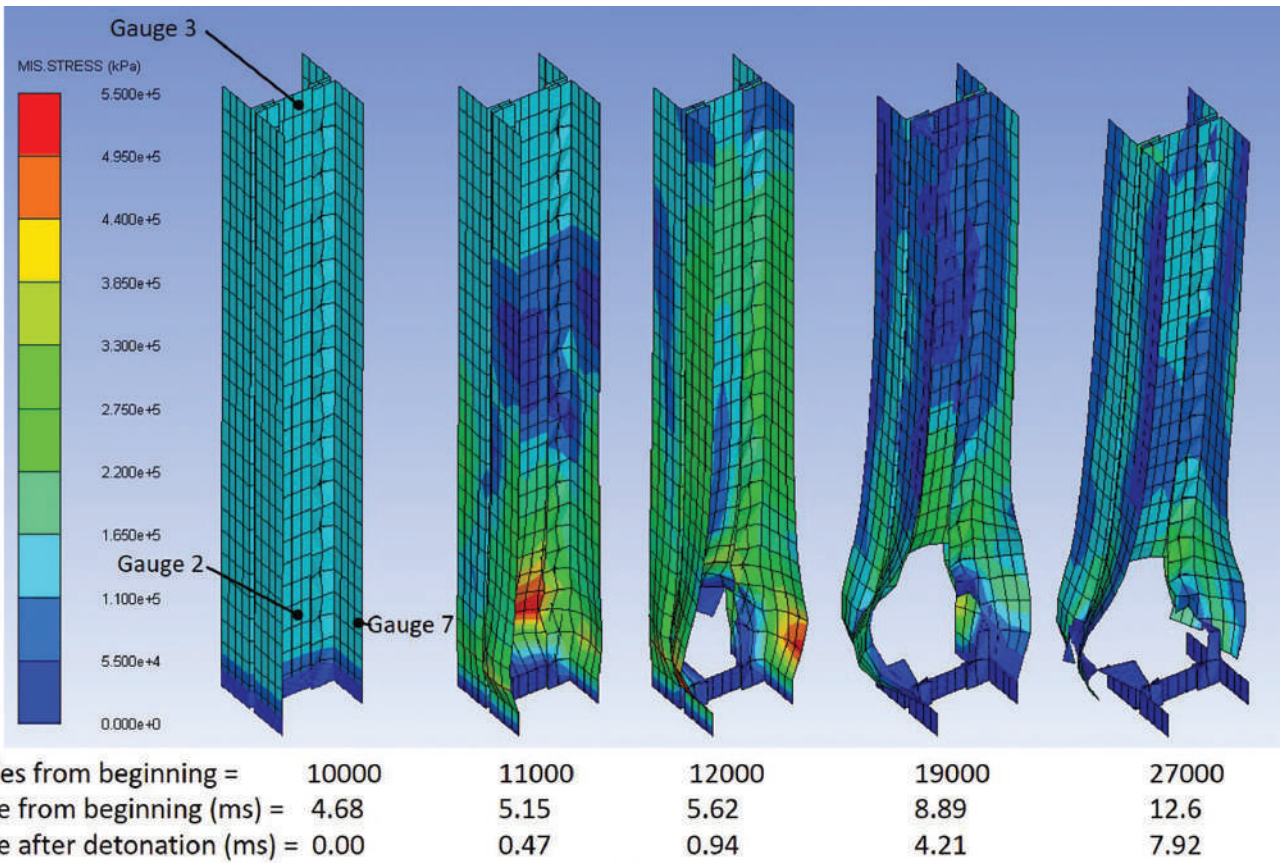


Fig. 16. Deformed shape changes over time with von Mises stress contours of a built-up column W14x99 model subject to $CW = 0.12Y$ at $SOD = 0.6X$ with the preloading.

with the preloading, web out-of-plane displacements were more than 10% of the flange width, and flange out-of-plane displacements were more than 10% of the member depth. Thus, both models resulted in the same Level 3, regardless of the preloading.

In the research by Sideri et al. (2017), the horizontal displacement as well as the axial force of each column were monitored over time to determine a column failure. It was appropriate and possible to monitor the axial force in the literature because the progressive collapse analysis model was composed of stick models or beam elements subjected to far-field detonations. The progressive collapse model in the literature is able to capture a member level failure mode, such as bending or flexural buckling (snap-through), but the model is not able to capture element level failure modes, such as flange flaring, web bulging, web puncturing, or flange severing, which are exemplified in Figure 6. On the other hand, for the individual column models subjected to close-field or near-contact detonations in the present study, the localized failure modes or deformed patterns

in Figure 6 are well captured and most critical to determine the degree of damages on each column and a potential column collapse. For this reason, instead of the time history of the axial force, time history of von Mises stress in Figure 15 is more appropriate and is critical to monitor signs of a column collapse at the component element level subjected to close-range or near-contact detonations.

A lateral deflection was appropriate to monitor in the progressive collapse model of the literature subjected to far-field detonations because the major failure mode is the bending failure and flexural buckling. However, the lateral deflection is not significant in the individual column model in this study because the majority of the detonation energy is consumed to either deform flanges and web locally, puncture a hole on web, or sever flanges, instead of bending the entire column member. Nevertheless, it is still crucial to monitor the out-of-plane deformations of the flange or web elements to determine a column collapse, based on whether the deformation is stabilized or continues to grow over time. The lateral deformations of flange and web elements

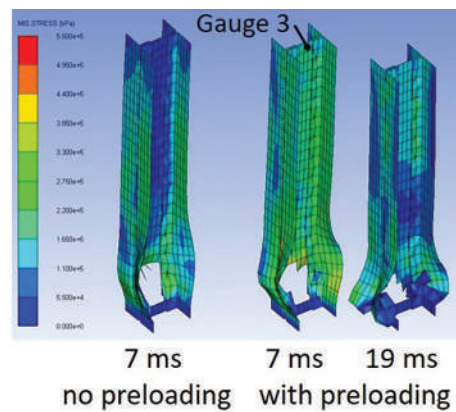
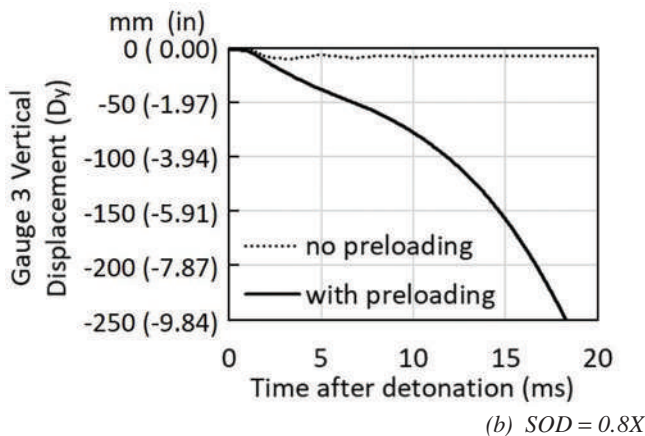
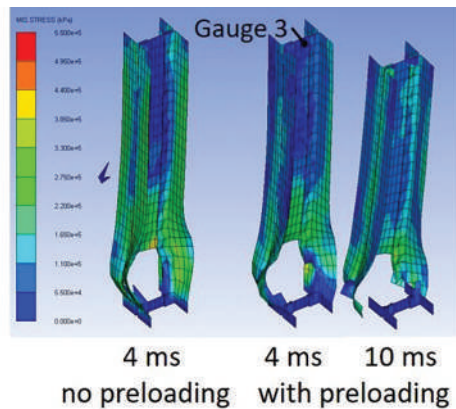
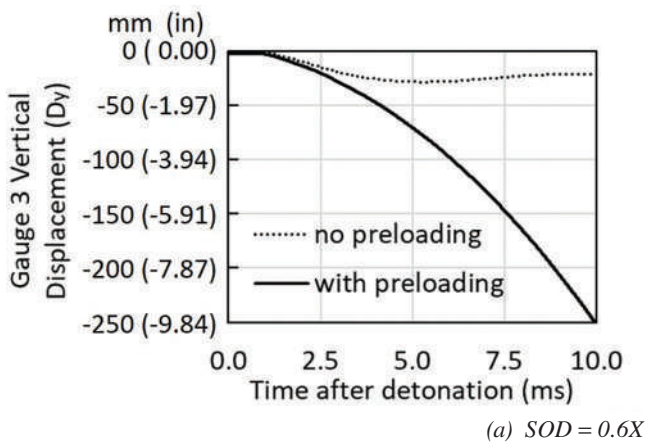


Fig. 17(a-b). Vertical in-plane displacement curves over time at Gauge 3 (left) and deformed shapes with von Mises stress contours (right) for built-up column W14×99 subjected to $CW = 0.12Y$ at various SOD.

were demonstrated in Figure 18 for this purpose. In order to supplement column failure, vertical displacement of the column was monitored in Figure 17, which is not available in the progressive collapse model by Sideri et al. (2017).

In this study, for columns subjected to close-range or near-contact detonations, several parameters were investigated and used to compare the cases with and without preloading in order to understand the effects of the service loads. Based on the investigation, it is concluded that the columns with Level 4 damages actually collapsed with the service loads; damage levels remained unchanged without and with service loads; and thus, the effects of service loads are insignificant with respect to the determination of the damage level and the column collapse. The same procedures and considerations were taken to determine and compare damage levels between the models without and with the preloading for more extensive ranges of CW and SOD in the next section.

NUMERICAL PARAMETRIC STUDY RESULTS

For each of the six different built-up sections described in Table 1, a numerical parametric study was performed, based on the model described in this paper. Each analysis model is defined by a column size, an SOD, and a CW. For each column size, six different SODs and five different CWs were considered, but one combination was used at a time for each model. Thus, there are 30 parametric study models per each column, resulting in a total of 180 models in the first set of the study, where no service loads were considered. In the second set of the study, 180 models were added to account for the preloading from the service loads prior to the blast analysis. Thus, there are a total of 360 models for the study. For each combination of SOD and CW for a given column, a high-fidelity, nonlinear, explicit FEA was performed. At the end of the analysis, a deformed shape and time history of displacements and von Mises stresses at a number of gauge points of the column were carefully reviewed and

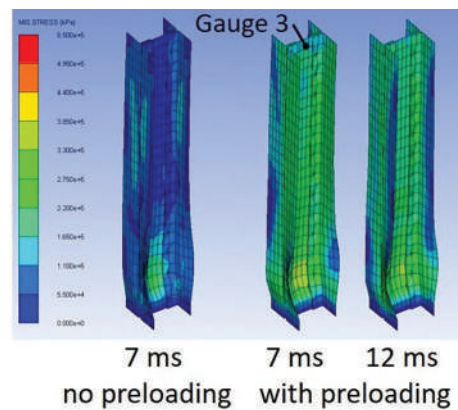
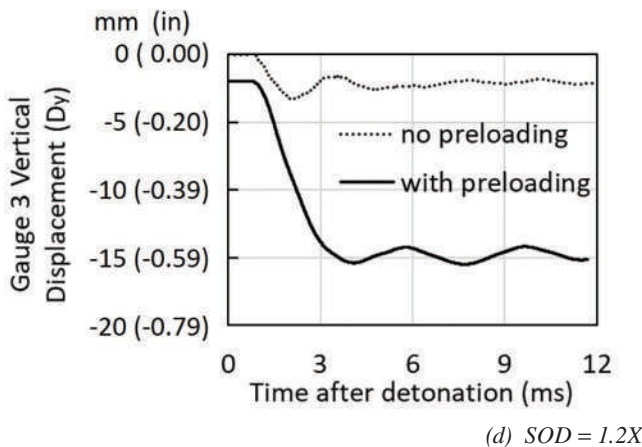
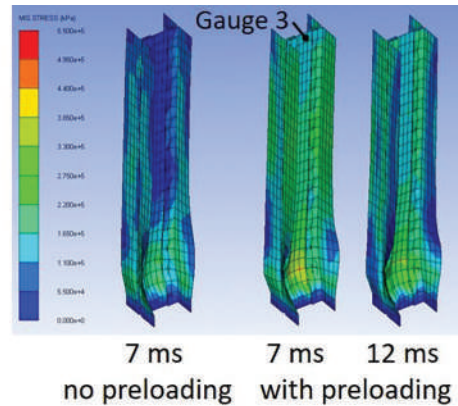
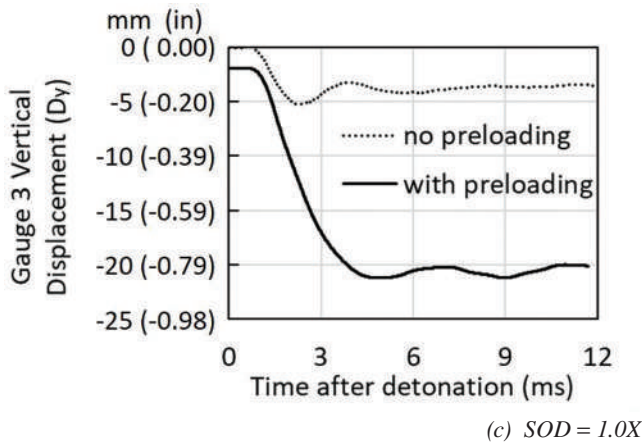
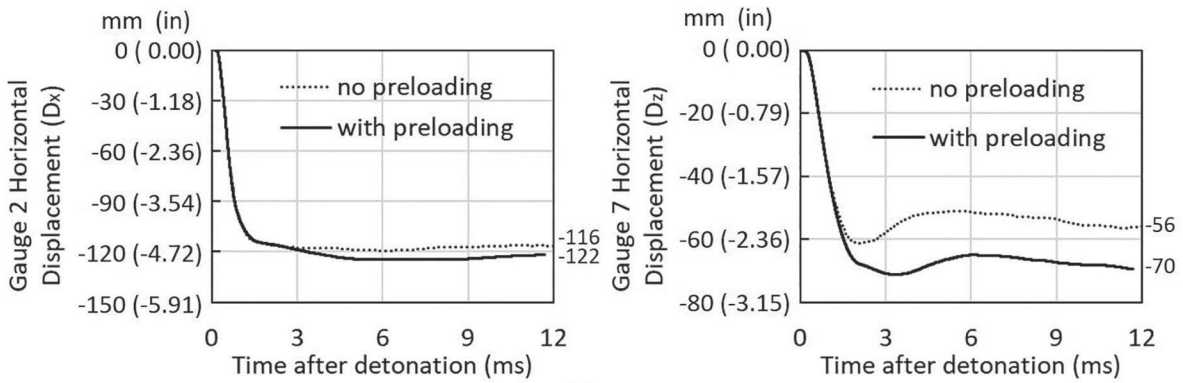
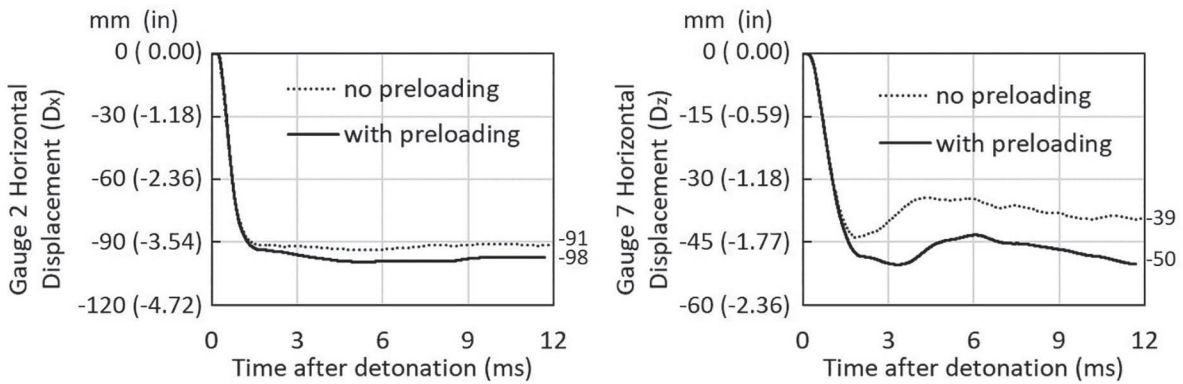


Fig. 17(c-d). Vertical in-plane displacement curves over time at Gauge 3 (left) and deformed shapes with von Mises stress contours (right) for built-up column W14×99 subjected to $CW = 0.12X$ at various SOD.



(a) $SOD = 1.0X$



(b) $SOD = 1.2X$

Fig. 18. Horizontal out-of-plane displacement curves over time at Gauge 2 on the web (x-direction) and Gauge 7 on the flange (z-direction) without and with preloading for built-up column $W14 \times 99$ subjected to $CW = 0.12Y$ at various SOD .

investigated, as exemplified in the previous section, and a damage level was determined in accordance with Table 5.

When the SOD was varied for a constant CW, the change of damage level is demonstrated in Figure 19 for a built-up column section equivalent to W14×176. As the SOD decreased, the column was more significantly damaged: The column damage level is inversely proportional to the SOD.

On the other hand, when the SOD was fixed, but the CW was varied, the change of damage level is exemplified in Figure 20 for a built-up column section equivalent to W14×99. As the CW increased, the column damage became more substantial: The column damage level is proportional to the CW.

From Figures 19 and 20, it is observed that the damage level for a given column depends on both SOD and CW. In order to present the damage level variation of a column more effectively, a contour plot was adopted. In the plot, the horizontal axis is SOD, while the vertical axis is CW. For a trial combination of SOD and CW, only one damage level is determined from a nonlinear explicit FEA, based on the damage level criteria specified in Table 5. The damage level, z , is recorded and displayed at a unique coordinate point (SOD, CW) on a two-dimensional (2D) graph. The schematic concept is depicted in Figure 21. This process was repeated for 30 models for each column, and the results

are presented on a contour plot, which is then repeated for all six columns in Figures 22 and 23, without and with the service loads, respectively.

In Figures 22 and 23, each solid dot represents a numerical model with a unique combination of SOD and CW, and its corresponding damage level result (z). Together with the scattered data of damage levels, representative contour lines are drawn in the graphs. The SOD values on the horizontal axis are expressed as fractions of a constant X ; while the CW values on the vertical axis are expressed as fractions of a constant Y . For security reasons and concerns, the actual constant numbers, X and Y , used on horizontal and vertical axes, respectively, are unreleased from the plots in Figures 22 and 23.

When the damage contours are compared among six different columns for the same range of CW and the same range of SOD in Figure 22, most area of the contour plot is covered with either damage Level 4 or 5 for built-up W14×43 and W14×99 columns. To identify CW and SOD combinations causing relatively less significant damages, the area covered by Level 3 or below is highlighted in gray for each of the six columns. As the column weight increases, the gray-colored area increases. Thus, it may be concluded that the column weight is directly proportional to the resistance to close-in detonations, but inversely proportional to the damage level.

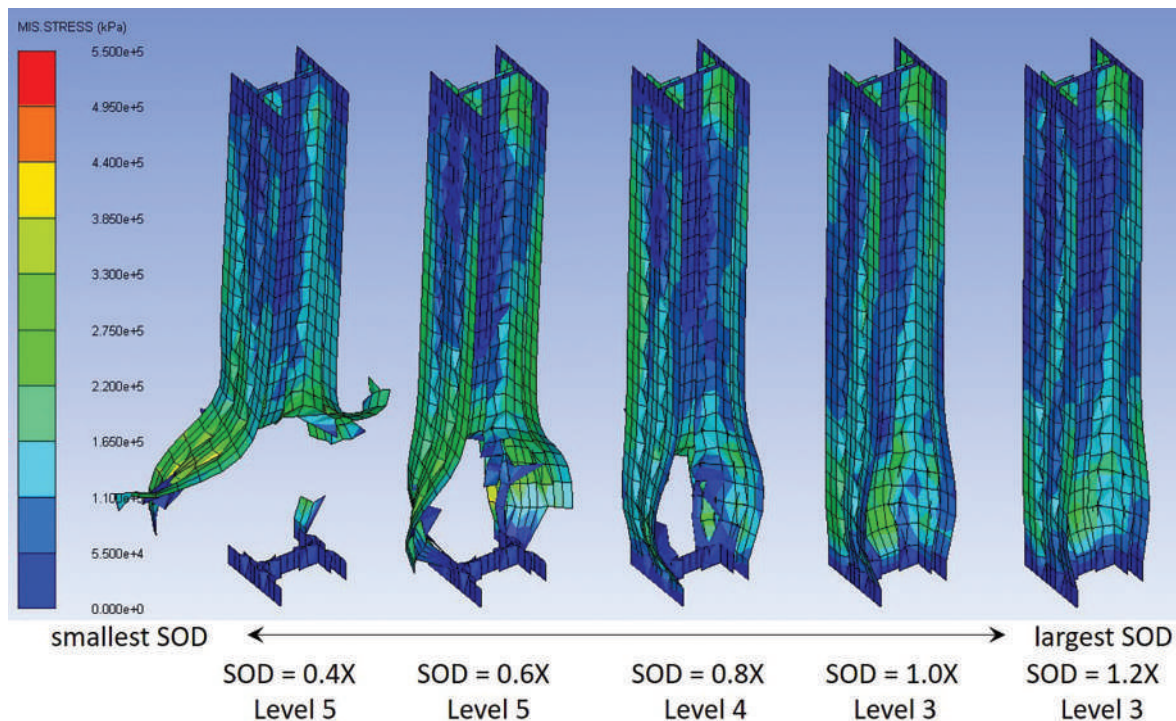


Fig. 19. Deformed shapes with von Mises stress and damage level variations per SOD for a built-up column section equivalent to W14×176 subjected to CW = 0.23Y.

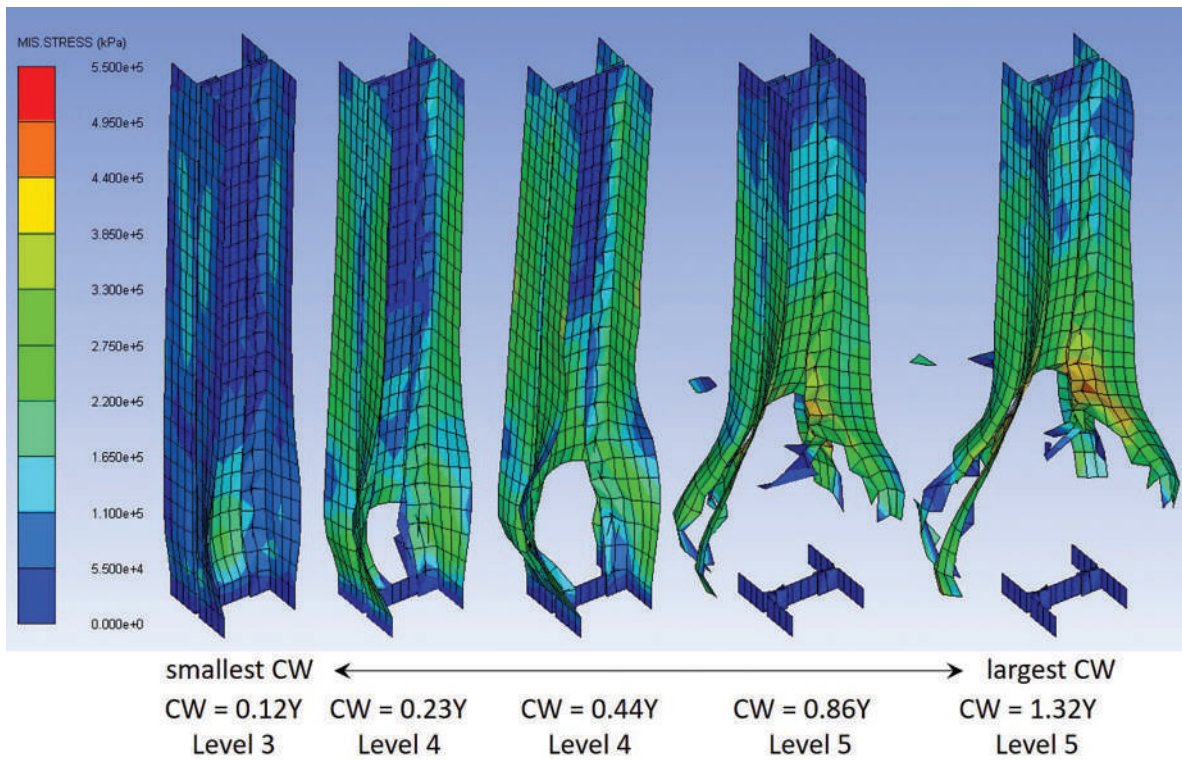


Fig. 20. Deformed shape with von Mises stress and damage level variations per CW for a built-up column section equivalent to W14×99, when $SOD = 1.2X$.

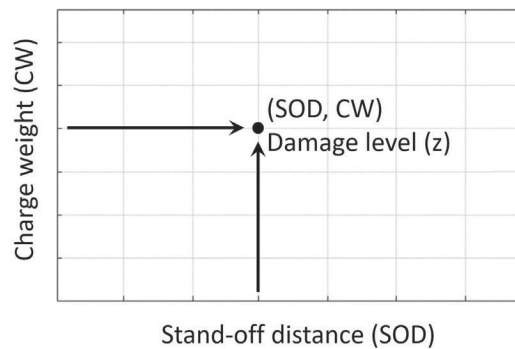


Fig. 21. Schematic concept of damage level plot for a column.

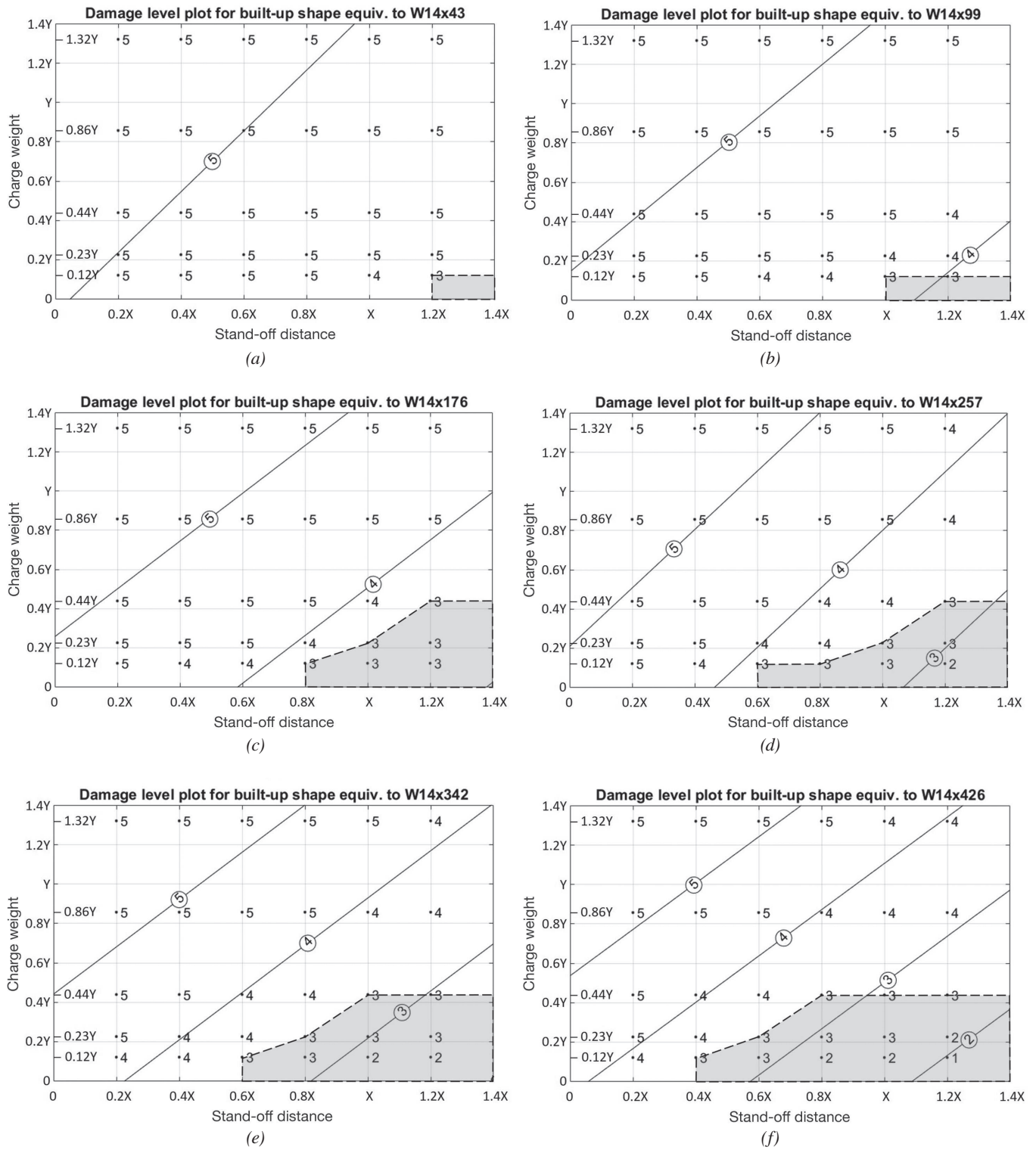


Fig. 22. Parametric study results for six built-up columns subjected to close-in detonations without preloading. Each number next to solid dot represents damage level for a given SOD and CW combination.

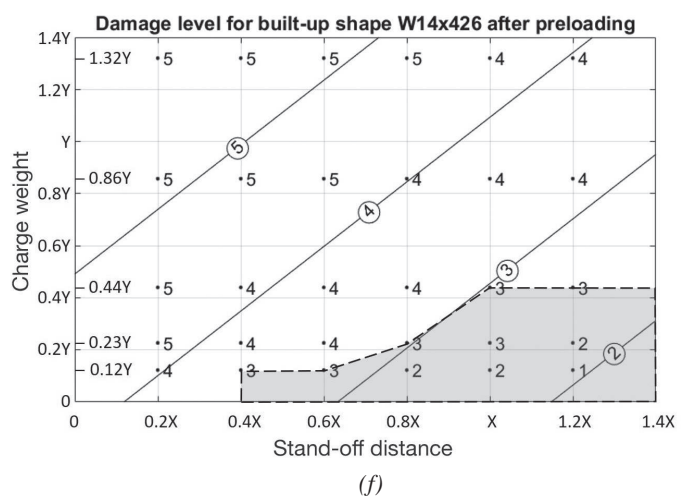
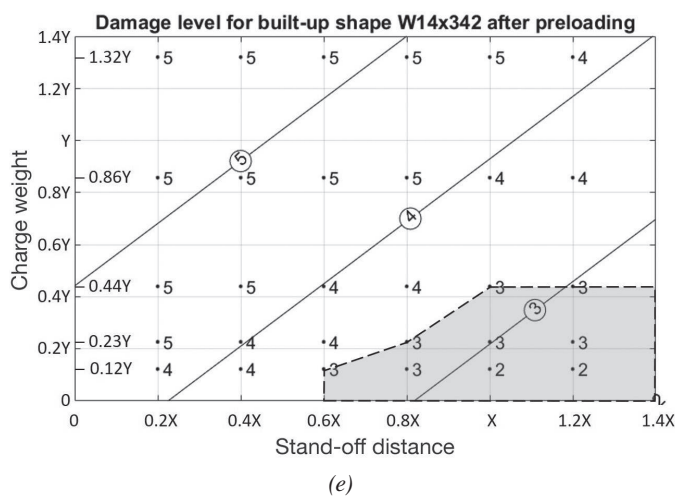
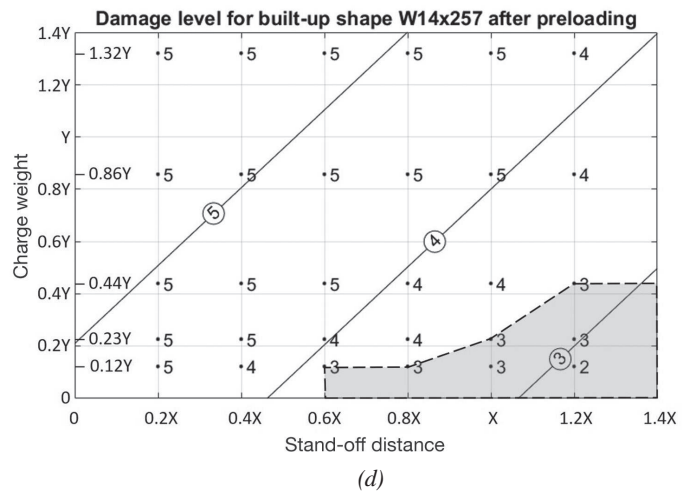
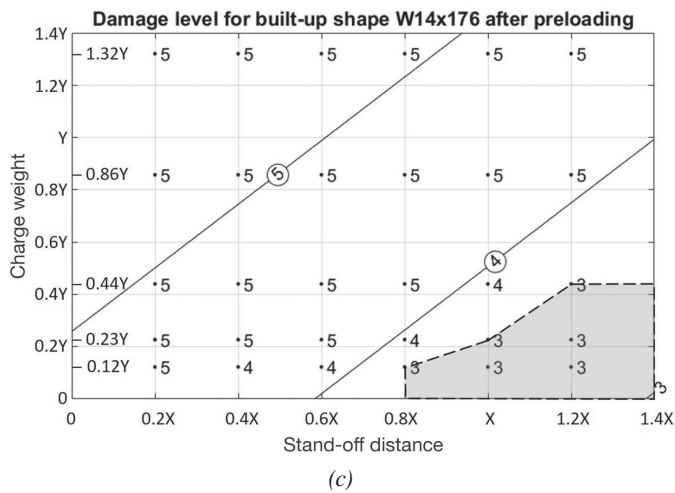
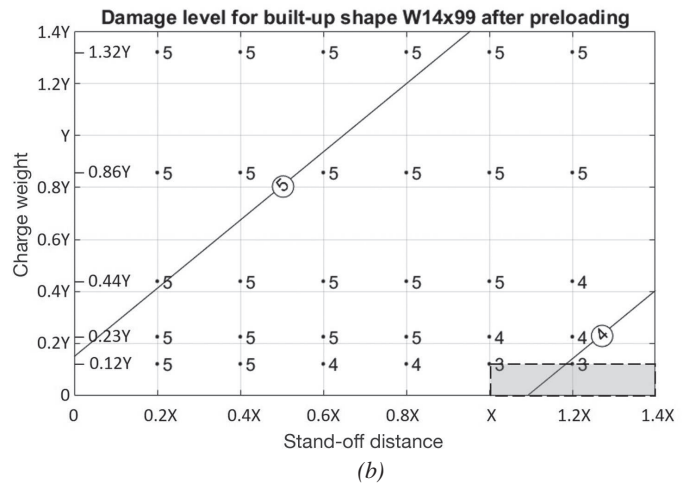
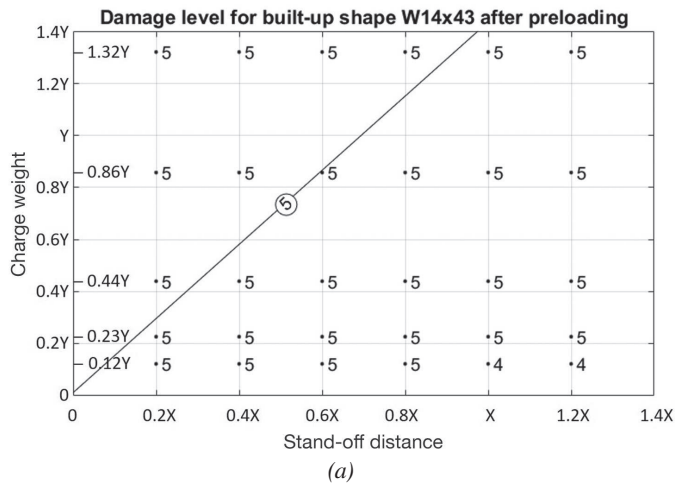


Fig. 23. Parametric study results for six built-up columns subjected to close-in detonations after preloading is applied to account for service loads. Each number next to solid dot represents damage level for a given SOD and CW combination.

Both the web and flange thicknesses of a standard wide-flange steel member listed in the AISC *Steel Construction Manual* (AISC, 2017) generally increase as the column weight increases. It is expected that the similar trend is observed in the existing built-up columns in transportation facilities. However, there may be situations where the web or flange plate is thinner than the equivalent standard shape based on a column weight, which could lead to underestimation of detonation damages. In order to address such potential imbalance of the web and flange thicknesses of a built-up column, an equivalent standard shape can be determined alternatively, based on either flange or web thickness, and the minimum shape can be used for conservative considerations.

Among the first 180 models without the preloading in Figure 22, there are 108 models labeled as Level 5 damages. These 108 models were excluded in the second set of analyses with the preloading because the first set models with Level 5 damages will still result in Level 5 damages with the addition of the preloading. Thus, only the remaining 72 models, labeled as Level 4 or below in Figure 22, were actually analyzed with the preloading for the second set of models, and the results are plotted in Figure 23.

When the gray areas covered by Level 3 or below damages are compared with and without the preloading in Figures 22 and 23, most columns resulted in the same area and the same damage levels. Thus, it is concluded that the effects of the service loads are insignificant for built-up steel columns subjected to close-in detonations in terms of determining the damage levels. The same observation was made when the four sample models of W14×99 column were compared thoroughly between the models without and with the preloading in the Effects of Preloading section. In addition, it is confirmed that the preloading caused collapses eventually for almost all columns labeled as Level 4 or 5 damages, which is consistent with the damage criteria in Table 5.

A few exceptions were observed in two extreme columns: the smallest and largest columns among the parametric study shapes. For built-up column W14×43 subjected to $CW = 0.12Y$ at $SOD = 1.2X$, no hole was punctured on the web without and with the preloading, but the column began to collapse with the preloading as shown in Figure 24(a). For this reason, the damage levels were given differently between the models without and with the preloading. W14×43 column is simply too flimsy to support close-in detonations of any practical combinations of CW and SOD considered in this study. As a minimum, built-up column equivalent to W14×99 or larger must be used for consideration of close-in detonations without adding any separate protective components.

For built-up column W14×426 subjected to the $CW = 0.23Y$ at $SOD = 0.6X$ and $CW = 0.44Y$ at $SOD = 0.8X$ cases,

no hole was punctured on the web, but the flange and web plates deformed significantly enough to buckle and collapse with the preloading, as shown in Figures 24(b) and 24(c). This kind of failure mode was not discovered in any other columns in this study. For the specific combinations of CW and SOD, the component plates are strong enough to prevent them from hole-puncturing or severing but not strong enough to avoid the buckling with the preloading. For this reason, the damage level is elevated from Level 3 without preloading to Level 4 with preloading. For all other cases of CW and SOD combinations, no changes were observed in the damage levels in between the cases without and with preloading, as shown in Figures 22 and 23.

SUGGESTED DESIGN METHODOLOGY

As defined in Table 5, in order to avoid a column collapse in a facility, a combination of SOD and CW must not result in Level 4 or 5 damages, as a minimum. The shaded area in the lower right corner in each of the plots in Figures 22 and 23 represents desirable combinations of SOD and CW that could result in Level 3 or less damages and avoid a column collapse. Bulging deformations observed in Level 3 or less damages could result in secondary moments in flanges or web, but they do not seem significant enough to cause a column collapse with the presence of service loads, except for the three exceptional cases described in the last section. Thus, it is likely that the upper-level passengers or building users could evacuate with a lower-level column subject to Level 3 or less damages. In addition, the design safety margins in the AISC *Specification for Structural Steel Buildings* (AISC, 2016) would likely provide some reserve capacity to allow the evacuation with the same damage levels. Mazurkiewicz et al. (2015) also reached a similar conclusion in terms of the relationship between the level of damage or deformation in the column and the remaining load-carrying capacity.

The contour plots in Figure 22 without the service loads match closely to Figure 23 with the service loads, except for a few extreme cases. For this reason, the contour plots in Figure 22 could still be used for preliminary design or cost-estimate purposes. However, for the final design purposes, detailed close-range blast FEA should be performed considering the service loads with the aid of Figure 23.

Each contour plot in Figures 22 and 23 was presented in a linear form because other mathematical models, such as quadratic or cubic forms, did not necessarily result in better representations of the scattered damage plots than the linear form. In addition, linear contour plots would be more useful in an attempt to develop blast mitigation design equations to cover the entire range of steel columns subjected to close-in detonations.

Using the damage contour plots in Figures 22 and 23,

overall preliminary design procedures are summarized as follows:

1. For a given built-up column, determine the closest matching standard shape in the AISC *Steel Construction Manual* (AISC, 2017), based on the weight, overall cross-sectional dimensions, and element thicknesses. This is the equivalent standard shape.
2. Based on a risk assessment of a facility, determine the design SOD and CW combinations for a project.
3. If the equivalent column size matches with one of the six sizes in Figures 22 and 23, which were investigated in this study, directly plug the SOD and CW variables into the plot to estimate the damage level.
4. If the column size does not match with one of the six sizes, plug the variables into the plots with the sizes immediately larger and smaller than the column to estimate the damage levels in the two plots. The damage level of the column under consideration could be estimated via linear interpolation between the two damage levels, based on column weights per unit length. Alternatively, engineers may prefer to choose one of the six plots with the size immediately smaller than the column under consideration to determine the damage

level conservatively. In place of the column weight, either column flange or web thickness could be used as a variable to estimate the equivalent section, if the thickness results in a conservative section.

If a given column is potentially subject to Level 4 or 5 damages, implement one of the following blast mitigation designs alone or combined:

- Increase the SOD by enlarging the architectural cladding size around the column. However, this option can result in reduction of the usable spaces around the column.
- Enforce and tighten access control so that the CW can be capped by a lower value.
- Replace the column with a larger standard AISC shape that can result in Level 3 or less damage under the given condition. However, there are several challenges with this method: The existing beams and girders framing into the column must be supported separately during the column replacement, and the crane access to hoist steel members in building interior spaces may be limited.
- Alternatively, strengthen the existing columns by adding thicker steel plates on the flanges and the web to come up with a larger equivalent column shape that can result in Level 3 or less damage under the given condition. If the

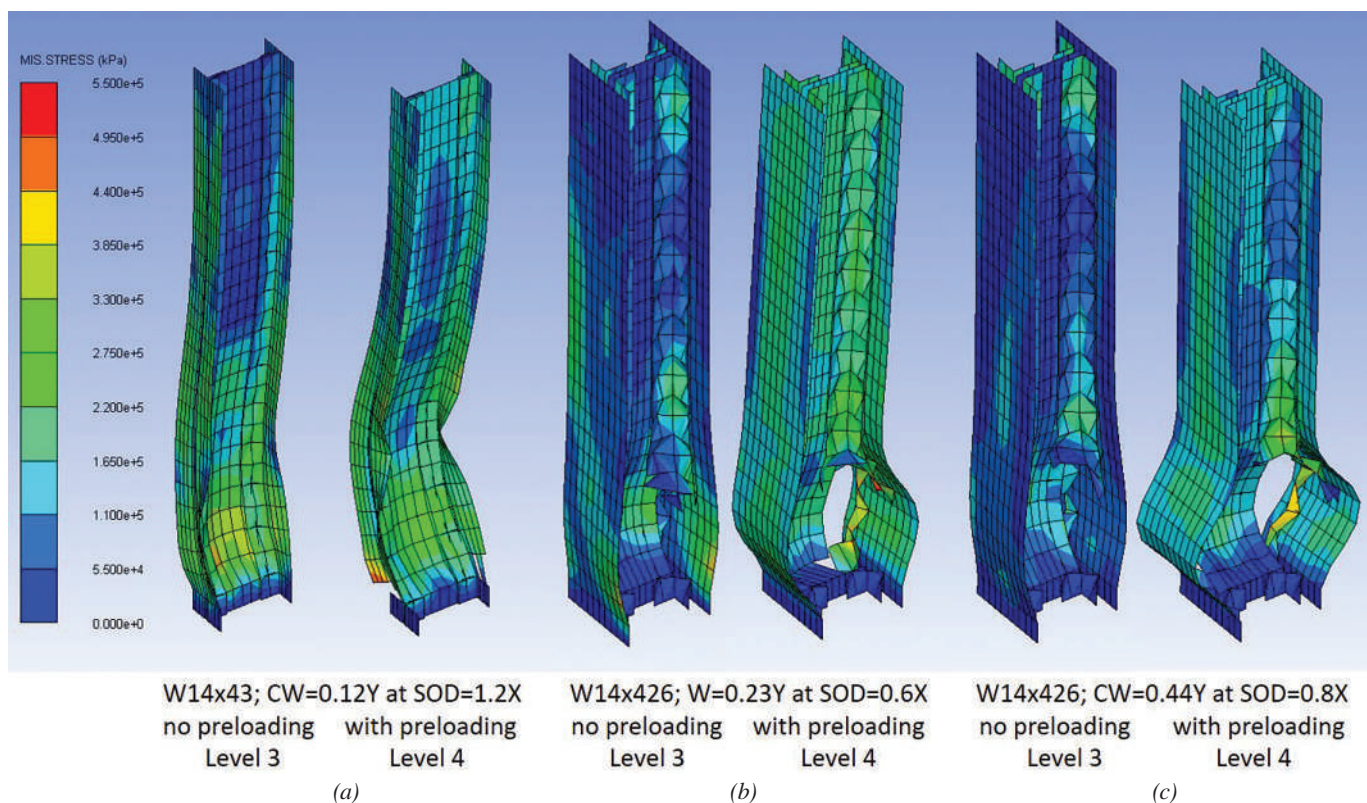


Fig. 24. Exceptional cases resulting in different damage levels in between models without and with preloading.

section does not match with an AISC standard section, either flange or web thickness could be used as a variable to estimate the equivalent section. In addition, the existing beams and girders framing into the column must also be supported separately during the column strengthening, because the existing rivets must be removed for the plate additions.

- Harden the column by adding encasement materials around the column over a sufficient height from the bottom, where possibly MPIED can be placed. This is based on traditional design approaches used against close-in or near-contact detonations, which was also used for mitigating potential risks of direct vehicular impacts. The added layers around the column should be designed in a way that the most blast energy is dissipated via sacrificing themselves, while the remaining energy is small enough to result in only minor damages to the column. Simultaneously, the outer layers could harden the column by supporting the flanges and web not to allow significant deformations. The sacrificial and hardening layers can be made from typical construction materials, such as steel plates, concrete fill, and reinforcement bars. Separate analyses are needed to design the outer layers, using explicit nonlinear FEA. The details of the analysis approaches are similar to what is discussed in this study but are beyond the scope of this study.

To use the damage contour plots in Figures 22 or 23 for a preliminary design, the following conditions must be satisfied:

- The existing column shapes are wide-flange columns built up from individual angles and plates similar to the examples shown in Table 1.
- The columns are made from the materials listed in Table 2 or stronger.
- The column sizes are similar to one of the shapes shown in Figures 22 and 23 or are equivalent to one of the W14 series standard shapes listed in the AISC *Steel Construction Manual* (AISC, 2017). The recommended minimum size to be considered for the design would be built-up shape equivalent to W14×99.
- The CW must be within the portable range that can be carried by a single person. The exact range of the CW is not disclosed for security reasons.
- The SOD must be within a few depths of the column size so that the architectural finish size can be within a practical range. The exact range of the SOD is not disclosed for security reasons.
- Corrosions and deterioration of the columns are beyond the scope of this study. If the existing column

is deteriorated significantly, account for the thickness reduction in choosing the equivalent shape.

- The service loads should not result in more than 60% of the yield stress in the column. If the service loads beyond this limit are expected, or the residual ultimate capacity is sought, separate analyses could be performed based on preloading larger than 60% of the yield stress. This is beyond the scope of the present study.

The six contour plots and design methodology presented in this study could be used for preliminary structural adequacy assessments of hundreds or thousands of built-up steel columns subjected to potential close-in detonations in most historic transportation facilities, such as rail or subway stations or tunnels, without going through expensive and time-consuming nonlinear, explicit FEA. This study could benefit local, state, or federal agencies in estimating project costs and decision making for essential blast evaluation or mitigation projects, but it could also benefit structural engineers in providing an efficient and practical tool for preliminary close-in detonation analysis, most of whom do not have access to sophisticated high-fidelity analyses. In addition, the contour plots and the design method developed in this study could be used for quality control purposes in other security projects, requiring similar nonlinear explicit FEA for close-in detonations. For final design purposes of critical columns subjected to close-in detonations, performing detailed nonlinear explicit FEA is recommended.

CONCLUSION

A new performance-based method was proposed in this work to evaluate steel columns in historic transportation facilities subjected to close-in detonations. Many historic transportation structural members are built-up steel sections composed of angles and plates connected with rivets. Using the mechanical properties of steel data, the five coefficients for a strain-rate dependent material model were determined. Practical ranges of charge weights and stand-off distances were determined for transportation facility columns subjected to close-in detonations. For six carefully chosen built-up steel columns, equivalent to standard AISC wide-flange sections, two series of parametric studies were conducted with and without service loads, using a high-fidelity, nonlinear, explicit FEA program. Six levels of damage criteria were proposed in this study for a performance-based design. Using the damage criteria, analysis results were presented in two sets of six contour plots. The contour plots can be directly used by practicing structural engineers for a quick evaluation of built-up transportation facility columns, subjected to close-in detonations, and basis for cost estimate and preliminary blast mitigation design.

ACKNOWLEDGMENTS

This research was sponsored by the U.S. Department of Transportation through UTRC (University Transportation Research Center) Region 2 (Award No. RF# 49198-21-28). Manhattan College also provided various resources to make this research possible. Their sponsorships are greatly appreciated.

REFERENCES

- AISC (1927), *Steel Construction Manual*, 1st Ed., American Institute of Steel Construction, New York, N.Y.
- AISC (1934), *Steel Construction Manual*, 2nd Ed., American Institute of Steel Construction, New York, N.Y.
- AISC (1946), *Steel Construction Manual*, 5th Ed., American Institute of Steel Construction, New York, N.Y.
- AISC (1953), *Historic Record Dimensions and Properties Rolled Shapes Steel and Wrought Iron Beams and Columns as Rolled in USA, Period 1873 to 1952 with Sources as Noted*, American Institute of Steel Construction, New York, N.Y.
- AISC (1963), *Manual of Steel Construction*, 6th Ed., American Institute of Steel Construction, New York, N.Y.
- AISC (2016), *Specification for Structural Steel Buildings*, ANSI/AISC 360-16, American Institute of Steel Construction, Chicago, Ill.
- AISC (2017), *Steel Construction Manual*, 15th Ed., American Institute of Steel Construction, Chicago, Ill.
- American Manufacturer (1900), *American Manufacturer and Iron World*, Vol. 67, No. 1, Pittsburg, Pa.
- Ansys (2015), *Ansys/Autodyn User's Manual*, Release 16.1, Ansys.
- ASCE (2010), *Design of Blast-Resistant Buildings in Petrochemical Facilities*, 2nd Ed., American Society of Civil Engineers, Reston, Va.
- ASCE (2011), *Blast Protection of Buildings*, ASCE/SEI 59, American Society of Civil Engineers, Reston, Va.
- ASTM (1936), *Standard Specifications for Steel for Buildings*, ASTM A9, ASTM International, West Conshohocken, Pa.
- ASTM (2014), *Standard Specification for Carbon Structural Steel*, ASTM A36, ASTM International, West Conshohocken, Pa.
- Baylot, J.T., Ray, J.C., and Hall, R.L. (2003), "Prediction Method for Response of Steel Bridge Beams and Girders to Blast and Fragment Loads," *Transportation Research Record: Journal of the Transportation Research Board*, 1827, Paper No. 03-2708, pp. 69–74.
- Brockenbrough, R.L. and Schuster, J. (2018), *Rehabilitation and Retrofit*, Design Guide 15, 2nd Ed., AISC, Chicago, Ill.
- Camp, J.M. and Francis, C.B. (1920), *The Making, Shaping and Treating of Steel*, 2nd Ed., Carnegie Steel Company, Pittsburgh, Pa.
- Century Dynamics (2005), *Autodyn Theory Manual*, Revision 4.3, Ansys.
- Davis, C., Sammarco, E., and Williamson, E. (2017), *Bridge Security Design Manual*, FHWA-HIF-17-032, Federal Highway Administration, U.S. Department of Transportation, Infrastructure Office of Bridges and Structures, Washington, D.C.
- DOD (2009), *Unified Facilities Criteria—Design of Buildings to Resist Progressive Collapse*, UFC 4-023-03, Change 3, U.S. Department of Defense, Washington, D.C.
- DOD (2014), *Unified Facilities Criteria—Structures to Resist the Effects of Accidental Explosions*, UFC 3-340-02, Change 2, U.S. Department of Defense, Washington, D.C.
- FEMA (2007), *Risk Management Series: Site and Urban Design for Security Guidance Against Potential Terrorist Attacks Providing Protection to People and Buildings*, FEMA 430, Federal Emergency Management Agency, Washington, D.C.
- Gilsanz, R., Hamburger, R., Barker, D., Smith, J.L., and Rahimian, A. (2013), *Design of Blast Resistant Structures*, Design Guide 26, American Institute of Steel Construction, Chicago, Ill.
- Jenkins, B.M. (1997), *Protecting Surface Transportation Systems and Patrons from Terrorist Activities: Case Studies of Best Security Practices and a Chronology of Attacks*, Mineta Transportation Institute, San Jose, Calif.
- Jenkins, B.M. and Gersten, L.N. (2001), *Protecting Public Surface Transportation Against Terrorism and Serious Crime: Continuing Research on Best Security Practices*, Mineta Transportation Institute, San Jose, Calif.
- Johnson, G.R. and Cook, W.H. (1983), "A Constitutive Model and Data for Metals Subjected to Large Strains, High Strain Rates and High Temperatures," *Proceedings of the 7th International Symposium on Ballistics*, Hague, Netherlands.
- Johnson, G.R. and Cook, W.H. (1985), "Fracture Characteristics of Three Metals Subjected to Various Strains, Strain Rates, Temperatures and Pressures," *Engineering Fracture Mechanics*, Vol. 21, No. 1, pp. 31–48.
- Krauthammer, T. (2008), *Modern Protective Structures*, CRC Press, Boca Raton, Fla.

- Krishnappa, N., Bruneau, M., and Warn, G.P. (2014), "Weak-Axis Behavior of Wide Flange Columns Subjected to Blast," *Journal of Structural Engineering*, ASCE, Vol. 140, No. 5.
- Lee, E., Finger, M., and Collins, W. (1973), *JWL Equation of State Coefficients for High Explosives*, Lawrence Livermore Laboratory, Livermore, Calif.
- Marchand, K.A. and Alfawakhiri, F. (2004), *Blast and Progressive Collapse*, Facts for Steel Buildings Number 2, American Institute of Steel Construction, Chicago, Ill.
- Mazurkiewicz, L., Malachowski, J., and Baranowski, P. (2015), "Blast Loading Influence on Load Carrying Capacity of I-Column," *Engineering Structures*, Vol. 104, pp. 107–115.
- Ngo, T., Mohotti, D., Remennikov, A., and Uy, B. (2015), "Numerical Simulations of Response of Tubular Steel Beams to Close-Range Explosions," *Journal of Constructional Steel Research*, Vol. 105, pp. 151–163.
- NYPD (2009), *Engineering Security Protective Design for High Risk Buildings*, New York City Police Department. Last accessed on June 07, 2019, https://www1.nyc.gov/assets/nypd/downloads/pdf/nypd_engineeringsecurity.pdf.
- Remennikov, A.M. and Uy, B. (2014), "Explosive Testing and Modelling of Square Tubular Steel Columns for Near-Field Detonations," *Journal of Constructional Steel Research*, Vol. 101, pp. 290–303.
- Rogers, G.F.C. and Mayhew, Y.R. (1995), *Thermodynamic and Transport Properties of Fluids SI Units*, 5th Ed., Blackwell Publishing, Oxford.
- Salmon, C.G., Johnson, J.E., and Malhas, F.A. (2008), *Steel Structures: Design and Behavior*, 5th Ed., Pearson, New York, N.Y.
- Schwer, L. (2007), "Optional Strain-Rate Forms for the Johnson Cook Constitutive Model and the Role of the Parameter Epsilon_0," LS-DYNA Anwenderforum, Frankenthal, Germany.
- Shin, J., Whittaker, A.S., Cormie, D., and Wilkinson, W. (2014), "Numerical Modeling of Close-in Detonations of High Explosives," *Engineering Structures*, Vol. 81, pp. 88–97.
- Sideri, J., Mullen, C.L., Gerasimidis, S., and Deodatis, G. (2017), "Distributed Column Damage Effect on Progressive Collapse Vulnerability in Steel Buildings Exposed to an External Blast Event," *Journal of Performance of Constructed Facilities*, ASCE, Vol. 31, No. 5.
- Ugural, A.C. and Fenster, S.K. (1994), *Advanced Strength and Applied Elasticity*, 3rd Ed., Prentice Hall.
- U.S. Army (1986), *Fundamentals of Protective Design for Conventional Weapons*, TM 5-855-1, Washington, D.C.
- Williamson, E.B. and Winget, D.G. (2005), "Risk Management and Design of Critical Bridges for Terrorist Attacks," *Journal of Bridge Engineering*, ASCE, Vol. 10, No. 1, pp. 96–106.
- Winget, D.G., Williamson, E.B., Marchand, K.A., and Gannon, J.C. (2005), "Recommendations for Blast Design and Retrofit of Typical Highway Bridges," *Transportation Research Record: Journal of the Transportation Research Board*, Vol. CD 11-S, pp. 1–8.

Reliability of HSS Cross Connections in Branch Axial Compression

Dillon F. Rudman, Quanhan Xi, Jeffrey A. Packer, and Kyle Tousignant

ABSTRACT

A method was recently proposed, by Wei and Packer (2021), for application of the 2016 AISC *Specification* (AISC, 2016) to rectangular HSS sidewall instability. The proposal was based on evidence from prior research and collated data from international experiments. Herein, this topic is further updated with very recent research, and suggested improvements by others. An expanded database containing both experimental and numerical (finite element) tests of rectangular HSS-to-HSS cross connections with chord sidewall failure is hence amassed, totaling 227 tests. An analysis of this data reinforces the recent recommendations.

A review is given of methods in use for determining the structural reliability of steel members and connections. Based on this, a reliability study is performed on the recent recommendations, using various closed-form reliability methods as well as Monte Carlo simulation, to determine appropriate resistance factors for use with nominal-strength design equations for HSS sidewall instability. The influence of many variables, in particular chord sidewall slenderness, live-to-dead load ratio, as well as material and geometric properties, on the structural reliability of full-width rectangular HSS-to-HSS cross-connections under branch axial compression is studied.

KEYWORDS: hollow structural sections, cross connections, sidewall instability, reliability, resistance factors, Monte Carlo simulation.

INTRODUCTION

The 2016 AISC *Specification for Structural Steel Buildings* (AISC, 2016), hereafter referred to as the AISC *Specification*, provisions for web stability under local compression loading were applied to HSS connections by Wei and Packer (2021) through a limited experimental study and an analysis of a database of full-width rectangular HSS cross-connection experimental tests. This study showed that the web local crippling limit state never governs for HSS grades up to 50 ksi yield and sidewall slenderness values up to 57. Connections meeting the requirements do not need to be checked for web local crippling as a limit state. The web local yielding limit state in the AISC *Specification* was

found to be very applicable to the full-width rectangular HSS cross (or X-) connection, illustrated in Figure 1.

Wei and Packer (2021) proposed to use the findings of Kuhn et al. (2019) to specify a limit for when the AISC *Specification* Chapter E can be used to determine the HSS chord sidewall (or web) compression buckling resistance. Instead of requiring the bearing length to be greater than the chord depth, as mentioned in the AISC *Specification* Commentary for I-shaped sections, a bearing length of greater than 0.25 of the chord depth was a more appropriate demarcation point for HSS connections (Kuhn et al., 2019). The effective length factor in the column buckling model is not stipulated by the *Specification* but was taken as 0.65 because rectangular HSS sidewalls resemble more of a fixed-fixed end restraint than a pin-pin end restraint. It was also determined that the branch angle of inclination, θ , does not have a definite impact on the cross-connection capacity; thus, the predicted cross-connection capacity (expressed as a force in an inclined branch) was conservatively limited to only the vertical force component of the branch member force (Wei and Packer, 2021). These proposals for applying the 2016 AISC *Specification* web compression limit states to rectangular HSS cross-connections are shown in Table 1. As with this current study, the connections were not susceptible to out-of-plane instability. With regard to Table 1 and thereafter, a list of symbol definitions is given at the end of the paper, but the symbols used herein are also in accord with the AISC *Specification*.

Dillon F. Rudman, WSP, Oakville, Ontario, Canada.
Email: dillon.rudman@wsp.com

Quanhan Xi, Department of Statistics, University of British Columbia, Vancouver, British Columbia, Canada. Email: johnny.xi@stat.ubc.ca

Jeffrey A. Packer, Department of Civil & Mineral Engineering, University of Toronto, Toronto, Ontario, Canada. Email: jeffrey.packer@utoronto.ca (corresponding)

Kyle Tousignant, Department of Civil & Resource Engineering, Dalhousie University, Halifax, Nova Scotia, Canada. Email: kyle.tousignant@dal.ca

Paper No. 2021-16

Table 1. Proposed Application of the 2016 AISC Specification Web Compression Limit States to Rectangular HSS Cross Connections, per Wei and Packer (2021)

Limit State	HSS-to-HSS Connection Nominal Strength, P_n (kips)	ϕ (Ω)
Web local yielding, interior	For $l_{end} > H$ $2F_y t \left(7.5t + \frac{H_b}{\sin\theta} \right)$ (1)	1.00 (1.50)
Web local crippling, interior	For $l_{end} \geq H/2$ $1.6t^2 \left(1 + \frac{3H_b}{H} \frac{\sin\theta}{H} \right) \sqrt{EF_y Q_f}$ (2)	0.75 (2.00)
Web compression buckling, interior, and $l_b \leq 0.25H$	For $l_{end} \geq H/2$ and $H_b/H\sin\theta \leq 0.25$ $\left(\frac{48t^3}{H-3t} \right) \sqrt{EF_y Q_f}$ (3)	0.90 (1.67)
Web compression buckling, interior, and $l_b > 0.25H$	For $l_{end} \geq H/2$ and $H_b/H\sin\theta > 0.25$ Use AISC Specification Equations E3-1, E3-2, and E3-3, with $K = 0.65$, L_c/r from Equation 4, and A_g (for each sidewall) from Equation 6	0.90 (1.67)



Fig. 1. Example of a full-width rectangular HSS cross connection, in vertical bracing.

For the web compression buckling limit state with $l_b > 0.25H$, the slenderness, λ or L_c/r , is calculated according to Equation 4 (Wei and Packer, 2021):

$$\lambda = \frac{KL}{r} = \frac{L_c}{r} = 3.46 \left(\frac{H}{t} - 3 \right) \sqrt{\frac{1}{\sin \theta}} \quad (4)$$

If the branch member is inclined, there is an allowance (indicated in Equation 4) resulting in a longer buckling length (Packer et al., 2009; IIW, 2012; ISO, 2013). A nondimensional slenderness, λ_c , can also be described by:

$$\lambda_c = \frac{\lambda}{\pi} \sqrt{\frac{F_y}{E}} \quad (5)$$

Using Equation 4, the critical stress, F_{cr} , can be determined for each chord sidewall or “column” from AISC *Specification* Section E3 and, using the cross-sectional area for each sidewall “column” (a load dispersion length multiplied by the wall thickness) given by Equation 6, the buckling strength of each sidewall can then be calculated.

$$A_g = \left(7.5t + \frac{H_b}{\sin \theta} \right) t \quad (6)$$

Herein, the topic of chord sidewall buckling in full-width rectangular HSS-to-HSS cross connections is further updated with recent research and suggested improvements by others. An evaluation of various failure models is conducted using data reflective of North American rectangular HSS strengths; a reliability study is then performed using various closed-form reliability methods, as well as Monte Carlo simulation (MCS), to determine appropriate resistance factors for use with the nominal-strength design equations recommended.

RECENT DEVELOPMENTS

Lan et al. (2021)

Recently, a review of competing proposals was performed by Wardenier et al. (2020) against a collated experimental and numerical database of full-width rectangular HSS-to-HSS cross connections in branch compression, which resulted in the following chord sidewall buckling equation, N_L (Lan et al., 2021):

$$N_L = C_f F_k (2H_b + 10t) \sqrt{\frac{1}{\sin \theta}} Q_f \quad (7)$$

where

$$F_k = \chi \left(\frac{H}{H_b} \right)^{0.15} \quad F_y \leq F_y \quad (8)$$

and

$$C_f = 1.1 - 0.1 \frac{F_y}{355} \leq 1.0 \quad (9)$$

The material factor (C_f in Equation 9, with F_y in MPa) was added to the proposed connection capacity by Lan et al. (2021) to cater for the influence of high-strength steels with a yield strength up to 139 ksi (960 Mpa). High-strength steel rectangular HSS connections have a larger elastic range, have material softening in the heat-affected zone, and are more prone than regular-strength steel rectangular HSS connections to production and fabrication imperfections (Lan et al., 2021). The branch angle effect of the proposed Equation 7 is in accordance with Davies and Roodbaraky (1987). Two possible methods were advocated for determining the buckling reduction factor χ : (1) using buckling curve c in EN 1993-1-1 (CEN, 2021), with a chord sidewall slenderness with an effective length factor of 0.5, and (2) a linear alternative given by:

$$\chi = 1.12 - 0.012 \frac{H}{t} \sqrt{\frac{F_y}{355}} \leq 1.0 \quad (10)$$

Despite the effort expended on achieving accurate nominal-strength models for the chord sidewall buckling limit state, in the format of Eurocode 3 (CEN, 2021), only a perfunctory reliability analysis was performed to obtain resistance expressions. Inclusion of the $(H/H_b)^{0.15}$ term in Equation 8 complicates the direct use of the AISC *Specification* Chapter E column buckling approach, so the method of Lan et al. (2021) is not considered further.

Kim and Lee (2021)

Kim and Lee (2021) performed a numerical and experimental study on rectangular HSS cross connections in which they proposed that, for full-width rectangular HSS cross connections, sidewall failure be idealized by a column model with a column width of H_b . Their proposed sidewall effective length factor, K , was variable, based on the branch and chord heights, as a value of 0.5 was found to be unconservative for high H_b/H . This variable K , with the corresponding width of the sidewall “column” based solely on H_b without any load dispersion, as shown in Equation 11, achieved better correlation with their database. The effect of branch angle was negligible; thus, it was neglected. The AISC-format connection strength equation for rectangular HSS cross-connection chord sidewall buckling under branch axial compression, with the Kim and Lee (2021) recommendations, N_{KL} , can be expressed by:

$$N_{KL} = 2F_{cr} H_b Q_f \quad (11)$$

where F_{cr} is determined by AISC *Specification* Section E3,

Steel Nominal Yield Stress	$2\gamma^*$ and 2γ Limit	l_b Limit
≤ 70 ksi (483 MPa)	50.5	$H_b/H\sin\theta > 0.25$

with:

$$K = 0.5 \sqrt{\frac{H_b}{H}} \quad (12)$$

DATABASE FOR FULL-WIDTH RECTANGULAR HSS CROSS-CONNECTION TESTS UNDER BRANCH COMPRESSION

As discussed previously, Wardenier et al. (2020) compiled an up-to-date database of recent tests, at the time, on rectangular HSS-to-HSS full-width cross connections with chord sidewall failure when subjected to branch compression [i.e., the database used by Lan et al. (2021)]. For the 51 experimental tests in that database, the source references of Fan (2017), Kuhn et al. (2019), Feldmann et al. (2016), and Pandey and Young (2020) were used. The latter two sources cover high-strength steel rectangular HSS connections with nominal yield strengths up to 139 ksi (960 Mpa)—far in excess of typical North American rectangular HSS strengths. The “numerical tests” (finite element models) included in the database were 21 by Yu (1997) and 152 by Kuhn (2018). In addition to other limits, Wardenier et al. (2020) screened their database to $2\gamma^* = H/t \leq 40$ because no data was included for high-strength steel rectangular HSS connections with larger H/t . (Also, in general, rectangular HSS sections with large $2\gamma^*$ are sensitive to geometric imperfections.)

Recently, Wei and Packer (2021) and Kim et al. (2019) each completed two further tests on rectangular HSS full-width cross connections under axial compression, beyond the Wardenier et al. (2020) database. These four tests have been added, herein, to the experimental tests in the Wardenier et al. database to produce a new, extended experimental database (of 55 tests in total). Very recently, a further 48 numerical tests were generated by Kim and Lee (2021) to investigate chord sidewall failure of rectangular HSS cross-connections in compression. These numerical tests, in addition to those of Yu (1997) and Kuhn (2018), were compiled to produce a new, extended numerical database (of 221 tests in total).

To both the extended experimental and numerical databases, screening was applied by the authors. First, all tests with a yield strength greater than 70 ksi (483 Mpa) were removed because North American rectangular HSS strengths rarely exceed this. The $2\gamma^*$ and 2γ limit was increased from the value of 40 used by Wardenier et al.

(2020) because data was available and high-yield HSS were not being considered. All tests with a bearing length less than 0.25 of the chord depth were also screened out to exclude tests failing by web (or sidewall) local yielding rather than sidewall buckling. (The limit state of sidewall local yielding is dealt with later in this paper.) Full data for the remaining 44 experimental and 183 numerical full-width rectangular HSS-to-HSS cross connections under branch axial compression from the extended database(s), which failed by chord sidewall buckling, are tabulated by Rudman (2021).

The parameter ranges for the experimental database are $\beta = 1.0$, $12.6 \leq 2\gamma \leq 42.2$, $12.6 \leq 2\gamma^* \leq 50.5$, $0.50 \leq \eta \leq 2.47$, $0.60 \leq \eta^* \leq 1.00$, $-0.87 \leq n_0 \leq 0$, $44^\circ \leq \theta \leq 90^\circ$, and $33 \text{ ksi (228 Mpa)} \leq F_y \leq 70 \text{ ksi (483 Mpa)}$. The 44 experimental rectangular HSS sections were either cold formed or hot finished; 14 have a non-90° angle, while the other 30 tests have a 90° angle. The parameter ranges for the numerical database are $\beta = 1.0$, $10 \leq 2\gamma \leq 35$, $10 \leq 2\gamma^* \leq 35$, $0.25 \leq \eta \leq 2.00$, $0.21 \leq \eta^* \leq 2.50$, $-0.80 \leq n_0 \leq 0.75$, $\theta = 90^\circ$, and $49 \text{ ksi (338 Mpa)} \leq F_y \leq 70 \text{ ksi (483 Mpa)}$. The 183 numerical rectangular HSS sections were either cold formed or hot finished. The prime limits of the screened database are shown in Table 2.

EVALUATION OF DESIGN PROPOSALS

The compiled and screened database was evaluated against the following design methods for sidewall buckling failure in rectangular HSS-to-HSS cross connections under branch axial compression:

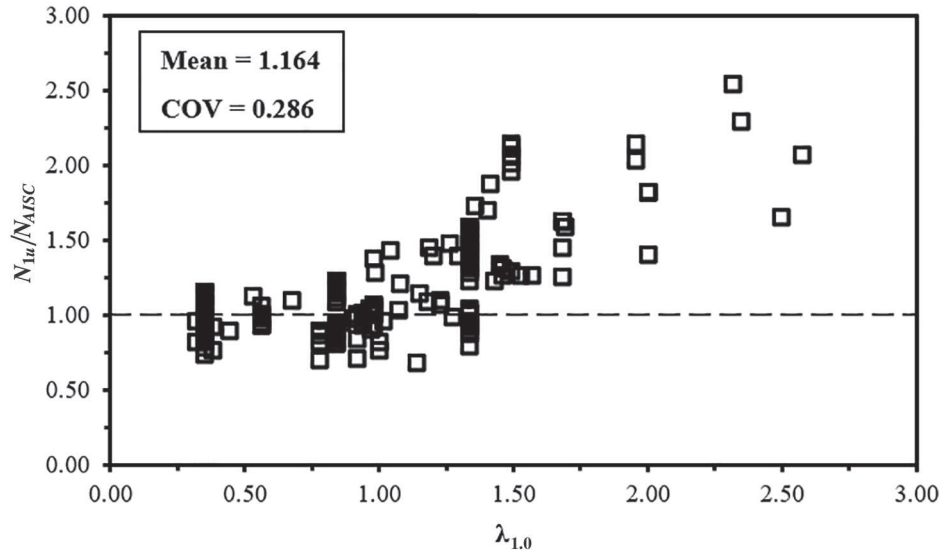
1. AISC *Specification* Chapter J, assuming Chapter E is applied for $l_b > H$, and (a) $K = 1.0$; (b) $K = 0.65$.
2. Wei and Packer (2021) proposal, assuming Chapter E is applied for $l_b > 0.25H$, and $K = 0.65$.
3. Kim and Lee (2021) recommendations.

For the combined database of 227 tests on full-width rectangular HSS-to-HSS cross-connection tests under branch axial compression, the resulting statistical evaluation of various design methods for chord sidewall buckling is shown in Figure 2. The mean and coefficient of variation (COV) of the ratios N_{1u}/N_{AISC} , N_{1u}/N_{WPP} , and N_{1u}/N_{KLL} are indicated on the plots, where N_{1u} represents the connection ultimate strength and N_{AISC} , N_{WPP} , and N_{KLL} represent nominal strength prediction models. It can be seen that all methods feature

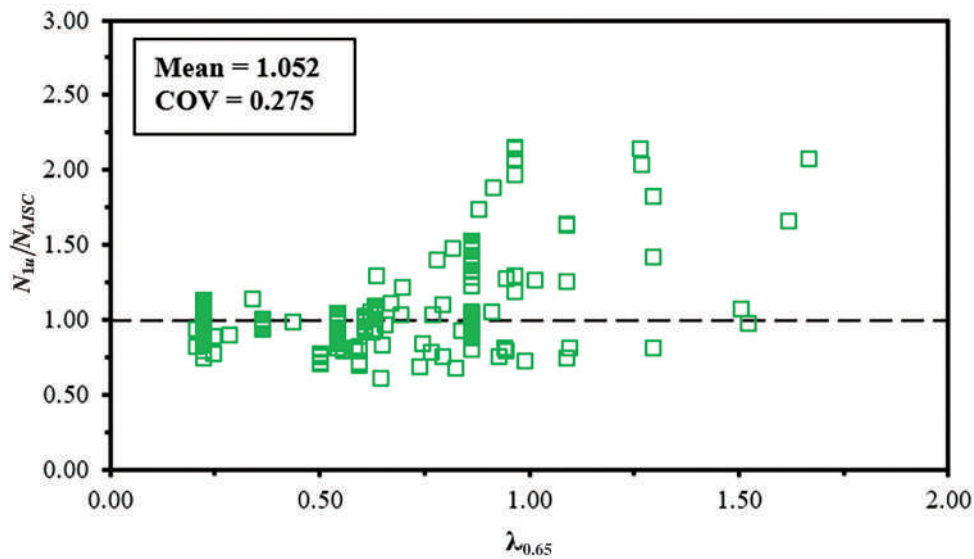
over- and underestimations of the ultimate strength. Figures 2(a) and 2(b) show correlations by applying the provisions of AISC *Specification* Chapter J to HSS and using the Chapter E column buckling approach for bearing lengths $l_b > H$. Regardless of the effective length factor used [$K = 1.0$ in Figure 2(a); $K = 0.65$ in Figure 2(b)], the COV is high, reflecting an imprecise model.

The Kim and Lee (2021) equation, Figure 2(d), consistently underpredicts the strength of connections with a low

sidewall slenderness and produces the largest mean ratio. This can be attributed to their proposed change to the width of the sidewall “column.” In low-slenderness HSS, the sidewall thickness adds a significant amount of width to the bearing length (due to load dispersion). Eliminating this width from the nominal-strength equation results in underpredicting connection strength. As the sidewall slenderness increases, the wall thickness contributes less to the width of the failure area, and the connection strength predictions



(a) 2016 AISC Specification Chapter J, Chapter E is applied for $l_b > H$, and using $K = 1.0$



(b) 2016 AISC Specification Chapter J, Chapter E is applied for $l_b > H$, and using $K = 0.65$

Fig. 2(a-b). Comparison of 227 rectangular HSS-to-HSS cross-connection test results against prediction methods.

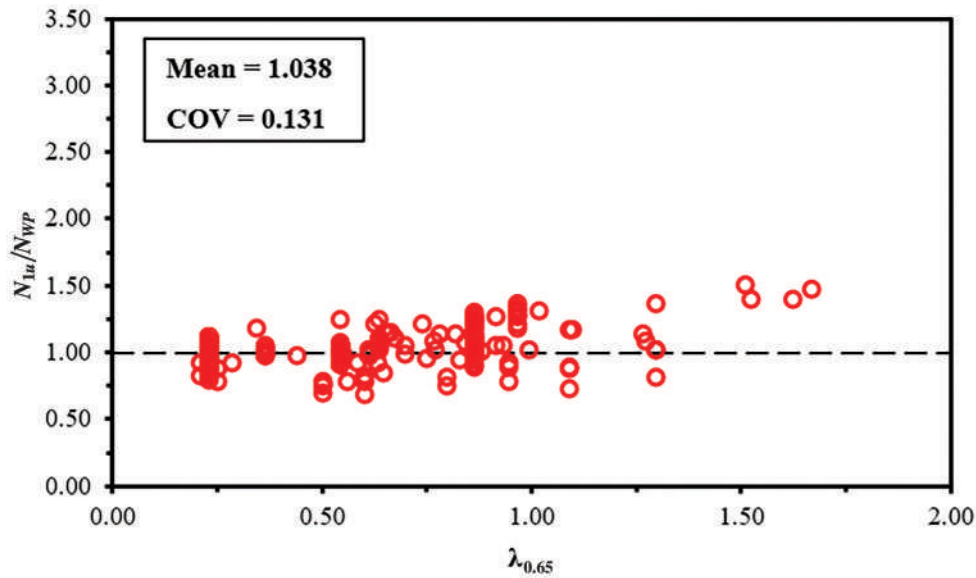
using the Kim and Lee (2021) equation become more accurate. This results in their proposed design equation producing a large COV and thus being an imprecise predictor of the connection strength.

The Wei and Packer (2021) proposed design method, Figure 2(c), produces the lowest actual-to-predicted mean ratio; however, it is still greater than 1.0. Significantly, it has a much lower COV than the other design models considered. Thus, the Wei and Packer (2021) proposal for HSS chord sidewall buckling (Table 1) is still recommended for

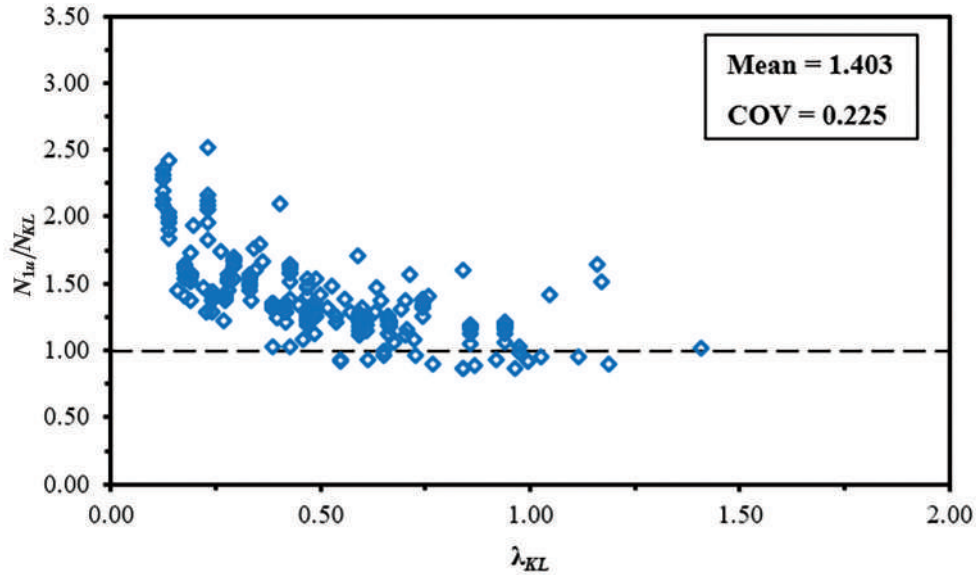
adoption. The following sections of this paper deal with determining the appropriate resistance factor, ϕ , for use with this design approach.

**STRUCTURAL RELIABILITY,
TARGET RELIABILITY INDEX,
AND RESISTANCE FACTORS**

It is well-known that engineering decisions must be made in the presence of uncertainties arising from inherent



(c) Wei and Packer (2021) proposal, Chapter E is applied for $l_b > 0.25H$, and using $K = 0.65$



(d) Kim and Lee (2021) proposal with variable K

Fig. 2(c-d). Comparison of 227 rectangular HSS-to-HSS cross-connection test results against prediction methods.

randomness in design parameters and imperfect modeling. Due to these uncertainties, potential risk arises in engineering design; therefore, safety factors are required to ensure an acceptable level of risk, and absolute reliability is an unattainable goal because of uncertainties (Ellingwood et al., 1980).

The structural reliability of a member or element is based on the limit state where the member's resistance, R , and the load effect, S , acting on the member are compared (Melchers and Beck, 2018). A failure event occurs under the following conditions, or any other equivalent criteria:

$$R - S < 0 \quad \frac{R}{S} < 1 \quad \ln(R) - \ln(S) < 0 \quad (13)$$

The randomness in the resistance of an element, R , and the load effect, S , can be accounted for by introducing dimensionless random variables. For the resistance, these random variables help account for variations in the properties of the element and the assumptions used in determining the resistance (Ravindra and Galambos, 1978). For the load effect, the random variables account for uncertainties in load intensities and structural analysis (Ravindra and Galambos, 1978). The random variable obtained by subtracting $\ln(S)$ from $\ln(R)$, is called the safety margin, g :

$$g = \ln(R) - \ln(S) = \ln(R/S) \quad (14)$$

and the probability of failure, p_F , of a structural element can thus be represented by:

$$p_F = P[g < 0] \quad (15)$$

The probability distribution of g is unknown in practice. However, if the assumption is made that R and S are independently log-normally distributed, then g is normally distributed, and a first-order probabilistic method requiring only the mean and standard deviation may be used (Ravindra and Galambos, 1978). These parameters may be summarized into a relative measure of safety, known as the safety index, β^+ , defined as follows (Ellingwood et al., 1980):

$$\beta^+ = \frac{g_m}{\sigma_g} \quad (16)$$

where g_m is the mean value of g and σ_g is the standard deviation of g . The reliability index can be conveniently interpreted as the distance from the mean to the origin, representing failure, in units of standard deviations. Substituting the expression in Equation 14 results in:

$$\beta^+ = \frac{\left[\ln\left(\frac{R}{S}\right) \right]_m}{\sigma_{\ln(R/S)}} \quad (17)$$

and Equation 17 may be approximated using first-order statistics of R and S :

$$\beta^+ \approx \frac{\ln\left(\frac{R_m}{S_m}\right)}{\sqrt{V_R^2 + V_S^2}} \quad (18)$$

where R_m and S_m are the means of the resistance and load effect and V_R and V_S are the corresponding COVs. Equation 18 includes a small-variance approximation [i.e., substitutions for $\ln(R/S)_m$ and $\sigma_{\ln(R/S)}$] that are valid when V_R and V_S are both less than about 0.30 (Ellingwood et al. 1980). If this condition is violated, β^+ can instead be determined by using Equation 19, which is exact if R and S are assumed to be independent log-normal random variables (Benjamin and Cornell (1970),

$$\beta^+ = \frac{\ln\left(\frac{R_m}{S_m} \sqrt{\frac{1+V_S^2}{1+V_R^2}}\right)}{\sqrt{\ln\left[(1+V_S^2)(1+V_R^2)\right]}} \quad (19)$$

In either case, the probability of failure, p_F , may be computed as:

$$p_F = \Phi[-\beta^+] \quad (20)$$

If R and S are instead described by independent normal distributions, a more appropriate formulation for the safety margin is:

$$g = R - S \quad (21)$$

In addition,

$$\beta^+ = \frac{R_m - S_m}{\sqrt{\sigma_R^2 + \sigma_S^2}} \quad (22)$$

and substitution of Equation 22 into Equation 20 for p_F yields an exact probability of failure.

The resistance of a structural steel member or connection, R , is often assumed to be a function of the material strength, the geometric properties, and a professional factor. The professional factor accounts for the imperfect nominal resistance design equation. Typically, these relationships are further assumed to be represented by actual-to-nominal ratios in the form:

$$R = MGPR_n \quad (23)$$

The material ratio, M , is the ratio of the actual-to-nominal relevant material property of the structural steel. The geometric ratio, G , is the ratio of the actual-to-nominal relevant geometric properties of the structural steel. The professional ratio, P , represents the ratio of observed capacity in tests (experimental or numerical) to predicted capacity,

with the latter based on measured material and geometric properties and a nominal strength model, R_n .

Similarly, the load effects on a steel member or connection can be assumed to be represented by the sum of the actual-to-nominal ratios for the applied loads and their nominal value. The load effect, S , can hence be written as:

$$S = \sum \delta_{S,i} S_{n,i} \quad (24)$$

where δ_S is the actual-to-nominal ratio for a load effect and S_n is the nominal load effect. The subscript i refers to the load effect under consideration (dead, live, etc.).

Load and resistance factor design (LRFD) and limit states design (LSD) criteria are based on an expression where the resistance of an element must be greater than the sum of the factored load effects acting on the element; that is,

$$\phi R_n \geq \sum_{i=1}^j \alpha_i S_{n,i} \quad (25)$$

The resistance side of the criterion is the product of the nominal resistance of the element, R_n , and a dimensionless resistance factor, ϕ . The load effect side of the criterion is the sum of the products between the various nominal load effects, S_n , and the associated dimensionless load factor, α_i .

Separation Factor Approach

Equation 18 can be rearranged and expressed as a first-order probabilistic design criterion with a central safety factor, θ_C (Ravindra and Galambos, 1978), which combines the uncertainties of both the resistance and load effects; that is,

$$R_m \geq \theta_C S_m \quad (26)$$

$$\theta_C = e^{(\beta^+ \sqrt{V_R^2 + V_S^2})} \quad (27)$$

Lind (1971) proposed the following linear approximation, Equation 28, to the square root of the sum of squares terms in the exponent of Equation 27, which allows for the separation of the resistance and load effect terms. In doing so, the resistance factor can be determined without knowledge of the load effects (and load factors can be determined without knowledge of the resistance). For a range of $1/3 \leq V_R/V_S \leq 3$, with $\alpha = 0.75$ (where α is the coefficient of separation), this approximation is within about 6%. Equation 29 is established through substitution of Equation 28 into Equations 27 and 26.

$$\sqrt{V_R^2 + V_S^2} = \alpha(V_R + V_S) \quad (28)$$

$$e^{(-\alpha\beta^+ V_R)} R_m \geq e^{(\alpha\beta^+ V_S)} S_m \quad (29)$$

Galambos and Ravindra (1973) extended this concept further by introducing two different separation factors, one for the load effects, and one for the resistance. They went

on to show that a value of $\alpha = 0.55$ on the resistance side of the equation gave a near-zero error and a standard deviation of 3% for a limited range of key variables. This was determined through an error minimization process considering combinations of dead, live, and wind load (Galambos and Ravindra, 1977). After the addition of random variables and linear approximations to the LRFD criterion, the resistance factor can be expressed as seen in Equation 30 (Ravindra and Galambos, 1978).

$$\phi = \frac{R_m}{R_n} e^{(-\alpha\beta^+ V_R)} \quad (30)$$

The value of β^+ was determined by selecting a standard design situation with the allowable stress design method and requiring that the LRFD criterion generally produce the same element to resist the forces. For structural elements, $\beta^+ = 3.0$, while for structural connectors, $\beta^+ = 4.5$ (Ravindra and Galambos, 1978).

Many past studies have taken R_m/R_n to simply be the ratio of observed capacity in tests (experimental or numerical) to predicted capacity, with the latter based on measured material and geometric properties and a nominal strength model. Therefore, V_R is also simply taken as the COV of the observed capacity in tests (experimental or numerical) to predicted capacity. The “separation factor approach” used throughout this study adopts this methodology, with a separation factor of $\alpha = 0.55$ in accordance with Ravindra and Galambos (1978). As noted earlier, a value of $\alpha = 0.75$ (Lind, 1971) has also been used, historically, with ACSE (2016) currently advocating for a value of $\alpha \approx 0.70$.

Expanded Separation Factor Approach

If M , G , and P are assumed to be independently log-normal, then the mean resistance, R_m , can be expressed using the ratio of mean to nominal resistance, δ_R :

$$R_m = \delta_R R_n \quad (31)$$

where

$$\delta_R = \delta_M \delta_G \delta_P \quad (32)$$

and δ_M , δ_G , and δ_P represent the mean values for M , G , and P , respectively. The COV of the resistance is well approximated by the square root of the sum of the squares of the three different COVs— V_M , V_G , and V_P —which are associated with δ_M , δ_G , and δ_P . The resistance factor equation can be seen in Equation 34.

$$V_R = \sqrt{V_M^2 + V_G^2 + V_P^2} \quad (33)$$

$$\phi = \delta_R e^{(-\alpha\beta^+ V_R)} \quad (34)$$

This approach applies to members whose resistance is a direct product of a geometric and material property. For

members, whose resistance is a product of many geometric and material properties, the contribution from each property must be determined over the range of the independent variable. The relative contribution of each of the distinct properties to the mean ratios and the related COVs can be approximated by mathematical manipulation of the resistance equation, using a partial derivative approach (Kennedy and Gad Aly, 1980). Depending on how the equation describing the property was determined, either on a solely mathematical basis or a semi-empirical or curve-fitting basis, different participation factors for the various properties will be determined (Kennedy and Gad Aly, 1980).

Effect of Material Parameters

The resistance of a structural steel column under compression loading is governed by its overall slenderness, which determines the critical buckling stress, which, in turn, depends on the radius of gyration (a geometric parameter), the yield stress, and the modulus of elasticity (material parameters). Thus, as the column slenderness varies, so does the dependency on the material parameters. Schmidt and Bartlett (2002) showed that for columns, using the overall flexural buckling equation in CSA S16 (CSA, 2019a), at low slenderness the yield strength contributes more to the material mean ratio and COV, while at high slenderness the radius of gyration and modulus of elasticity dominate. Because statistical parameters for materials are contingent on column slenderness, different resistance factors are therefore determined for various chord sidewall slenderness values. This results in a range of resistance factors (or alternatively safety indices) for rectangular HSS sidewalls under branch compression.

Lognormality of the Resistance

Equations 23 and 32 are convenient due to the log-normality assumption. When the material strength, geometric properties, and professional factor are independently log-normal, so is the resistance. A log-normal distribution can be described entirely through its mean and COV (second-order statistical parameters). If the log-normality assumption is true, then the probability of failure, or reliability index, can be determined through the mean and COVs of material strength, geometric properties, and professional factor. Reliability analysis techniques make this assumption in order to predict the probability of failure, or reliability index, using second-order statistical parameters from survey and test data. In a recent paper by Xi and Packer (2021), this assumption was assessed for the resistance.

The data for actual-to-predicted nominal strength (professional factor) that are obtained from experimental or

numerical tests are often a poor fit to normal or log-normal probability distributions. The typical data for actual-to-nominal distributions of the material and geometric properties of HSS sections are generally a reasonable fit to normal or log-normal probability distributions. When all the data is combined, the resistance distribution has a more regular shape (Xi and Packer, 2021). Xi and Packer used actual-to-nominal data of the material strength from Liu (2016) and actual-to-nominal data of the geometric properties from Kennedy and Gad Aly (1980), as well as actual-to-predicted test data from rectangular HSS-to-HSS cross connections with chord sidewall failure from Wei and Packer (2021) and Bu et al. (2021). It was shown that the combined resistance obtained by a simulation procedure closely approximated a log-normal distribution even if some of the data was seemingly incompatible (Xi and Packer, 2021). Despite having an irregular distribution for the professional factor, the expanded separation factor approach can be used for evaluating the reliability of HSS connections.

As an example of this effect, Figure 3(a) shows the actual-to-predicted ultimate strength correlation for the limit state of web buckling, using the method of Wei and Packer (2021) and the experimental data for full-width HSS cross connections from that paper. After sampling from this professional factor histogram, plus typical distributions for material and geometric properties, the numerically simulated resistance (using 1.9 million samples) is shown in Figure 3(b). The continuous curve (red line) represents the best-fit log-normal distribution using an iterative maximum likelihood estimation (MLE) technique. The statistical parameters given in Figure 3 pertain to the histograms.

Approximate FORM Approach

Nowak and Lind (1979) showed that the load side of the LRFD inequality (Equation 25) can be considered in determining the resistance factor (or, alternatively, the reliability index) by using the following equation:

$$\phi = \delta_R \frac{\sum \alpha_i S_{n,i}}{S_m} e^{\left[-\beta^+(V_R^2 + V_S^2)^{1/2}\right]} \quad (35)$$

The most accurate results for this first-order reliability method (FORM) occur when both the resistance and load side of the LRFD reliability inequality have a log-normal distribution. Of late, it has become common practice to consider the load side of the LRFD reliability inequality when determining resistance factors, and it is even stipulated by some standards such as CSA S408-11 (CSA, 2011). Considering only the basic combination of dead and live loads, Schmidt and Bartlett (2002) determined the following expressions for the reliability index and resistance factor:

$$\beta^+ = \frac{1}{\sqrt{V_R^2 + V_S^2}} \ln \left\{ \frac{\delta_R}{\phi} \left[\frac{\alpha_D + \alpha_L (L/D)}{\delta_D + \delta_L (L/D)} \right] \right\} \quad (36)$$

$$\phi = \delta_R \left[\frac{\alpha_D + \alpha_L (L/D)}{\delta_D + \delta_L (L/D)} \right] e^{(-\beta^+ \sqrt{V_R^2 + V_S^2})} \quad (37)$$

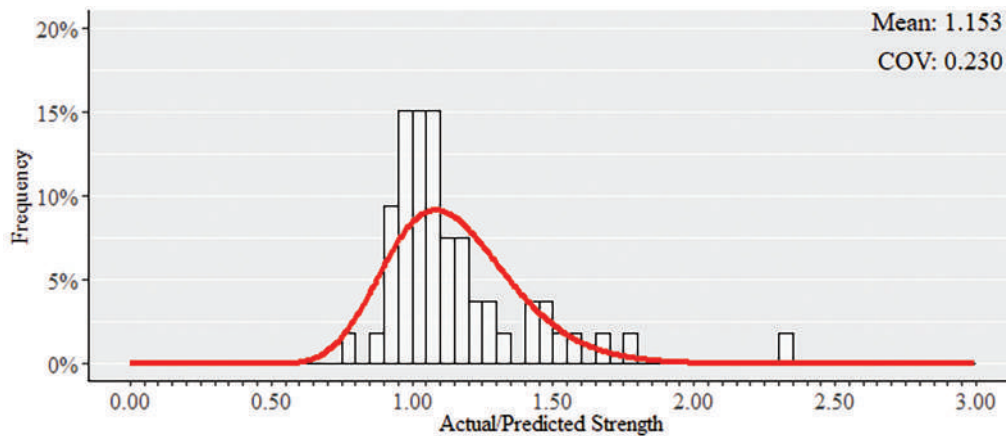
where δ_R is the mean ratio of the resistance and is comprised of three different mean ratios in accordance with the expanded separation factor approach, V_R is the COV of the resistance per the expanded separation factor approach, V_S is the COV of the load effects, α_D and α_L are the load factors for dead and live loads, δ_D and δ_L are the bias coefficients for dead and live loads, and L/D is the live-to-dead load ratio. Only the combination of dead and live loads is considered in this paper.

Schmidt and Bartlett (2002) also computed the resistance factor over a range of L/D ratios. This results in a range of

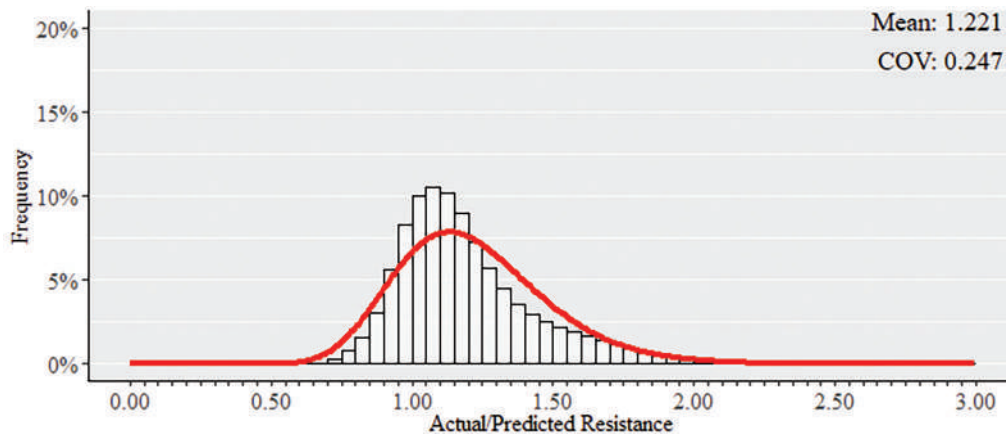
reliability indices for a particular structural steel member (or connection). The load effect was assumed to have a log-normal distribution because the L/D ratio for steel members typically exceeds 1.0, thus the log-normal live load distribution component dominates the load effect (Schmidt and Bartlett, 2002). Galambos (2006) has also used both the load side of the LRFD reliability inequality and the L/D ratio to determine resistance factors.

Reliability Method of CSA S408-11

The Canadian Standards Association provides a standard, CSA S408-11 (CSA, 2011), with guidelines for the development of limit states design standards. Annex B.2.5 of CSA S408-11 provides a so-called Approximate Method (an approximate FORM) for calculating the resistance factor to achieve target reliability values for arbitrary limit states. Annex B.2.5 cites Equation 35, which is to be used with load factors and load combinations specified in a loading standard such as NBC (2020) or ASCE (2016). Applying the



(a) Statistical correlation for professional factor only



(b) Statistical correlation for numerically simulated resistance

Fig. 3. Resistance smoothing effect produced by sampling from multiple histograms (Xi and Packer, 2021).

basic dead plus live load combination to the approximate FORM analysis, and expressing the equation as a function of the L/D ratio, gives the resistance factor in Equation 37. Annex B.2.5 of CSA S408-11 states that the COV of the load effects can be determined by Clause 14.15.2.3 of CSA S6:19 (CSA, 2019b), which is given by Equation 38 for dead plus live load.

$$V_S = \frac{\sqrt{(\delta_D V_D)^2 + [\delta_L V_L (L/D)]^2}}{\delta_D + \delta_L (L/D)} \quad (38)$$

Reliability Method of AISI S100-16

Chapter K of American Iron and Steel Institute S100-16 (AISI, 2016) provides a method to determine the resistance factor of a cold-formed structural steel resistance equation by direct testing. This method uses the LRFD criterion to determine the resistance factor but simplifies the load side to a single load combination ($1.2D + 1.6L$) and $L/D = 5$ (Meimand and Schafer, 2014). The resistance factor given by AISI S100, Section K2.1.1 (AISI, 2016) is in an “expanded separation factor” form:

$$\phi = C_\phi (\delta_M \delta_G \delta_P) e^{-\beta^+ \sqrt{V_M^2 + V_G^2 + C_P V_P^2 + V_S^2}} \quad (39)$$

where C_ϕ is a calibration coefficient and C_P is a correction factor for sample size. For the material factor and the fabrication factor, the means (δ_M and δ_G , respectively) are to be determined from statistical analysis but are not to be greater than the values given in Table K2.1.1-1, while the COVs (V_M and V_G , respectively) are not to be less than the values given in Table K2.1.1-1 (AISI, 2016). The calibration coefficient, target safety index, and COV for the load effects are predetermined factors based on LRFD criteria, with the mean value of the professional factor given by:

$$\delta_P = \frac{\sum_{i=1}^{n_t} \frac{R_{t,i}}{R_{n,i}}}{n_t} \quad (40)$$

where n_t is the number of tests, R_t is the tested strength, and R_n is the nominal strength by a rational engineering analysis. The subscript i denotes an individual test within a series of tests. The correction factor for sample size is given by:

$$C_P = \frac{\left(1 + \frac{1}{n_t}\right)m}{m-2} \quad (41)$$

where m is the number of degrees of freedom ($m = n_t - 1$). The COV for the test results is given by:

$$V_P = \frac{\sigma_P}{\delta_P} \quad (42)$$

where σ_P is the standard deviation of the ratio of actual-to-nominal strengths.

Monte Carlo Simulation Approach

As yet another alternative to the previous approaches, Monte Carlo techniques can be used to randomly sample from the various resistance and load effect parameter distributions to determine a possible resistance and load effect scenario for a member or connection. This process closely approximates the probabilistic behavior of the resistance and load effect for the desired design scenario with a large number of samples. This sampling technique is known as a Monte Carlo simulation (MCS). Kennedy and Baker (1984), Lundberg and Galambos (1996), Hong and Zhou (1999), and others have undertaken such MCSs. MCS is also advocated as a reliability analysis method in some codes and standards (e.g., CSA S408-11).

RESISTANCE FACTOR EVALUATION FOR WEI AND PACKER (2021)

In this study, statistical parameters were taken as $\delta_D = 1.05$ and $V_D = 0.10$ for the dead load effect and as $\delta_L = 0.78$ and $V_L = 0.32$ for the live load effect (Schmidt and Bartlett, 2002). Dead loads can be more accurately predicted than live loads, and for comparison, values of $\delta_D = 1.0$ and $V_D = 0.08$ were used in a previous reliability study of tubular connections in offshore structures (Packer and Kremer, 1988). Values of $\alpha_D = 1.20$ and $\alpha_L = 1.60$ were used, per ASCE/SEI 7-16 (ASCE, 2016), and material statistical parameters of $\delta_M = 1.178$ and $V_M = 0.086$ per Xi and Packer (2021). These material parameters are based on a survey done by Liu (2016) on variations in yield stress of A500 (ASTM, 2021) dual-certified Grade B/C rectangular HSS. The geometric statistical parameters, $\delta_G = 0.975$ and $V_G = 0.025$, were adopted from a survey by Kennedy and Gad Aly (1980), but the proposed design method depends on multiple rectangular HSS geometric properties, such as chord thickness and height. The geometric statistical parameters taken in this study are the lowest mean ratio and the highest COV, from all the contributing properties, to be conservative. The target safety index, β^+ , for the ductile connections under consideration was assigned to be 3.0, which is in accord with the Commentary to 2016 AISC *Specification* Section B3.1. A target safety index of 3.0 is now a commonly accepted level of safety for public buildings, corresponding to a notional probability of structural failure of 1.35×10^{-3} (Packer and Kremer, 1988).

For the AISI S100-16 reliability method, the material and geometric statistical parameters were compared with the requirements in Chapter K of that specification. The only statistical parameter that was in accordance with the requirements was the geometric ratio (mean). The other statistical

parameters were hence taken from Table K2.1.1-1. The calibration coefficient and COV for the load effect were taken as $C_\phi = 1.52$ and $V_S = 0.21$, respectively, due to use of the LRFD format (AISI, 2016). The target reliability index, β^+ , was assigned to be 2.5 because the connection resistance is dependent on the HSS members and the use of the LRFD equation (AISI, 2016).

The professional factor statistical parameters used for the Wei and Packer (2021) proposed approach for the chord sidewall compression buckling limit state are taken from the results of the combined database: $\delta_P = 1.038$ and $V_P = 0.131$ [see Figure 2(b)]. (The professional factors from the experimental and numerical databases, separately, are similar to the combined values.)

SIDEWALL COMPRESSION BUCKLING

Closed-Form Solutions

The resistance factor for chord sidewall compression buckling can be determined by the various closed-form methods. Two different sets of material statistical parameters can be used to determine the resistance factors: (1) parameters based only on the yield stress and (2) parameters that depend on the chord sidewall slenderness.

Based on Chord Yield Stress

Using the previously noted material statistical parameters for yield stress, the resistance factor is 0.836 for the separation factor approach and 0.917 for the expanded separation factor approach. The resistance factors over a range

of L/D ratios, using the approximate FORM analysis in CSA S408-11, can be seen in Figure 4, wherein the dip at a L/D ratio of about 0.2 is due to the intersection of the two factored load combinations from ASCE/SEI 7 (ASCE, 2016): $1.4D$ (dead load only) and $1.2D + 1.6L$. By equating these two loading situations with mean loads, one obtains $(L/D) = 0.168$. The resistance factor using the AISI S100-16 approach is 0.857.

Based on Chord Sidewall Slenderness

A mathematical manipulation of the equations describing the critical yield stress for columns in axial compression was performed to determine the relative contribution of each distinct property to the material statistical parameters. The material statistical parameters depend on the yield stress, radius of gyration (which in turn depends on the thickness), and modulus of elasticity. The statistical parameters were taken as $\delta_r = 0.975$ and $V_r = 0.025$ for radius of gyration and $\delta_E = 1.000$ and $V_E = 0.019$ for modulus of elasticity, from Kennedy and Gad Aly (1980). Although δ_M and V_M can be shown to vary with the chord sidewall slenderness, material statistical parameters at the average chord sidewall slenderness of the combined database were chosen to determine the resistance factors for the various methods. The average slenderness of the database is 0.619, which results in $\delta_M = 1.134$ and $V_M = 0.070$.

For the separation factor approach, these material statistical parameters do not change the resistance factor determined previously because the separation factor approach (as used herein) is based on only the professional factor parameters. The expanded separation factor approach, on

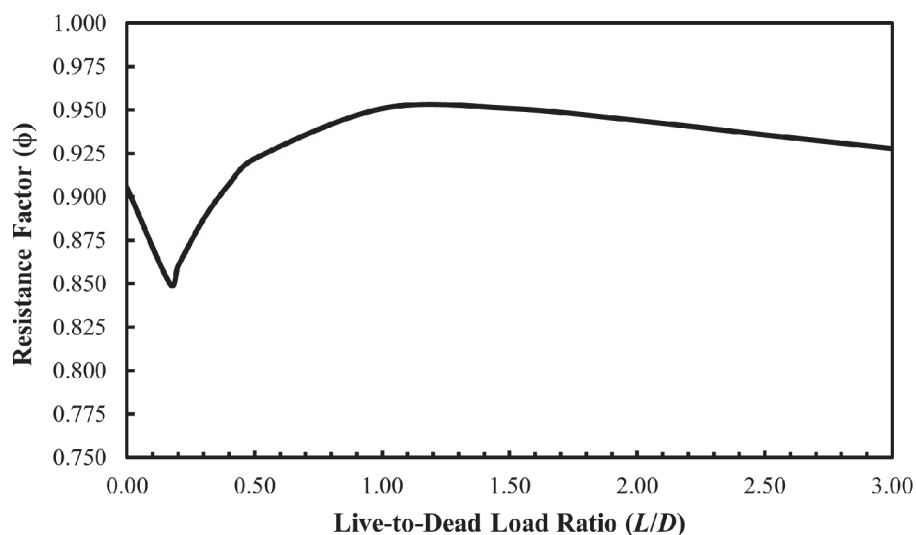


Fig. 4. Resistance factor for the Wei and Packer (2021) proposed buckling method, using the approximate FORM analysis in CSA S408-11, with material statistical parameters based on yield stress.

the other hand, produces a resistance factor of 0.894 (compared to 0.917 previously). For the approximate FORM analysis in CSA S408-11, the resistance factors over a range of L/D values are shown in Figure 5 and these can be seen to be lower than those in Figure 4, and for the AISI S100-16 reliability method, statistical parameters based on chord sidewall slenderness do not meet the material requirements of Chapter K; thus, the resistance factor is retained as the one determined with just the yield stress (0.857).

Participating Variables for MCS

As can be seen in Table 1, the participating random variables in the Wei and Packer (2021) method for sidewall

compression buckling resistance are the material strength (yield stress), modulus of elasticity, chord thickness, chord height, branch height, and the professional factor.

Material strength variations for ASTM A500 dual-certified Grade B/C rectangular HSS compiled by Liu (2016) were used (Figure 6), from which the raw data ($n_i = 3018$) was obtained. The continuous curve (red line) in Figure 6, and subsequent histograms for variables, represents the best-fit log-normal distribution using the aforementioned iterative MLE technique. Statistical parameters given in the figures pertain to the histograms.

For modulus of elasticity, the variation determined by Galambos and Ravindra (1978) was used. A log-normal distribution was created (on the basis of its limitation to

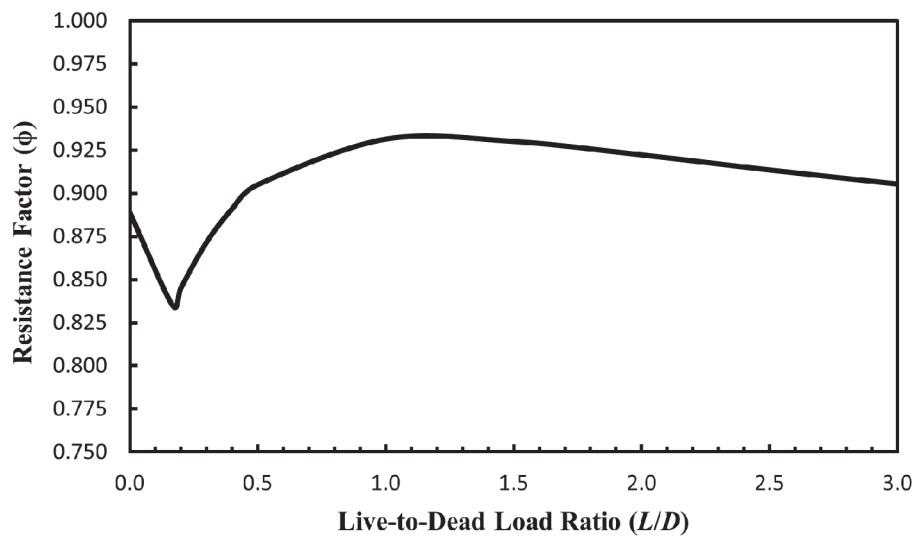


Fig. 5. Resistance factor for the Wei and Packer (2021) proposed buckling method, using the approximate FORM analysis in CSA S408-11, with material statistical parameters based on chord sidewall slenderness.

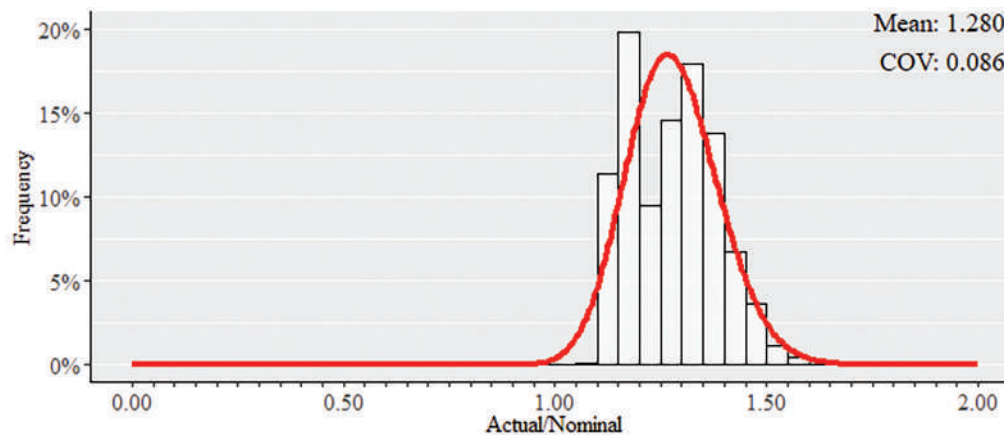


Fig. 6. ASTM A500 dual-certified Grade B/C rectangular HSS yield stress variation (Liu, 2016).

Table 3. Representative Connections for Monte Carlo Simulation

Connection Number	Chord Member $H \times B \times t$	Branch Member $H_b \times B_b \times t_b$	H (in.)	t (in.)	H_b (in.)	θ (°)	$H_b/H\sin\theta$	H/t
1	6×6× $\frac{3}{8}$	3×6× $\frac{3}{8}$	6.00	0.349	3.00	90	0.50	17.2
2	6×6× $\frac{3}{8}$	6×6× $\frac{3}{8}$	6.00	0.349	6.00	90	1.00	17.2
3	6×6× $\frac{3}{8}$	12×6× $\frac{3}{8}$	6.00	0.349	12.0	90	2.00	17.2
4	6×6× $\frac{3}{8}$	12×6× $\frac{3}{8}$	6.00	0.349	12.0	60	2.31	17.2
5	6×6× $\frac{3}{8}$	12×6× $\frac{3}{8}$	6.00	0.349	12.0	45	2.83	17.2
6	8×8× $\frac{3}{8}$	4×8× $\frac{3}{8}$	8.00	0.349	4.00	90	0.50	22.9
7	8×8× $\frac{3}{8}$	8×8× $\frac{3}{8}$	8.00	0.349	8.00	90	1.00	22.9
8	8×8× $\frac{3}{8}$	12×8× $\frac{3}{8}$	8.00	0.349	12.0	90	1.50	22.9
9	8×8× $\frac{3}{8}$	8×8× $\frac{3}{8}$	8.00	0.349	8.00	60	1.16	22.9
10	8×8× $\frac{3}{8}$	8×8× $\frac{3}{8}$	8.00	0.349	8.00	45	1.41	22.9
11	12×12× $\frac{3}{8}$	12×4× $\frac{3}{8}$	12.0	0.349	4.00	90	0.33	34.4
12	12×12× $\frac{3}{8}$	12×6× $\frac{3}{8}$	12.0	0.349	6.00	90	0.50	34.4
13	12×12× $\frac{3}{8}$	12×8× $\frac{3}{8}$	12.0	0.349	8.00	90	0.67	34.4
14	12×12× $\frac{3}{8}$	12×12× $\frac{3}{8}$	12.0	0.349	12.0	90	1.00	34.4
15	12×12× $\frac{3}{8}$	12×12× $\frac{3}{8}$	12.0	0.349	12.0	60	1.16	34.4
16	12×12× $\frac{3}{8}$	12×12× $\frac{3}{8}$	12.0	0.349	12.0	45	1.41	34.4
17	16×16× $\frac{3}{8}$	16×8× $\frac{3}{8}$	16.0	0.349	8.00	90	0.50	45.8
18	16×16× $\frac{3}{8}$	16×12× $\frac{3}{8}$	16.0	0.349	12.0	90	0.67	45.8
19	16×16× $\frac{3}{8}$	16×16× $\frac{3}{8}$	16.0	0.349	16.0	90	1.00	45.8

a non-negative value) from the statistical parameters in Galambos and Ravindra (1978). Samples were then taken from this log-normal distribution.

Geometric variations were determined through the surveys of Kennedy and Gad Aly (1980). The raw data for the rectangular HSS thickness ($n_t = 302$) and height ($n_t = 149$) surveys could not be obtained, so sampling was performed directly from the histograms. The sampling procedure followed was to select a histogram bin with probability proportional to its reported frequency, then to simulate a value uniformly within the limits of the bin (Xi and Packer, 2021). Figures 7 and 8 show the geometric variations used.

Professional factor variations were obtained from the combined database compiled herein by comparing the actual connection strength with the nominal strength predicted by Wei and Packer (2021). Sampling was thus performed from the histogram in Figure 9. Professional factors were not binned into various combinations (by branch angle, chord sidewall slenderness, and bearing length) as the number of tests within each bin would, in that case, be too minimal.

For the load effect, variations in dead load generally resemble a normal distribution (Ellingwood et al., 1980),

whereas variations in live load can generally be described by a Gumbel distribution (Ellingwood and Culver, 1977). Herein, an equivalent log-normal distribution for the variations of dead load was created, per Ellingwood et al., based on the statistical parameters for normal distribution given in Schmidt and Bartlett (2002). For the live load, an equivalent log-normal distribution, as derived by Schmidt and Bartlett, has been used. Samples were then taken from these distributions.

MCS Method

A representative set of 19 full-width ($\beta = 1.0$) connections, listed in Table 3, was formulated for rectangular HSS-to-HSS axially loaded cross connections, covering the parametric range of $17.2 \leq 2\gamma^* \leq 45.8$, $0.33 \leq H_b/H\sin\theta \leq 2.83$, and $45^\circ \leq \theta \leq 90^\circ$. A nominal yield stress, F_y , of 50 ksi (345 MPa) was used. A reliability index was determined using Equation 16 for each one of the representative connections, using a given resistance factor and a particular L/D ratio, by sampling 1 million times from the participating variable distributions. Details of the sampling method, using MATLAB, can be found in Rudman (2021). This

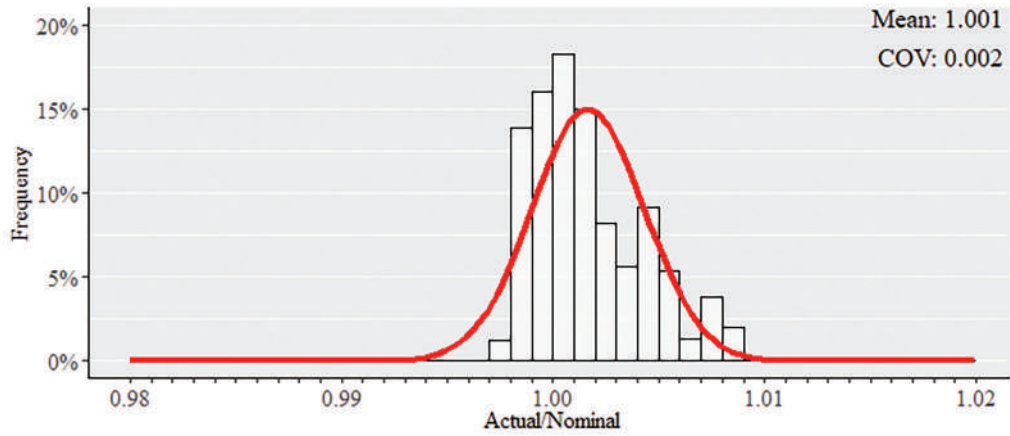


Fig. 7. Rectangular HSS depth and width variation data by Kennedy and Gad Aly (1980).

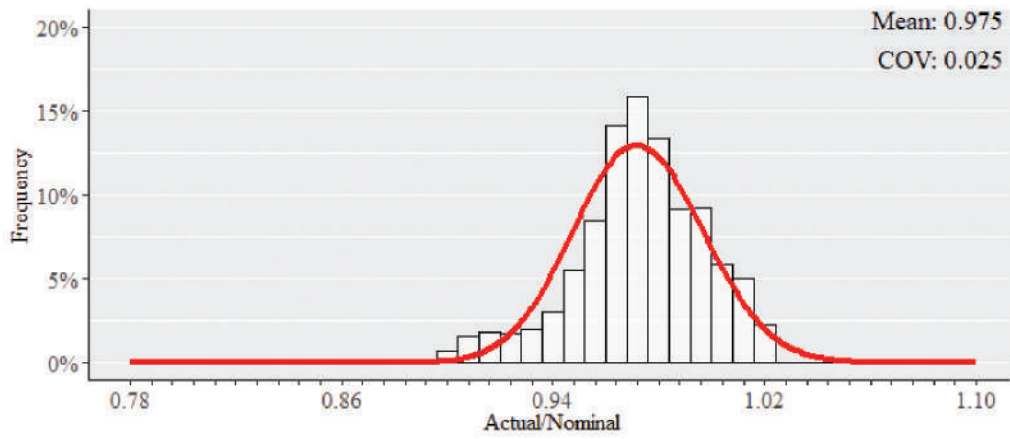


Fig. 8. Rectangular HSS thickness variation data by Kennedy and Gad Aly (1980).

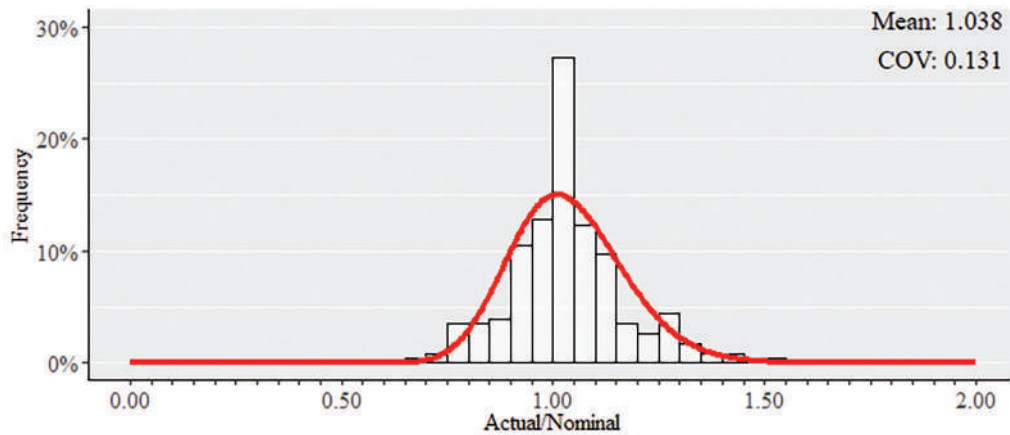


Fig. 9. Professional factors using the Wei and Packer (2021) proposed buckling method.

procedure was then repeated for a range of L/D ratios from 0 to 3.0; for resistance factors of 0.8, 0.85 and 0.90; and for each representative connection. For all simulations, the overall load effect distribution is approximately log-normal, and similarly, the resistance distribution is approximately log-normal, despite deviations from log-normality in the material survey and professional factor data, as shown previously. Thus, Equation 16, where the resistance and load effect distributions are both log-normal, can be used. Figures 10 and 11 display typical resistance and load effect distributions, respectively, determined for the set of representative connections.

MCS Results

A reliability index at each L/D ratio and resistance factor was determined by taking the average reliability index from each of the 19 connections. Figure 12 shows that $\phi = 0.90$ achieves suitable results as the reliability index is greater

than 3.0 for the majority of the L/D ratios investigated and does not fall below 2.6 for any L/D ratio, which is the minimum that is currently expected (Commentary to 2016 AISC Specification Section B3.1).

The 19 representative connections cover the key variables in rectangular HSS-to-HSS cross connections. To investigate the chord sidewall slenderness effect, the average reliability index at each L/D ratio was determined for connections with the same chord sidewall slenderness (17.2, 22.9, 34.4, and 45.8, in the set of representative connections). Figure 13 shows that the reliability index decreases by about 0.1 when the chord sidewall slenderness is high (45.8). This is an expected result and is a reason the upper limits of validity have been set on chord sidewall slenderness in rectangular HSS cross connections. To investigate the bearing length effect, the average reliability index at each L/D ratio was determined for the connections in three categories: bearing length ratio ($H_b/H\sin\theta$) less than 1.0,

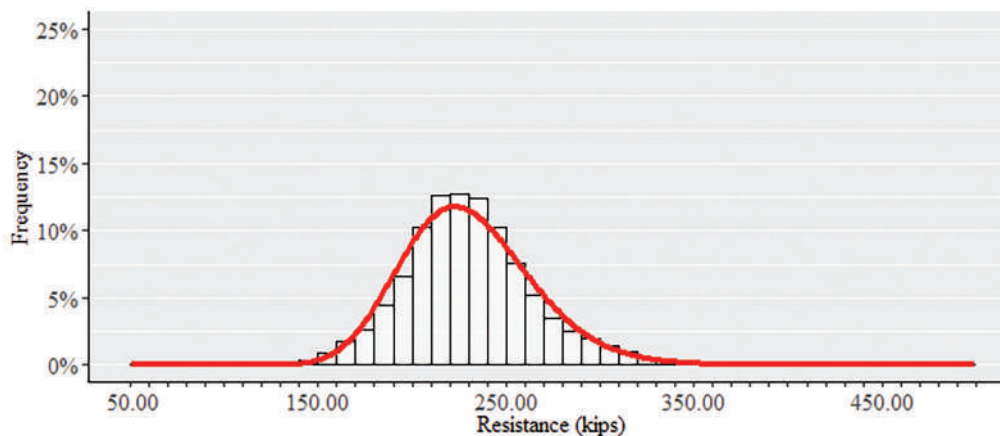


Fig. 10. Resistance for Connection 6, with $L/D = 1.0$ and $\phi = 0.90$.

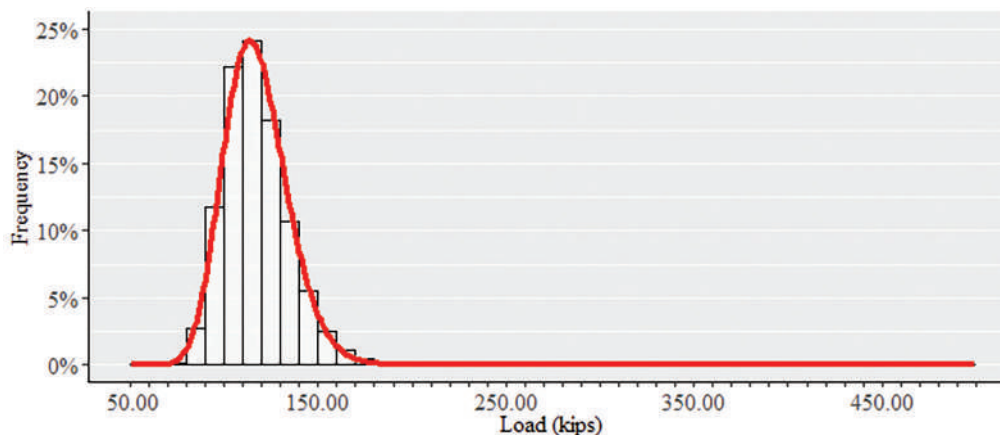


Fig. 11. Load effect for Connection 6, with $L/D = 1.0$ and $\phi = 0.90$.

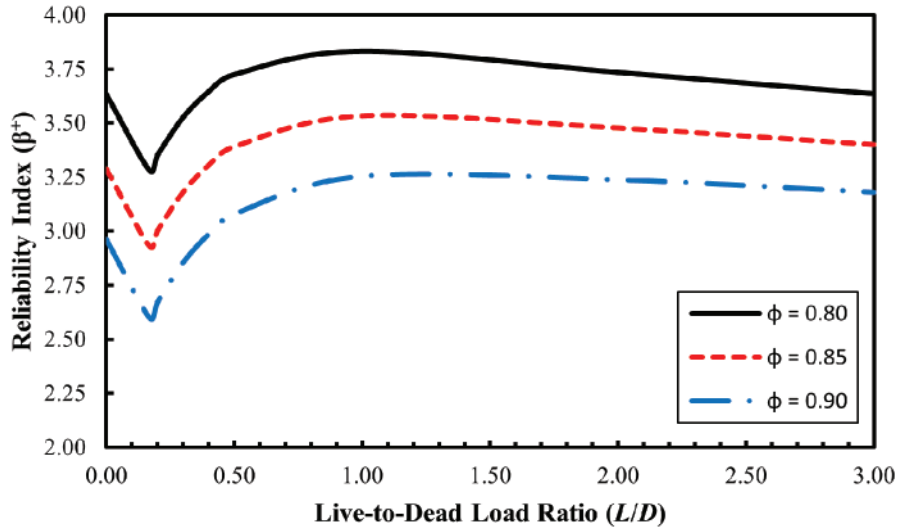


Fig. 12. Reliability index vs. L/D ratio for the Wei and Packer (2021) proposed buckling method, using a MCS with various ϕ factors.

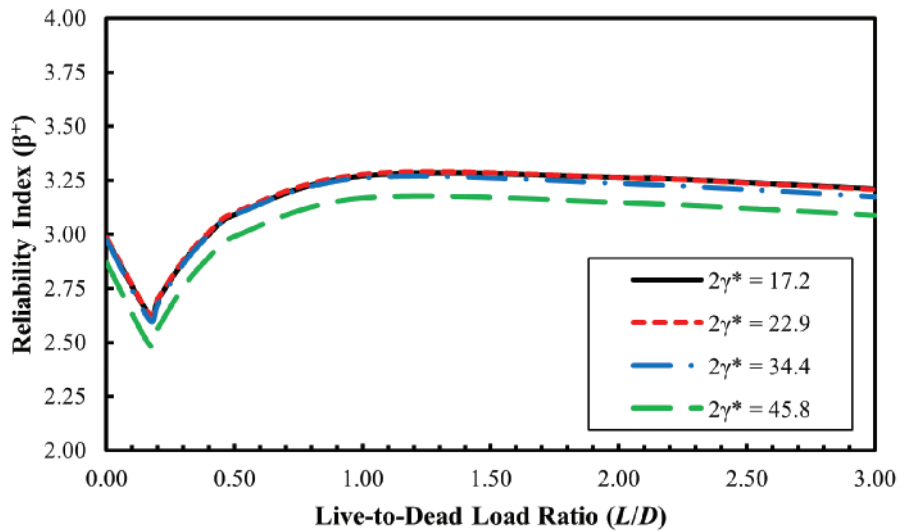


Fig. 13. Effect of chord sidewall slenderness on reliability index, for the Wei and Packer (2021) proposed buckling method, by MCS with $\phi = 0.90$.

bearing length ratio between 1.0 and 2.0, and bearing length ratio greater than 2.0. Figure 14 illustrates that the bearing length effect is captured well by the proposed method.

SUMMARY

The closed-formed solution methods produce a resistance factor based on an input target reliability index, whereas the MCS method used herein produces a reliability index given a resistance factor. In order to compare the various reliability methods, the closed-formed solutions were manipulated to input a resistance factor and output a reliability index. The AISI S100-16 method is henceforth discounted due to its set target reliability of 2.5; the target reliability index for all other closed-form methods and the MCS method is 3.0. The separation factor approach and the expanded separation factor approach are independent of the L/D ratio; therefore, the reliability index for these methods applies to all L/D ratios. Figures 15 and 16 compare each of the methods, using $\phi = 0.90$.

The closed-form equations using the material statistical parameters adjusted for slenderness produce more conservative estimates of the reliability index compared to the yield stress material statistical parameters. This is expected as the mean-to-nominal ratio of the material statistical parameters adjusted for slenderness is lower.

MCS is a numerical method and is the most accurate reliability analysis. Using the yield stress parameters, the approximate FORM analysis in CSA S408-11 produces reliability index values that are within 0.10 of the MCS for all L/D ratios (Figure 15). Using the parameters adjusted for slenderness, the approximate FORM analysis in CSA S408-11 produces statistically indistinguishable reliability index values for $L/D \leq 0.50$, and values within 0.25 of the MCS (but on the conservative side) for $L/D > 0.50$ (Figure 16).

The expanded separation factor approach generates an unconservative reliability index value for $L/D \leq 0.50$, no matter which set of material statistical parameters are used. For $L/D > 0.50$, the yield stress parameters produce a surprisingly accurate reliability index value that is within 0.05 of the MCS values, while the parameters adjusted for slenderness produce a conservative reliability index value by about 0.30. The closed-form equations using the material statistical parameters of the yield stress create more accurate predictions of the reliability index (measured against MCS) than the case of material parameters adjusted for slenderness. All further comparisons are therefore based on the closed-form equations using yield stress material statistical parameters.

The separation factor approach produces extremely conservative predictions of the reliability index. This is expected since it only accounts for the professional factor.

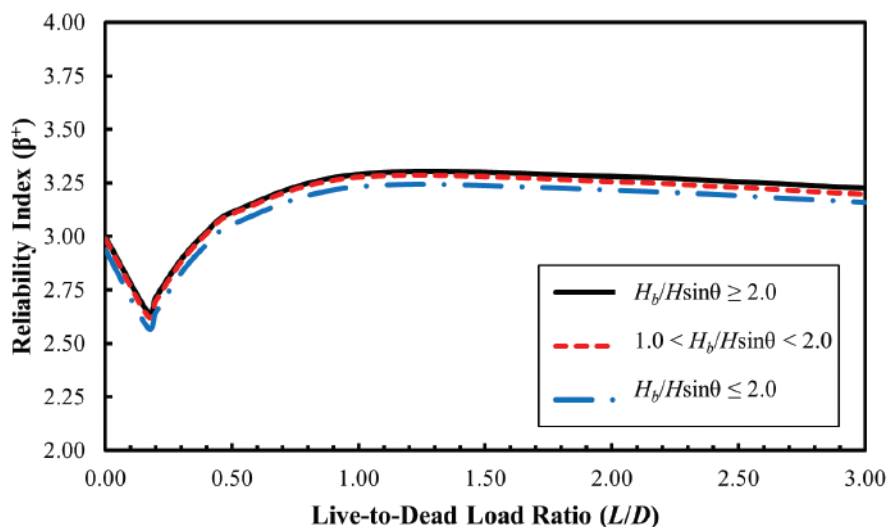


Fig. 14. Effect of bearing length on reliability index, for the Wei and Packer (2021) proposed buckling method, by MCS with $\phi = 0.90$.

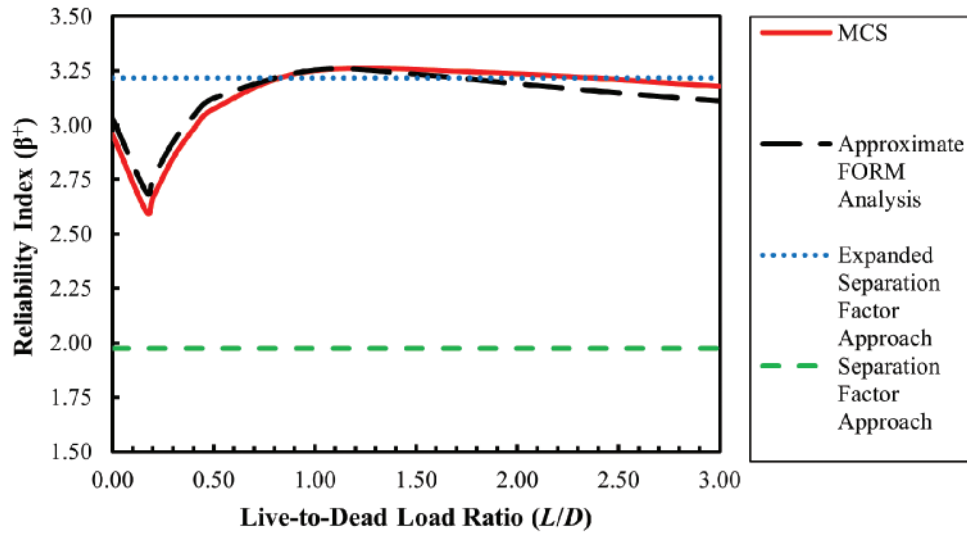


Fig. 15. Reliability index vs. L/D ratio for the Wei and Packer (2021) proposed buckling method, using closed-form solutions and MCS, with yield stress material statistical parameters.

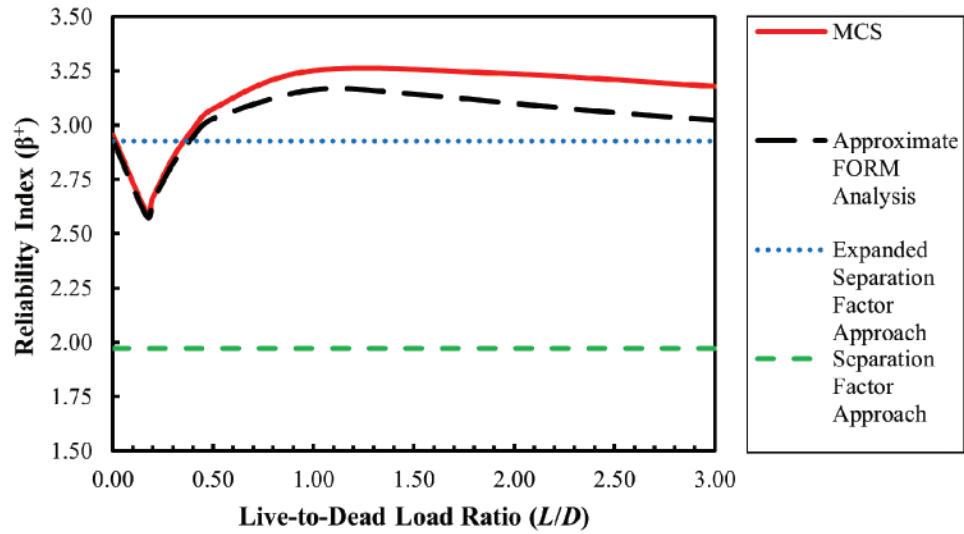


Fig. 16. Reliability index vs. L/D ratio for the Wei and Packer (2021) proposed buckling method, using closed-form solutions and MCS, with material statistical parameters adjusted for chord slenderness.

The expanded separation factor approach method produces much better predictions of the reliability index than the separation factor approach because it accounts for the material, geometric, and strength properties, as well as the professional factor. The material strength property (F_y) actual-to-nominal ratio usually has a mean (bias) much greater than 1.0 for HSS, and this is the main contributing factor in generating higher predictions for the reliability index. The expanded separation factor approach can still produce unconservative results for $L/D < 1.0$. For steel buildings, however, typical design L/D ratios exceed 1.0, and the expanded separation factor approach provides accurate predictions in this L/D range due to the uncertainties in live loading.

The approximate FORM analysis from CSA S408-11 thus appears ideal for determining the reliability index of HSS connections. This method illustrates the dependency of the reliability index on the L/D ratio and generates results that are very similar to MCS, yet requires much less time and effort to complete. From the preceding analysis, it can be concluded that, for the Wei and Packer (2021) proposed buckling method, $\phi = 0.90$ is appropriate. With this resistance factor, the reliability index is greater than 3.0 for the majority of the L/D ratios assessed and does not fall below 2.6 for any L/D ratio—the minimum currently expected (Commentary to the 2016 AISC *Specification* Section B3.1).

SIDEWALL LOCAL YIELDING

The approximate FORM analysis from CSA S408-11 was also used to evaluate Equation 1 (Table 1) for the sidewall

local yielding limit state by using the existing database from Wei and Packer (2021). The resulting professional factor statistical parameters for Equation 1, in conjunction with this database, are $\delta_P = 1.193$ and $V_P = 0.150$ (Xi and Packer, 2021). Figure 17 shows the reliability index determined for the range of L/D ratios with $\phi = 1.0$. The reliability index is greater than 3.0 for most L/D ratios assessed and does not fall below 2.6 for any L/D ratio, thus supporting the choice of $\phi = 1.0$ for the Wei and Packer (2021) proposed local yielding design equation.

CONCLUSION

Several alternative methods for predicting the nominal strength of HSS webs under local compression loading are evaluated using a large contemporary database of experimental and numerical results totaling 227 tests. For rectangular HSS-to-HSS full-width cross connections under branch axial compression, it is found that the proposal of Wei and Packer (2021) accurately predicts the connection strength, without the further modifications suggested by Kim and Lee (2021). It is thus recommended that the Wei and Packer (2021) proposed approach for chord sidewall compression on rectangular HSS-to-HSS axially loaded cross connections (given in Table 1) be adopted. Monte Carlo simulation shows that the reliability index decreases for connections with a high chord sidewall slenderness; it is therefore recommended that the limit on chord sidewall slenderness be $H/t \leq 35$. Three key points for the Commentary to the AISC *Specification*, to facilitate the application of Chapter J to rectangular HSS sidewall compression, are:

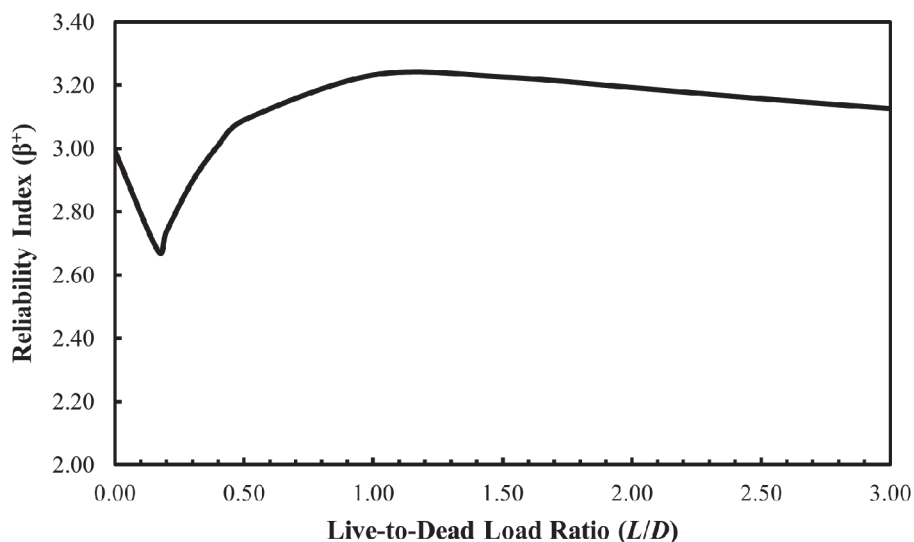


Fig. 17. Reliability index vs. L/D ratio for Wei and Packer (2021) proposed local yielding equation, using the approximate FORM analysis in CSA S408-11.

1. An effective length factor of $K = 0.65$ is recommended because it represents the fixed-fixed end condition for the chord sidewalls, in welded connections.
2. The F_{cr} equation (column buckling method) should be used for a bearing length greater than 0.25 of the chord depth.
3. The branch angle of inclination should not be considered because assuming only vertical force components is conservative, pragmatic, and simple.

A reliability analysis was performed for the Wei and Packer (2021) proposed web compression buckling method. This was assessed using various closed-form methods as well as a Monte Carlo simulation. Comparing all the reliability methods, an approximate FORM analysis given in CSA S408-11 produced excellent results, comparable to Monte Carlo simulation. The approximate FORM analysis generates a reliability index for any desired live-to-dead load ratio, avoids the complexity of Monte Carlo simulation, and is recommended. The review and application of contemporary reliability methods herein is instructive for other researchers determining resistance factors.

For the Wei and Packer (2021) proposed method for the web compression buckling limit state, a resistance factor of $\phi = 0.90$ is recommended, which is also the same value used for compression members in the AISC *Specification* Section E1. This resistance factor is included in Table 1 to determine available connection strength. The approximate FORM analysis in CSA S408-11 was also applied to evaluate the Wei and Packer (2021) proposed method for the web local yielding limit state, and a resistance factor of $\phi = 1.00$ is recommended. This is also the same value as used for this limit state in the AISC *Specification* Section J10.2, and this resistance factor is given for Equation 1 in Table 1.

ACKNOWLEDGMENTS

Financial support for this project was provided by MITACS and NSERC (Natural Sciences and Engineering Research Council of Canada). Appreciation is extended to Professor Judy Liu (Oregon State University) for provision of data.

SYMBOLS

A_g	Cross-sectional area of element, in. ²
B	Width of rectangular HSS chord member, perpendicular to the plane of the connection, in.
B_b	Width of rectangular HSS branch member, perpendicular to the plane of the connection, in.
C_f	Material factor

C_p	Correction factor for sample size
C_ϕ	Calibration coefficient
D	Dead load, kips
E	Modulus of elasticity of HSS member, ksi
F_{cr}	Critical buckling stress of HSS chord member, ksi
F_k	Chord sidewall failure stress, including a reduction for application to design, ksi
F_y	Yield stress of HSS chord member, ksi
G	Ratio of actual-to-nominal geometric property
H	Height of rectangular HSS chord member, parallel to the plane of the connection, in.
H_b	Height of rectangular HSS branch member, parallel to the plane of the connection, in.
K	Effective length factor
L	Live load, kips; length of member, in.
L_c	Effective length of the member = KL , in.
M	Ratio of actual-to-nominal material property
N_{1u}	Axial ultimate strength of a connection for a test (or numerical calculation), expressed as a force in the branch, kips
N_{AISC}	Axial ultimate strength of a connection, per the AISC <i>Specification</i> , expressed as a force in the branch, kips
N_{KL}	Axial ultimate strength of a connection, per Kim and Lee (2021), expressed as a force in the branch, kips
N_L	Axial ultimate strength of a connection, per Lan et al. (2021), expressed as a force in the branch, kips
N_{WP}	Axial ultimate strength of a connection, per Wei and Packer (2021), expressed as a force in the branch, kips
P	Professional factor = ratio of observed capacity in tests (experimental or numerical) to predicted capacity
P_n	Connection nominal strength, kips
Q_f	Chord-stress interaction parameter
R	Resistance, kips
R_m	Mean resistance, kips
R_n	Nominal resistance, kips
R_t	Tested resistance/strength, kips
S	Load effect, kips
S_m	Mean load effect, kips

S_n	Nominal load effect, kips	β	Ratio of branch width to chord width (B_b/B), perpendicular to the plane of the connection
V_D	Coefficient of variation for dead load	β^+	Reliability or safety index
V_E	Coefficient of variation for modulus of elasticity	2γ	Ratio of chord width to wall thickness for rectangular HSS (B/t)
V_G	Coefficient of variation for relevant geometric properties	$2\gamma^*$	Ratio of chord height to wall thickness for rectangular HSS (H/t)
V_L	Coefficient of variation for live load	δ_D	Ratio of mean to nominal for dead load
V_M	Coefficient of variation for relevant material properties	δ_E	Ratio of mean to nominal for modulus of elasticity
V_P	Coefficient of variation associated with δ_P	δ_G	Mean value of G
V_R	Coefficient of variation for resistance	δ_L	Ratio of mean to nominal for live load
V_r	Coefficient of variation for radius of gyration	δ_M	Mean value of M
V_S	Coefficient of variation for load effect	δ_P	Mean value of P
g	Safety margin	δ_R	Ratio of mean to nominal for resistance
g_m	Mean of the safety margin	δ_r	Ratio of mean to nominal for radius of gyration
i	Subscript that denotes the load effect under consideration (dead, live, etc.); subscript that denotes an individual test	δ_S	Ratio of mean to nominal for load effect
l_b	Bearing length of the load, measured parallel to the axis of the chord member, in.	η	Ratio of branch height to chord width for rectangular HSS (H_b/B)
l_{end}	Distance from the near side of the connecting branch or plate to the end of chord, in.	η^*	Ratio of branch height to chord height for rectangular HSS (H_b/H)
m	Degrees of freedom, $n_t - 1$	θ	Acute angle between the branch and chord, degrees
n_0	Ratio of stress in the chord connecting face to the chord yield stress (+ indicates chord tensile stress; - indicates chord compressive stress)	θ_C	Central safety factor
n_t	Number of tests	λ	Slenderness of a column or chord sidewall = KL/r
p_F	Probability of failure	$\lambda_{0.65}$	Nondimensional chord sidewall slenderness with an effective length factor of 0.65
r	Radius of gyration, in.	$\lambda_{1.0}$	Nondimensional chord sidewall slenderness with an effective length factor of 1.0
t	Design wall thickness of rectangular HSS chord member, in.	λ_C	Nondimensional chord sidewall slenderness
t_b	Design wall thickness of rectangular HSS branch member, in.	λ_{KL}	Nondimensional chord sidewall slenderness with the Kim and Lee (2021) effective length factor
Ω	Safety factor	σ_P	Standard deviation of the ratio of actual-to-nominal strength
α	Coefficient of separation, generally taken as 0.55	σ_R	Standard deviation of R
α_D	Load factor for dead load	σ_S	Standard deviation of S
α_L	Load factor for live load	σ_g	Standard deviation of g
		ϕ	Resistance factor
		χ	Reduction factor for (column) buckling

REFERENCES

- AISC (2016), *Specification for Structural Steel Buildings*, ANSI/AISC 360-16, American Institute of Steel Construction, Chicago, Ill.
- AISI (2016), *North American Specification for the Design of Cold-Formed Steel Structural Members*, AISI S100-16, American Iron and Steel Institute, Washington, D.C.
- ASCE (2016), *Minimum Design Loads and Associated Criteria for Buildings and Other Structures*, ASCE/SEI 7-16, American Society of Civil Engineers, Reston, Va.
- ASTM (2021), *Standard Specification for Cold-Formed Welded and Seamless Carbon Steel Structural Tubing in Rounds and Shapes*, ASTM A500/A500M-21, ASTM International, West Conshohocken, Pa.
- Benjamin, J.R. and Cornell, C.A. (1970), *Probability, Statistics, and Decision for Civil Engineers*, McGraw-Hill, New York, N.Y.
- Bu, X.D., Wei, F., and Packer, J.A. (2021), “Laterally Offset RHS X-Connections,” *Journal of Structural Engineering*, ASCE, Vol. 147, No. 1, 04020286.
- CEN (2021), *Eurocode 3: Design of Steel Structures—Part 1–8: Design of Joints*, prEN 1993-1-8, European Committee for Standardization, Brussels, Belgium.
- CSA (2011), *Guidelines for the Development of Limit States Design Standards*, CSA S408-11, Canadian Standards Association, Toronto, Canada.
- CSA (2019a), *Design of Steel Structures*, CSA S16:19, Canadian Standards Association, Toronto, Canada.
- CSA (2019b), *Canadian Highway Bridge Design Code*, CSA S6:19, Canadian Standards Association, Toronto, Canada.
- Davies G. and Roodbaraky K. (1987), “The Effect of Angle on the Strength of RHS Joints,” *Proceedings of the International Meeting on Safety Criteria in Design of Tubular Structures*, Tokyo, Japan.
- Ellingwood, B. and Culver, C. (1977), “Analysis of Live Loads in Office Buildings,” *Journal of the Structural Division*, ASCE, Vol. 103, No. 8, pp. 1,551–1,560.
- Ellingwood, B., Galambos, T.V., MacGregor, J.G., and Cornell, C.A. (1980), “Development of a Probability Based Load Criterion for American National Standard A58,” *Special Publication 577*, National Bureau of Standards, Gaithersburg, Md.
- Fan, Y. (2017), “RHS-to-RHS Axially Loaded X-Connections Offset towards an Open Chord End,” M.A.Sc. Thesis, University of Toronto, Toronto, Canada.
- Feldmann, M., Schillo, N., Schaffrath, S., Viridi, K., Björk, T., Tuominen, N., Veljkovic, M., Pavlovic, M., Manoleas, P., Heinisuo, M., Mela, K., Ongelin, P., Valkonen, I., Minkkinen, J., Erkkilä, J., Pétursson, E., Clarin, M., Seyr, A., Horváth, L., Kövesdi, B., Turán, P., and Somodi, B. (2016), “Rules on High Strength Steel,” Publications Office of the European Union, Luxembourg.
- Galambos, T.V. (2006), “Reliability of the Member Stability Criteria in the 2005 AISC Specification,” *International Journal of Steel Structures*, Vol. 4, No. 4, pp. 223–230; and *Engineering Journal*, AISC, Vol. 43, No. 4, pp. 257–265.
- Galambos, T.V. and Ravindra, M.K. (1973), “Tentative Load and Resistance Factor Design Criteria for Steel Buildings,” Research Report No. 18, Civil and Environmental Engineering Department, Washington University, St. Louis, Mo.
- Galambos, T.V. and Ravindra, M.K. (1977), “The Basis for Load and Resistance Factor Design Criteria of Steel Building Structures,” *Canadian Journal of Civil Engineering*, Vol. 4, pp. 178–189.
- Galambos, T.V. and Ravindra, M.K. (1978), “Properties of Steel for Use in LRFD,” *Journal of the Structural Division*, ASCE, Vol. 104, No. 9, pp. 1,459–1,468.
- Hong, H.P. and Zhou, W. (1999), “Reliability Evaluation of RC Columns,” *Journal of Structural Engineering*, ASCE, Vol. 125, No. 12, pp. 784–790.
- IIW (2012), *Static Design Procedure for Welded Hollow Section Joints—Recommendations*, 3rd Ed., IIW Doc. XV-1402-12, International Institute of Welding, Genoa, Italy.
- ISO (2013), *Static Design Procedure for Welded Hollow Section Joints—Recommendations*, ISO 14346, International Organization for Standardization, Geneva, Switzerland.
- Kennedy, D.J.L. and Baker, K.A. (1984), “Resistance Factors for Steel Highway Bridges,” *Canadian Journal of Civil Engineering*, Vol. 11, pp. 324–334.
- Kennedy, D.J.L. and Gad Aly, M. (1980), “Limit States Design of Steel Structures—Performance Factors,” *Canadian Journal of Civil Engineering*, Vol. 7, pp. 45–77.
- Kim, J.H., Lee, C.H., Kim, S.H., and Han, K.H. (2019), “Experimental and Analytical Study of High-Strength Steel RHS X-Joints under Axial Compression,” *Journal of Structural Engineering*, ASCE, Vol. 145, No. 12, 04019148.
- Kim, S.H. and Lee, C.H. (2021), “Chord Sidewall Failure of RHS X-Joints in Compression and Associated Design Recommendations,” *Journal of Structural Engineering*, ASCE, Vol. 147, No. 8, 04021111.

- Kuhn, J. (2018), "Numerical Study of Full-Width, RHS-to-RHS, X-Connections under Transverse Compression," Master's Thesis, Karlsruhe Institute of Technology, Karlsruhe, Germany.
- Kuhn, J., Packer, J.A., and Fan, Y. (2019), "Rectangular Hollow Section Webs under Transverse Compression," *Canadian Journal of Civil Engineering*, Vol. 46, pp. 810–827.
- Lan, X., Wardenier, J., and Packer, J.A. (2021), "Design of Chord Sidewall Failure in RHS Joints Using Steel Grades up to S960," *Thin-Walled Structures*, Vol. 163, 107605.
- Lind, N.C. (1971), "Consistent Partial Safety Factors," *Journal of the Structural Division*, ASCE, Vol. 97, No. 6, pp. 1,651–1,670.
- Liu, J. (2016), "Updates to Expected Yield Stress and Tensile Strength Ratios for Determination of Expected Member Capacity in the 2016 AISC Seismic Provisions," *Engineering Journal*, AISC, Vol. 53, No. 4, pp. 215–228.
- Lundberg, J.E. and Galambos, T.V. (1996), "Load and Resistance Factor Design of Composite Columns," *Structural Safety*, Vol. 18, pp. 169–177.
- Meimand, V.Z. and Schafer, B.W. (2014), "Impact of Load Combinations on Structural Reliability Determined from Testing Cold-Formed Steel Components," *Structural Safety*, Vol. 48, pp. 25–32.
- Melchers, R.E. and Beck, A.T. (2018), *Structural Reliability Analysis and Prediction*, 3rd Ed., Wiley, Hoboken, N.J.
- NBC (2020), *National Building Code of Canada*, NBC 2020 Part 4, National Research Council, Ottawa, Canada.
- Nowak, A.S. and Lind, N.C. (1979), "Practical Bridge Code Calibration," *Journal of the Structural Division*, ASCE, Vol. 105, No. 12, pp. 2,497–2,510.
- Packer, J.A. and Kremer, J.S.M. (1988), "A Reliability Assessment of Tubular Joint Specifications," *Canadian Journal of Civil Engineering*, Vol. 15, pp. 167–175.
- Packer, J.A., Wardenier, J., Zhao, X.L., van der Vegte, G.J., and Kurobane, Y. (2009), *Design Guide for Rectangular Hollow Section (RHS) Joints under Predominantly Static Loading*, CIDECT Design Guide No. 3, 2nd Ed., CIDECT, Geneva, Switzerland.
- Pandey, M. and Young, B. (2020), "Structural Performance of Cold-Formed High Strength Steel Tubular X-Joints under Brace Axial Compression," *Engineering Structures*, Vol. 208, 109768.
- Ravindra, M.K. and Galambos, T.V. (1978), "Load and Resistance Factor Design for Steel," *Journal of the Structural Division*, ASCE, Vol. 104, No. 9, pp. 1,337–1,353.
- Rudman, D.F. (2021), "Reliability of RHS X-Connections in Branch Axial Compression," M.A.Sc. Thesis, University of Toronto, Toronto, Canada.
- Schmidt, B.J. and Bartlett, F.M. (2002), "Review of Resistance Factor for Steel: Resistance Distributions and Resistance Factor Calibration," *Canadian Journal of Civil Engineering*, Vol. 29, pp. 109–118.
- Wardenier, J., Lan X.Y., and Packer J.A. (2020), "Evaluation of Design Methods for Chord Sidewall Failure in RHS Joints Using Steel Grades up to S960—State of the Art," IIW Doc. XV-E-489-20.
- Wei, F. and Packer, J.A. (2021), "AISC Provisions for Web Stability under Local Compression Applied to HSS," *Engineering Journal*, AISC, Vol. 58, No. 1, pp. 11–32.
- Xi, Q. and Packer, J.A. (2021), "Assessing the Probabilistic Assumptions behind Structural Reliability via Simulation," Canadian Society for Civil Engineering Annual Conference, Virtual, Canada, STR230.
- Yu, Y. (1997), "The Static Strength of Uniplanar and Multiplanar Connections in Rectangular Hollow Sections," Ph.D. Thesis, Delft University of Technology, Delft, The Netherlands.

Future Hot-Rolled Asymmetric Steel I-Beams

JUDY LIU

INTRODUCTION

Ongoing research on future hot-rolled asymmetric steel I-beams is highlighted. This study is currently under way at Texas A&M University, led by Dr. Matthew Yarnold, Assistant Professor in the Department of Civil and Environmental Engineering. Dr. Yarnold's research interests include building structural systems, bridge infrastructure, hybrid building energy-structure performance, and engineering education. Dr. Yarnold has been recognized for his teaching and research with the Robert J. Dexter Memorial Award, ASCE Nashville Branch Engineering Educator of the Year, an AISC Early Career Faculty Award, and AISC's Milek Fellowship. The four-year Milek Fellowship is supporting this research on the behavior of hot-rolled asymmetric I-beams. The research team is part way through year three of the four-year study. Selected results from a manufacturing study, full-scale experiments, and an initial sizing study are highlighted, along with a preview of future work.

MOTIVATION FOR THE STUDY

This investigation into the behavior of hot-rolled asymmetric I-shapes, or "A-shapes," is motivated by the expected gains in structural, fabrication, and construction efficiency.

Judy Liu, PhD, Research Editor of the AISC *Engineering Journal*, Professor, Oregon State University, School of Civil and Construction Engineering, Corvallis, Ore. Email: judy.liu@oregonstate.edu

Improvements in steel building economy can be realized for shallow residential and commercial floor systems. Built-up asymmetric shapes have demonstrated advantages in composite construction, whether with precast or cast-in-place concrete. Precast concrete panels can be supported on the wider bottom flanges; the narrower top flange does not interfere with the panel during placement (Figure 1). This type of assembly could also be used for deep metal decking. For conventional cast-in-place concrete with the deck slab supported on the top flange, a narrower flange corresponds to its relatively low contribution to the strength and stiffness of the composite flexural member. However, the top flange is important for the bare-steel member's ability to support the construction loads. Currently, gains in structural and construction efficiency are outweighed by fabrication costs. Fabrication of current asymmetric shapes can be labor and material intensive with welding of pieces cut from two separate sizes of hot-rolled sections or welding of hot-rolled shapes and plates (Stoddard and Yarnold, 2022). Production of hot-rolled A-shapes would reduce fabrication costs while maintaining structural and construction efficiency.

RESEARCH GOAL AND PLAN

With the long-term goal of regular mill production of hot-rolled A-shapes, the research team is conducting an integrated numerical and experimental investigation into the behavior of these asymmetric shapes. The team aims to develop recommended A-shape cross-sections with comparable or improved structural efficiency compared to built-up asymmetric shapes (Stoddard and Yarnold, 2022). Over

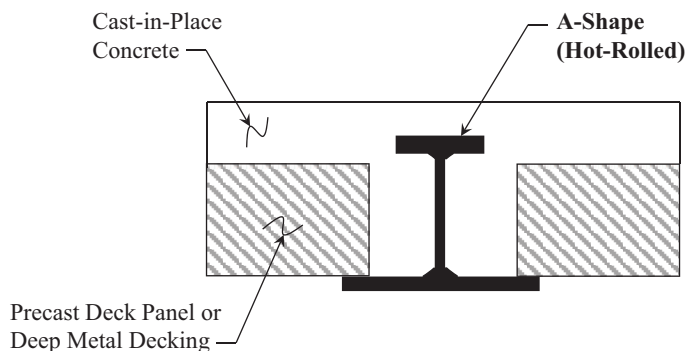


Fig. 1. Schematic of A-shape with cast-in-place concrete on deep metal decking or precast panel.

the first two years of the project, the team conducted a manufacturing study, initial concept design and experimental testing, and an initial sizing study for residential facilities. Analytical models have also been developed and are being used to refine A-shape sizing. Experimental validation studies are also under way in the third year of the project, and year four will see a final shape study and results synthesized into design aids.

MANUFACTURING STUDY

Future production of the asymmetric shapes requires consideration of practical limitations and potential issues with hot-rolling of the A-shapes. Proportioning and sizing guidance was provided by mill experts. The producers also raised concerns about residual stresses and deformations after hot-rolling and cooling. A computational study and proof-of-concept (POC) beams were used to address those concerns.

Steel Mill Guidance

The steel mill guidance came from experts across different disciplines and producers. The three U.S. steel producers were Nucor, Steel Dynamics, and Gerdau. Industry roll-pass engineers, roll-pass designers, metallurgical engineers, roll-mill supervisors, and product developers collaborated with the researchers on recommendations for A-shape production. Cost considerations motivated a recommendation to match final flange dimensions with those of currently rolled shapes. Other sizing guidance included proportioning of shapes to have equal top and bottom flange areas, minimum web thickness of 0.50 in., and flange-to-web thickness ratios no larger than 2.0. Enlarged fillets were recommended to reduce cracking in the flange-to-web connection. A-shapes will be produced using ASTM A992/A992M steel.

Residual Stresses

Hot-rolled shapes develop residual stresses while cooling at the mill. Some steel experts expressed concerns for excessive residual compressive stresses and adverse impact on A-shape flange buckling. Those concerns were addressed through finite element modeling and reference to POC beams.

A three-dimensional, thermal-mechanical, finite element (FE) modeling approach was developed through a sensitivity study and reference to past research. A coupled thermal-displacement analysis utilized the nonlinear transient thermal and stress analysis capabilities of ABAQUS/CAE. Single tetrahedral elements were used through the flange and web thicknesses of simulated A-shapes. Element type and meshing were chosen with consideration for flange

stress profiles, modeling of the flange-to-web fillets, and computational processing time. A modeled beam length of three times the depth allowed for sufficient development of the stresses (Stoddard, 2022). Beams were supported at corners only with pins or rollers to allow for free contraction. Temperature-dependent properties, such as elastic modulus and Poisson's ratio, were modeled based on published test results. The initial temperature of 2,372°F mimicked pre-rolling conditions; the beams then cooled to an ambient temperature of 68°F. Additional details can be found in Stoddard and Yarnold (2022).

The thermomechanical validation study included comparisons with POC beams. Simulated A-shapes were created with longitudinal cuts along the top flanges of W12×65 beams, as shown in Figure 2. The simulated A-shape had half the top flange width of the original W-shape. This procedure did not provide the correct grain structure for the rolled shapes but avoided the expense of retooling an entire roll line (Stoddard and Yarnold, 2022). The beams were reheated to approximately 1,740°F. Noncontact temperature measurements taken during the cooling process (Figure 3) were compared with the FE model results. Differences ranged from 1.9% to 15.8%, with larger differences being attributed to factors such as a slight wind in the facility. Additional information and a description of the literature comparison portion of the thermomechanical validation study can be found in Stoddard and Yarnold (2022).

The computational parametric study explored variations on two W-shapes. The W8×31 and W18×76 were selected to represent two section depths found in composite construction. The width or thickness of the top flange was then varied from 25% to 200% of the original. There were 30 unique cross sections, and the "limits produced unrealistic extreme cases that were included to determine the full spectrum of behavior" (Stoddard and Yarnold, 2022).

The residual stresses in the webs were most affected by variations in the flange properties. The beams were largely insensitive to changes in the flange thickness or width. The biggest changes in flange residual stress were seen with the width-to-thickness ratio, b/t . A b/t limit was introduced, corresponding to a flange residual stress of approximately 30% of the yield stress. Additional details on the residual stress study can be found in Stoddard (2022).

Deformations

Deformations (curvature) resulting from the cooling process were examined. A concern was that excessive deformations would require more rotary straightening and cause issues with handling throughout the mill. In addition, 30 ft beams were modeled and analyzed using the procedure described for the residual stress study. Initial imperfections were considered but were shown to have minimal impact on

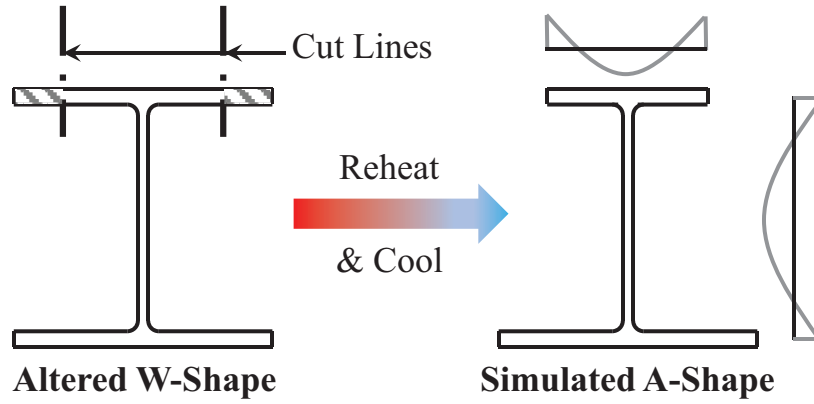


Fig. 2. W-shape altered, reheated, and cooled to simulate a hot-rolled A-shape; residual stresses qualitatively graphed on the simulated A-shape.



Fig. 3. Noncontact temperature measurements being taken of the cooling A-shapes.

the cooling deformations. The resulting camber was compared with the ASTM limit for a channel, another asymmetric hot-rolled section. Some beams did exceed the limit but were deemed to have small enough deformation to be corrected with rotary straightening (Stoddard and Yarnold, 2022). No cross-sectional limitation for cooling deformations was placed on future A-shapes. Additional details on the deformation study can be found in Stoddard (2022).

FULL-SCALE FEASIBILITY EXPERIMENTS

Full-scale experiments were used to evaluate the constructability and performance of a steel-concrete composite floor system with A-shapes. These experiments focused on A-shape beams with shallow precast panels and a cast-in-place topping slab. The experiments included three different phases of testing and contributed knowledge on the behavior of shallow composite steel-concrete members using A-shapes.

Experimental Setup

The test specimen and setup began with the steel frame for the construction loading (placement of panels), followed by the cast-in-place topping, and then vertical loading by the hydraulic actuator. There were three A-shape beams in parallel that spanned between stub columns and supported precast concrete panels with a cast-in-place topping (Figure 4). The load frame straddled the test specimen at mid-span. The center A-shape beam was loaded by an actuator and spreader beam.

The overall geometry of the test specimen was dictated by the laboratory and POC beams used. The floor tie-down locations are at 3 ft spacing. The load frame could be

configured for 3 ft increments as well. With consideration for the POC beams, the tie-down locations, and the physical dimensions of the stub columns and load frame, a 6 ft POC beam spacing and approximate 23 ft length were chosen.

The test specimen used simple connections with modifications at the edge beams. Bolted double-angle connections connected all POC A-shape beams to the columns. However, concerns about eccentric loading of the edge beams during concrete topping placement prompted additions of top and seat angles at those locations. These angles were welded to the edge beam flanges and bolted to the columns. The top and seat angles could be unbolted at a later stage, converting the edge beams back to a simply supported condition (Yarnold, 2022; Davis, 2022).

Instrumentation included strain gages and string potentiometers for displacement measurements. The strain gages were placed on the top and bottom flanges of all beams at three different cross sections. One cross section was at beam mid-span; the other two were located 3 ft to either side. The displacement measurements were taken at the beam mid-span location. Each beam had a vertical displacement measurement. One edge beam also had two lateral displacement measurements that could be used to calculate rotation. Additional details of the test setup, instrumentation, and loading can be found in Davis (2022).

Experimental Results

The initial system experiment was designed to capture composite A-shape considerations and behavior at construction and in service. The experiments included Test 1: Precast panel placement, Test 2: Concrete topping slab, and Test 3: In-service and ultimate strength testing. The knowledge gained helped to inform the initial sizing of A-shapes.

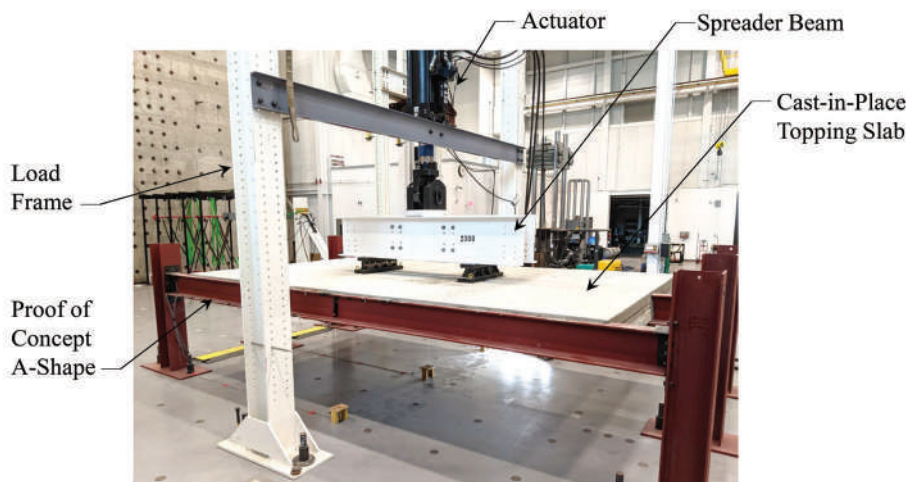


Fig. 4. Test setup for the full-scale experiment.

Test 1: Precast Panel Placement

The precast panel placement test explored panel loading for different scenarios and beam boundary conditions. The 8-in.-thick, 4 ft × 6 ft hollow-core precast panels, supported on the beams' bottom flanges, were placed in two different sequences for a simply supported center beam and fixed-fixed edge beams. For loading scenario one, precast panels 1–5 were placed in order in one bay, and then panels 6–10 placed in the next bay, as shown in Figure 5(a). For loading scenario three, panel placement alternated between adjacent bays—that is, panel 1 in one bay, followed by panel 2 in the adjacent bay, and so on, as shown in Figure 5(c). For loading scenario two, the bolts in the top and seat angles were removed to revert back to pinned beam-to-column connections, and then one bay was loaded with panels 1–5, as shown in Figure 5(b).

Loading scenario two provided the most significant results. The center and edge beams experienced heavier torsional demands than in the other loading scenarios. The measured and theoretical combined bending and torsional stresses were compared, as were the edge beam rotations. Maximum measured and predicted stresses were 5.01 ksi and 5.29 ksi, respectively. The measured edge beam rotation of 1.62° compared favorably to the theoretical rotation of 1.76°. The theoretical stresses and rotations were conservative, due in part to the assumption of pure “pin” connections at the beam ends.

Test 2: Concrete Topping Slab

In preparation for casting of the concrete topping slab, spray expanding foam and silicone caulk were used to seal voids and joints between elements, such as the joint between the precast panel and bottom beam flange. Plywood formwork was built and fitted to the test specimen to achieve 1½ in. of cover over the top beam flanges. A grid of No. 4 Grade 60 reinforcing steel at 16 in. on center was hand tied and supported on 3 in. chairs and the center beam top flange. The slab was cast using a concrete dump bucket attached to the laboratory's overhead crane. During curing, the slab was sprayed with water every 6 hr. There was no need to cover the slab in the laboratory's temperature-controlled environment (Yarnold, 2022).

Concerns motivated deformation and capacity limit state checks for the construction loading. Measured out-of-plane rotation of the edge beams during the concrete pour was approximately 53% of the 4° limit. The researchers noted that while the rotations were “better than that anticipated,” the edge beams would likely be stiffened for the torsional demands in a real building. Lateral torsional buckling (LTB) of the center beam exhibited a demand-to-capacity ratio of 0.45. Here, the researchers noted that the predicted capacity did not consider the stabilizing effect of the load placed at the bottom flange rather than at the top of the beam (Yarnold, 2022; Davis, 2022). The results suggested potential improvements and greater efficiencies in A-shape designs.

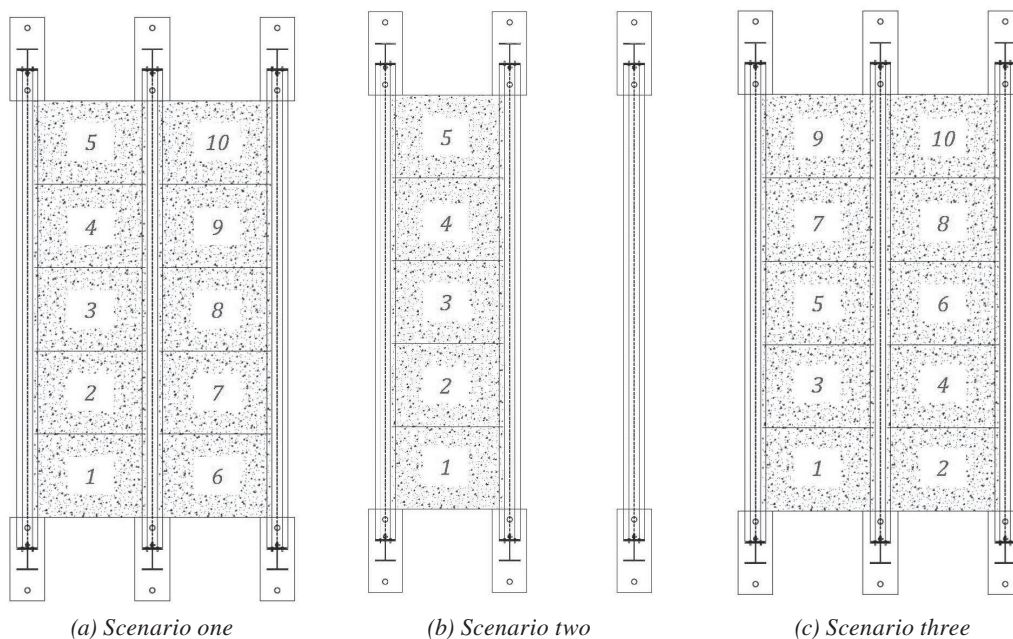


Fig. 5. Order of panel placement for loading.

Test 3: In-Service and Ultimate Strength Testing

With the test frame shown in Figure 4, 220 kip hydraulic actuator, and a spreader beam, a four-point bending test was applied at the center test beam. The load was applied with two steel pin assemblies attached to the spreader beam and spaced 6 ft apart. This created a constant moment region in the center of the beam. A loading rate of 2 kips per minute was used for evaluation of the in-service and ultimate strengths. The in-service loading was the equivalent of 100 psf for the floor system. The ultimate loading was equivalent to 500 psf.

The in-service loading results confirmed the viability of A-shapes for composite floor systems. Strain measurements were relatively low and corresponded to the expected neutral axis location for a fully composite section. Deflections were also low. For the design service load of 100 psf, the measured midspan deflections were on the order of the beam span/3000. The deflections easily satisfied a limit of span/360 (Yarnold, 2022; Davis 2022).

The ultimate strength test results suggested options for design. At a loading corresponding to 500 psf, there was a loss of composite action between the concrete and steel for the center beam. The load redistributed to the edge beams and was sustained for 20 min until unloading. Load at failure corresponded to 54% of the composite capacity. Mechanical connections or other means to increase the steel-concrete bond could be considered in design. Such means might be warranted for longer spans and/or loads, but the strength increase would come at the cost of construction speed and efficiency (Yarnold, 2022).

Theoretical vs. Experimental Comparison

Comparisons between the experimental results and theoretical predictions provided additional insights for analysis and design of these floor systems. Assumptions for the theoretical predictions include ideally pinned and fixed to

establish bounds for the partially restrained connections, a 25%–50%–25% load distribution across the three beams, a composite beam effective width corresponding to the beam tributary width, and fully composite behavior. The measured strains and displacements for the center beam did show closer to ideal pinned connection behavior, as well as more fixity at the supports for the edge beams. The design assumption of pinned, or simple, connections was deemed to be conservative and appropriate (Davis, 2022). As mentioned previously, the data also confirmed composite action between the concrete and encased steel section at service-level loads. There are no mechanical connections; the composite behavior is developed from bond and friction (Yarnold, 2022). Additional details of the tests and comparisons can be found in Davis (2022).

INITIAL SIZING STUDY FOR RESIDENTIAL FACILITIES

A shallow-depth residential floor system case study was used to investigate the flange and web sizing of A-shapes. The case study utilized the configuration seen in the experiment—A-shapes supporting precast concrete panels and a cast-in-place topping slab. Flange and web geometries were varied for different beam depths, spans, and spacing. Beam depths and spacing ranged from 8 to 12 in. deep and 10 to 26 ft, respectively. In addition, 20 to 30 ft span lengths were considered.

The analytical study followed the loading from the initial construction stages to the building in service. Construction load cases (Load Cases 1, 2a, 2b) were noncomposite, and the in-service loading case was composite (Load Case 3) (Figure 6). The construction loads considered an eccentric loading for precast panel placement (Load Case 1), a uniform flexural demand from the concrete topping and construction live load of 20 psf (Load Case 2a), and an eccentric loading resulting in flexural and torsional demands (Load

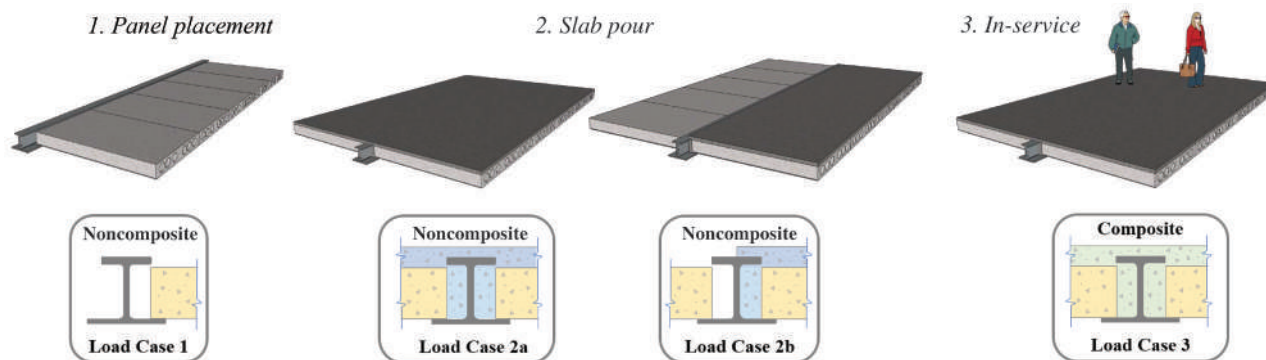


Fig. 6. Load cases for the initial sizing study for residential facilities.

Case 2b). The beam end supports are modeled as pinned connections. The out-of-plane rotation limit was set at 4° , and beam span/240 is the service dead plus live load deflection limit. For the building in service, the composite A-shape beams were designed for a live load of 100 psf and a live load deflection limit of beam span/360. Following AISC Design Guide 11, *Vibrations of Steel-Framed Structural Systems Due to Human Activity* (Murray et al., 2016), the beams were also designed for a floor vibration live loading of 8 psf and a walking excitation loading of 65 lb (Stoddard, 2022).

A collection of A-shape cross sections was evaluated for the construction and in-service design parameters. Cross-sectional properties were dictated by the previously mentioned manufacturing constraints and seat width for the precast panels. Top flange areas were set equal to the bottom flange areas. Web thicknesses were constrained to at least 0.5 in. or half of the top flange thickness. Bottom flanges were required to be 4 in. wider than the top flange to provide a 2 in. seat for the panel. The collection was developed by varying the top flange geometry and adjusting the other parameters.

Controlling limit states varied by load case. Out-of-plane rotation controlled the A-shape designs for Load Case 1. The service dead and live load deflection limit controlled for Load Case 2a. Stability [i.e., lateral-torsional buckling (LTB)] was a controlling limit state for Load Cases 2a and 2b. Normalized moment capacities versus cross-sectional

area are shown in Figure 7. Highlighted in Figure 7(a) are the ranges of moment capacity for the varying A-shape proportions. Figure 7(b) summarizes the controlling limit states of elastic LTB, inelastic LTB, and compression flange local buckling (CFLB). Meanwhile, vibration was the major design consideration for Load Case 3.

FUTURE RESEARCH

Future work is focused on refining the A-shape recommendations by revisiting limitations and conservative assumptions to improve the modeling, update sizing, conduct new experimental validation studies, and generalize the results for design. Limitations included the use of normal-weight concrete for one topping slab depth and one compressive strength. The team will investigate the potential advantages for variations in compressive strength and use of lightweight concrete. The team will also explore increased strength and stiffness versus higher dead load for different topping slab thicknesses. The rotation limit of 4.0° requires further investigation and justification. Conservative assumptions, including those made for initial vibration calculations, will be refined. Modeling and sizing of A-shapes will be updated accordingly, as experimental validation studies further expand knowledge about behavior of the recommended shapes. The research team will synthesize results from the analytical and experimental studies to produce design aids with supporting documentation.

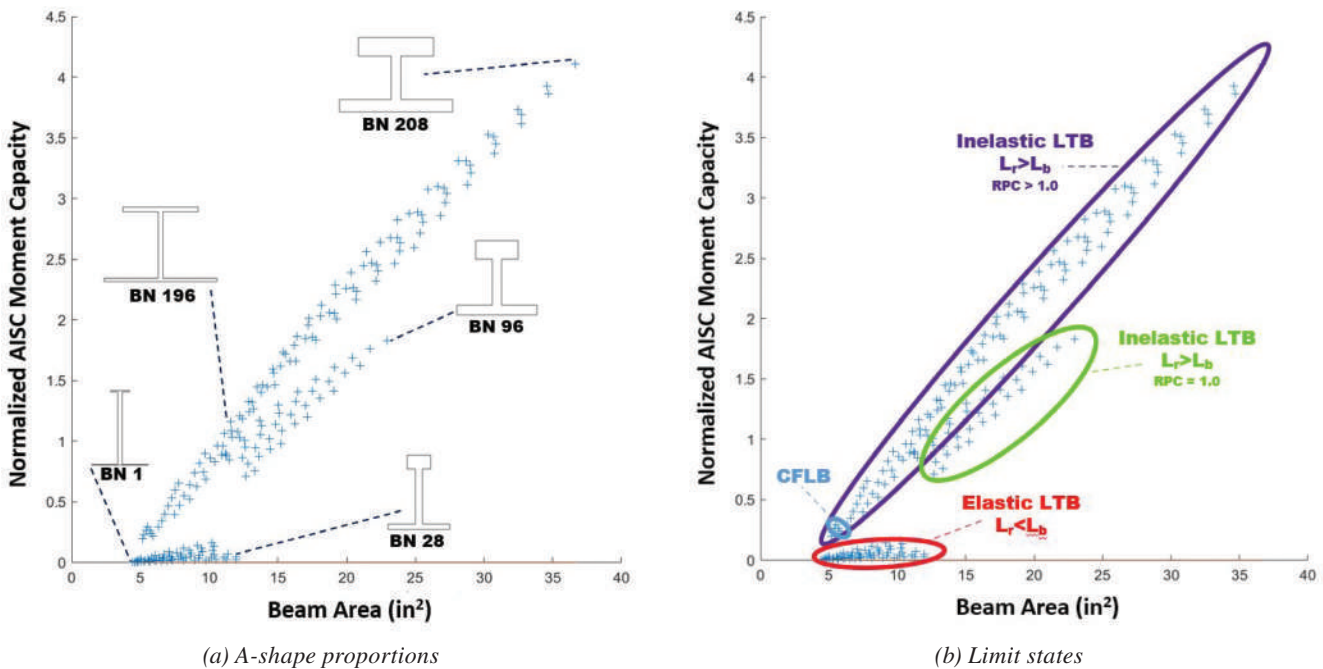


Fig. 7. Normalized moment capacity vs. beam area organized by A-shape proportions and limit states.

ACKNOWLEDGMENTS

Thank you to Dr. Yarnold for his many contributions to this article. The work of graduates Eric Stoddard (Ph.D.) and Sheyenne Davis (M.S.), Ph.D. student Chase Ottmers, and undergraduate student Santiago Chavez is also recognized. The research is sponsored by the American Institute of Steel Construction (AISC); Devin Huber, Director of Research, is the project manager. The researchers would like to thank AISC Research Oversight Committee members Margaret Matthew (AISC), Chris Garrell (AISC), Chia-Ming Uang (University of California–San Diego), Tom Sabol (Englekirk), Joe Zona (Simpson Gumpertz & Heger), Ronnie Medlock (High Steel), Duff Zimmerman (Cooper Steel), Tabitha Stine (Nucor), Shane Vernon (Nucor), Christopher Hoyt (Gerdau), Scott Meaney (Gerdau), Rafael Garcia (Gerdau), Robert Carter (Steel Dynamics), Drew Seely (Steel Dynamics), and Richelle Wilson (Steel Dynamics). Any findings or recommendations are those of the researchers and do not necessarily reflect the views of the sponsor.

REFERENCES

- Davis, S. (2022), “Full Scale Floor System Testing for Future Hot-Rolled Asymmetric Steel I-Beams,” M.S. Thesis, Texas A&M University, College Station, Texas.
- Murray, T.M., Allen, D.E., Ungar, E.E., and Davis, D.B. (2016), *Vibrations of Steel-Framed Structural Systems Due to Human Activity*, Design Guide 11, AISC, Chicago, Ill.
- Stoddard, E.A. (2022), “Behavior of Hot Rolled Asymmetric Steel I-Beams: Concept to Construction,” Ph.D. Dissertation, Texas A&M University, College Station, Texas.
- Stoddard, E. and Yarnold, M (2022), “Residual Stress and Global Deflection Limits for Future Hot-Rolled Steel Asymmetric I-Beams,” *Journal of Structural Engineering*, ASCE, Vol. 148, No. 1, [https://doi.org/10.1061/\(ASCE\)ST.1943-541X.0003204](https://doi.org/10.1061/(ASCE)ST.1943-541X.0003204).
- Yarnold, M. (2022), “Behavior of Hot Rolled Asymmetric Steel I-Beams,” Status Report 2—AISC Milek Fellowship Report, American Institute of Steel Construction, Chicago, Ill.

Guide for Authors

Scope *Engineering Journal* is dedicated to the improvement and advancement of steel construction. Its pages are open to all who wish to report on new developments or techniques in steel design, research, the design and/or construction of new projects, steel fabrication methods, or new products of significance to the uses of steel in construction. Only original papers should be submitted.

General Papers intended for publication should be submitted by email Margaret Matthew, editor, at matthew@aisc.org.

The articles published in the *Engineering Journal* undergo peer review before publication for (1) originality of contribution; (2) technical value to the steel construction community; (3) proper credit to others working in the same area; (4) prior publication of the material; and (5) justification of the conclusion based on the report.

All papers within the scope outlined above will be reviewed by engineers selected from among AISC, industry, design firms, and universities. The standard review process includes outside review by an average of three reviewers, who are experts in their respective technical area, and volunteers in the program. Papers not accepted will not be returned to the author. Published papers become the property of the American Institute of Steel Construction and are protected by appropriate copyrights. No proofs will be sent to authors. Each author receives three copies of the issue in which his contribution appears.

Manuscripts Manuscripts must be provided in Microsoft Word format. Include a PDF with your submittal so we may verify fonts, equations and figures. View our complete author guidelines at aisc.org/ej.



Smarter. Stronger. Steel.

American Institute of Steel Construction
130 E Randolph St, Ste 2000, Chicago, IL 60601
312.670.2400 | aisc.org/ej